PREDICTION OF PERMANENT DEFORMATION IN RAILWAY TRACK

Xiaoyi Shi

BEng., MSc.

Thesis submitted to the University of Nottingham

For the degree of Doctor of Philosophy

April 2009

To my parents

ABSTRACT

This research investigated the deformation behaviour of railway ballast, particularly the vertical settlements under repeated traffic loading. Experiments were conducted to study ballast deformation and particle breakage under different confining pressures and loading conditions. Computational analysis was deployed to calculate the stress level within the ballast layers. A ballast settlement model was developed using the experimental data and analytical results. Full-scale cyclic loading tests simulating the railway trackbed were finally carried out to validate and adjust the settlement model.

The experimental programme of this research comprised large scale triaxial tests, Composite Element Test (CET) and simulation under a full-scale Railway Test Facility (RTF). Within the triaxial tests, a series of monotonic, cyclic and multi-stage loading tests were carried out. Results from the monotonic triaxial tests including friction angle, initial stiffness, cohesion, dilation angle and hardening behaviour were fed into a finite element method (FEM) simulation of ballast directly under a sleeper using the ANSYS computer program. The extended Drucker-Prager model with hardening, which simulates the plastic

behaviour of granular materials under relatively large loads, was adopted in the FEM analysis in order to account for the inelastic behaviour of railway ballast.

The FEM analysis provided the crucial stress level estimations anticipated in the ballast layers beneath a loaded sleeper. Meanwhile, cyclic and multi-stage loading triaxial tests under different confining pressures were conducted to obtain empirical equations which describe the deformation of ballast under a single stress condition. A ballast settlement model was then developed as a function of the number of loading cycles, the magnitude of the load and the formation stiffness, which predicts the resultant vertical settlement beneath a sleeper under repeated traffic loading. The ballast settlement model was then validated in the CET and RTF.

The CET is a full-scale simulation of a sleeper section under repeated traffic loading. The RTF on the other hand is a full-scale three sleeper rig that simulates passing traffic by applying sinusoidal loading to the sleepers. The aim of the CET and RTF was to validate the settlement model in a realistic track environment. Both the CET and RTF are designed to investigate the settlement of the sleeper and the ballast at different depths. The test results have confirmed the predictions of the ballast settlement model that the most significant vertical settlement occurred in the top layer of ballast directly beneath a sleeper.

The settlement model was presented with the main influencing factors of ballast properties, stress condition and compaction method. Based on the ballast

settlement model, a better understanding of railway track life performance could be obtained. Moreover, this will also benefit the design of appropriate maintenance and renewal strategies.

ACKNOWLEDGEMENTS

First and foremost, I would like to thank Dr. Nick Thom for his excellent guidance and tireless supervision throughout the course of this research project. His enthusiasm and passion has been my constant source of motivation.

I would like to thank Professor Stephen Brown and Professor Glen McDowell, co-supervisors, for their invaluable advice, suggestions and encouragement.

I am also grateful to Barry Brodrick, Ian Richardson and Andrew Maddison who have been immense figures in my research with their technical support. I am also thankful for Barry's proof reading on the technical issue in this dissertation.

My gratitude is also due to Ka Ho Li, Jiantao Wu and Junwei Wu, for the many interesting discussion on engineering and life, and making this research very much enjoyable. The same can be said for Tao Lu, Cho Ching Kwan and Bhanitiz Aursudkij for the many fascinating discussion in the research room and laboratory. Many thanks to all the colleagues and friends, particularly Pic, Riccardo, Ted, Phil and Nono, for making this journey so much easier. In addition, I would also like to thank Kiki, Leo, Josh and James who kindly spent hours proof-reading my thesis and gave me valuable comments.

My gratitude to the sponsoring organisation of this project – NTEC and the University of Nottingham, without the kind contribution in finances, it would not have been possible to complete the project.

Finally, I would like to thank my fiancée Jiang Yan for her constant encouragement, sacrifices and support throughout the period of this project. I cannot forget also my parents and all other members of my family who were with me right from the very start. They have always been my source of motivation.

DECLARATION

The work described in this thesis was conducted at the University of Nottingham, Department of Civil Engineering between October 2005 and October 2008. I declare that the work is my own and has not been submitted for a degree of another university.

LIST OF CONTENTS

LIST OF FIGURES

LIST OF TABLES

NOTATION

a	constant related to ballast properties
b	coefficient related to confining pressure
B	coefficient
c	cohesion
c'	coefficient (between 0.25 and 0.55)
C	constant from integration
C_1, C_2	input material parameters in ANSYS
CET	composite element test
C_r	compaction ratio
d	intercept of yield surface in *p'-q* stress space
DAF	dynamic amplification factor
E_0	initial stiffness
F	coefficient related to confining pressure
fnN	shape factor
F_l	amplitude of loading
FEM	finite element method
g	acceleration of gravity
G_i	initial value of shear modulus
h	depth

h_0	initial height
Δh	height change
H / D	height to diameter ratio of triaxial test sample
k	modulus of subgrade reaction
K_i	initial value of bulk modulus
$k_1,\ k_2$	empirical constants
$K_1,\ K_2,\ K_3$	regression coefficients
L	stress path length
LVDT	linear variable differential transformer
M_1	constant
M_r	resilient modulus
MISO	multi-linear isotropic
N	number of cycles
p'	mean normal effective stress
p^0	modified mean effective stress $= \sqrt{3} \cdot p'$
p_a	reference pressure 100kPa
p_c	contact pressure of a foundation
PSD	particle size distribution
q	deviator stress
q^0	modified deviator stress $= \sqrt{2/3} \cdot q$
q_f	deviator stress at failure

$q_{initial}$	initial deviator stress
q_{peak}	maximum deviator stress = $q_{\max}$
Q	flow potential
Q_{static}	static wheel load
$Q_{centrifugal}$	increase in wheel load due to centrifugal force
Q_{wind}	increase in wheel load due to wind
$Q_{dynamic}$	dynamic wheel load components
R	ratio of axial strain due to effect of principal stress rotation
RTF	railway test facility
s	scaling factor
S	settlement
S_N	settlement after a number of cycles N
S_1	initial settlement
SD	standard deviation
V_0	initial volume
ΔV	volume change
$(q/p')_{\max}$	maximum stress ratio
$(q/p')_p$	peak stress ratio
u	pore water pressure
y	track settlement
α	input material parameter in ANSYS
β	angle of yield surface in p'-q stress space

$\beta_1,\ \beta_2,\ \beta_3$	parameters describing settlement behaviour
σ	normal stress
σ'	effective stress
σ_1'	major principal stress
σ_2'	intermediate effective stress
σ_3'	minor effective stress
σ_x'	effective stress in x direction
σ_y'	effective stress in y direction
σ_z'	effective stress in z direction
$\sigma_{a,\max}$	maximum axial stress
$\sigma_Y(\varepsilon_{pl})$	yield stress
σ_t	shear stress = τ
σ_v / σ_h	principal stress ratio
ρ	density
$\tau_{\max}$	maximum shear stress
ε_1	permanent strain after first cycle
$\varepsilon_{1,r}$	resilient axial strain
$\varepsilon_{3,r}$	resilient radial strain
ε_a	permanent axial strain
ε_a^p	permanent axial strain in principal stress rotation condition

$\varepsilon_{initial}$	initial strain
ε_N	permanent strain after number of cycles (N)
ε_s	permanent shear strain
ε_v	volumetric strain
$d\varepsilon_{ij}^{e}$	elastic strain increment
$d\varepsilon_{ij}^{p}$	plastic strain increment
ϕ	frictional angle
ϕ_p	peak friction angle
ψ	dilation angle
υ	Poisson's ratio
θ'	sum of principal stress or bulk stress
μ	constant (less than 1)

CHAPTER 1

1. INTRODUCTION

1.1 Background and Problem Definition

The railway network plays an important role in the transport system of the UK and many other countries of the world. Around three million passengers travel by rail every day within the UK and twenty billion tonne kilometres of freight are transported every year (Network Rail, 2007). To allow a safe, reliable and efficient rail network and to provide a good ride quality, the vertical profile of a railway track has to be maintained at a satisfactory level. One area that has been identified by railway corporations as financially expensive is the maintenance of the track substructure. In the UK, Network Rail is committed to spending £1.16 billion in 2006/07 and over £1 billion each year during 08/09 and 09/10 on track maintenance (Network Rail, 2007). Moreover, traditional ballasted track remains the mainstay of most new and upgraded railways.

In order to meet safety standards and to have acceptable ride quality the railway tracks require a specific level and alignment. Suiker *et al.* (2005) indicated that in conventional ballasted railway tracks, the level and alignment of the track

structure strongly rely on the mechanical characteristics of the granular substructure, which is composed of a ballast layer, a subballast layer and subgrade layer. When track irregularities exceed allowable limits, either traffic speed restrictions or maintenance has to be carried out (Selig and Waters, 1994).

Although ballast usually comprises hard and strong angular particles, it undergoes gradual and continuing degradation under cyclic rail loading, which in turn increases settlement of the railway track. Particle degradation can also increase the magnitude of track settlement and accelerate ballast fouling. The pumping of the subgrade clay is a major cause of ballast fouling. The fine particles either from clay pumping or ballast degradation increase the compressibility. The fine particles also fill the void spaces between larger aggregates and reduce the drainage characteristics of ballast. The fouling of ballast usually increases track settlement and may cause differential track settlement. In severe cases, fouled ballast needs to be cleaned or replaced to keep the track up to its desired stiffness, bearing capacity, alignment and level of safety.

Selig and Waters (1994) indicated that vertical settlement is a major problem especially when it occurs non-uniformly or differentially along a short length of track. Prediction of differential permanent deformation under operational conditions is crucial to improving the railway system. However, the key limitation for prediction is our current poor understanding of ballasted trackbed performance and the absence of a realistic stress-strain constitutive settlement model including plastic deformation under a large number of load cycles. The development of a

proper scientific understanding of the dynamic load deformation response and granular ballast interactions would, therefore, have enormous benefits in the design of track systems, the development and maintenance strategies, the assessment of track system performance and the optimisation of whole life and whole system costs.

This project concentrates on the railway ballast settlement. A flowchart shown in Figure 1.1 describes the way in which the various strands of this project interact and contribute to meet the final aim. The monotonic triaxial tests were designed to provide parameters for finite element method (FEM) modelling that allowed the analysis of stress distribution in a railway track section. In contrast, the cyclic and multi-stage triaxial tests were utilised to develop the ballast settlement equations, which were able to calculate the permanent deformation of ballast at a constant pressure condition after a certain amount of cyclic loading. The permanent deformation of railway track was predicted by a railway settlement model, which is the combination of the FEM simulation and the constitutive settlement equation. To achieve the project objectives, another two large-scale experimental facilities, the Composite Element Test (CET) and the Railway Test Facility (RTF), were used to validate and refine the ballast settlement model. Both the CET and the RTF were to provide the ballast settlement underneath the sleeper at different depths. Furthermore, the RTF provided a full-scale testing of a three-sleeper track section to simulate cyclic loading of a passing train including the effect of principal stress rotation.

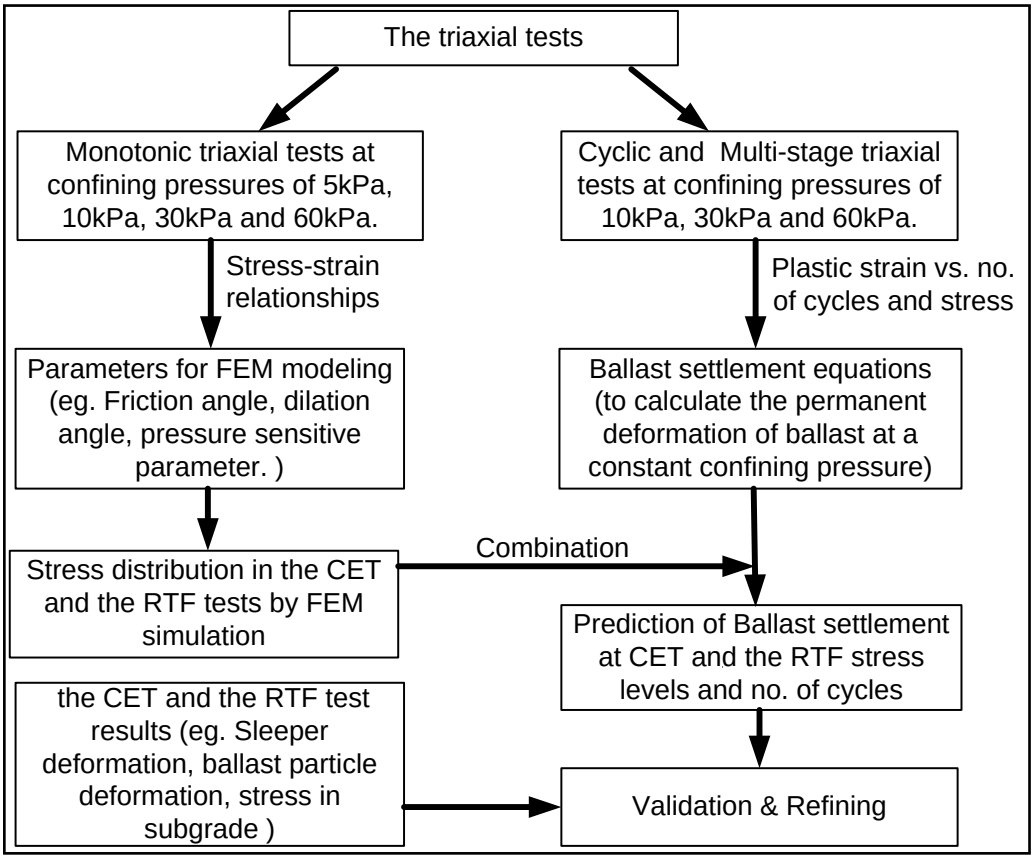

Figure 1.1 Project flowchart

1.2 Objectives of Research

The research described in this thesis aims to improve understanding of railway ballast in addition to developing a realistic method of predicting the permanent deformation of railway track. The specific objectives of this research study are outlined below:

- To investigate the stress-strain and degradation response of ballast under monotonic, cyclic and multi-stage loading at various confining pressures.

- To identify the deformation behaviour of ballast in the CET and the RTF under field-simulated cyclic loading and boundary conditions.

- To utilise facilities and material models readily available in the FEM program ANSYS to calculate the stress distribution in the CET and the RTF.

- To develop a realistic constitutive model for the prediction of permanent deformation in railway track. The constitutive model will be able to compute and predict the deformation for a given load magnitude, trackbed quality and number of cycles.

- To evaluate and verify the constitutive railway settlement model by comparing the model prediction with the CET and the RTF experimental results.

1.3 Thesis Outline

This thesis is divided into eight chapters. A summary of the remaining chapters is given below.

Following this introductory chapter, Chapter 2, a literature review, begins with a general appreciation of various track components and functions. This is followed

by an examination of railway ballast, which includes ballast specifications and deformation mechanisms. Overviews of resilient and permanent deformation behaviour of granular material are presented in the same section. An introduction to the various types of railway settlement mathematical models is presented in the next section. Lastly, finite element modelling of granular material is reviewed.

In Chapter 3, the large-scale triaxial apparatus and test procedures are introduced. Triaxial tests with various loading patterns were carried out, which included monotonic, cyclic and multi-stage triaxial tests. In the monotonic tests, stress-strain behaviour, frictional angle and initial stiffness, and particle breakage are discussed. In the cyclic and the multi-stage tests discussion includes permanent and resilient axial strain, volumetric strain, Poisson's ratio and resilient modulus against number of cycles.

Chapter 4 presents the CET facilities and test procedures. The CET test results include the permanent deformation of ballast particles at different depths.

Chapter 5 presents the RTF experimental results which include sleeper settlement, stress in the top layer of the subgrade, permanent deformation and resilient movement of ballast particles at different depths. All the CET and the RTF test results will be used to validate the railway settlement model.

In Chapter 6, stress distribution within the ballast layer was simulated by the FEM program ANSYS with extended Drucker-Prager material model. Initial

simulations concentrate on material modelling according to the triaxial test results. The second phase of simulation is focused on modelling and analysis of the CET and the RTF.

In Chapter 7, from the cyclic and multi-stage triaxial test results, a series of settlement equations are developed as a function of load cycles, stress conditions and ballast properties. Additionally, in this chapter the settlement model is validated by the CET and RTF test results.

Chapter 8 summarises the main findings of this research study, which include the triaxial tests, CET, RTF, FEM simulation and the railway settlement model. Finally, several recommendations are made for further research. This chapter is followed by a list of references.

CHAPTER 2

2. LITERATURE REVIEW

2.1 Introduction

In conventional track design, ballast degradation and associated plastic deformation are not taken into account directly. Consequently, frequent remedial actions and expensive track maintenance are required. To some extent, this problem is due to a poor understanding of ballast behaviour in railway track. In this chapter, the current state of research pertaining to the behaviour of railway ballast is reviewed. This literature review aims to detail all of the background information required for the subsequent five chapters: the triaxial test, the Composite Element Test (CET), the Railway Test Facility (RTF), finite element method (FEM) analysis and railway track settlement modelling. Topics described in this chapter include four main sections: track components and functions, ballast, mathematical modelling of granular material and FEM analysis of granular material.

2.2 Track Components and Functions

Railway track is designed to provide an economical and safe transportation system for passenger and freight traffic. This requires a track stable enough in alignment under various speeds and axle loadings. A traditional ballasted railway track system consists of a superstructure on top of a substructure, as Figure 2.1 shows. The superstructure comprises the following components: rail, fastening system, sleepers and ties. The substructure is composed of ballast, subballast, and subgrade. During a train passage, the wheel loads from the train spread from the superstructure to the substructure through the sleeper-ballast interface. The functions and characteristics of every component in both the superstructure and the substructure will be further discussed.

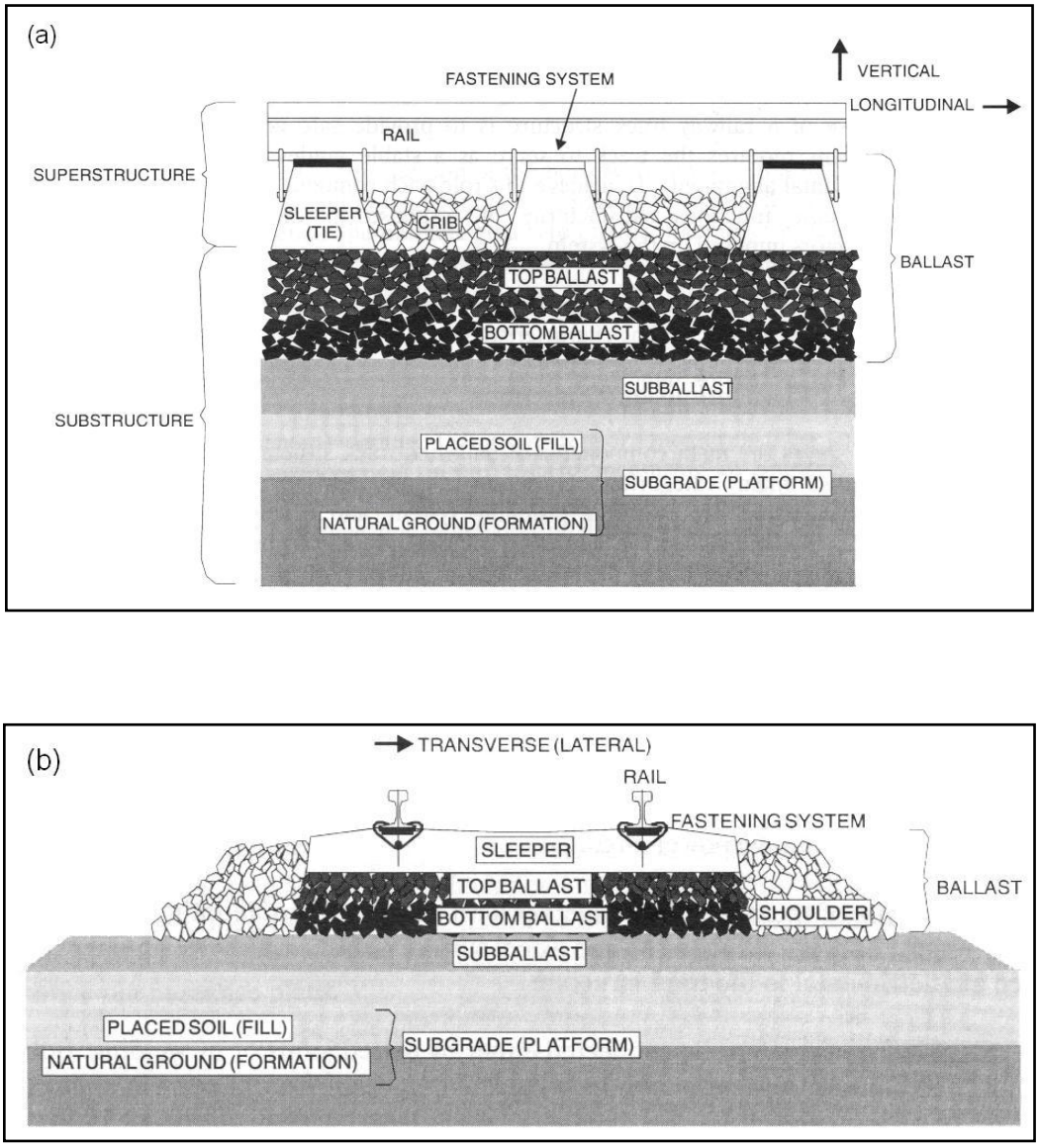

Figure 2.1 Superstructure and substructure components of a railway line, (a) lateral view, and (b) longitudinal view (Selig and Waters, 1994)

2.2.1 Track Components

Rails are longitudinal steel members to direct train wheels; the only parts of the track component that come into direct contact with the train. Therefore, the rails transfer concentrated wheel loads to the supporting sleepers. The rails must be stiff enough to carry the wheel loads with minimum deflection between sleeper supports. The vertical and lateral profile of the rails must be coupled with the profile of the wheels, as any defect on the rail or wheel surface might cause a significant magnitude of dynamic load which is detrimental to the railway track structure. Rail sections may be connected by bolted joints or welding, and these joints may lead to large impact loads from trains that affect the track components below.

The fastening system is used to hold the rails onto the sleepers, to ensure fixing of the rails. Depending on the type of the sleeper and geometry of the rail, various kinds of fastening systems are utilised. In some situations, rail pads are used on top of the sleepers to absorb the energy generated by the traffic movements. Besides resisting vertical, lateral, longitudinal and overturning movements of the rail, the fastening system can aid in damping traffic vibrations, and prevent or reduce rail/sleeper attrition.

The main functions of sleepers are to provide a solid, even and flat platform for the rails, and support the rail fastening system. They are laid on the top of a compacted ballast layer. Sleepers receive the rail loads and distribute them over a

wider ballast area to decrease the stress to an acceptable level. In addition, the sleepers can be used to resist lateral, longitudinal as well as vertical rail movement through anchorage of the superstructure into the ballast. Sleepers can be made of wood, concrete or steel. Currently, timber and concrete sleepers are the most common types of sleepers, which are used worldwide. Steel sleepers are expensive so this type is only used in special situations.

Railway ballast can be defined as granular coarse aggregate.. According to Selig and Waters (1994), traditionally, angular, crushed hard stones and rocks, uniformly graded, free of dust and dirt and not prone to cementing action have been considered good ballast materials. Ballast is a granular material with high bearing capacity that is placed above subballast or subgrade to act as a platform, to support the track superstructure. Its main function is to spread the high loads of passing axles to the subgrade. In doing this, there are high stresses transmitted through the ballast. Moreover, ballast provides a certain amount of resiliency as well as energy absorption for the railway track. The source of ballast varies between different areas, depending on the quality and availability of the material. Ballast index characteristics include particle size, shape, gradation, surface roughness, particle density, bulk density, strength, durability, hardness, toughness, resistance to attrition and weathering. More details of ballast materials will be discussed in section 2.3.

Subballast is composed of well-graded crushed rock or sand gravel mixtures, and it sits between the ballast and the subgrade material. The subballast layer

transmits and distributes stress from the ballast layer to the subgrade over a larger area to reduce the magnitude of resultant stress. Furthermore, another important function is to prevent interpenetration between the ballast and subgrade layer. Subballast acts as a filter to stop upward migration of subgrade particles into the ballast and penetration of coarse ballast into subgrade. In particular, some of the functions of the subballast may be achieved through the use of sand or geosynthetic materials like membrane and filter fabrics.

Subgrade provides the foundation on which the track is constructed. It can be existing natural soil or placed soil. The subgrade must be stiff and have enough bearing strength and stability to avoid excessive settlement. Lack of the required quality will result in an unacceptable disturbance of the track system, and even ballast and subballast will not stay in very good condition.

2.2.2 Track Forces

In order to design an adequate railway track substructure and understand how ballast works on a railway track, it is necessary to know the type and magnitude of forces that are imposed on the railway track during its lifetime. Generally, these loads are exerted by the sleepers on the ballast layer through wheel-rail-sleeper interactions. There are two main forces acting on the ballast: the vertical force of the moving train and the squeezing action of tamping during maintenance work. The vertical force consists of static and dynamic components. The static load is

due to the dead weight of the superstructure and train, whereas the dynamic load is a function of the speed of the train and the track conditions. Selig and Waters (1994) found that the high squeezing force of maintenance tamping caused significant damage to ballast.

The vertical downwards force at the rail-wheel contact point, as shown in Figure 2.2, tends to lift up the rail and sleeper some distance away from the contact point (Selig and Waters 1994). With the advancing wheel, the uplifted sleeper will be forced down creating a high impact load onto the ballast particles and the track structure as a whole. As previously mentioned, the impact force is very much dependent on the train speed and load. Meanwhile, this movement can cause a pumping action in the ballast, which can cause deterioration of track structure components and increase the ballast settlement by exerting a higher force on the ballast and pumping up fouling materials from sub-layers (Selig and Waters 1994).

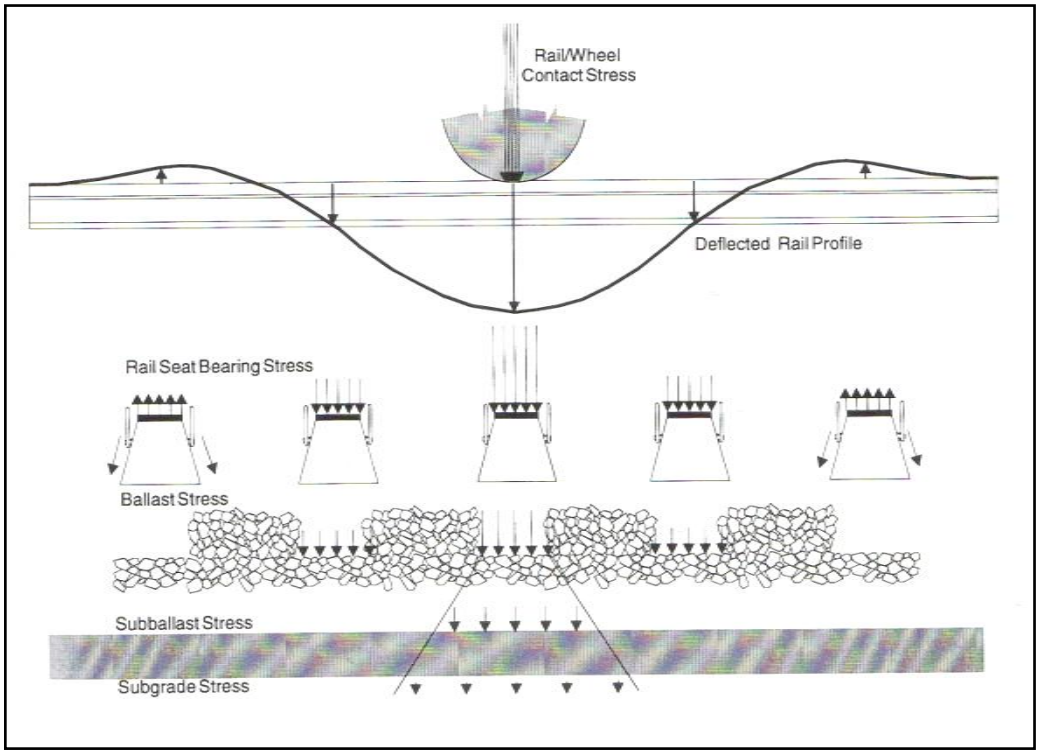

Figure 2.2 Uplift of rails (Selig and Waters, 1994)

According to Selig and Waters (1994), the vertical wheel force consists of a static component, equal to the weight of the train divided by the number of wheels, in addition to a dynamic variance. Furthermore, they stated that vertical dynamic variation, such as bounce and forces caused by wheel flats or wheel/rail defects, could cause huge impacts and vibrations.

Esveld (1989) concluded that the total vertical wheel load on the rail could be classified into two groups: quasi-static load and dynamic load, which is similar to Selig and Waters' point. The quasi-static load is composed of the following components:

$$Q_{total} = Q_{quasi-static} + Q_{dynamic} \qquad \text{(Equation 2.1 (a))}$$

$$Q_{quasi-static} = Q_{static} + Q_{centrifugal} + Q_{wind} \qquad \text{(Equation 2.1 (b))}$$

where,

Q_{static} = static wheel load = half the static axle load measured on straight horizontal,

$Q_{centrifugal}$ = increase in wheel load on the outer rail in curves in connection with non-compensated centrifugal force,

Q_{wind} = increase in wheel load due to wind,

$Q_{dynamic}$ = dynamic wheel load components.

The dynamic component ($Q_{dynamic}$) is the most uncertain part of the wheel load. Esveld (1989) proposed that the dynamic wheel load could be considered as a fatigue load. Additionally, Jeffs and Tew (1991) suggested that the major factors affecting the magnitude of dynamic load component could be listed as follows: speed of train, static wheel load, wheel diameter, vehicle unsprung mass, track condition, track construction and vehicle condition.

The other main force acting on railway track is maintenance tamping, which has been recognised as the most effective method to correct and restore track geometry. It is a very common railway maintenance technique used at present. Track force on the ballast is achieved through squeezing the ballast, and this high squeezing force causes ballast breakage which significantly increases ballast deterioration. Maintenance tamping will be further discussed in the next section.

In addition, Selig and Waters (1994) realised that besides the vertical force and the squeezing action of tamping, ballast was also subjected to lateral and longitudinal forces which were much harder to predict than vertical forces. Lateral forces are parallel to the axis of the sleeper. These are from two principal sources: lateral wheel force and buckling reaction force. Longitudinal forces are parallel to the rails. They are from several sources: locomotive traction force including force required to accelerate the train, breaking force from the locomotive and cars. Thermal expansion and contraction of rails and rail wave action.

2.2.3 Track Geometry Maintenance

Railway tracks may deform both vertically and laterally under repeated loads. Although these deviations are relatively small, they reduce riding quality, increase dynamic loads and even damage the track system. Track maintenance is the total process of maintenance and renewal required to ensure that the track meets safety and quality standards. Esveld (1989) presented maintenance and renewal that were undertaken on the basis of control data obtained from measuring systems, visual observation, financial-economic data and local conditions. In the following sections, ballast fouling and track maintenance techniques will be discussed in detail.

Ballast Fouling

Ballast fouling indicates contamination of ballast by the presence of fines. According to Selig and Waters (1994), the life and performance of a railway track is mainly dependant on the ballast layer. However, the ballast layer is very likely to be contaminated by various sources. In addition, Selig and Waters (1994) summarised a study at the University of Massachusetts based on a variety of mainline track conditions across North America to identify the sources of fouling materials, which is shown in Figure 2.3. It indicated that ballast breakage was the main source of fouling material, while the minor sources of fouling materials are infiltration from underlying granular layer and surface, subgrade infiltration or sleeper wear. Detailed sources of ballast fouling are given in Table 2.1.

Due to ballast fouling, railway track performance decrease including higher permanent deformation and poor drainage occur under repeated loading from traffic. Track progressively moves vertically and laterally causing deviation from the desired geometry. Because these deviations are generally irregular, ride quality decreases and the dynamic load increase, causing increased geometry deterioration. In order to reduce ballast fouling, in practice, ballast cleaning and replacement with fresh ballast should be carried out. If the ballast is extremely dirty, it may need to be totally replaced. The contamination problem requires the use of ballast with high crushing resistance.

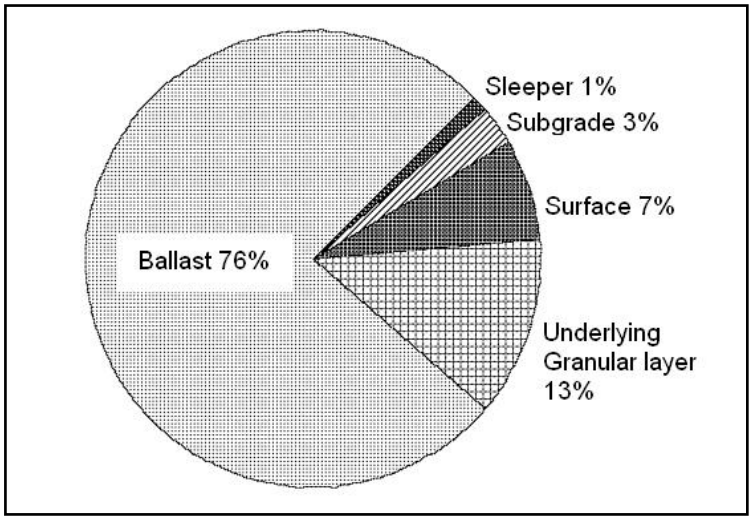

Figure 2.3 Major source of ballast fouling (Selig and Waters, 1994)

Table 2.1 Sources of ballast fouling (Selig and Waters, 1994)

1. Ballast breakage Handling (at quarry; during transporting; from dumping) Thermal stress from heating (desert) Chemical weathering (inc. acid rain) Tamping damage Traffic damage (repeated load; vibration; hydraulic action of slurry)
2. Infiltration from ballast surface Delivered with ballast Dropped from the train Wind blown Water borne Splashing from adjacent wet spots
3. Sleeper wear
4. Infiltration from underlying granular layers Old track bed breakdown Subballast particle migration from inadequate gradation
5. Subgrade infiltration

Track Maintenance Techniques

In the UK, before conducting any maintenance operation, trackbed deterioration measurement should be carried out. A high speed track recording car (HSTRC) uses a system of lasers to obtain a continuous profile of the track. This is expressed as the standard deviation of the track level relative to a moving mean level. Greater standard deviation means a greater degree of the unevenness of the track. The HSTRC also carries video equipment to facilitate visual track inspection. In order to optimise the maintenance operations and prediction of maintenance periods, a better understanding of the effect of maintenance procedures is required. According to Selig and Waters (1994), the majority of track maintenance is carried out mechanically. There are two available maintenance procedures applied to correct track: tamping and stoneblowing.

Ballast tamping has been widely used all over the world to correct track geometry. The tamping procedure includes lifting the rail and inserting tines which will vibrate, hence squeezing the ballast underneath the sleeper into position. Figure 2.4 illustrates the tamping procedures.

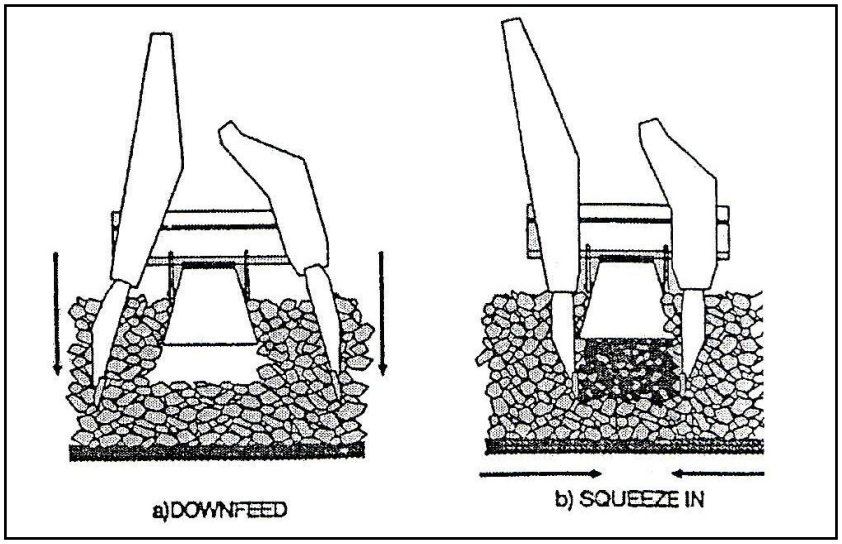

Figure 2.4 Tamping procedures (Selig and Waters, 1994)

Although ballast tamping is an effective method to adjust the track geometry, there are still some disadvantages. Tamping causes ballast damage, loosening of ballast bed and reduces track resistance to lateral displacement and buckling. Consequently, loosening ballast and ballast breakage induce subsequent settlement in the track. Moreover, increasingly frequent maintenance will be required. The influence of tamping on track settlement is shown in Figure 2.5.

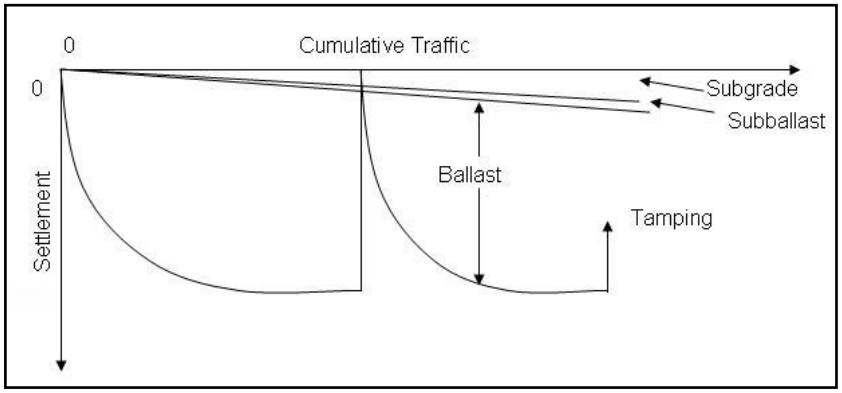

Figure 2.5 Contribution of ballast to track settlement, and the influence of tamping (Brown and Selig, 1991)

The key to the development of stone blowing is the observation that ballast has a memory of the shape from which it has deteriorated prior to each tamping operation (Esveld, 1989). The stoneblowing principle is that the sleeper is lifted to create a void, then a pipe is inserted into the ballast alongside the sleeper and small size stones are blown down into any gap which exists between the bottom of the sleeper and the ballast, which is outlined in Figure 2.6.

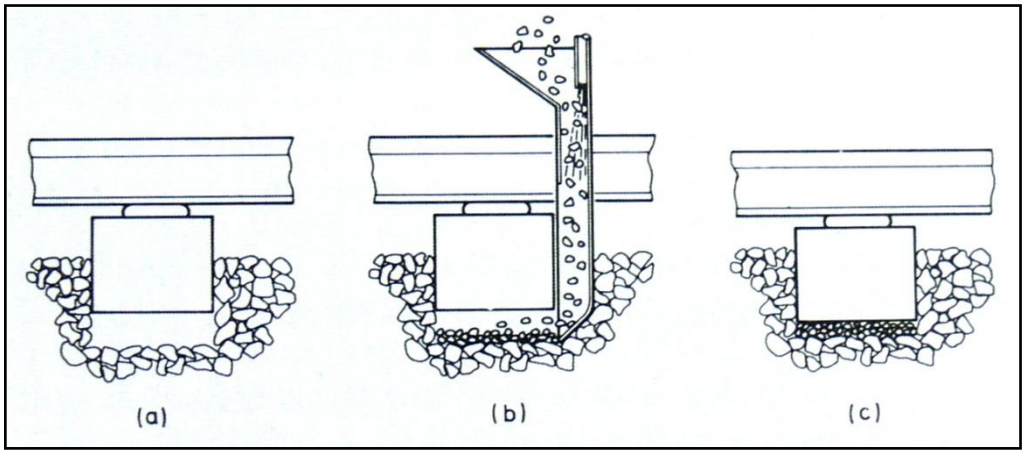

Figure 2.6 Stoneblowing principles (Esveld, 1989)

According to Cope and Ellis (2001), since stoneblowing does not damage the existing track ballast, unlike tamping, the degradation of the ballast to unwanted fine material is eliminated which should increase the duration of intervals between ballast replacements.

After several cycles of tamping and years of train load application, the ballast gets excessively fouled, and its function is impaired. According to Selig and Waters (1994) the loss of performance mainly occurs when the fouling materials contain

silt and clay-size particles. These particles reduce the void space, make the void size smaller, and combine with the fines to form abrasive slurry, hence increase the possibility of significant ballast deterioration. Eventually, the ballast will need to be cleaned and probably partially replaced. This is carried out using a ballast cleaning machine. Ballast could be removed from a track by using purpose-built ballast cleaners, but without the need to remove the rails and sleepers. These propelled on-track machines are designed to excavate the ballast below and around the sleepers. The excavated material is conveyed to sieves where the fines are separated from the ballast and the re-usable stone is then returned to the track behind the cutter bar (Cope and Ellis 2001). A ballast cleaner is shown as Figure 2.7.

Figure 2.7 A ballast cleaner in action

Cope and Ellis (2001) indicated that ballast cleaners were most suitable for the screening of long lengths of track where the ballast was not contaminated with cohesive material, such as clay or slurry. However, when the ballast is extremely dirty, it may need to be totally removed, rather than using ballast cleaning, and replaced with fresh ballast. In this case, the ballast cleaner cuts the ballast and conveys it into wagons. Salim (2004) suggested that to minimise further quarrying

for fresh ballast and thus protect the environment, and to minimise the track construction and maintenance cost, discarded waste ballast can also be cleaned and recycled to the track. He also indicated that the performance of recycled ballast required detailed investigation, both in the laboratory and on the track.

2.3 Ballast

Track settlement is generally only treated as a significant problem when it occurs non-uniformly over a short length. Many researchers (e.g. Gaskin and Raymond, 1976; Selig and Waters, 1994) concluded that over 50% of the total deformation of railway track originated from the ballast layer. Railway ballast is produced by crushing rock and sieved to get the desired particle size. Its main function is to spread the high loads of passing axles to the subgrade. Thus, ballast materials are required to be hard, durable, angular, and free of dust and dirt. In this section, ballast specification, ballast deformation mechanisms, resilient behaviour and permanent strain behaviour of granular material will be discussed.

2.3.1 Ballast Specifications

Ideally, ballast used for railway track should have high stiffness, high strength, crushing resistance, chemical resistance and be free from dust. High stiffness can

reduce stress to weaker underlying materials, reduce track deflection under load and reduce bending stresses in the rails. The reason for high strength is to reduce build-up of deformation under traffic loading and impart horizontal stability to the track. Besides these functions, ideal ballast should not be affected by dirt from above, soil contamination from below, rainfall, frost and chemical weathering. Additionally, ballast should absorb noise and surplus energy from vibration, meanwhile, allow easy maintenance and be sufficiently workable.

The strength of ballast particles is probably the most important factor directly governing ballast degradation, and indirectly settlement and lateral deformation of the railway track (Salim, 2004). If an individual particle is overstressed, it will fracture and the ballast particles will re-orientate themselves. Fracturing will continue until re-orientation is completed, meaning that there are enough particle contacts for each not to be at too high a stress.

The mechanical behaviour of ballast is affected by the particle size. Indraratna *et al.* (1998) indicated that the peak friction angle decreased slightly with an increasing grain size at confining pressures which were less than 300kPa. The effect of particle size on friction angle became negligible when the stress was over 400kPa. Raymond and Diyaljee (1979) concluded that smaller ballast particles deformed less when the stress level did not exceed a critical value. However, smaller ballast particle size had lower final compaction strength than larger ballast. Selig (1984) recommended that the ideal ballast should be of 10-50mm size with some particles beyond this range. The larger particles stabilise the track and the

smaller particles reduce the contact forces between particles and minimise breakage. In the UK, properties of ballast were specified in Railtrack Line Specification (RT/CE/S/006, 2000). Ballast dimensions recommended to be used from the 1st April 2005 are shown in Figure 2.8. From this figure, it can be seen that the track ballast should have a consistent mixture of sizes mainly between 32mm and 50mm.

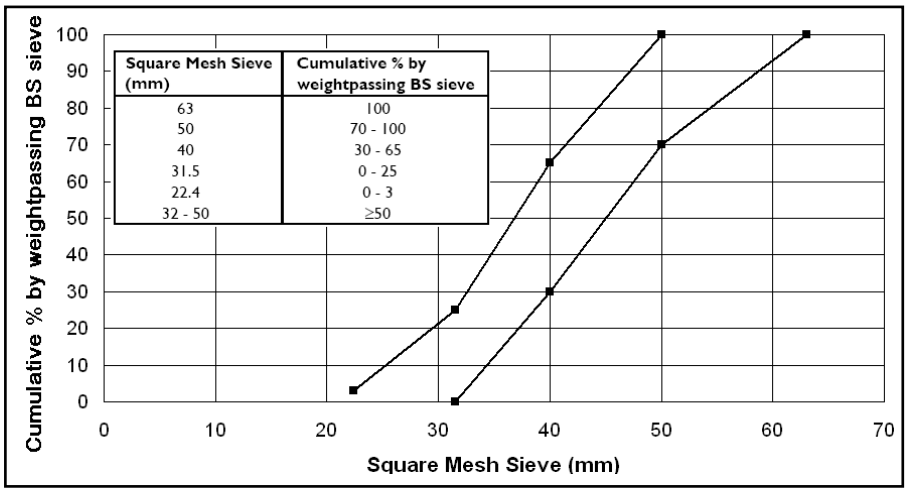

Figure 2.8 Specification for ballast particle size distribution (RT/CE/S/006, 2000)

2.3.2 Ballast Deformation Mechanisms

Selig and Waters (1994) concluded that there were two main modes in which granular material deformed: frictional slip and particle breakdown. During each passing axle load, either of these modes of deformation can be occurring at a different point within the ballast. They are interdependent mechanisms causing the ballast to be a continually changing material. The key form of deformation is

frictional slip between ballast particles. It should be noted that frictional slip does not only imply permanent deformation, but it takes place during normal repeated loading as well, first one way then back again. However, a small part of the slip is not recovered each time, which forms the permanent deformation. Ballast particles slip back to release the energy stored elsewhere. Liao *et al.* (1995) defined slip as the relative motion of particles in contact under applied load. Ballast abrasion is a phenomenon where very small particles break off from the grain surface. Festag and Katzenbach (2001) indicated that ballast abrasion took place when the particles slipped or rolled over each other during shear deformation, and might occur even at low stress level.

Thom (2005) concluded that the train load caused a certain percentage of ballast particle breakage in addition to ballast contact slip. Festag and Katzenbach (2001) defined particle breakage as the dissection of grains into parts with nearly the same dimension and stated that it generally occurred in the high stress domain. Grain breakage might be absent if the stress level was low compared to particle strength. According to McDowell *et al.* (1996), the probability of particle breakage in an aggregate increase with an increase in applied macroscopic stress and particle size, and reduction in coordination number (i.e. number of contacts with neighbouring particles.). However, Lekarp *et al.* (2000a) pointed out that the true nature of the deformation mechanism of aggregates in a granular layer was not yet fully understood.

2.3.3 Resilient Behaviour of Granular Material

The deformation response of granular material under repeated loading is commonly characterised by a permanent deformation as well as a recoverable resilient deformation, which will be discussed in this section. During each traffic cycle, the difference between the maximum strain exerted from the peak load and the permanent strain when the ballast is unloaded is recoverable strain, which is known as the resilient strain, as illustrated in Figure 2.9. The resilient modulus can be calculated as the repeated deviator stress divided by the recoverable axial strain during unloading in the triaxial test (Seed *et al.*, 1962) as shown in the equation below:

$$Mr = \frac{q}{\varepsilon_{1,r}} \qquad \text{(Equation 2.2)}$$

where Mr = resilient modulus, q = transient deviator stress $= \sigma_1' - \sigma_3'$, $\varepsilon_{1,r}$ = recoverable (resilient) axial strain during unloading.

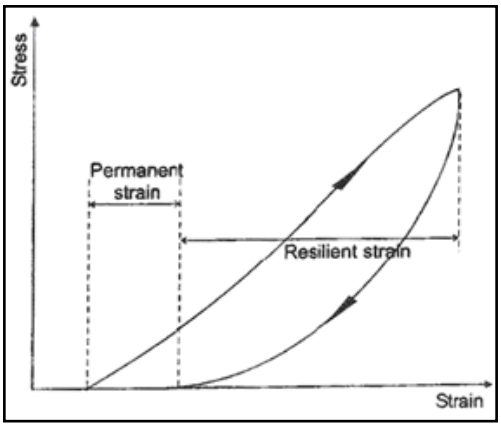

Figure 2.9 Strains in granular materials during one cycle of load application (Wright, 1983)

The resilient behaviour of granular material may be affected by several factors as described below: stress state, stress history, loading sequence, number of loading cycles, aggregate type, geometry (shape and texture), aggregate grading and moisture content.

The major effect on resilient behaviour is stress, including stress state, stress history and stress sequence. Lekarp *et al.*, (2000a) agreed that the resilient modulus increased considerably with an increase in confining pressure and sum of principal stresses, which has been agreed by many researchers (e.g. Hicks and Monismith, 1971; Uzan, 1985; Thom and Brown, 1989; Sweere, 1990). Hicks and Monismith (1971) concluded that the predominant factor affecting resilient modulus was the bulk stress (the sum of the three principal stresses with the maximum load applied), and the resilient modulus was expressed as a function of the sum of principal stresses or bulk stress in the loaded state.

From triaxial tests on well graded crushed basalt, Rowshanzamir (1995) concluded that the loading sequence did not affect resiliency. Similar results have been reported by Raad and Figueroa (1980). Dehlen (1969) reported that resilient modulus could be affected by stress history as a consequence of progressive densification, particle rearrangement, and the development and dissipation of excess pore water pressure.

The amount of resilient strain generally decreases with number of cycles, i.e. the resilient modulus increases gradually with the number of repeated load applications. Eventually, the resilient modulus comes to an approximately constant value after a certain number of repeated loads and the material behaves in an almost purely resilient manner. Selig and Waters (1994) studied the change of the resilient modulus over a number of load applications in a triaxial apparatus, as shown in Figure 2.10. It appears that the amount of resilient strain generally decreases with number of cycles, which is similar to the findings of other researchers (e.g. Dehlen, 1969; Brown, 1974; Khedr, 1985).

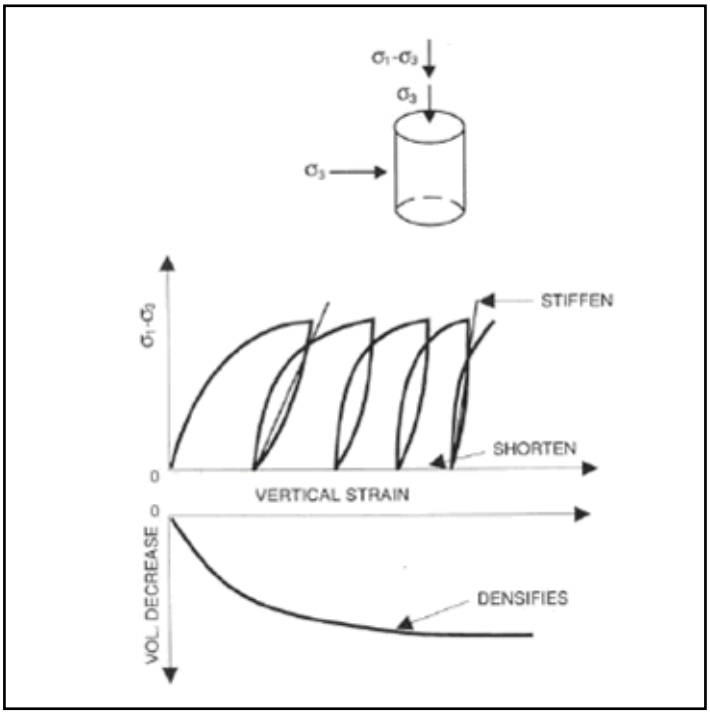

Figure 2.10 Ballast behaviour in the cyclic triaxial test (Selig and Waters, 1994)

Referring to aggregate type, Zaman *et al.* (1994) subjected six materials (three limestones, sandstone, granite and rhyolite) to cyclic loading and found that the

type of aggregate significantly influenced the resilient response, with the resilient modulus for the various materials differing by 20-50%. Many researchers (e.g. Allen and Thompson, 1974; Yoder and Witczak, 1975; Barksdale and Itani, 1989) found that the resilient modulus was enhanced when the particle shape became more angular and the texture rougher. Thom and Brown (1989) have reported that crushed aggregate, having angular to subangular shaped particles, provides better load spreading properties and a higher resilient modulus than uncrushed gravel with subrounded and rounded particles.

The effect of grading on the resilient modulus has been deemed minor when compared to other influences. Zaman *et al.* (1994) witnessed an insignificant change (< 10%) in resilient modulus when the coefficient of uniformity (C_u) was increased from 43.3 to 65.6. Thom and Brown (1988) studied the effect of grading on the shear stiffness of crushed limestone and identified that uniform specimens were marginally stiffer. Knutson and Thompson (1977) indicated that well graded ballast had a slightly higher resilient modulus than the more uniform ballast.

Besides the influences above, Lekarp *et al.*, (2000a) also reported that the effect of moisture on resilient modulus depended on the degree of saturation. At low degrees of saturation, the moisture content has negligible effect on resilient modulus. However, the resilient modulus decreases considerably for high degrees of saturation, especially as the aggregate approaches complete saturation.

2.3.4 Permanent Strain Behaviour of Granular Material

Permanent strain of granular material caused by repeated traffic loading is defined as the irrecoverable strain during unloading, as shown in Figure 2.9. The permanent strain behaviour under cyclic loading is affected by many factors: stress level, principal stress rotation, initial density, grading, number of load cycles, moisture content, loading sequence and loading frequency.

Stress Level

The stress level is one of the most important factors affecting the development of permanent deformation in granular materials. Selig and Waters (1994) indicated that the permanent strain of ballast was a function of both the confining pressure and the cyclic deviator stress. Knutson (1976) concluded that permanent strain accumulated after a certain number of repeated loads was directly related to the ratio of deviator stress to confining stress, as shown in Figure 2.11. Clearly, confining pressure and the cyclic deviator stress have a significant effect on permanent strain accumulation. Lower confining pressure permits higher plastic strain; higher repeated deviator stresses lead to a higher plastic strain over a given number of cycles. Brown (1974) conducted triaxial tests on crushed granite and ascertained that the permanent axial strain increased with decreasing confining pressure. Shahnazari and Towhata (2002) identified that specimens with higher confinement had superior strength and exhibited greater resistance to deformation.

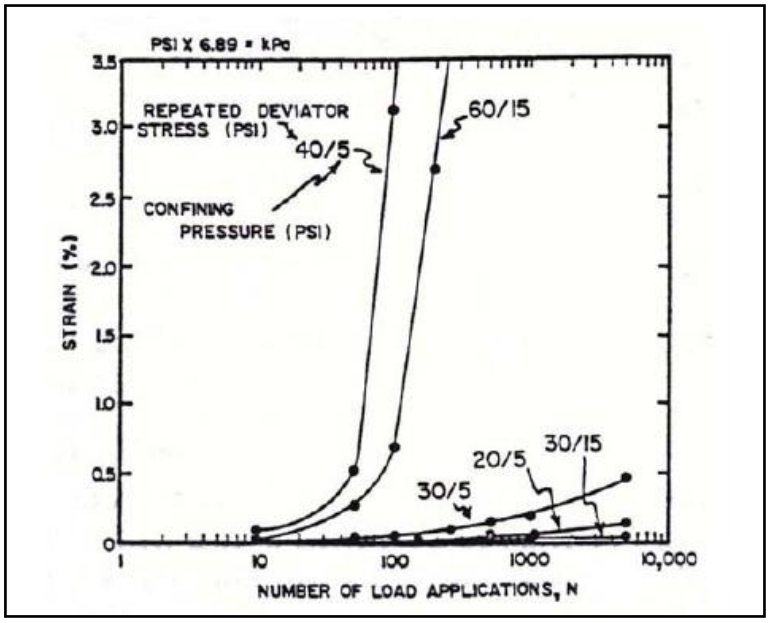

Figure 2.11 The effect of stress ratio on permanent strain (Knutson, 1976)

The amplitude of the applied deviator stress has a significant influence on the permanent deformation characteristics of granular materials under cyclic loading. Selig and Waters (1994) stated that when a specimen was subjected to multiple magnitudes of loading, the largest load had the greatest effect on the degree of settlement. ORE (1970) showed that a small number of high amplitude loads were much more important than a large number of minor loads in establishing track deterioration. Olowokere (1975) found that volumetric strain and axial strain increased with deviator stress magnitude under cyclic loading, as shown in Figure 2.12. This figure shows significant increase of volumetric strain and axial strain due to the increase of the deviator stress ratio. Stewart (1986) indicated that the permanent strain in the first cycle increased significantly when the load amplitude was increased. Furthermore, he noted that an increase in load amplitude beyond

the maximum historical stress level increased the settlement immediately, and also increased the long-term cumulative strain.

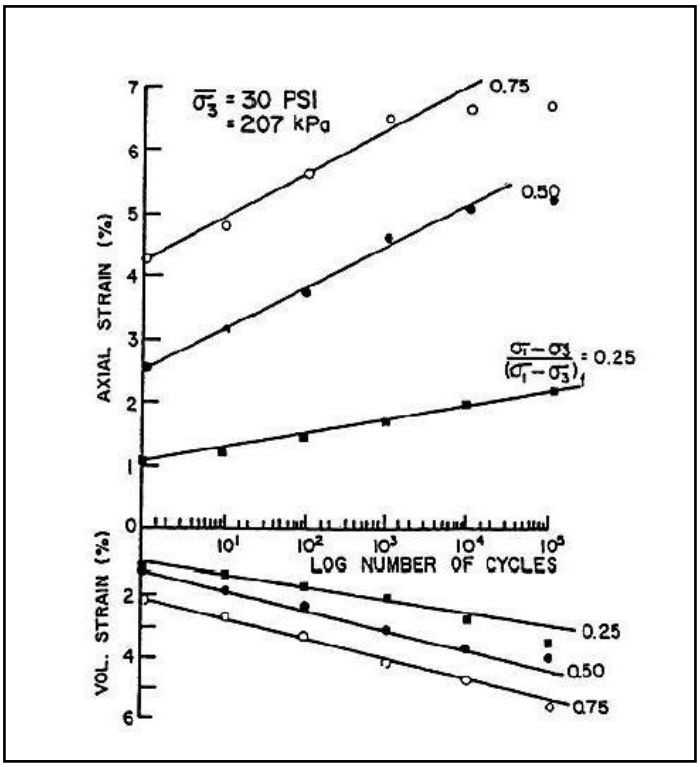

Figure 2.12 Effect of deviator stress magnitude on axial and volumetric strain (Olowokere, 1975)

Principal Stress Rotation

Figure 2.13 illustrates that an element in a pavement structure is subjected to stress pulses. Lekarp *et al.* (2000b) indicated that the principal stress axes were rotated as the load passed, therefore, test samples subjected to principal stress rotation showed larger permanent strain than samples without. However, the effect of principal stress reorientation on permanent strain was not fully understood.

Lim (2004) noted that there was little principal stress rotation for ballast near the bottom of the sleepers. Since the major principal stress in the ballast directly underneath the sleeper was vertical, this would increase rapidly as the passing load approached and would reduce significantly as the load moved away from the sleeper. Therefore, most principal stress rotation occurred in the deeper layer of ballast. The amount of ballast experiencing principal stress rotation was shown to depend on the stiffness of the ballast and subgrade layers.

Thom and Dawson (1996) carried out a series of tests with the hollow cylinder apparatus and found that the permanent strain increased significantly when stress cycling was accompanied by principal stress rotation. Ishikawa and Sekine (2007) developed a small scale laboratory model test apparatus and a multi-ring shear apparatus to examine the effects of principal stress rotation on cyclic plastic deformation in granular material. It was revealed that the difference in loading methods has a considerable influence on cyclic plastic deformation of granular material; the cumulative axial strain increases with an increase in the rotational angle of the principal stress axis.

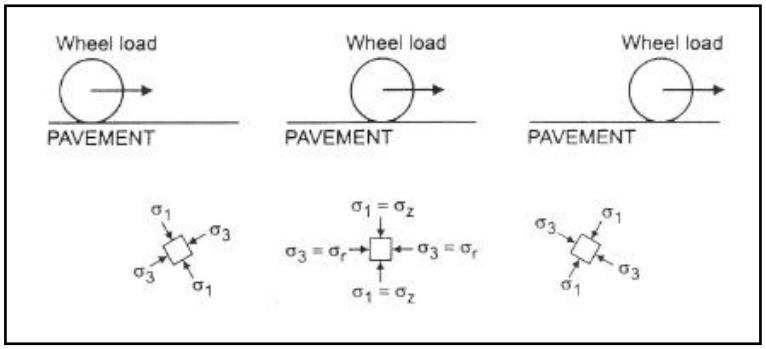

Figure 2.13 Stress beneath rolling wheel load (Brown, 1996)

Initial Density and Grading

The initial density state, as described by degree of compaction, has an effect on plastic strain accumulation as well. Knutson (1976) stated that for constant confining pressure repeated load triaxial tests on limestone ballast, specimen density had a significant effect on permanent deformation. The lowest density produced the highest plastic strain in a given number of cycles. Furthermore, the effect of initial density could be described by degree of compaction. Thom (1988) studied the plastic strain by varying the compaction level and grading, as illustrated in Figure 2.14(a). The grading parameter in Figure 2.14(a) was used in the experiment to define the particle size distribution of each sample as shown in Figure 2.14(b). Furthermore, the sample compaction in the tests was performed by tamping in five layers each of 30mm thickness with a 38mm diameter rod. The compaction effect was controlled manually. The uncompacted specimens with uniform grading compared to the lightly and heavily compacted specimens, resulted in the most plastic strain. In comparison, with the same grading, heavily compacted specimens led to the least permanent strain. Furthermore, the effect of grading on plastic strain was significant when the specimens were uncompacted or lightly compacted. However, little permanent deformation difference could be detected for all gradings when the specimens were heavily compacted.

After a series of triaxial tests on railway ballast, Lackenby (2006) concluded that specimen particle size distribution (PSD) had a significant effect on permanent

straining characteristics; significant axial strains and greater volumetric compression were associated with lower uniformity coefficient (C_u) gradations.

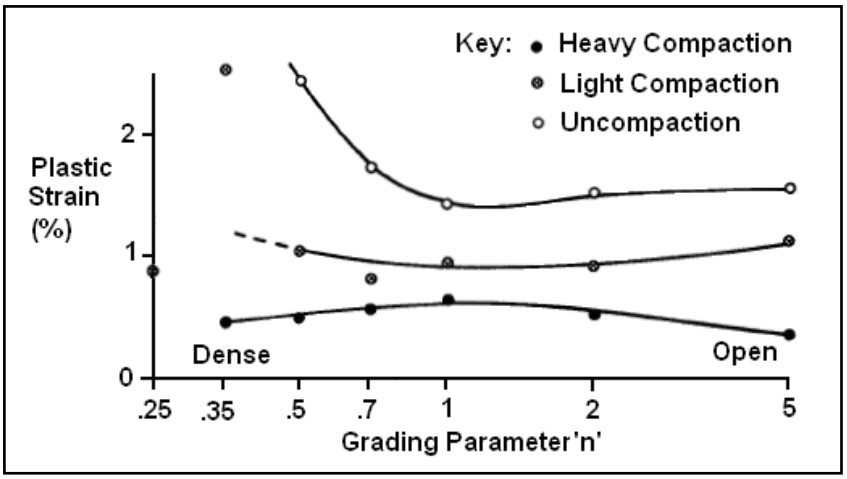

Figure 2.14(a) Effect of grading and compaction on plastic strain (Thom, 1988)

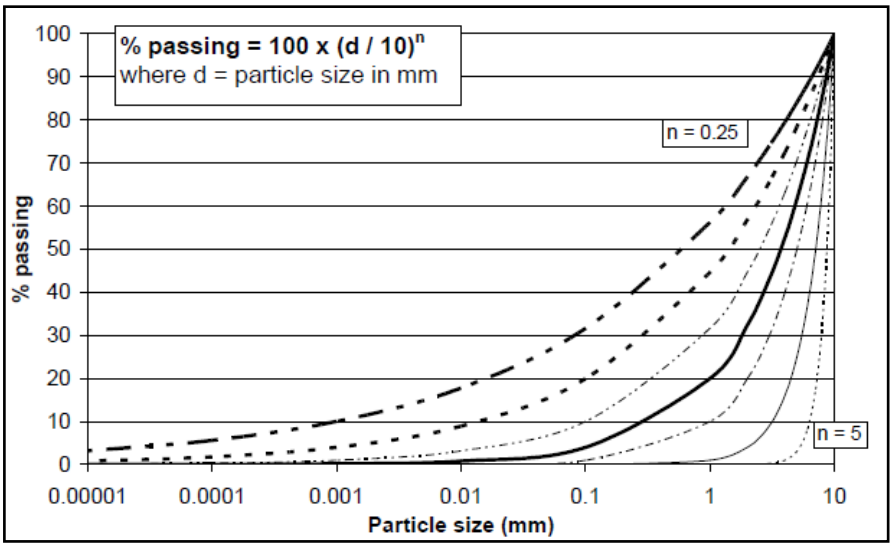

Figure 2.14(b) Particle size distribution of different samples (Thom, 1988)

Number of Load Cycles

Permanent deformation in granular materials under repeated loading is accumulated over an increasing number of load cycles. However, the degree and

rate of deformation with number of load cycles are considered as additional important aspects that have been studied. Shenton (1975) reported that track settlement immediately after tamping increased at a decreasing rate with the number of axles (Figure 2.15(a)). Additionally, he pointed out that the track settlement might be approximated by a linear relationship with the logarithm of load cycles (Figure 2.15(b)). The observation that settlement or vertical strain accumulated approximately logarithmically with the number of load cycles was also reported by other researchers (e.g. Raymond and Williams, 1978; Brown and Selig, 1991; Raymond and Bathurst, 1994; Selig and Waters, 1994).

Various researchers (Jeffs and Marich 1987, Ionescu *et al.* 1998) concluded that the permanent deformation of ballast could be characterised by two phases. The first phase was the initial consolidation where the ballast was compressed to a higher density and rapid settlement occurred. In the second phase the settlement was slower and there was an approximately linear relationship between the settlement and the number of load applications. However, according to Lekarp (1997) and Lekarp and Dawson (1998), the achievement of stable behaviour, when permanent strain rate decreases with increasing number of loading cycles, could only occur when the applied stresses were low. In contrast, higher stresses would result in a continuous increase of permanent strain.

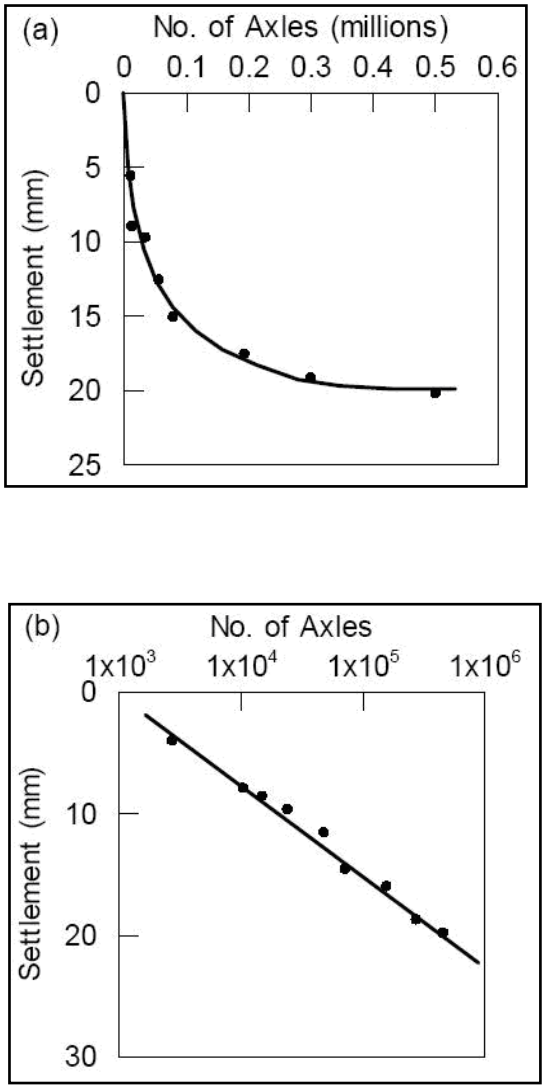

Figure 2.15 Settlement of track after tamping (a) on plain scale, (b) on semi-logarithmic scale (Shenton, 1975)

Moisture Content

The combination of a high degree of saturation and low permeability leads to high pore pressure, low effective stress and low stiffness. As a result, the deformation resistance in granular materials decreases (e.g. Maree *et al.*, 1982; Thom and Brown 1987; Dawson *et al.* 1996). Thom and Brown stated further that a relatively small increase in water content could induce a significant increase in

permanent strain rate. According to Dawson (1990), the stress-strain behaviour of granular materials could be improved substantially by draining the system.

Loading Sequence

The sequence of loading does not affect permanent strain accumulation (Selig and Waters, 1994). Figure 2.16 shows a typical result of permanent strain accumulation for different loading sequences, where the deviator stress changes after every 1000 load applications. Clearly, the final permanent strains for all the different loading sequences are approximately equal.

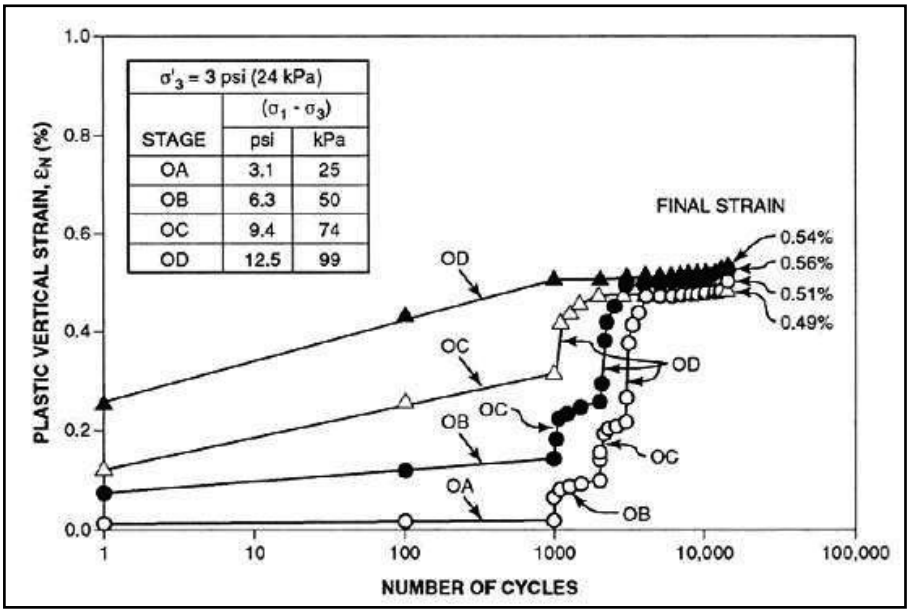

Figure 2.16 Effect of difference in sequence of loading on permanent strain (Knutson, 1976)

Loading Frequency

Due to the various train speeds, it is important to study the influence of the frequency of loading on railway ballast. Shenton (1974) carried out a series of

cyclic loading tests, varying the frequency from 0.1 to 30Hz and maintaining other variables constant. Figure 2.17 shows the plot of normalised strain at the same value of deviator and confining stress. Shenton concluded that the loading frequency would not significantly affect the accumulation of permanent strain. However, these findings should not be confused with the dynamic forces generated by high train speed. Kempfert and Hu (1999) reported that in-situ measurement of dynamic forces in the track had a strong positive relationship with train speeds. Eisenmann *et al.* (1994), furthermore, stated that settlement was significantly influenced by high train speeds due to the dynamic forces.

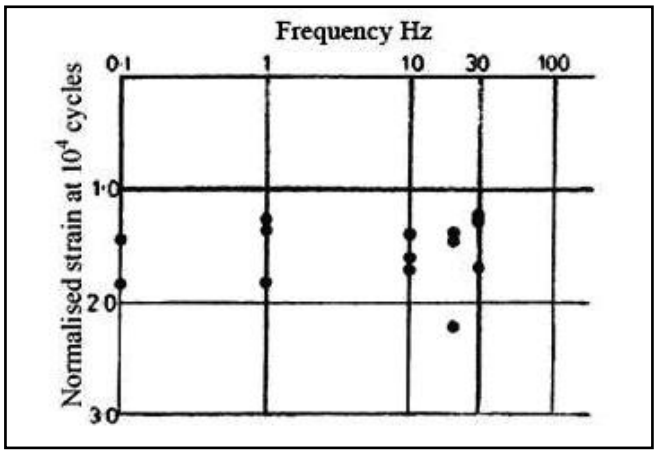

Figure 2.17 Effect of loading frequency on permanent strain (Shenton, 1974)

Other Factors

Moreover, besides the factors mentioned previously, another important factor for railway ballast is tamping. Dahlberg (2001) stated that the settlement of ballasted track occurred in two major phases. One is directly after tamping, during which the settlement is relatively fast until the gaps between the ballast particles have been reduced, and the ballast becomes compacted. The second phase of settlement

is slower and there is a general linear relationship between settlement and number of load applications. Selig and Waters (1994) indicated that initial loading strain developed rapidly and was only partially recovered during unloading. The initial high plastic strain is due to large local stresses at the particle contact points, causing the individual particles to become overstressed, fracture and thus reorientate themselves. This fracturing will continue to occur until enough particle contact points appear, and each is not too stressed. This means that as the number of load applications from passing traffic increases, the plastic strain increment generally reduces. In addition, Boyce *et al*. (1976) carried out cyclic loading tests on crushed rock and found that excessive permanent deformation could be influenced by the magnitude of resilient strain.

2.4 Mathematical Models of Granular Materials

2.4.1 Models for Resilient Deformation Behaviour

As discussed in Section 2.3.3, the resilient behaviour of granular material is affected by several factors, and the effect of stress parameters is the most significant. It should be noted that effective stress (σ') acting on a soil is usually calculated from two parameters, total stress (σ) and pore water pressure (u) according to: $\sigma' = \sigma - u$. However, in this research, dry railway ballast was used.

Thus the effective stress is equal to the total stress (i.e. σ'=σ). In this section, a summary of the models of resilient behaviour is presented.

A majority of the models found in the literature are based on the data from laboratory tests. Dunlap (1963) indicated that the resilient modulus (Mr) increases with confining pressure. The expression based solely on the effect of confining pressure is given as:

$$Mr = k_1 \sigma_3'^{k_2} \qquad \text{(Equation 2.3)}$$

where k_1 and k_2 = empirical constants, and σ_3' = effective confining pressure.

In addition, Pezo (1993) realised that it is necessary to include deviator stress in the resilient behaviour analysis and expressed the relationship as:

$$Mr = N_1 q^{N_2} \sigma_3'^{N_3} \qquad \text{(Equation 2.4)}$$

where N_1, N_2 and N_3 = empirical constants, q = deviator stress and σ_3' = effective confining pressure.

The most popular material model for resilient behaviour analysis is that proposed by Hicks and Monismith in 1971. This model suggests that the resilient modulus is proportional to the sum of the principal stresses or bulk stress, and is commonly known as the $k-\theta'$ model:

$$Mr = k_1 \theta'^{k_2} \qquad \text{(Equation 2.5)}$$

where k_1 and k_2 = empirical constants, θ' = sum of principal stresses or bulk stress.

The simplicity of the k-θ' model has made it extremely useful and widely accepted for analysis of stress dependence of material stiffness. The k-θ' model assumes a constant Poisson's ratio, which is then used to calculate radial strain. However, many researchers (Hicks, 1970; Hicks and Monismith, 1971; Brown and Hyde, 1975; Boyce, 1980; Sweere, 1990 and Kolisoja, 1997) have shown that Poisson's ratio is not a constant and varies with applied stresses.

May and Witczak (1981) indicated that the in situ resilient modulus of a granular layer is a function not only of the bulk stress but also of the magnitude of the shear strain induced mainly by shear, or deviator stress..

Generally, resilient behaviour of granular material can be described by the Uzan model also known as the universal model, taking into account confining pressure and deviator stress. The predicted Mr value can be obtained from following equation:

$$Mr = K_1 p_a \left(\frac{\theta'}{p_a}\right)^{K_2} \left(\frac{q}{p_a} + 1\right)^{K_3} \qquad \text{(Equation 2.6)}$$

("+1" in last term wasn't included in the original Uzan version) where K_1, K_2 and K_3 are regression coefficients; θ' is the sum of principal stresses; p_a is the reference pressure 100kPa. q is the deviator stress. Thompson *et al.* (1998) pointed out that the model and its modifications consider both the confining pressure and deviator stress effects. They further presented that these models are shear stress related; and best for routine use giving reasonable results.

Furthermore, Thompson *et al.* (1998) and Lekarp *et al.* (2000a) indicated that another approach adopted in predicting the resilient modulus of granular material could be based on establishing a relationship for volumetric and deviator strains. Boyce (1980) proposed a $K-G$ model, giving volumetric and deviator strains in the following forms:

$$\varepsilon_v = (\frac{1}{K_i}) p'^{\mu} \left[1 - \beta (\frac{q}{p'})^2 \right] \quad \text{(Equation 2.7)}$$

$$\varepsilon_q = (\frac{1}{3G_i}) p'^{\mu} (\frac{q}{p'}) \quad \text{(Equation 2.8)}$$

where K_i and G_i = initial values of bulk and shear moduli respectively, μ = constant (less than 1), $\beta = (1-\mu)K_i/(6G_i)$, q = deviator stress and p′= mean effective stress. In the Boyce model, the material is assumed to be isotropic, which enables the model to express the response moduli as functions of the stress invariants. According to Brown and Hyde (1975), there are three advantages of using bulk and shear moduli for nonlinear materials: (1) no assumptions of linear-elastic behaviour are needed in the calculations; (2) the shear and volumetric components of stress and strain are treated separately; and (3) it has a more realistic physical meaning in a 3D stress regime than the resilient modulus and Poisson's ratio. Moreover, Lekarp et al. (2000a) indicated that the application of the shear-volumetric approach in dealing with the nonlinear response of granular materials is advantageous in theory. However, models of this kind are usually more complex in nature and the parametric values are more difficult to

determine from collected test data and isotropy is assumed for materials that are frequently known to be unisotropic.

2.4.2 Models for Permanent Deformation Behaviour

Models for predicting railway track deterioration are normally based on the assumption that the granular material is linear elastic (Dahlberg 2001). As only the elastic material properties are needed, these models are easy to use. However, the permanent deformation of a railway track cannot be predicted, as no information is available on inelastic behaviour. Therefore, in this section, mathematical modelling of railway ballast inelastic deformation behaviour is reviewed. Various researchers have empirically modelled the permanent deformation of ballast under cyclic loading, and this will be discussed in the following sections.

One of the most widely used mathematical models for calculating the permanent deformation was developed by Alva-Hurtado and Selig (1981). The permanent strain (ε_N) after a number of cycles (N), can be approximately related to the permanent strain after one cycle (ε_1), by the expression:

$$\varepsilon_N = \varepsilon_1(1 + C \log N) \qquad \text{(Equation 2.9)}$$

where C is a dimensionless constant controlling the rate of growth of deformation. Typical values are between 0.2 and 0.4 (Selig and Waters 1994).

Hettler (1984) found that the accumulation of permanent deformation was proportional to the logarithm of the number of load cycles and expressed the results by the lognormal model as follow:

$$S_N = S_1(1 + c' \ln N) \qquad \text{(Equation 2.10)}$$

where the factor *c'* takes values between 0.25 and 0.55. This model is quite close to Alva-Hurtado and Selig's model, except that the settlement is expressed instead of strain in Hettler's model. Furthermore, Hettler (1984) suggested the initial settlement (S_1) in Equation 2.10 might be a non-linear function of the amplitude of the load (F_l). From measurements, S_1 was estimated as follows:

$$S_1 = sF_l^{1.6} \qquad \text{(Equation 2.11)}$$

where *s* is a scaling factor. In this formula, the settlement after a large number of loading cycles is dependent on the settlement after the first cycle.

Based on laboratory and field experiments, Shenton (1985) suggested a settlement law which is shown as Equation 2.12. The settlement is considered to be proportional to the fifth root of the number of load cycles. This agrees well with site measurements up to 10^6 load cycles, given in the form:

$$S_N = K_1 N^{0.2} + K_2 N \qquad \text{(Equation 2.12)}$$

where the constants K_1 and K_2 are selected to make the second term become significant only for values of load cycles (*N*) larger than 10^6. The values of the

constants K_1 and K_2 depend on a number of factors, such as axle load, rail section, sleeper spacing, and track and foundation stiffness.

Sato (1995) suggested that the track settlement (S_N) under repeated loading (N) could be expressed by an equation of the form:

$$S_N = \beta_3(1-e^{-\beta_1 N}) + \beta_2 N \qquad \text{(Equation 2.13)}$$

where the loading factor (N) represents either a number of load cycles of the track or a tonnage carried by the track. The constants β_1, β_2 and β_3 in the equation are parameters describing the short-term and long-term settlement behaviour.

Thom (2006) suggested that settlement was a function of load cycles, which he based on results from the full-scale Railway Test Facility (RTF) in the University of Nottingham. The following equation has been found to be a reasonable fit to the RTF data.

$$S_N = (\log_{10} N - 2.4)^2 \qquad \text{(Equation 2.14)}$$

where N represents the number of load cycles of the track. Furthermore, he proposed that settlement at any different load level and subgrade variation can be described as follow:

$$S_N = (\log_{10} N - 2.4)^2 \times (\sigma/160) \times (47/k) \qquad \text{(Equation 2.15)}$$

where σ is the stress under the sleeper, k is the modulus of subgrade reaction, which is the constant of proportionality between the contact pressure of a foundation (P_c) and the settlement of the foundation (S), defined as: $k = P_c/S$.

Besides modelling permanent strain with respect to number of load applications, several researchers have attempted to predict the permanent strain with respect to stress condition. Pappin (1979) suggested permanent shear strain rate could be a function of the stress path length in *p*–*q* space and the applied shear stress ratio. Additionally, a shape factor for the variation of permanent strain with the number of load cycles was calculated. The total shear strain was expressed as:

$$\varepsilon_s = (fnN)L(\frac{q^0}{p^0})^{2.8}_{\max} \qquad \text{(Equation 2.16)}$$

where ε_s is permanent shear strain, fnN is a shape factor based on the number of load cycles (N), L is stress path length, q^0 is modified deviator stress $=\sqrt{2/3}\cdot q$, and p^0 is modified mean effective stress $=\sqrt{3}\cdot p'$.

In addition, Raymond and Williams (1978) used the stress ratio ($q_{max}/q_{failure}$) to characterise the results of permanent deformation tests. Thom (1988) suggested that permanent shear strain was better related to the stress ratio ($q_{failure}$-q_{max})/$q_{failure}$. The plastic shear strain model in usable format was presented as:

$$\varepsilon_s = -\frac{1}{L}\ln[(\frac{q_f - q_{\max}}{q_f}) - \frac{1}{M_1}(\sigma_t + \frac{1}{3}\sigma_s)\ln N] \qquad \text{(Equation 2.17)}$$

where L, M_1 are constants, q_f is the deviator stress at failure in monotonic tests, q_{max} is the maximum deviator stress during the cyclic load application, σ_t is the shear stress, and σ_s is the mean stress.

Thom (2006) reviewed several permanent deformation equations and concluded that: there were considerable difference between the models; the relationship

between settlement and traffic volume varied from linear to logarithmic; the lack of any material-dependent parameters, nor any discrimination between train types, suspension system arrangement, train speed etc. was a clear indicator that all such models were approximate, indeed they were all represent, in effect, a best-fit approximation to the data for a particular type of railway in a particular country and with subgrade and ballast types typical of that country.

2.5 Finite Element Modelling of Granular Material

2.5.1 Introduction to the Finite Element Method

A granular material is a collection of distinct particles which displace relative to each other, and forces between particles only exist when there is a contact between particles. These discrete characteristics of granular materials lead to a tremendous amount of complex behaviour, much of which has not yet been satisfactorily understood. According to Dundall and Strack (1979), the mechanical behaviour of granular material could be investigated by the discrete element method (DEM) both microscopically and macroscopically. Furthermore, the DEM has the advantage that it enables the investigation of some features which are not easily measured in laboratory tests, such as interparticle friction, distribution of contact forces, coordination number and particle movement. Although DEM provides a detailed advanced simulation, it is much more time consuming

compared with the finite element method (FEM). FEM provides an alternative way to simulate granular material deformation behaviour and stress distribution.

FEM analysis has been widely used as one of the most versatile numerical techniques for engineering analysis. It can be applied to solve problems in solid mechanics, fluid mechanics, heat transfer and vibrations. In the FEM analysis, the model domain is divided into a finite number of elements. In solid models, displacements in each element are directly related to the nodal displacements, which connect each element. The nodal displacements are then related to the strains and the stresses in the elements. FEM tries to arrive at the nodal displacements, so that the stresses are in equilibrium with the applied loads. Once the equations are solved, the actual strains and stresses in all the elements can be found.

FEM analysis with computer aided engineering systems is commonly organised into three different parts: pre-processor, processor, and post-processor. In the pre-processor part, the model is built by defining material properties, element formulation, and geometry. Additionally, loads and boundary conditions are entered as well. With this information, the processor can compute the stiffness matrix of the model, as well as the force vectors. After that, the equilibrium equations are solved and the solution is generated in the form of displacement values. The last, but most critical, step in the entire analysis is the post-processor. The output model should be interpreted and understood based on a knowledge of

mechanics. This is critical for applying correct results to solve real engineering problems, and in identifying when modelling mistakes have been made.

The main limitation of FEM analysis of granular material is to choose a material model, which can accurately capture the material mechanical behaviour. At present, the theory of linear elastic analysis to study stress-strain conditions in a pavement is widely used in mechanistic pavement design. In linear elastic analysis, each layer is characterised by Young's modulus and Poisson's ratio. However, it can only approximate the variation of stiffness for granular materials. Hence, FEM analysis of granular material should take into account the nonlinear stress-strain relationship.

In this research, the commercial finite element analysis application ANSYS Version 11.0 was used. Similar to other general, commercial finite element packages, the ANSYS program has many computing capabilities, ranging from a simple, linear, static analysis to a complex, nonlinear, transient dynamic analysis. The ANSYS user's manual indicates that this program is a general-purpose program, which can be used for almost any type of finite element analysis in virtually any industry such as automobiles, aerospace, railways, etc. In ANSYS Version 11.0, the extended Drucker-Prager model is available to model frictional materials, which are typically granular-like soils and rock, and exhibit stress-dependent yield (i.e. the material becomes stronger as the stress increases). Furthermore, and also applicable to model materials in which the tensile and compressive yield strengths are significantly different.

Instead of complex three-dimensional (3D) models, due to the geometry and load conditions, finite element models can be simulated by two-dimensional (2D) axisymmetric, plane stress or plane strain models. In 2D axisymmetric systems, models are changed from $x-y-z$ directions to a $R-\theta-Z$ polar coordinate system. The advantage of analysis in a 2D axisymmetric system is that it is less complex and uses significantly less computer resources. As the single circular load and confining pressure in triaxial tests can be analysed using a 2D axisymmetric approach, it is generally recommended by many researchers in the simulation of triaxial tests (e.g. Hoff *et al.*, 1999; Arnold, 2004; Salim, 2004).

Plane stress and plane strain models are two other approaches for the analysis of 2D problems. Plane stress models assume very thin geometries, where minor principal stress across the thickness is zero. Because of the thin geometry and zero minor principal stress, this model is clearly not suitable for this railway track analysis. In contrast, plane strain models assume the thickness in the horizontal plane is infinite. Geometry across the thickness does not change (i.e. the horizontal strain is nil). Additionally, the loading is assumed to extend infinitely in the horizontal plane as well. The plane strain model is accurate enough to capture the mechanical behaviour of granular material in railway track and pavements and is widely used by many researchers (e.g. Jacobs *et al.*1992; Long *et al.* 2002; Arnold, 2004).

A 3D model is normally developed based on several 2D models. Although 3D models have the potential to take into account realistic geometry, loading and bounding conditions more accurately, they are more time-consuming and complex, where degrees of freedom and element types need to be carefully chosen and require more experience. Mohammad et al. (2003) analysed a 3D model in ANSYS on a typical three-layer flexible pavement system with a predefined crack. Additionally, railway tracks have been simulated in 3D by many other researchers (e.g. Gustavson and Gylltoft, 2002; Chen *et al.* 2005; Banimahd and Woodward, 2007).

2.5.2 Elastoplastic Material Models

Most common engineering materials exhibit a linear stress-strain relationship up to a stress level known as proportional limit. Plastic behaviour happens when stress exceeds a yield point. Beyond this limit, the stress-strain relationship will become nonlinear, where materials undergo significant increase in strain for very small increase in stress. Such increase in strain is termed plastic flow of the material. Additionally, nonlinear stress-strain relationships in an elastoplastic model can cause changes of material stiffness at different load levels. A typical elastoplastic stress-strain curve is shown in Figure 2.18. In an elastoplastic material, the total strain of a material is considered as the sum of recoverable elastic strain and permanent plastic strain components, expressed as:

$$d\varepsilon_{ij} = d\varepsilon_{ij}^{e} + d\varepsilon_{ij}^{p} \qquad \text{(Equation 2.18)}$$

where $d\varepsilon_{ij}^{e}$ = elastic strain increment and $d\varepsilon_{ij}^{p}$ = plastic strain increment.

The numerical functions that define a material behaviour at the yield limit are termed yield functions or yield criteria. The elastoplastic material behaviour after yielding can be defined as perfectly plastic, strain hardening or strain softening plasticity. Chen (1994) indicated that both Mohr-Coulomb and Drucker-Prager criteria satisfy most of the characteristic behaviour of granular materials. Both criteria are commonly used for modelling granular materials, and will be studied in the subsequent two sections.

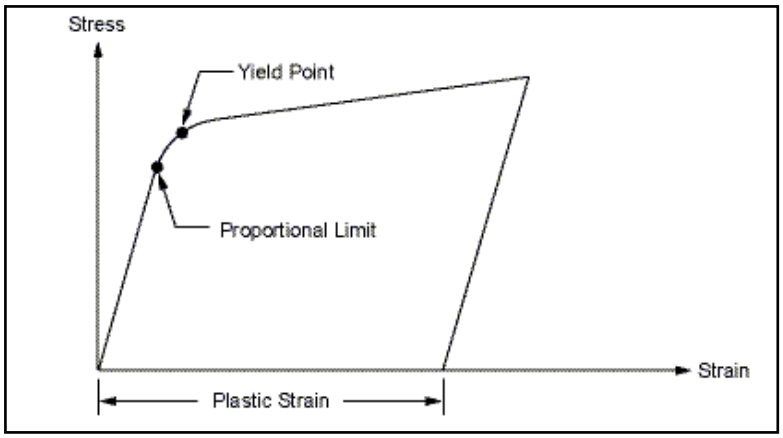

Figure 2.18 Elastoplastic stress-strain curves (ANSYS, 2007)

Mohr-Coulomb Model

In 1882, Mohr presented a theory for analysing stress that contended a material failed because of a critical combination of normal stress and shearing stress, not from either maximum normal or shear stress alone. The Mohr-Coulomb model

assumes a linear relationship between shear strength and normal stress. The model is based on plotting Mohr's circle for states of stress at failure in the plane of the maximum and minimum principal stresses. The failure line is the best fit straight line that touches these Mohr's circles. Figure 2.19 shows the Mohr-Coulomb failure model in 2D $\tau - \sigma$ stress space. Equation 2.19 presents the Mohr-Coulomb failure line.

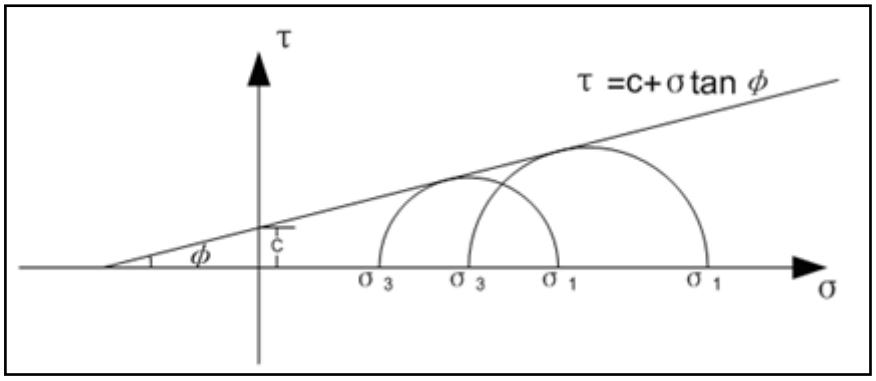

Figure 2.19 Mohr-Coulomb failure model in 2D $\tau - \sigma$ stress space

$$\tau = c + \sigma \tan\phi \qquad \text{(Equation 2.19)}$$

where,

τ = shear stress,

c = cohesion,

σ = normal stress,

ϕ = frictional angle.

In the Mohr-Coulomb model, the tensile strength of a material can be controlled by cohesion. The cohesion is the component of shear strength of granular material that is independent of inter-particle friction.

The Mohr-Coulomb model is an elastic and perfectly plastic model with associated and non-associated flow rules. The yield surface of this criterion can be presented as a hexagonal pyramid extended into compressive principal stress space, as shown in Figure 2.20. However, the six-face yield surface causes numerical difficulties along each edge, because the normal vector of the yield surface can't be uniquely defined along the edge lines. Therefore, the Drucker-Prager model was introduced to solve the numerical calculation problems.

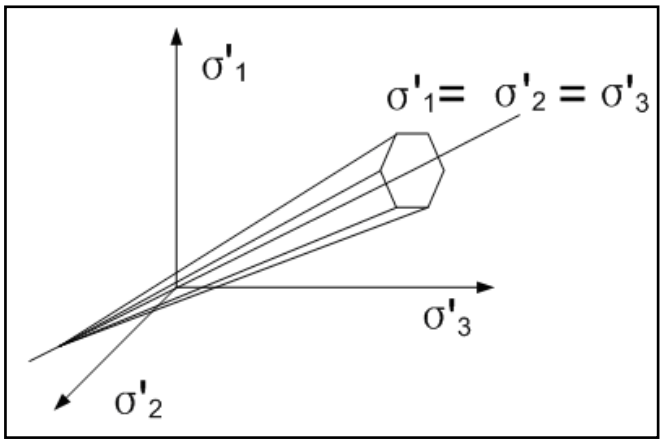

Figure 2.20 View of Mohr-Coulomb failure surface in 3D space of principal stresses

Drucker-Prager Model

The Drucker-Prager model is an elastoplastic model based on either associated or nonassociated flow rules. The yield surface does not change with progressive yielding, hence there is no hardening rule and the material is elastic-perfectly plastic. This criterion can be defined as a yield surface (F_s) in a *p'-q* stress space

given by Equation 2.20 and shown in Figure 2.21. The failure surface in 3D space of principal stresses is simplified to a cone, as shown in Figure 2.22. Unlike the Mohr-Coulomb criterion, the circular shape of the Drucker-Prager yield surface can be readily defined in finite element formulations.

$$F_s = q - p' \tan \beta - d = 0 \qquad \text{(Equation 2.20)}$$

where,

q = principal stress difference,

p' = mean effective stress,

β = the angle of the yield surface in *p'-q* stress space,

d = the intercept of the yield surface in *p'-q* stress space.

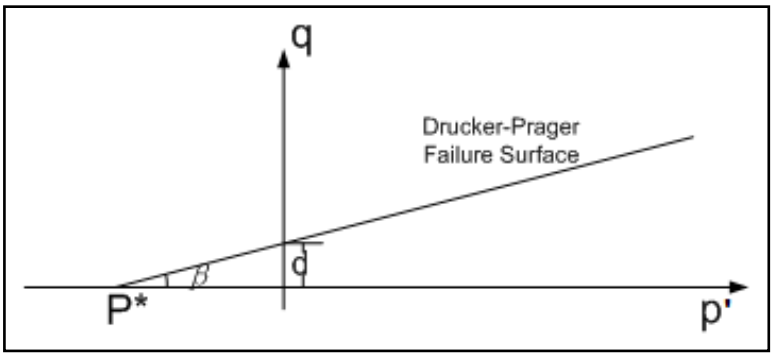

Figure 2.21 Drucker-Prager yield surface in 2D *p'-q* stress space

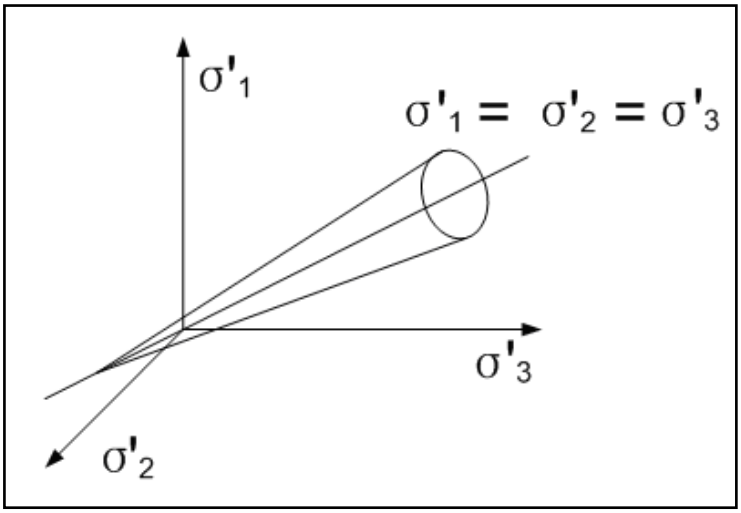

Figure 2.22 View of Drucker-Prager failure surface in 3D space of principal stresses

Extended Drucker-Prager Model

The extended Drucker-Prager model with hardening can capture the mechanical behaviour of granular materials better than the Mohr-Coulomb and Drucker-Prager models. In ANSYS version 11.0, three yield criteria are provided in this set of models. They offer differently shaped yield surfaces in the meridional plane (i.e. *p'*–*q* plane): a linear form, a hyperbolic form and a general exponent form. The yield surface can be changed with progressive yielding using isotropic hardening plasticity material options.

The yield function with linear form is given by Equation 2.21 and shown in Figure 2.23:

$$F_s = q + \alpha p' - \sigma_Y(\varepsilon_{pl}) = 0 \qquad \text{(Equation 2.21)}$$

where,

α = material parameter referred to as pressure sensitive parameter,

q $= [\frac{3}{2}\{s\}^T[M]\{s\}]^{\frac{1}{2}}$, $\{s\}$ = deviatoric stress vector,

$\sigma_Y(\varepsilon_{pl})$ = yield stress of material,

p' = mean effective stress = $\frac{1}{3}\times(\sigma_x'+\sigma_y'+\sigma_z')$.

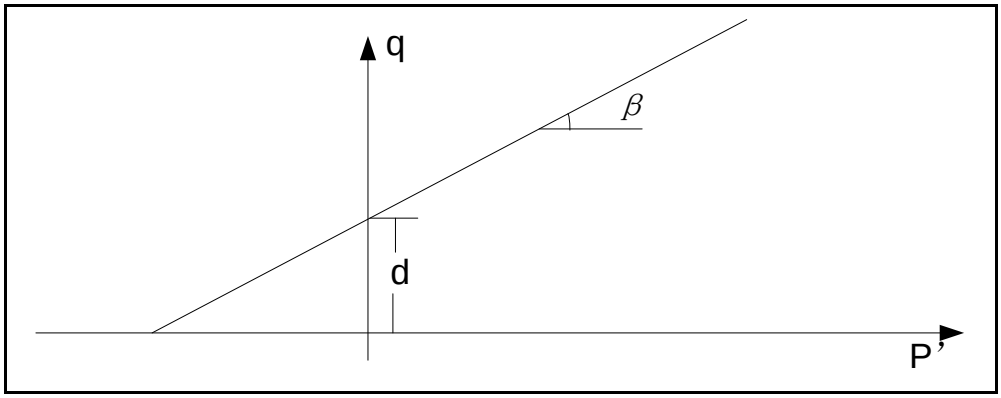

Figure 2.23 Linear Drucker-Prager yield surface in the meridional plane

The yield function with hyperbolic form is given by Equation 2.22 and shown in Figure 2.24:

$$\sqrt{a^2+q^2}+\alpha p'-\sigma_Y(\varepsilon_{pl})=0 \qquad \text{(Equation 2.22)}$$

where,

a = material parameter characterising the shape of yield surface,

α, q, p', $\sigma_Y(\varepsilon_{pl})$ are defined as Equation 2.21.

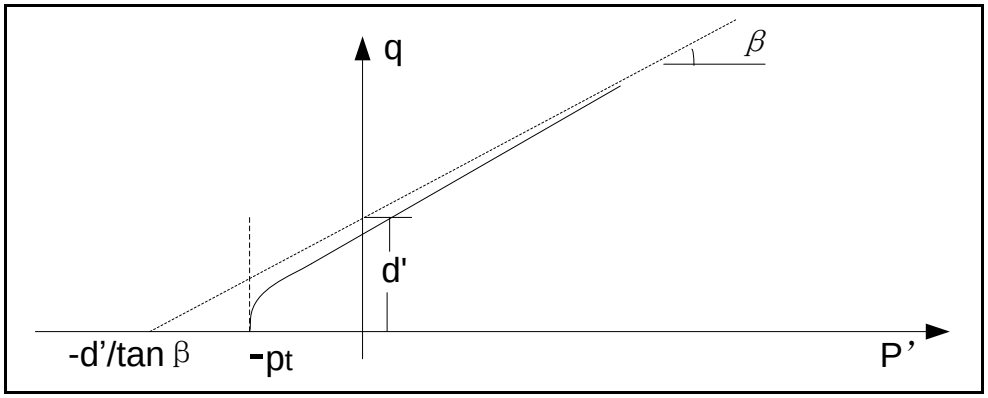

Figure 2.24 Hyperbolic yield surface in the meridional plane

The yield function with power law form is given by Equation 2.23 and shown in Figure 2.25.

$$q^b + \alpha p' - \sigma_Y^b(\varepsilon_{pl}) = 0 \qquad \text{(Equation 2.23)}$$

where,

b = material parameter characterising the shape of yield surface,

α, q, p', $\sigma_Y(\varepsilon_{pl})$ are defined as Equation 2.21.

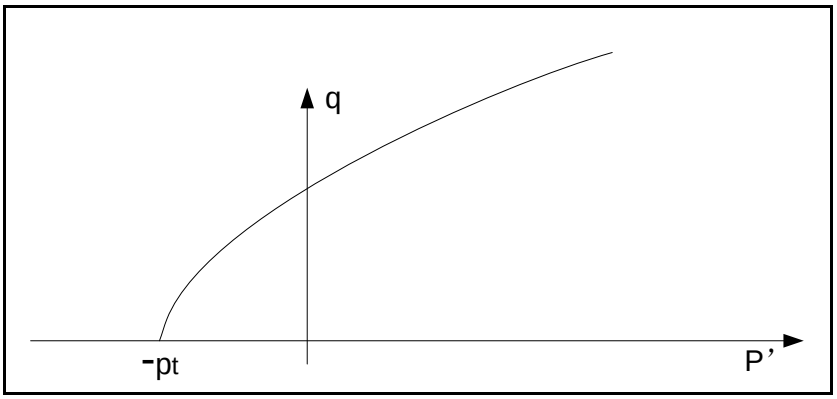

Figure 2.25 Exponent form yield surface in the meridional plane

The relationship between plastic strain ratio and stress ratio is termed the flow rule governing the mechanism of plastic deformation. The flow rule defines the subsequent increment of the plastic strain of a yielding body subjected to further loading. This is established through the concept of flow potential *Q*, which defines the direction of plastic strain increment given by:

$$\varepsilon_{pl} = \lambda \frac{\partial Q}{\partial \sigma} \qquad \text{(Equation 2.24)}$$

where λ = plastic multiplier, that depends on the state of stress and load history. If the potential and yield functions coincide with each other, the flow rule is called the associated flow rule. Otherwise, the non-associated flow rule applies. As the associated flow rule is utilised in the extended Drucker-Prager material model in ANSYS, the flow potential *Q* for linear form is defined as:

$$Q = q + \alpha p' - \sigma_Y(\varepsilon_{pl}) \qquad \text{(Equation 2.25)}$$

Similarly, the flow potential *Q* for hyperbolic form is defined as:

$$Q = \sqrt{a^2 + q^2} + \alpha p' - \sigma_Y(\varepsilon_{pl}) \qquad \text{(Equation 2.26)}$$

Similarly, the flow potential *Q* for power law form is defined as:

$$Q = q^b + \alpha p' - \sigma_Y^b(\varepsilon_{pl}) \qquad \text{(Equation 2.27)}$$

The hardening rule describes the changing of the yield surface with progressive yielding, so that the stress states for subsequent yielding can be established. Isotropic hardening is utilised in the extended Drucker-Prager model in ANSYS. In isotropic hardening, the yield surface remains centred about its initial centreline

and expands in size as the plastic strains develop. Figure 2.26 (a) shows isotropic work hardening in the σ_1'–σ_2' plane and Figure 2.26 (b) shows hardening in the *p'*-*q* plane.

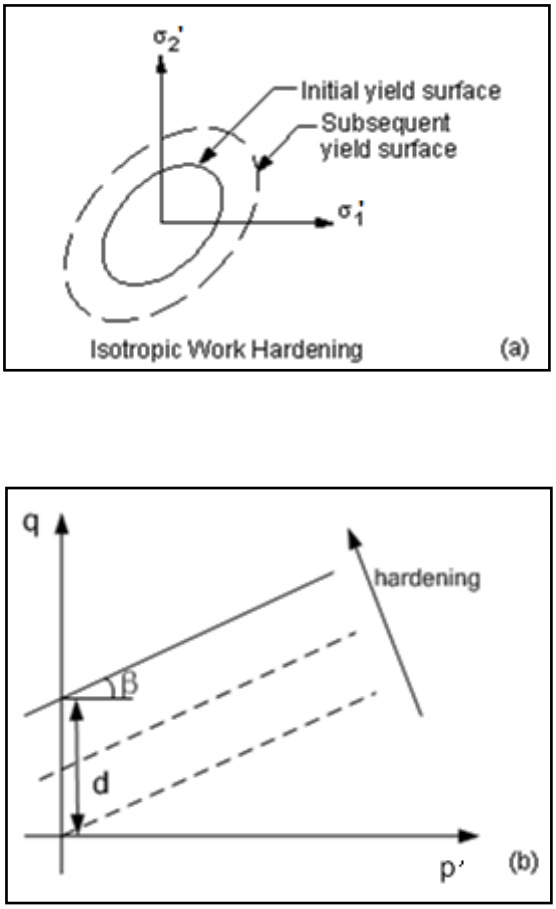

Figure 2.26 Isotropic hardening in (a) $\sigma_1 - \sigma_2$ plane, (b) *p'*-*q* plane

The choice of model depends largely on the analysis type, the kind of material, the experimental data available for calibration of the model parameter and the range of stress values that the material is likely to experience. However, the linear model is intended primarily for applications where the stresses are for the most

part compressive. Hence, an extended Drucker-Prager model with linear yield criterion will be used to simulate railway ballast deformation and stress conditions in this research.

The input parameters for extended Drucker-Prager models can be obtained by matching experimental triaxial test data. In the triaxial test, the specimen is confined by a compressive stress, which is held constant during the test. The loading is an additional tension or compression stress applied in one direction. The calibration between experimental triaxial test data and the extended Drucker-Prager model will be discussed in Chapter 6.

2.6 Chapter Summary

The components of railway tracks and their functions, in particular the ballast layer, have been reviewed in this chapter. Railway tracks are designed to ensure safe operation at specified levels of speed and load. A conventional ballasted railway track system consists of a superstructure on the top of a substructure. Railway ballast is a crushed granular material placed as the top layer of the railway track substructure where the sleeper is embedded. Its main function is to spread the high loads of passing axles to the subgrade. Moreover, ballast provides a certain amount of resiliency as well as energy absorption for the railway track. Ideal ballast used for railway track should have high stiffness, high strength, crushing resistance, chemical resistance and be free from dust.

Railway ballast deforms in two main modes: frictional slip and particle breakage. These are interdependent mechanisms causing the ballast to be a continually changing material. In addition, as previously discussed, there are many parameters that influent the resilient and permanent behaviour of granular material under repeated loading. The literature reveals that the resilient behaviour of granular material may be affected by several factors: stress state, stress history, loading sequence, number of loading cycles, aggregate type, geometry (shape and texture), aggregate grading and moisture content. The main influences on permanent behaviour are: stress level, principal stress rotation, initial density, grading, number of load cycles, moisture content, loading sequence and loading frequency.

Modelling is an important requirement in dealing with material performance. This review presented mathematical models to describe the resilient and permanent responses of granular materials. The resilient behaviour is significantly affected by the stress states, while most permanent deformation models focus on the track settlement due to the loading on the track and the load cycles. Although researchers have presented mathematical formulations that fit their particular data, great effort is clearly needed in developing more general and theoretically based models.

Currently, FEM analysis is widely used in railway and geotechnical engineering. It is generally recommended that analysis with non-linear material should be conducted using a simpler 2D model rather than a complex 3D model, although

the 2D model is less accurate Therefore, 2D axisymmetric, plane stress and plane strain models have been reviewed in detail. Due to the geometry and loading conditions, triaxial tests could be simulated by a 2D axisymmetric finite element model. Railway track is able to be simplified to a plane strain condition with infinite horizontal thickness.

The elastoplastic material models for characterising the nonlinear stress-strain properties of railway ballast have been reviewed. Mohr-Coulomb, Drucker-Prager and extended Drucker-Prager models have been presented in detail. As a conclusion, the extended Drucker-Prager model with hardening can capture the mechanical behaviour of granular material better than the others. This material model will be utilised in the FEM simulation of railway ballast, which will be presented in Chapter 6.

CHAPTER 3

3. TRIAXIAL TEST

3.1 Introduction

The triaxial test is one of the most versatile and useful laboratory tests for the characterisation of granular material properties. A triaxial specimen was considered as the basis for developing a relationship between the stress, strain and particle breakage. Therefore, in order to investigate the mechanical response of ballast under monotonic and cyclic loading, and to calibrate the simulation model, a series tests were conducted in the large-scale triaxial apparatus. The whole triaxial experimental programme of this research study has been divided into three categories: the monotonic triaxial test, the cyclic triaxial test and the multi-stage triaxial test.

Results from the monotonic triaxial tests are fed into a finite element modelling of ballast using the ANSYS computer program to simulate the stress distribution. A series of cyclic and multi-stage loading triaxial tests were carried out to obtain settlement equations which describe the settlement of ballast under a single stress

condition. A ballast settlement model was then developed as a function of the number of loading cycles, the magnitude of load and the formation stiffness, which predicts the resultant vertical settlement beneath a sleeper under repeated traffic loading.

In this test a sample of ballast particles is sealed in a rubber membrane subjected to uniform external pressure and then loaded axially. The constant confining pressures were held to simulate the mean pressure due to geostatic stresses in railway track. The axial loading was to mimic the passing train loading spreading from the sleeper. However, the triaxial test is still an approximate approach to simulate the in-situ railway track. As the confining pressure in the triaxial test of this research is constant during each test stage, while, in-situ condition, the horizontal stress within the ballast increases when the wheel loading is approaching and decrease when the wheel loading is leaving. Furthermore, triaxial test assumes axisymmetric stress conditions within in the ballast, which, however, is not true in reality. The details of sample preparation, instrumentation, test procedures and results are described in the following sections.

3.2 Large Scale Triaxial Apparatus

The conventional triaxial samples are 37-50mm in diameter, while the maximum ballast grain size used in this project can be 50mm. To overcome this problem, either scale-down test materials or a large-scale triaxial apparatus should be

utilised. Kaya (2004) investigated stress-strain behaviour of scale-down railway ballast with a maximum particle size not more than one over six that of the specimen diameter of the available triaxial apparatus. However, full size railway ballast was used in a large-scale triaxial apparatus to obtain realistic strength, deformation and degradation characteristics in this project. This large-scale triaxial apparatus was developed by GDS Instruments specifically for ballast research projects. It is designed for a testing sample of 300mm diameter and 450mm height and is hydraulically actuated with a large diameter triaxial cell suitable for samples with large particle sizes such as railway ballast. This system is capable of carrying out both monotonic and dynamic triaxial tests, all under computer control. All monotonic, cyclic and multi-stage triaxial tests were performed on dry ballast with constant confining pressure in this project. Figure 3.1(a) shows the large scale triaxial apparatus testing system at the laboratory in the University of Nottingham. The triaxial load apparatus has been schematised in Figure 3.1(b). It consists of a high frequency test rig, a confining pressure system, volume change measurement system and computer control system. The principle of this system is to use water in an inner cell which is direct contact with the sample. Air at a specified pressure is direct to an outer cell so that the water in the neck is pressurised and consequently a confining pressure is applied to the sample. Any change in the volume of the sample will displace an equivalent volume of water in the inner cell. The volume change is measured by a differential pressure transducer by recording the head difference between inner cell water level and a fixed water level in the reference tube (Figure 3.1(b)). This method was preferred due to the irregular outer surface profile of the sample cause by the large size and angular shape of the

ballast. At the beginning of each test, the water levels in both the inner cell and the reference tube are equal. If the sample in the inner cell expands the water level in the inner cell rise while the water level in the reference tube stay the same. The differential pressure transducer reading is converted to a volume change based on the know cross section areas of the inner cell neck and the reference tube. Further detailed description of for this apparatus is presented in "A laboratory study of railway ballast behaviour under traffic loading and tamping maintenance" by Aursudkij(2007).

According to Aursudkij (2007), triaxial tests carried out by this facility were repeatable. The permanent axial and volumetric strains, resilient modulus, Poisson's ratio and breakage could be reproduced with small discrepancies from different tests.

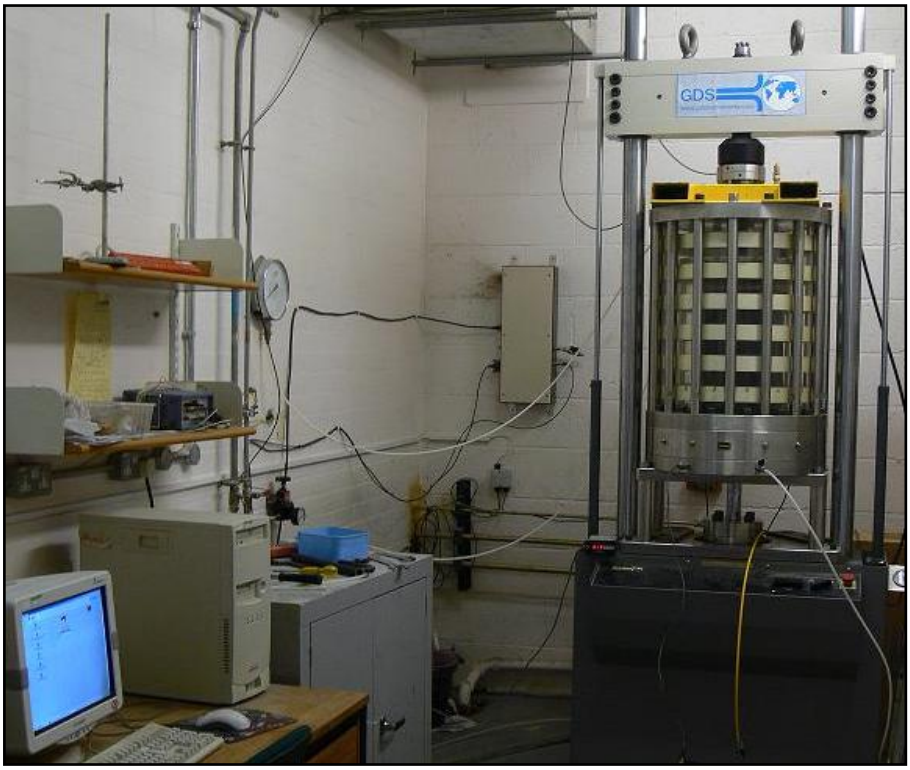

Figure 3.1 (a) Large scale triaxial apparatus testing system at the laboratory

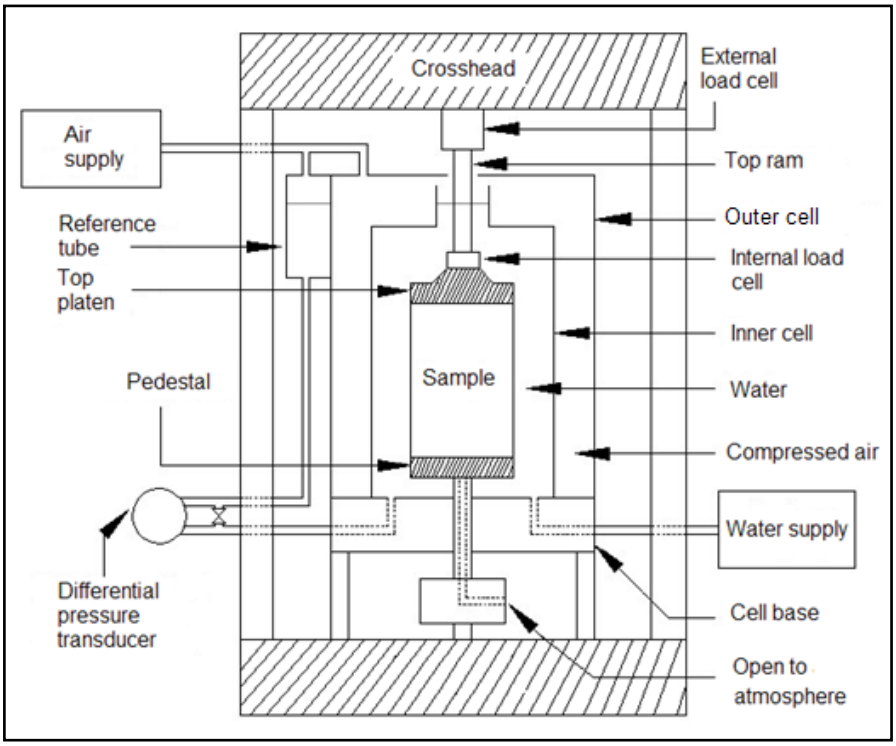

Figure 3.1 (b) Components of triaxial load apparatus

3.3 Preparation of Ballast Samples

The cylindrical ballast sample used in triaxial tests has a height of H=450mm and a diameter of D=300mm, corresponding to an aspect ratio of H/D=1.5. The ratio is smaller than Bishop and Green's (1965) suggestion of H/D=2. They believed the end friction caused an increase in the angle of shearing resistance. Hence, during the triaxial test, the diameter of the sample was not uniform throughout its whole height and this therefore affected the calculation of volumetric strain. However, instead of measuring the diametral strain, the volumetric strain is measured directly by a differential pressure transducer in this project. Furthermore, as Aursudkij (2007) described, the aspect ratio of 1.5 enabled an easier and more economical design of the cells in this apparatus.

According to Skoglund (2002), the typical value of D/d_{max} ratio in triaxial tests is 5-7, where D is specimen diameter and d_{max} is maximum particle size. The reason behind is that the diameter must be sufficiently large so that there are enough particles across the diameter to give a sufficiently representative sample. Fair (2003) also reported that the D/d_{max} ratio from different researcher varied from 4.7 to 10. As the maximum ballast particle size in this triaxial test was 50mm, the ratio D/d_{max}=6, which is within the reasonable range according to both Skoglund (2002) and Fair (2003).

In this project, only one kind of ballast was used to ensure the repeatability and validity of results. The ballast was from Glensanda Quarry in Scotland. After

consideration of the size of ballast sample, ballast with dimensions between 22.4mm and 50mm was used in the triaxial tests. Figure 3.2 shows the ballast size distribution in each test sample and the Railtrack Line Specification (RT/CE/S/006) limits. From this figure it can be seen that the grading of each sample was slightly different, but they are all within the specification limits.

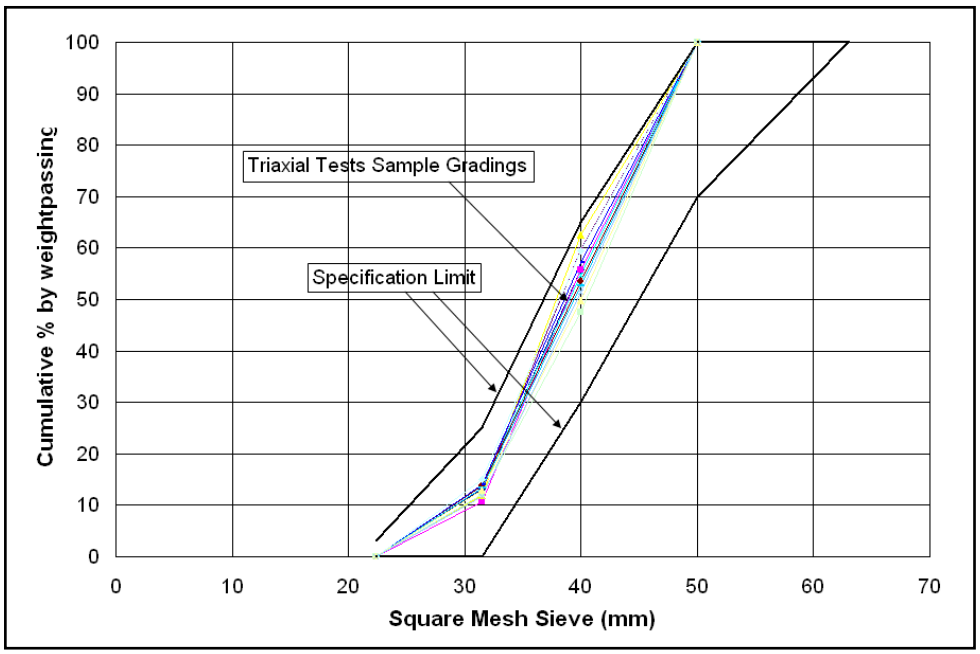

Figure 3.2 Grading of the triaxial test samples and the ballast specification

As a ballast sample consists of large regular particles with large void spaces, ballast samples were compacted on a vibration table to make sure that they were compacted to match the density of ballast in field. The ballast samples were prepared by placing and compacting three layers of ballast particles of equal thickness of 150 mm. Each layer was vibrated for 10 seconds on a vibration table with a surcharge of 20kg on top of the layer. This method of layered compaction is also used during in situ construction of ballast and subballast layers (Selig and

Waters 1994). The top layer of the sample was levelled by hand to ensure enough contact between ballast sample and the top cap.

In order to avoid membrane puncturing by the sharp edges of the ballast particles, the ballast samples were enclosed by a latex membrane of 2mm thickness. Thick rubber membranes can provide extra confining pressure to a triaxial test sample. However, both Indraratna *et al.* (1998) and Key (1998) agreed that the confinement provide by the membrane was negligible compared to the confining pressure. Indraratna *et al.* (1998) further stated that with 4mm thick membranes, it was found that under test with 1kPa confining pressure, the maximum correction was below 8%. Besides membrane thickness, membrane penetration is another issue needs to be considered. The membrane penetration causes errors in the effective confining stress during an undrained triaxial test on a coarse grained granular material (Miura and Kawamura, 1996 and Kramer *et al.*, 1990). However the triaxial test results were not corrected for membrane penetration in this analysis, since for relatively dry materials the error made by ignoring the membrane penetration is commonly small; e.g. Hjortnase-Pedersen and Molenkamp (1982) reported a difference of 0.0003 (mm/mm) in deviator strain for triaxial test results with and without correction for membrane penetration. Membrane penetration also effects volume change readings, but this is only an important issue if cell pressure changes. The membrane was connected with the top cap and the base pedestal by neoprene O rings. Also, seal tape and steel O rings were used to avoid air leaks. The base pedestal facilitated the connection of the loading frame. Then two circular latex sheets sandwiching silicon grease were

place at the top and bottom of the sample to reduce the friction with the top and the base pedestals.

During the building of the sample, the membrane was held against the wall of the compaction steel mould. After the sample was built, the top cap was attached on the top of the sample. As soon as the ballast sample was sealed, the compaction mould was removed while a temporary vacuum was created to keep the sample standing. Subsequently, the internal and external chambers were installed. A constant confining air pressure was applied to the external chamber. The air pressure was measured via both the pressure gauge and the pressure system which is connected to a computer. The regulation of the pressure was provided by means of an external pressure control system. The drainage of the specimen was controlled by valves under the facility base plate. During the test, drainage from the sample to atmospheric pressure occurred freely; therefore the pressure inside the sample equalled the atmospheric pressure.

The sample deformation in the vertical direction was measured by an external displacement transducer that was connected to the computer. A computer program was developed to store the measured vertical displacement, the vertical load, and the confining pressure every five seconds. As the differential pressure transducer for volume measurement tended to drift slightly from test to test, volume change was compared by checking the water level inside the neck of the internal chamber after each load step.

3.4 Test Procedures and Programme

According to Selig and Alva-Hurtado (1982), the in-situ confining pressure of self standing ballast perpendicular to the rail was approximately 5-40kPa based on assumed ballast coefficients of lateral earth pressure. Furthermore, the box test by Selig and Waters (1994) showed that the horizontal stress at the loaded and unloaded states would varies approximately from 15kPa to 60kPa as shown in Figure 3.3. In this research monotonic tests were carried out to determine the maximum stress level that could be applied in the cyclic triaxial tests and calibrate the numerical model. Therefore, four monotonic tests were carried out in a displacement controlled fashion with different cell pressures: 5kPa, 10kPa, 30kPa and 60kPa. After the monotonic tests, all the cyclic and multi-stage triaxial tests were performed at three different confining pressures: 10kPa, 30kPa, and 60kPa. Seven cyclic triaxial tests were carried out at each cell pressure with $(q/p)_{max}$ ratios of 1.7 and 2.0. Furthermore, all multi-stage tests had an increasing $(q/p)_{max}$ ratio from 1.7, 2.0, 2.1 to 2.2. The triaxial test plan is summarised in Table 3.1. The dry unit weight of the ballast samples presented in Table 3.1 is around 1540 kN/m^3, determined from the mass of the ballast used and the dimension of the mould. It should be noted that the number of each test includes the test series, cell pressure and $(q/p)_{max}$ ratio (only in Test series 2 and 3).

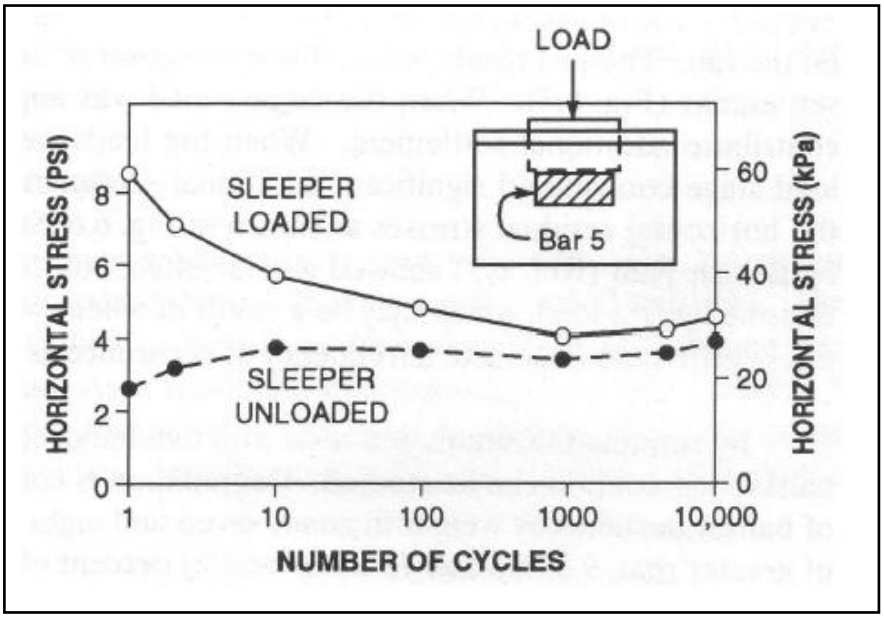

Figure 3.3 Effect of repeated load on horizontal stress in box test (Selig and Waters, 1994)

For safety reasons, all triaxial tests were continued only until the axial strain reached around 12%, which was to avoid the sample touching the inner cell according to Aursudkij's (2007) previous experience. After sample preparation, the sample was fitted in the inner and outer cells with the selected cell pressure and a seating load of 1kN. After the instrumentation installation, the sample was then loaded at a rate of 1mm/min until the axial strain reached approximately 12%.

In each cyclic test, the sample was subjected up to 100,000 continuous cycles of axial loading. After preparation, the sample was put under a seating load of 1kN. In order to avoid sudden heavy impact on the sample, instead of starting the cyclic loading directly, the load was slowly brought to the mean load first at a rate of 0.5kN/min and then cyclic loading was started.

For the first 5 cycles, the samples were loaded for a duration of 5 minutes per cycle, and then from cycle 6 to 30, they were loaded with a frequency of 1 minute per cycle. After that, most parts of the test were performed with a frequency of 4Hz until cycle 100,000. However, cycles 31-100, 181-200, 481-500, 981-1000, 1,981-2,000, 4981-5000, 9981-10000, 19981-20000, 49981-50000, and 99981-100000 were loaded at 0.2Hz to obtain the resilient sample volume changes. This is because a cyclic triaxial test with a frequency of 4Hz is too fast for the differential pressure transducer to register the sample volume change. As the differential pressure transducer cannot register the differential pressure instantaneously.

Table 3.1 Triaxial test plan in this project

Test series	No. of tests	Test number	Cell pressure (kPa)	$(q/p)_{max}$	Density (kg/m^3)
Test series 1. Monotonic test	4	T1-5	5	N/A	1550
		T1-10	10	N/A	1547
		T1-30	30	N/A	1531
		T1-60	60	N/A	1591
Test series 2. Cyclic test	7	T2-10/1.7a	10	1.7	1451
		T2-10/1.7	10	1.7	1542
		T2-10/2.0	10	2.0	1545
		T2-30/1.7	30	1.7	1545
		T2-30/2.0	30	2.0	1533
		T2-60/1.7	60	1.7	1539
		T2-60/2.0	60	2.0	1540
Test series 3. Multi-stage test	3	T3-10m	10	1.7/2.0/2.1/2.2	1544
		T3-30m	30	1.7/2.0/2.1	1537
		T3-60m	60	1.7/2.0	1541

Each multi-stage triaxial test had a constant cell pressure of 10kPa, 30kPa, or 60kPa. However, the $(q/p)_{max}$ ratio was increased from 1.7, 2.0, 2.1 to 2.2 until the sample failed or an axial strain of 12% was reached. Initially, a low $(q/p)_{max}$ ratio of 1.7 was used. After 10,000 cycles if 12% axial strain was not reached, the test would move to the next stage with a higher $(q/p)_{max}$ ratio of 2.0. A ratio of 2.1 would be used in the third stage and, if the sample did not fail, then a ratio of 2.2 would be adopted in the fourth stage. The test procedures in each stage were the same as those for cyclic triaxial tests.

After each test, ballast samples were sieved again to check for particle breakage. According to Aursudkij's (2007) previous test experience, the differential pressure transducer tended to drift slightly from test to test. Transducer calibration therefore had to be performed before every single test to obtain accurate data. Volume change was compared by reading water level on the scale of the inner cell neck.

3.5 Data Analysis Methods

For each triaxial test, the axial stress, axial strain and volumetric strain were recorded every five seconds. All the data were transferred to Excel spreadsheets for post-processing. Based on the data, peak compressive strength, friction angle, dilation angel, Poisson's ratio, resilient modulus, and initial stiffness, can be calculated. The following methods were used for the calculations.

Peak Compressive Strength

The value of peak compressive strength was taken as the greatest axial compressive stress achieved during the test. However, this is dependent on the confining pressures.

Friction Angle

The peak friction angle of ballast is conveniently calculated from the triaxial test results of peak principal stress ratio, by rearranging the Mohr-Coulomb failure criterion, as given in the following relationship:

$$\left(\frac{\sigma_1'}{\sigma_3'}\right)_p = \frac{1+\sin\phi_p}{1-\sin\phi_p} \qquad \text{(Equation 3.1)}$$

where ϕ_p is the peak friction angle, σ_1' is major principal stress and σ_3' is minor principal stress. Moreover, cohesion in Equation 3.1 is assumed to be zero.

From Equation 3.1 we can easily derive Equation 3.2:

$$\phi_p = \arcsin(q_{peak}/(2\sigma_3'+q_{peak})) \qquad \text{(Equation 3.2)}$$

where q_{peak} is maximum deviator stress. Thus Equation 3.2 relates the peak frictional angle with the peak deviator stress.

Dilation Angle

The dilation angle (ψ) is calculated from the slope of the expansive portion of volumetric strain versus axial strain increase. The slope is calculated by a linear fit

to the data from the greatest volumetric contraction to the end of the test. The dilation angle calculation expression is:

$$\psi = \frac{d\varepsilon_v}{d\varepsilon_a} \qquad \text{(Equation 3.3)}$$

Poisson's Ratio

In the cyclic triaxial tests, the Poisson's ratio equals resilient axial strain divided by resilient radial strain, as shown in Equation 3.4:

$$\upsilon = \varepsilon_{1,r} / \varepsilon_{3,r} \qquad \text{(Equation 3.4)}$$

where υ is Poisson's ratio, $\varepsilon_{1,r}$ is resilient axial strain and $\varepsilon_{3,r}$ is resilient radial strain.

Resilient Modulus

As described in the literature review, resilient modulus can be calculated using Equation 2.2.

Initial Stiffness

The initial stiffness (i.e. the tangent modulus at zero axial strain) from a monotonic triaxial test can be defined as the slope of the initial portion of the curve of deviator stress against axial strain:

$$E_0 = dq_{initial} / d\varepsilon_{initial} \qquad \text{(Equation 3.5)}$$

where E_0 is initial stiffness, $dq_{initial}$ is initial increase of deviator stress and $d\varepsilon_{initial}$ is initial increase of strain.

3.6 Test Results

3.6.1 Monotonic Triaxial Tests

A series of four monotonic triaxial tests was carried out, with the confining pressures of 5kPa, 10kPa, 30kPa and 60kPa. All these tests were continued up to axial strains of 12%. The variations of deviator stress ($q = \sigma_1' - \sigma_3'$) and volumetric strain ($\varepsilon_v = \Delta V / V_0$) with the axial strain ($\varepsilon_a = \Delta h / h_0$) of ballast under monotonic triaxial loading are shown in Figure 3.3 and Figure 3.4 respectively.

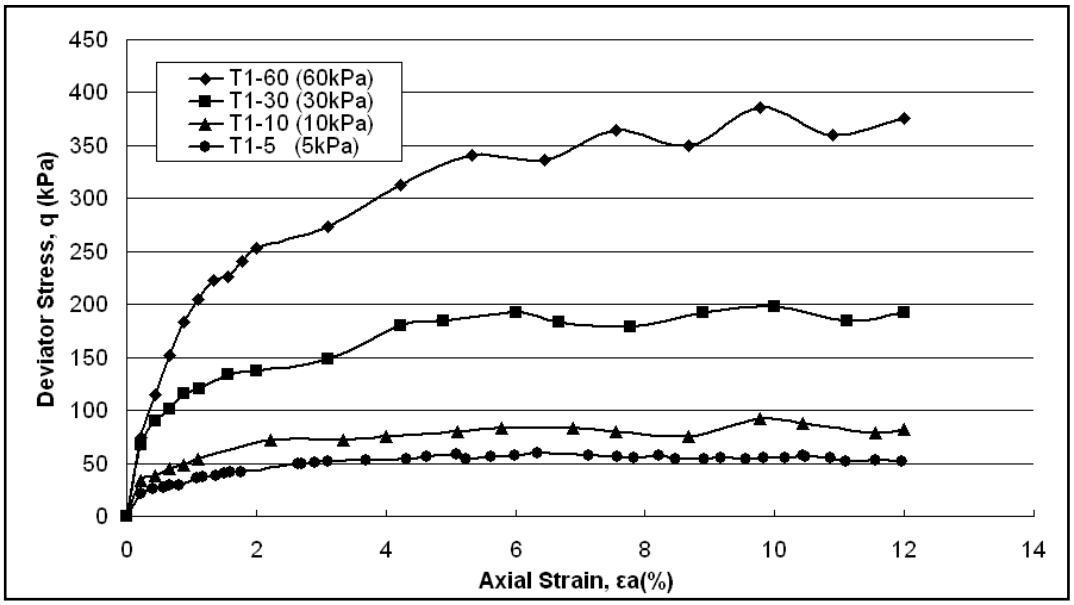

Figure 3.3 Deviator stress – axial strain behaviour of ballast under monotonic loading

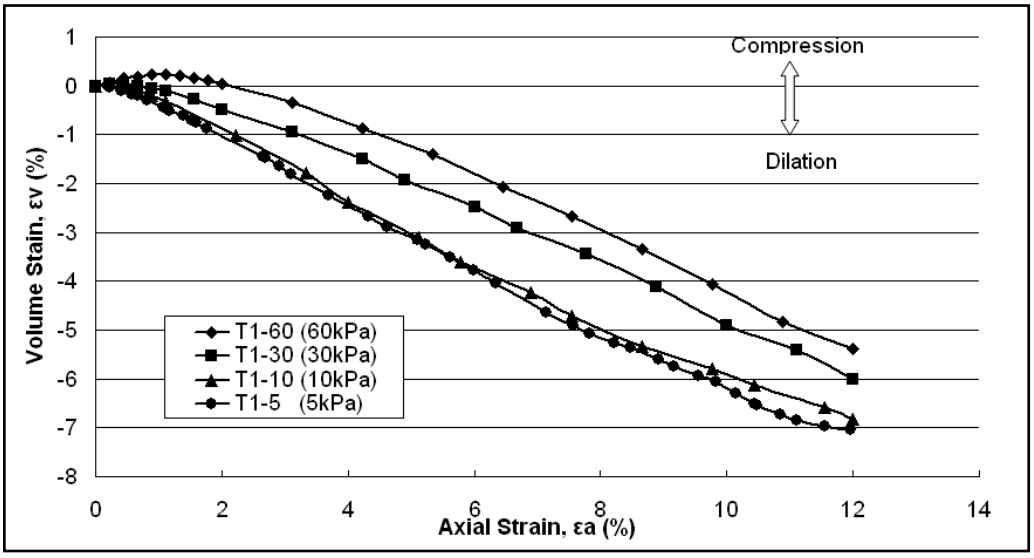

Figure 3.4 Volume change behaviour of ballast under monotonic loading

It can be seen from Figure 3.3 that an increase in confining pressure increases the deviator stress at a given strain level. Furthermore, the deviator stress eventually reaches peak. So, these peak stresses q_{peak} can be regarded as failure for ballast samples. The values of q_{peak} at different confining pressures are plotted in the Figure 3.5. Obviously, higher confining pressure leads to higher peak deviator stress. The test results reveal that the peak deviator stresses q_{peak} of all ballast samples lie approximately on a straight line between confining pressures of 5kPa and 60kPa.

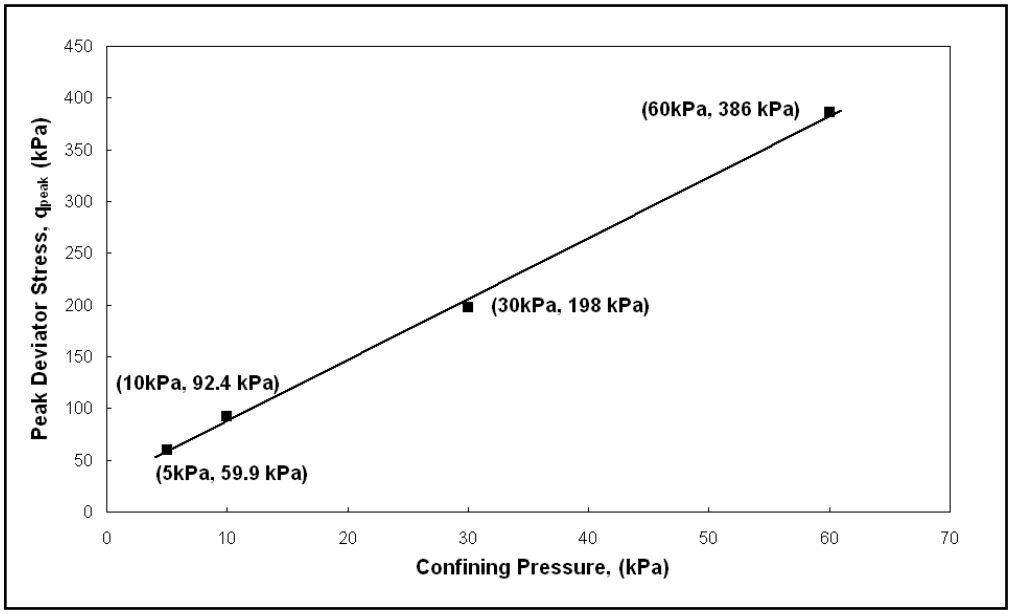

Figure 3.5 Peak deviator stress versus confining pressure under monotonic loading

From Figure 3.4 it can be seen that the volume of the ballast sample decreases firstly (compression, represented by positive ε_v). After that the volumetric strain shifted towards dilation (i.e. ε_v became negative). The test with 5kPa confining pressure has the largest dilation corresponding to it largest $(q/p')_{max}$ according to Figure 3.7.

Meanwhile, the dilation angle could be calculated from the volume change behaviour of ballast under monotonic loading. The calculation method is shown in Figure 3.6. According to Equation 3.3, the dilation angle (ψ) is calculated from the slope of the expansive portion of volumetric strain versus axial strain increase. Figure 3.6 shows that the dilation angle under lower confining pressure is slightly larger than that under higher confining pressure. However, the average dilation angle ψ = 0.58 radians (33^o) was chosen for use in computer simulation.

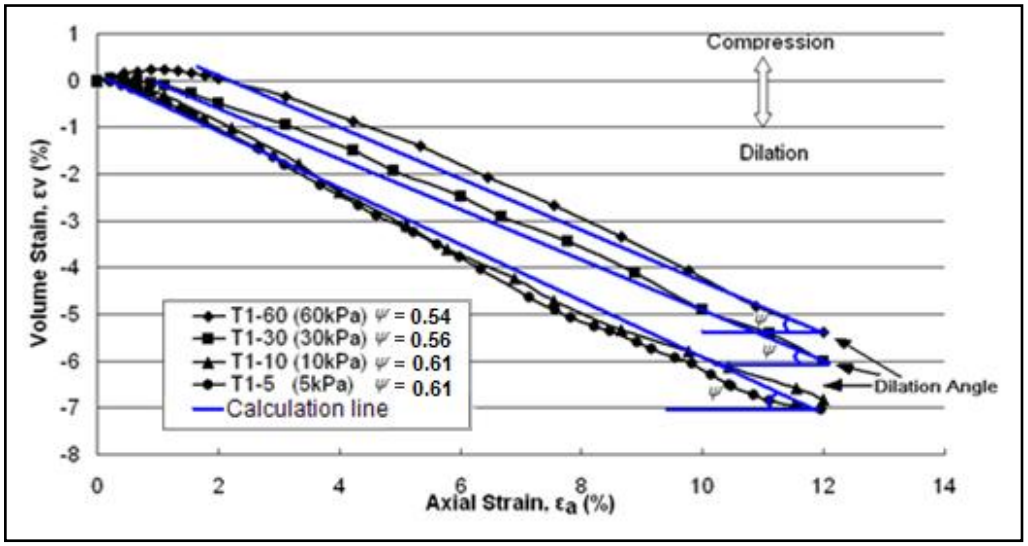

Figure 3.6 Dilation angle calculation using the monotonic loading results

Figure 3.7 shows the variation of deviator stress ratio ($\eta=q/p'$) with increasing axial strain (ε_a). This figure reveals that the deviator stress ratio increases rapidly initially and then remains stable at higher strain levels. It was noted in this figure that a lower confining pressure led to a higher peak stress ratio.

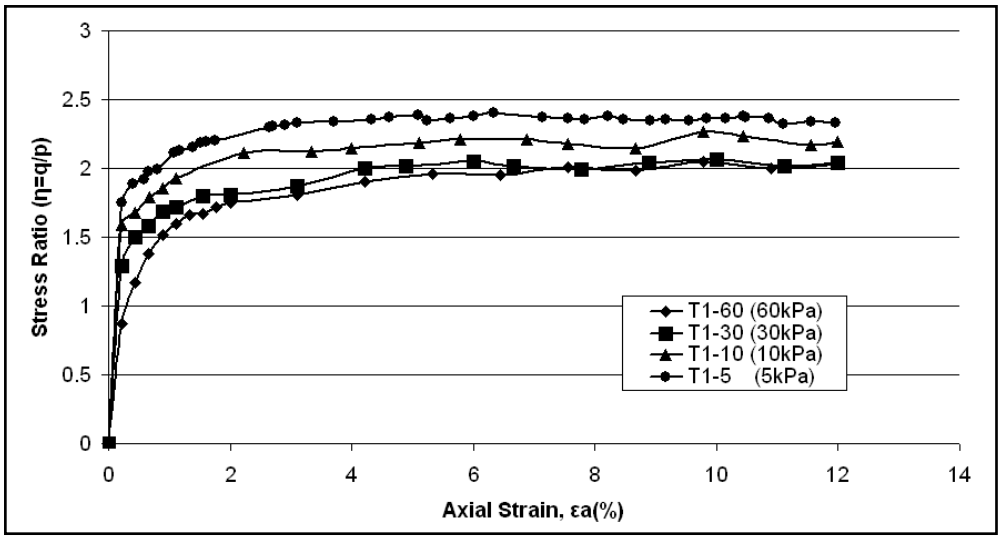

Figure 3.7 Stress ratio (η) versus axial strain (ε_a) plot for ballast under monotonic loading

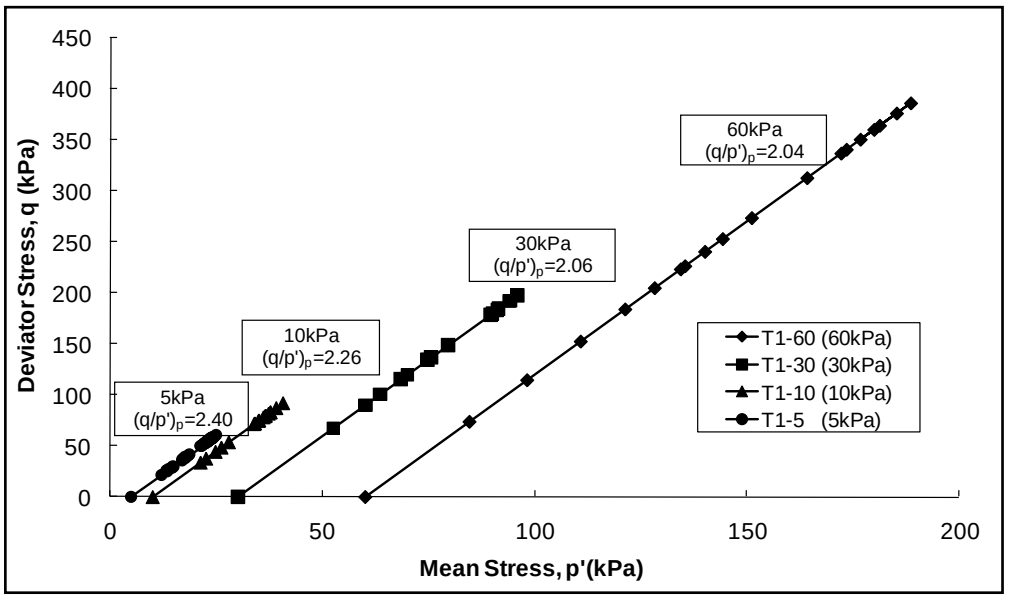

Figure 3.8 Deviator stress vs. mean effective stress in monotonic triaxial tests

Figure 3.8 shows *q-p* stress paths form the triaxial test in Series 1. As mentioned in Section 3.4, the stress paths chosen were to represent the in-situ stress conditions of the ballast perpendicular to the rail. Obviously, an increase in confining pressure increases the mean effective stress, which leads to higher peak deviator stress.

The peak friction angles of ballast obtained from monotonic triaxial tests and initial stiffness were calculated and listed in Table 3.2, where cohesion was assumed to be zero during the calculation. It reveals that the peak friction angle decreases with increasing confining pressure. The initial stiffness of ballast increases with increasing confining pressure.

Table 3.2 Initial stiffness and friction angle from Series 1 triaxial tests

Test Number	Cell Pressure (kPa)	Initial Stiffness (MPa)	Friction Angle (degree)
T1-5	5	9.7	58.98
T1-10	10	15.4	55.28
T1-30	30	30.4	50.12
T1-60	60	33.2	49.72

Ballast samples were sieved again to check for particle breakage after each test. Figure 3.9 shows the particle size distributions of the samples after monotonic tests. Only the particle sizes smaller than 22.4mm, the nominal minimum particle size prior to testing, were shown in this figure. It can be seen that the breakage increases with increasing cell pressure in the monotonic tests. This finding agrees with Key (1998) and Indraratna *et al*. (1998).

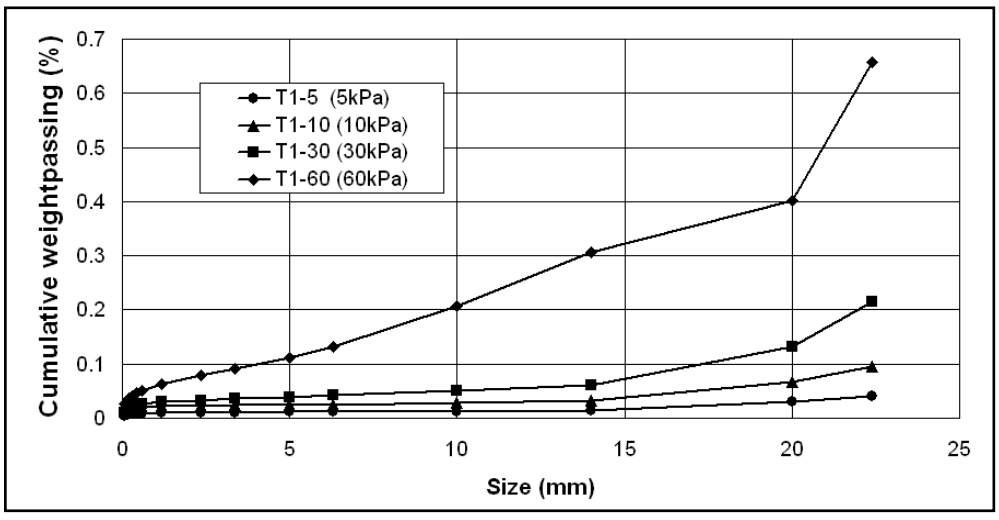

Figure 3.9 Particles smaller than 22.4mm from the monotonic triaxial tests

3.6.2 Cyclic Triaxial Tests

After the monotonic loading triaxial tests, a series of cyclic tests was carried out to investigate the permanent deformation behaviour against number of loading cycles. Cyclic tests were then used to develop a settlement model, which is discussed in Chapter 7. The cyclic triaxial test consists of the repeated loading of a cylindrical ballast sample. Cyclic stress and the confining pressure reproduce the stress range in a railway track ballast layer. In order to compare with the monotonic tests, the cyclic triaxial tests were carried out at three confining pressures 10kPa, 30kPa and 60kPa. In each test, the sample was subjected up to 100,000 continuous haversine pulses of axial stress. The axial strain, volumetric strain and changes in particle size distribution at the end of the test were measured. At the same time, the effects of stress ratio and confining pressure level were observed. The results of triaxial tests were compared with the results of the simulated traffic loading tests in the Railway Test Facility (RTF) and numerical simulation results. According to the failure loads in monotonic tests, different axial stress levels were used in different confining pressure conditions. The details of seven triaxial tests were listed in Table 3.1.

Initially, two tests under each confining pressure condition, 10kPa, 30kPa and 60kPa, a total of six tests, were intended to be used in Test Series 2. However, due to the large permanent strain in Test S2-10/1.7a (probably because the initial density of Test S2-10/1.7a was relatively low compared to the average initial

density of other tests), a repeat test S2-10/1.7 with the same stress condition was carried out.

Figure 3.10 and Figure 3.11 show the permanent axial strain against number of cycles. The following points can be concluded from these figures. With the same cell pressure, permanent axial strain increases with increasing maximum stress ratio ($(q/p)_{max}$) .With the same $(q/p)_{max}$, the sample deforms more at increased cell pressure (except S2-10/1.7a).

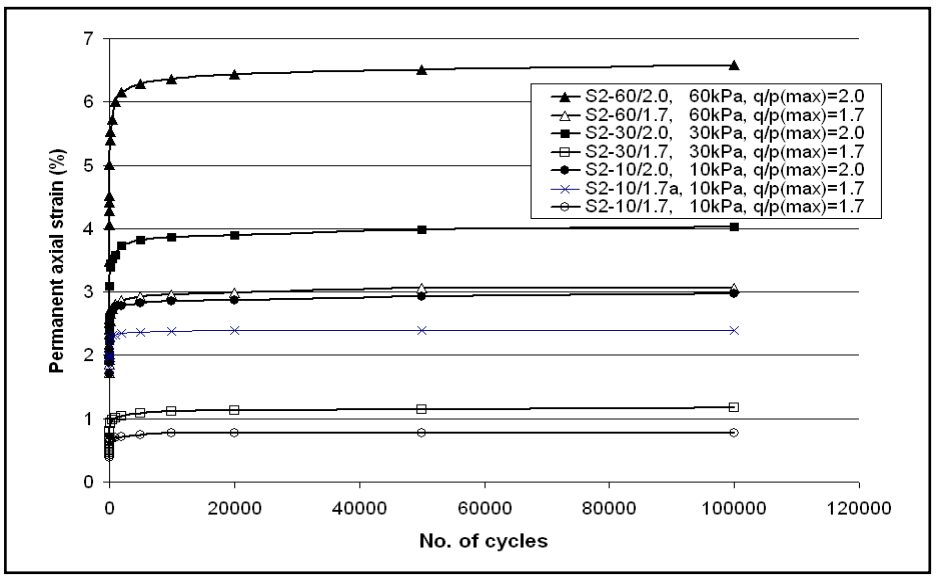

Figure 3.10 Permanent axial strain versus number of cycles

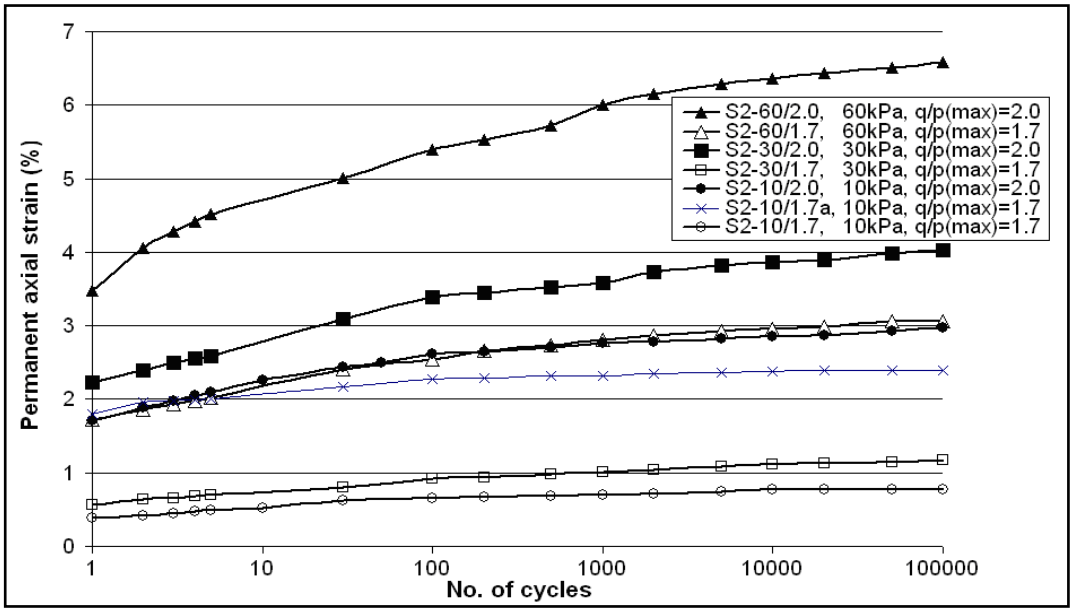

Figure 3.11 Permanent axial strain versus number of cycles on a logarithmic scale

Figure 3.12 illustrates permanent volumetric strain against number of cycles. According to this figure, the permanent volumetric strain is more compressive or less dilative with decreased $(q/p)_{max}$ under the same confining stress. With the same $(q/p)_{max}$, the permanent volumetric strain is more compressive with increased cell pressure. Tests S2-60/1.7 and S2-60/2.0 show compressive behaviour during cyclic loading. S2-Tests 30/1.7 and S2-30/2.0 show slightly compressive behaviour. However, S2-10/1.7a, S2-10/1.7 and S2-10/2.0 show neither dilation nor compression.

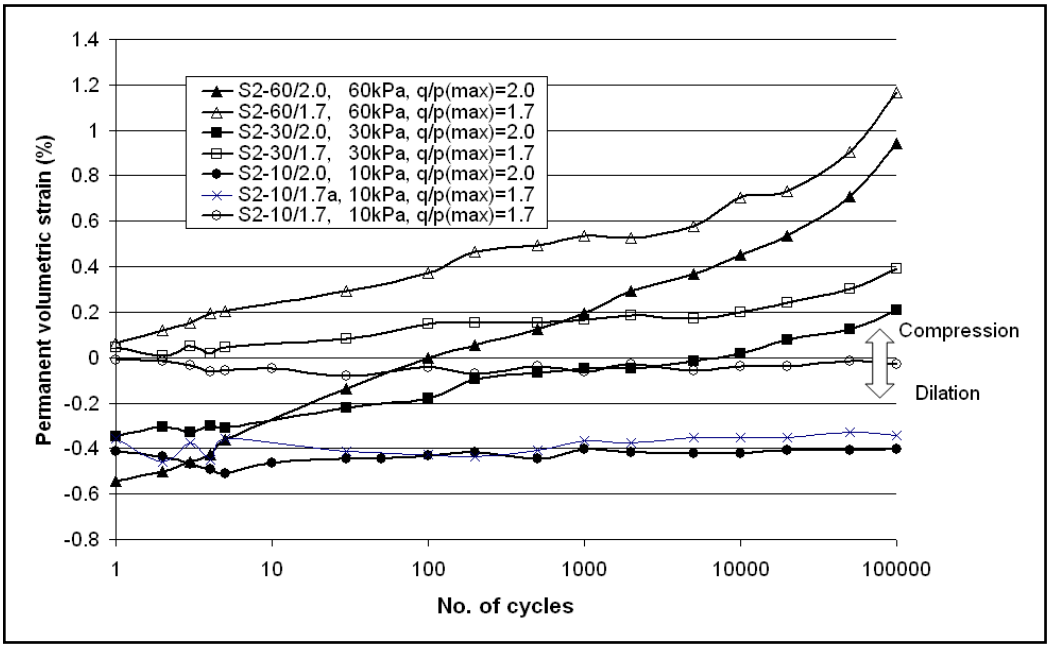

Figure 3.12 Permanent volumetric strain versus number of cycles

The resilient modulus (M_r) response to number of cycles in each cyclic test is plotted in Figure 3.13. Except for the cell pressure of 10kPa, resilient modulus increases more rapidly during the first 100 cycles than during later cycles. According to this figure, the resilient modulus depends strongly on stress condition. With the same $(q/p)_{max}$ the resilient modulus increases with confining pressure. Furthermore, the resilient modulus increases with increasing $(q/p)_{max}$ under the same cell pressure.

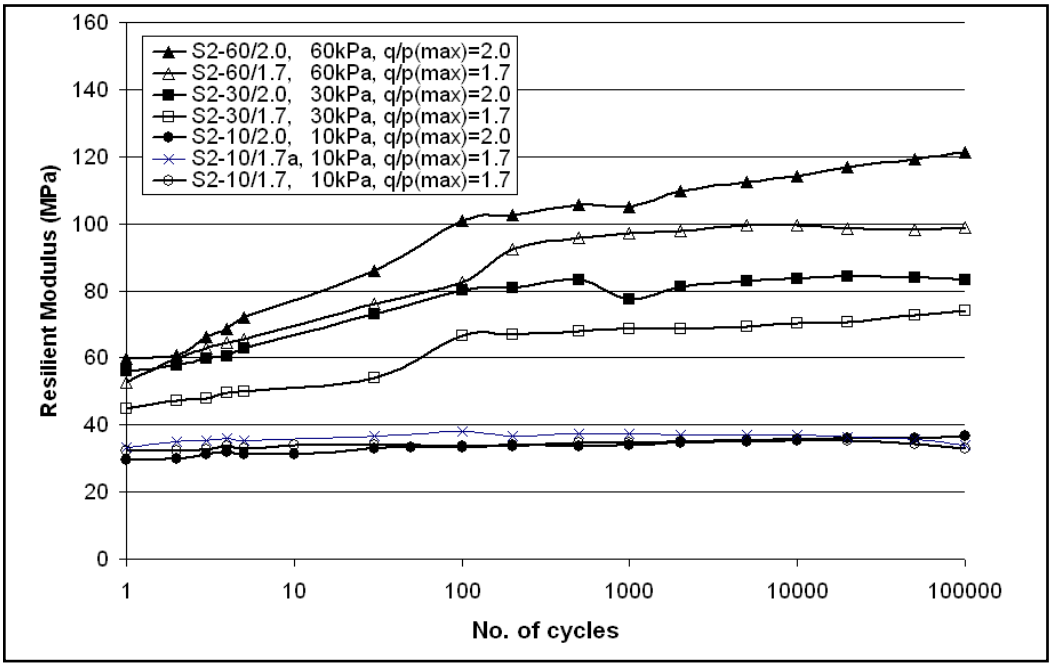

Figure 3.13 Resilient modulus versus number of cycles

Figure 3.14 plots Poisson's ratio against the number of cycles. It can be seen that with the same $(q/p)_{max,}$ the Poisson's ratio increases with increasing confining pressure. This matches the finding s from Aursudkij (2007) and many researcher in the review of Lekarp *et al.* (2000a). Moreover, the Poisson's ratio becomes stable after the first 100 cycles and varies from 0.22 to 0.35 for different confining pressures. The Poisson's ratio fluctuates significantly during the first 100 cycles and this may be due to the fact that the ballast particle movement and breakage are complicated and uncertain at the beginning of the cyclic tests. Furthermore, this issue may also be caused by the membrane penetration, which causes the errors in the triaxial test results. Similar unstable triaxial test results for Poisson's ratio can also be detected in Aursudkij's (2007) research.

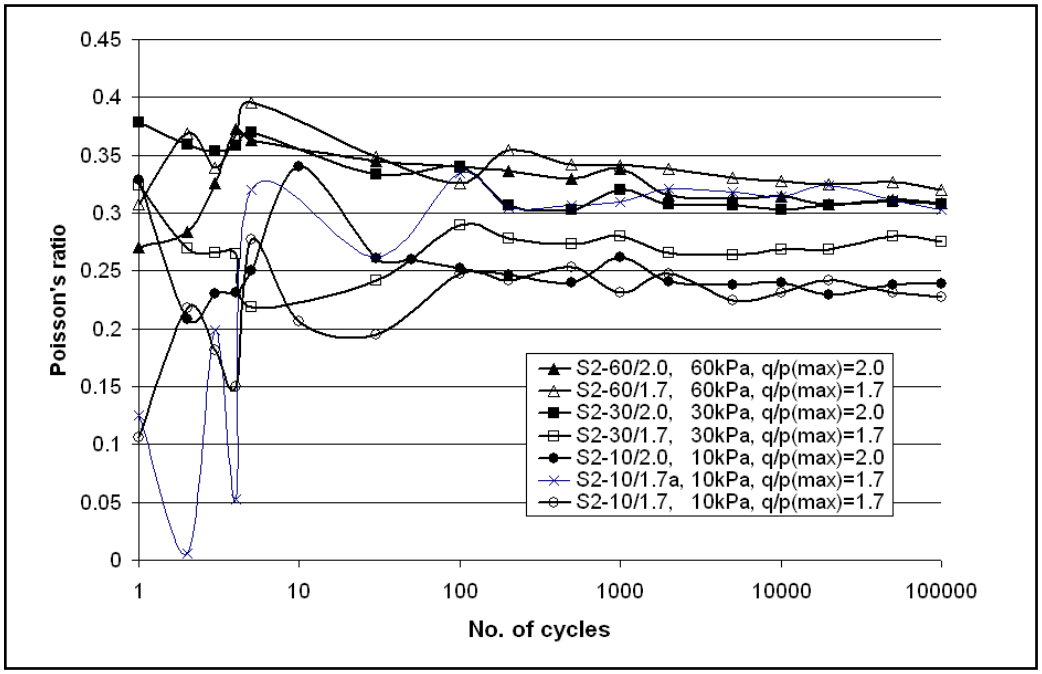

Figure 3.14 Poisson's ratio versus number of cycles from test

Figure 3.15 (a), (b), (c), (d) and (e) show the particle size distributions of the samples after the cyclic triaxial tests. As for the monotonic tests, only particle sizes smaller than 22.4mm are shown in these figures. From Figure 3.15 (a), (b) and (c), it can be seen that with the same confining stress, the breakage increases with increasing maximum stress ratio $(q/p)_{max}$. Figure 3.15 (d) and (e) show that breakage increases with increasing cell pressure, if the maximum stress ratios in the cyclic triaxial tests are the same.

Furthermore, ballast particle breakage is related to permanent deformation. Figure 3.16 shows the relationship between permanent axial strain and ballast particle breakage in cyclic triaxial tests after 100,000 cycles. Ballast particle breakage is represented by cumulative weight passing in percentages as shown in Figure 3.15 (a), (b), (c), (d) and (e). From Figure 3.16, it can be seen that the ballast

permanent deformation has a strong positive relationship with ballast particle breakage in the cyclic triaxial tests.

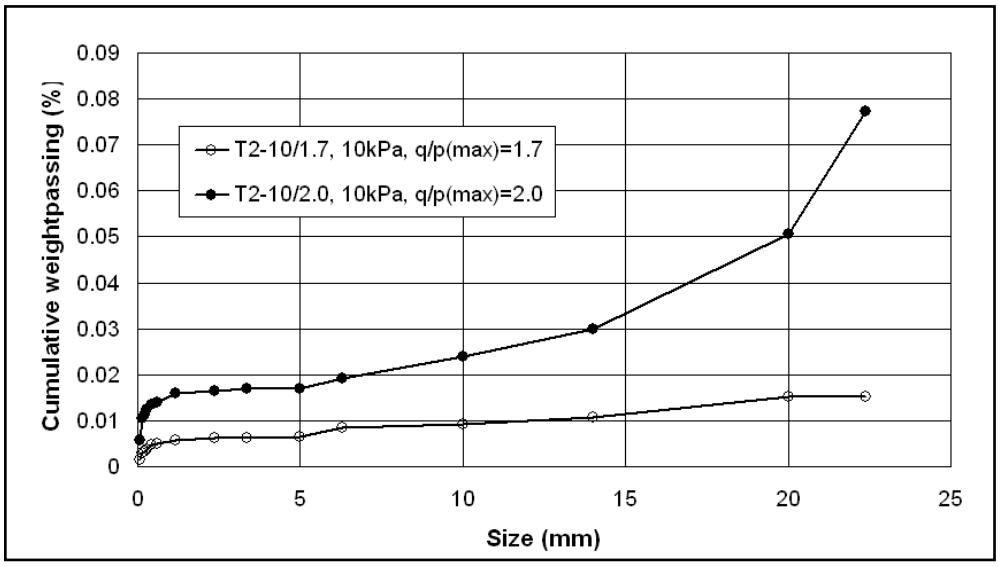

Figure 3.15 (a) Particles smaller than 22.4mm from the cyclic triaxial test with 10kPa cell pressure

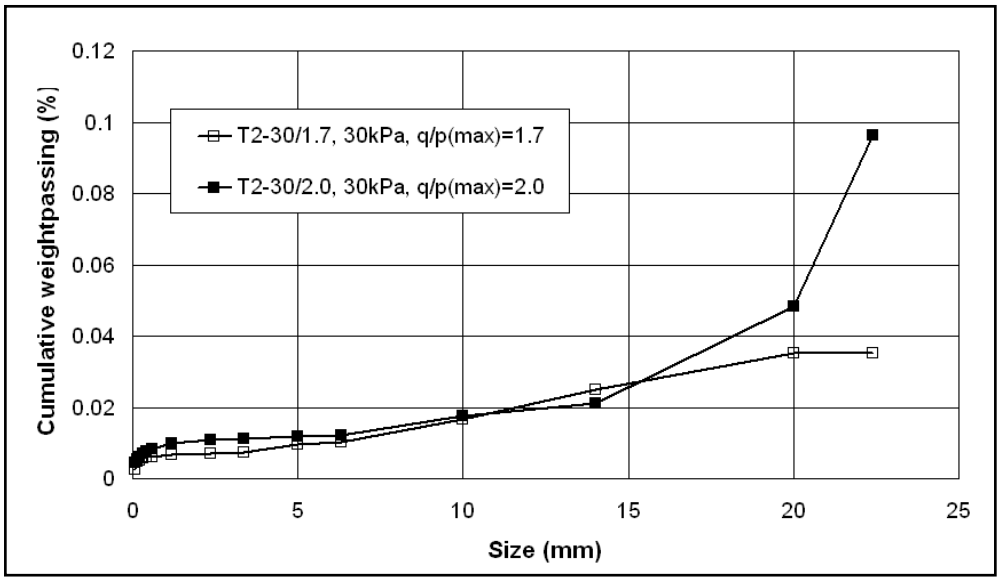

Figure 3.15 (b) Particles smaller than 22.4mm from the cyclic triaxial test with 30kPa cell pressure

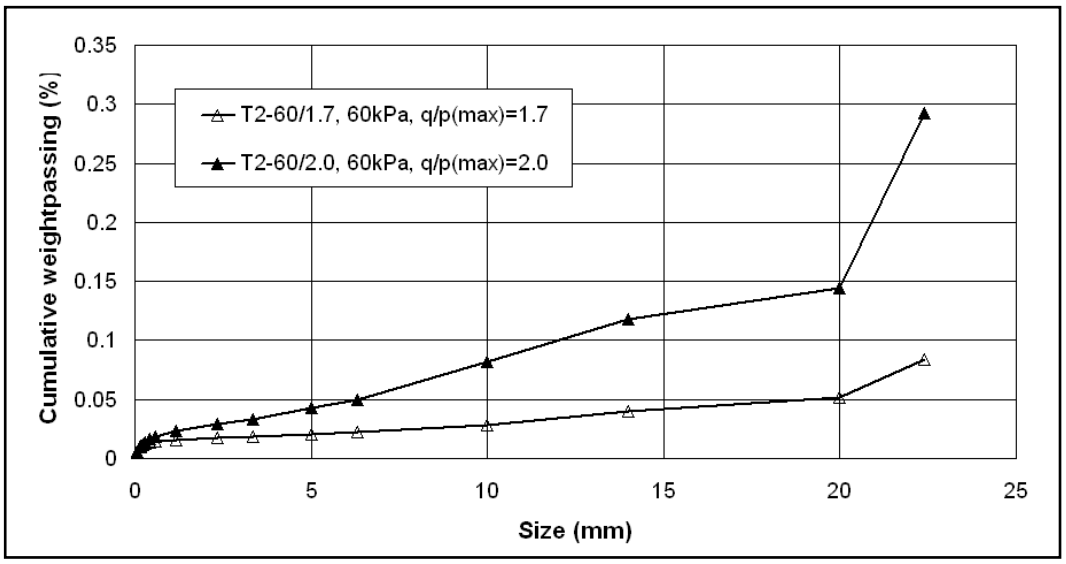

Figure 3.15 (c) Particles smaller than 22.4mm from the cyclic triaxial test with 60kPa cell pressure

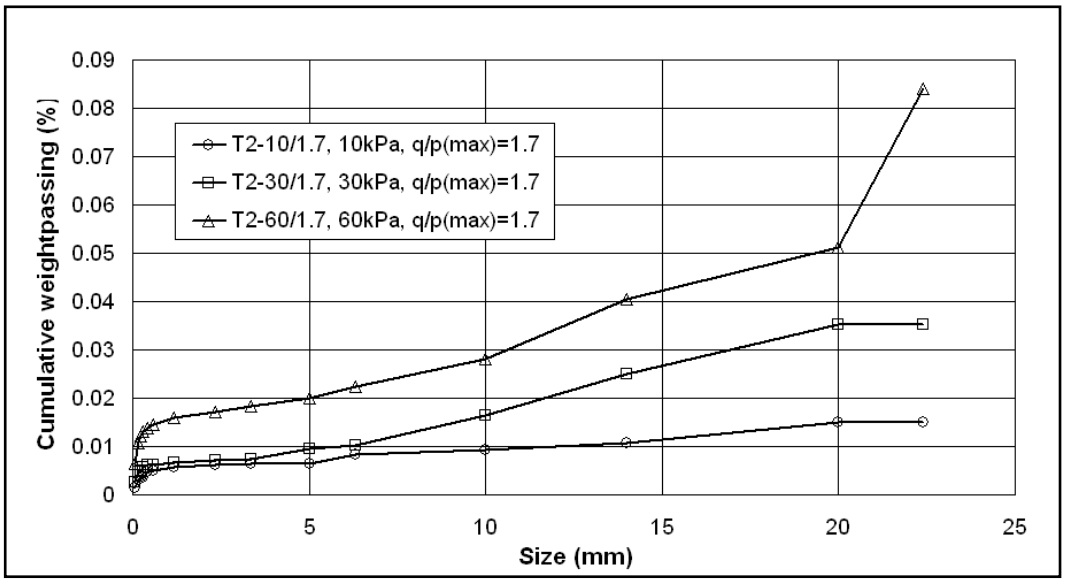

Figure 3.15 (d) Particles smaller than 22.4mm from the cyclic triaxial test with stress ratio 1.7

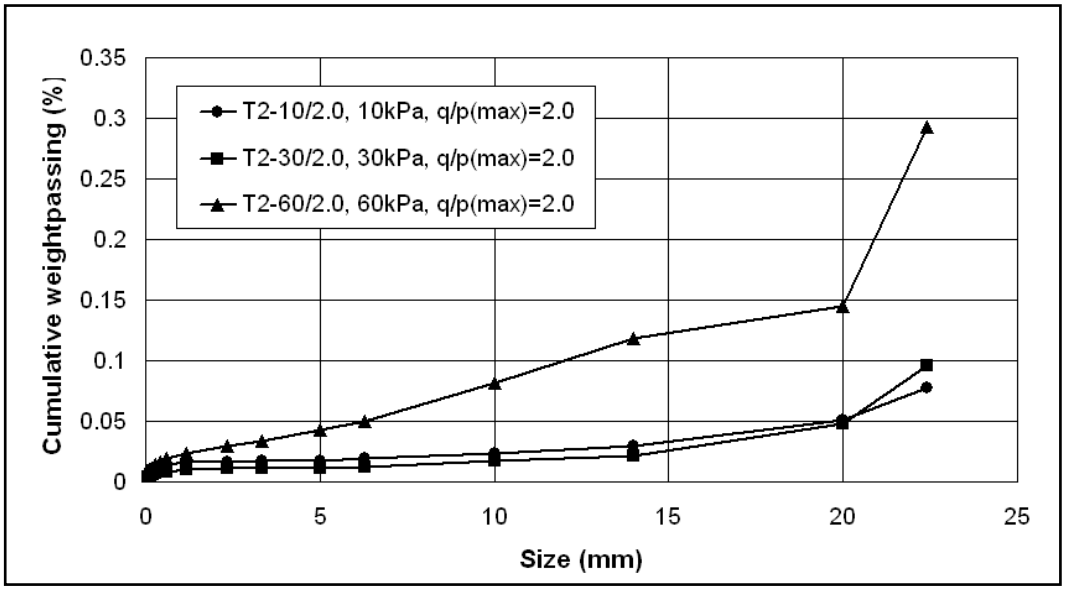

Figure 3.15 (e) Particles smaller than 22.4mm from the cyclic triaxial test with stress ratio 2.0

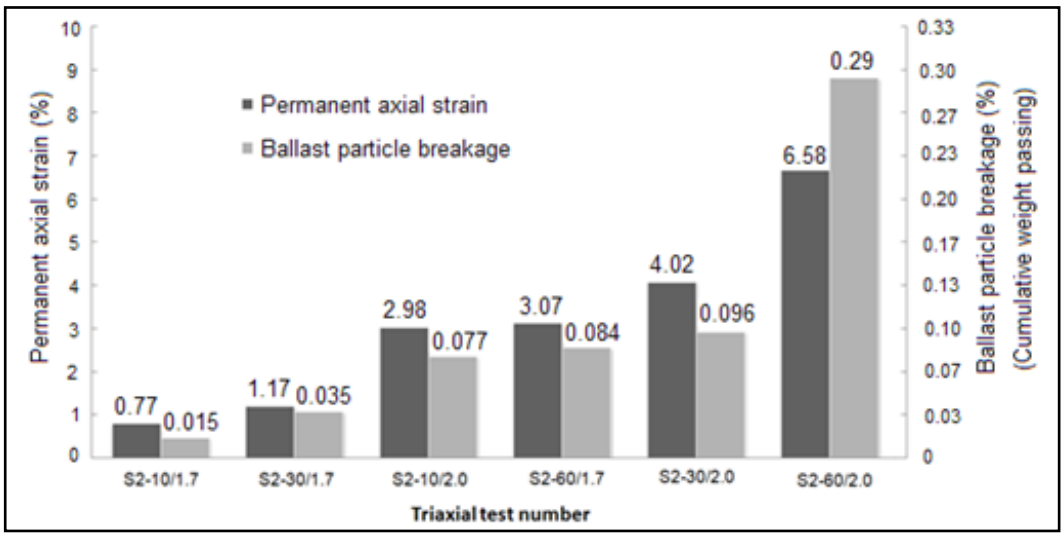

Figure 3.16 Permanent axial strain and modified ballast breakage of cyclic triaxial tests after 100,000 cycles

3.6.3 Multi-stage Triaxial Tests

Three multi-stage triaxial tests were completed in this project. The reason for carrying out multi-stage tests was to obtain the ballast behaviour under higher values of $(q/p)_{max}$, which will be useful when fitting experimental data to a model. Four stages were carried out in each multi-stage triaxial test. The cell pressure was constant in each test, while the $(q/p)_{max}$ increased from 1.7 to 2.0, then 2.1 and 2.2 for different stages. However, some samples failed before reaching stage 4.

The permanent axial strain against number of cycles for multi-stage triaxial tests is plotted in Figures 3.17, 3.18 and 3.19. From these figures, the initial plastic deformation of each stage can be seen except where failure occurred, and was then followed by stabilisation. The amount of plastic strain usually increased with increasing $(q/p)_{max.}$

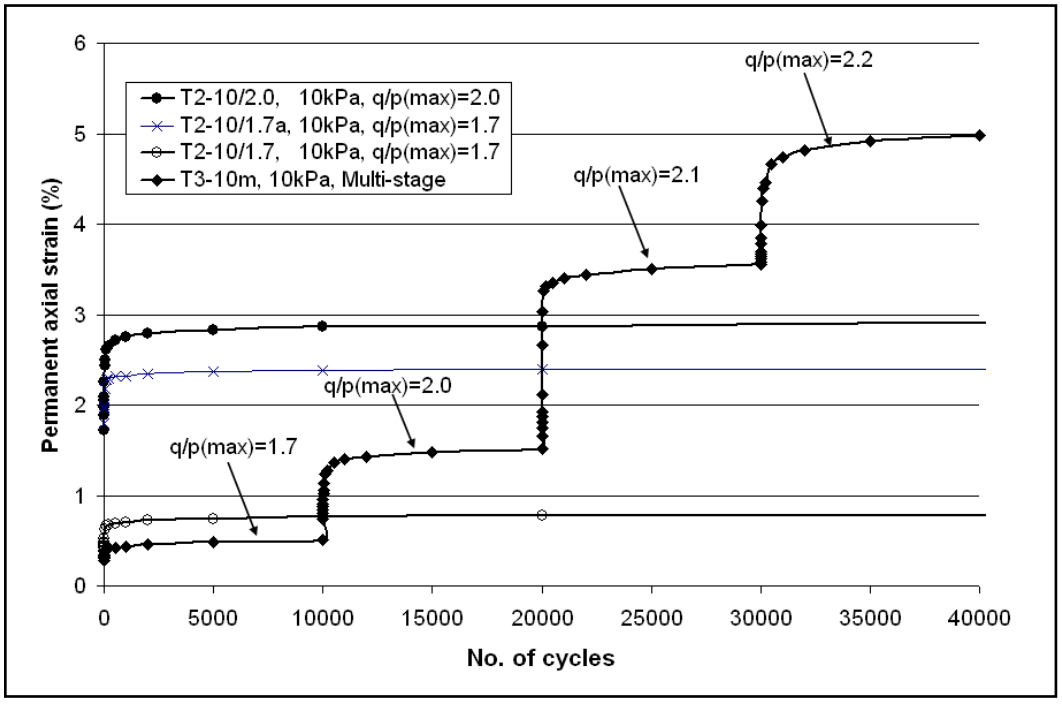

Figure 3.17 Permanent axial strain versus number of cycles from test T3-10m

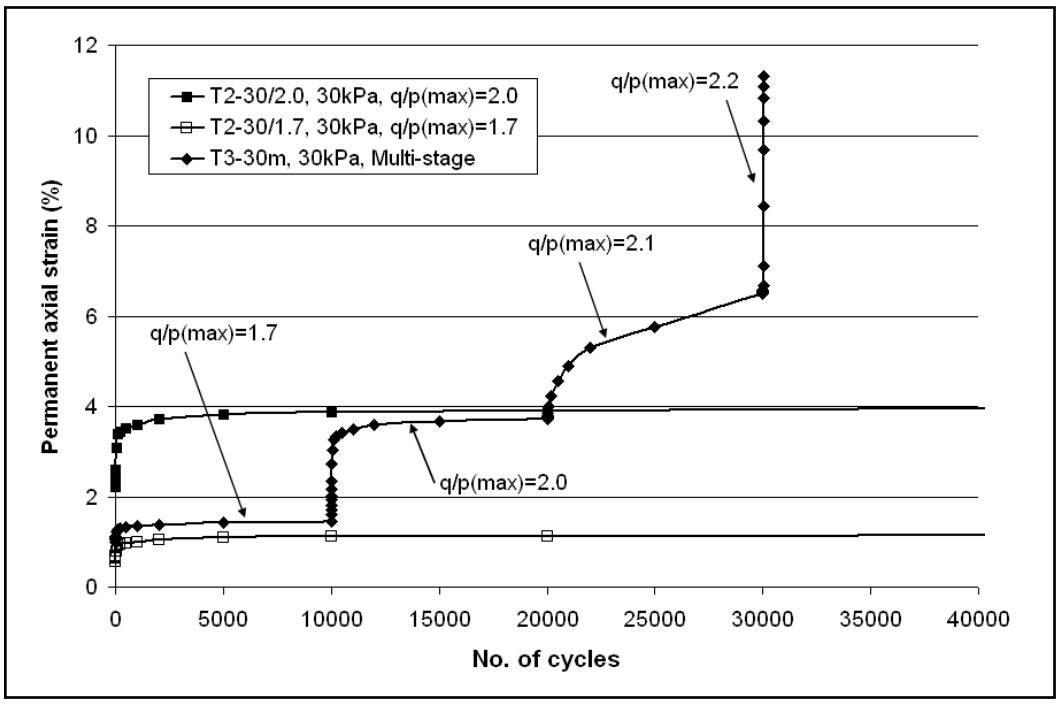

Figure 3.18 Permanent axial strain versus number of cycles from test T3-30m

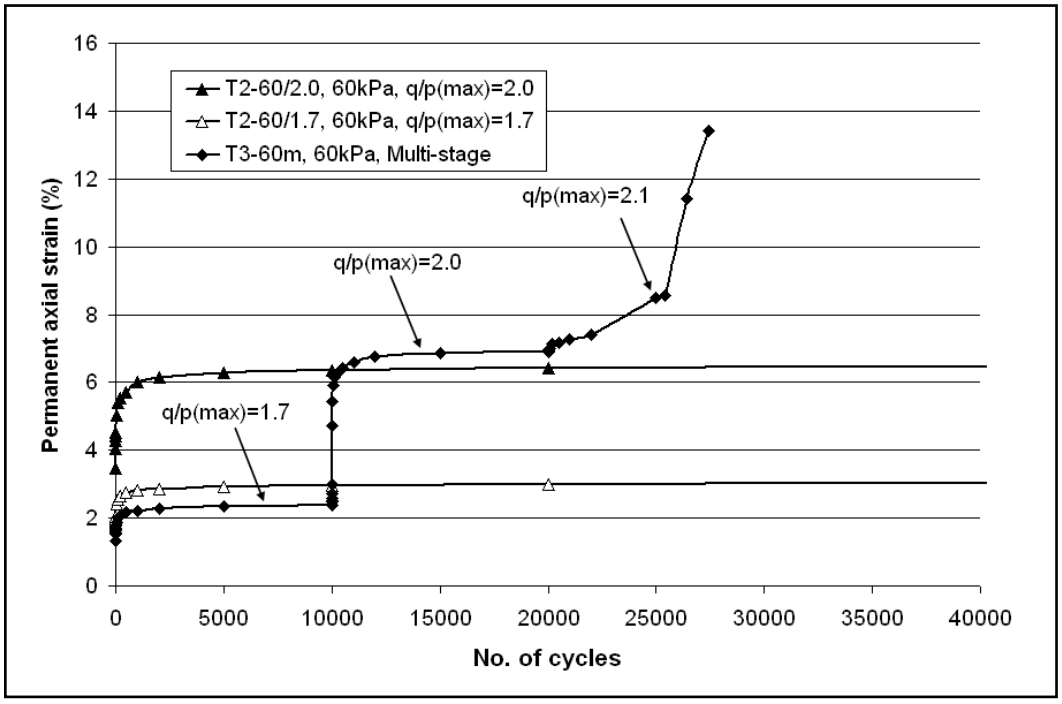

Figure 3.19 Permanent axial strain versus number of cycles from test T3-60m

From previous monotonic triaxial tests, the $(q/p)_{max}$ value in test T1-10 was 2.26, which is higher than the $(q/p)_{max}$ values used in T3-10m (1.7, 2.0, 2.1 and 2.2). Therefore, in Figure 3.17 sample failure did not occur during the four stages, although it can be seen that in the 4th stage ($(q/p)_{max}$ = 2.2) the deformation developed more quickly than in the previous three stages. From the test results, it can be seen that the permanent axial strain in the multi-stage cyclic test with $(q/p)_{max}$ of 2.0 was smaller than that from cyclic test T20-10/2.0. This probably occurred because pre-compaction took place in the previous stage. Also, when compared with the first stage of test T3-10m, the ballast deformation in test S2-10/1.7a is much higher. This is further evidence of the need for the repeat test T2-10/1.7.

Figure 3.18 shows the permanent axial strain against number of cycles from test T3-30m. Only three stages were completed in this test, as the sample failed in stage 4. According to Figure 3.7, the $(q/p)_{max}$ in test S1-30 was 2.06, which is lower than in both stage 3 (2.1) and stage 4 (2.2). This is probably because of the pre-compaction during the first two stages, during which the ballast was rearranged and the sample became stronger. Although the $(q/p)_{max}$ value in stage 3 is 2.1, which is higher than the maximum value of 2.06 in the monotonic tests, the sample did not fail after 10,000 cycles. However, the deformation developed much more quickly than during the previous two stages. The sample eventually failed at the beginning of the stage 4 with $(q/p)_{max}$ of 2.2.

The permanent axial strain behaviour of the multi-stage triaxial test with 60kPa confining pressure is presented in Figure 3.19. In this test, only the first two stages were completed. The third stage was stopped when the permanent strain was over 12%. From Figure 3.7, the $(q/p)_{max}$ in monotonic test with 60kPa cell pressure is 2.04, which is smaller than the value used in third stage 2.1.

Figures 3.20, 3.21 and 3.22 show the permanent volumetric strain against number of cycles for multi-stage triaxial tests. From these figures it can be seen that there is rapid dilation at the beginning of each stage. This is probably because of the sudden increase of deviator stress. According to Figure 3.20, following the rapid start, the permanent volumetric strain stabilized in T3-10m. However, Figures 3.21 and 3.22 show a slow contraction after a dilated start. Furthermore, when

tests T3-30m and T3-60m reached their failure stage, the samples dilated significantly.

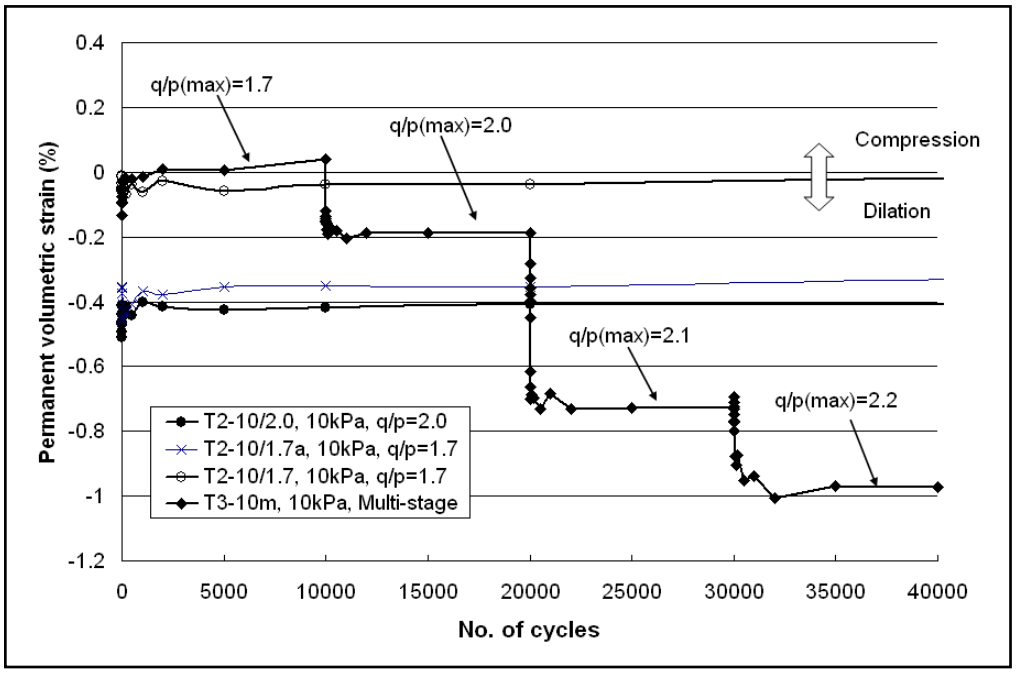

Figure 3.20 Permanent volumetric strain versus number of cycles from test T3-10m

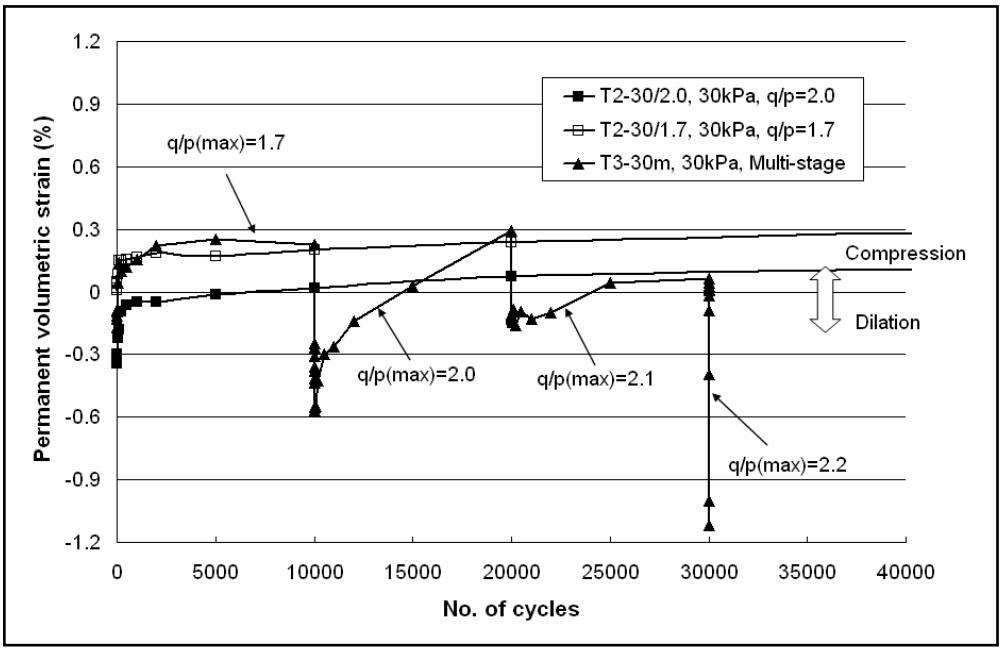

Figure 3.21 Permanent volumetric strain versus number of cycles from test T3-30m

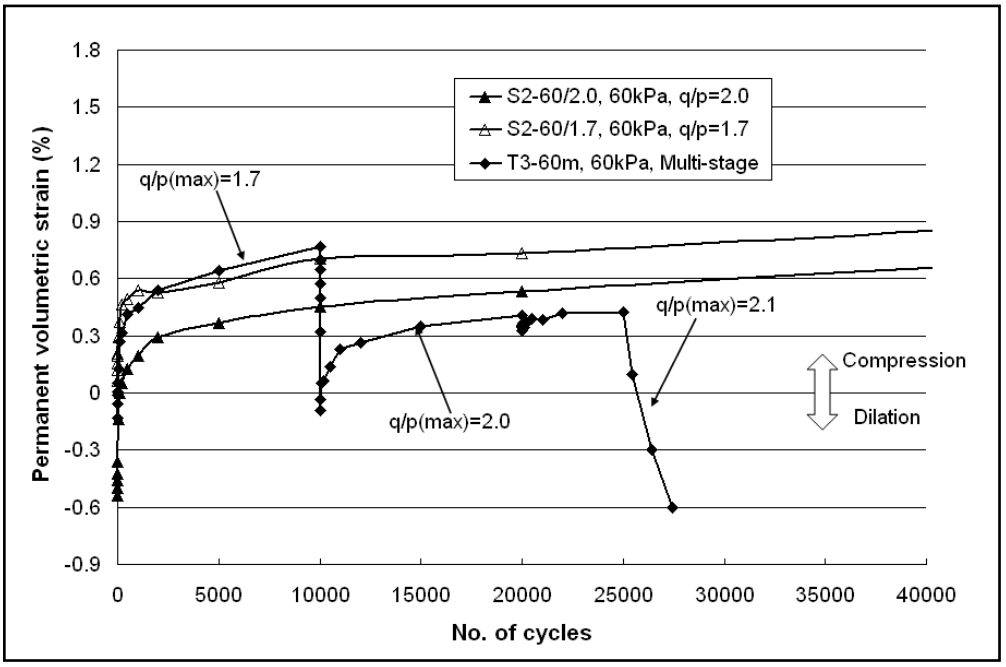

Figure 3.22 Permanent volumetric strain versus number of cycles from test T3-60m

Figure 3.23 shows the particle size distributions of the samples after the triaxial tests in Series 3. It can be seen that although all three tests reached a failure condition, breakage increased with increasing confining pressures.

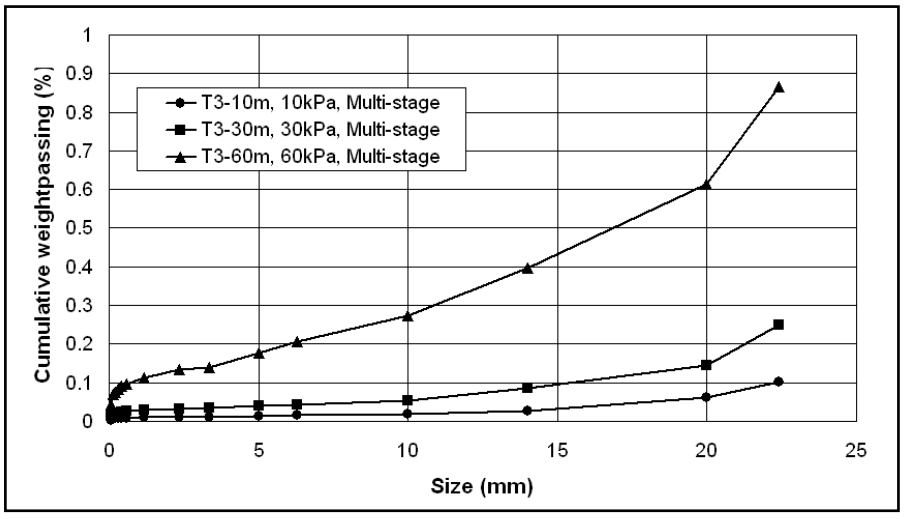

Figure 3.23 Particles smaller than 22.4mm from the multi-stage triaxial tests

3.7 Chapter Summary and Discussion

The aim of triaxial tests was to investigate the stress-strain and degradation response of ballast under monotonic, cyclic and multi-stage loading at various confining pressures. Unlike conventional triaxial tests, this large scale triaxial apparatus measures axial displacement and volume change instead of axial and radial displacement. The volume changes are measured with a differential pressure transducer and checked with the water level reading in the inner cell.

Four monotonic triaxial tests with cell pressures of 5kPa, 10kPa, 30kPa and 60kPa were carried out in the triaxial test series 1. Peak strength was measured in each sample. The tests were conducted to investigate the ballast behaviour and to obtain parameters, such as friction angle (ϕ), initial stiffness (E_0), dilation angle (ψ) and ballast hardening behaviour, all of which were to be used in numerical trackbed simulation, which will be discussed in Chapter 6.

A total of seven cyclic tests and three multi-stage triaxial tests were conducted to investigate the effects of cyclic loading stress ratio, confining pressure and the number of cycles on the permanent strain, resilient modulus and the breakage of ballast. In addition to the normal cyclic triaxial tests (constant stress ratio during each test), multi-stage triaxial tests were conducted, having an increasing stress ratio at each test stage. The multi-stage triaxial tests were an extension of the

cyclic loading tests to cover the full spectrum of stresses expected in the railway trackbed.

The triaxial test results show the railway ballast material to be highly nonlinear with respect to stress condition and number of cycles, which are two major factors that influence the ballast deformation. However, it should be noted that the stress condition in the triaxial test S2-10/1.7a were the same as S2-10/1.7 but with 6% lower initial density, which showed over 100% more permanent deformation after 100,000 cycles. The rate of permanent deformation was decreasing with increasing load cycles in low stress rate condition. However, when the stress ratio was approaching failure stress condition, the rate of permanent deformation was remaining constant or increasing with increasing wheel loads.

The ballast degradation under static loading revealed that particle breakdown increases with confining pressure. Unlike static loading, there is no direct linear relationship between the magnitude of breakage and confining pressure in cyclic triaxial tests. Instead, breakage is most significant with permanent deformation. However, it was believed that during the cyclic triaxial tests, most degradation occurs during the early stages but also accumulates with increasing number of loadings due to fatigue. Furthermore, both the cyclic and multi-stage triaxial test results were analysed to develop a constitutive settlement model for the prediction of permanent deformation in railway track in a given load magnitude, trackbed quality and number of load cycles, which will be discussed in Chapter 7.

CHAPTER 4

4. COMPOSITE ELEMENT TEST (CET)

4.1 Introduction

Both the Composite Element Test (CET) and the Railway Test Facility (RTF) were utilised in this project. Though the RTF is a better representation of real railway track, it is much more time-consuming than the CET because of the full-scale construction involved. The CET provides an approximate simulation of the situation beneath a sleeper in a simplified format. It can be an alternative way to check repeatability and validate model equations. Before the CET and the RTF tests, a new instrument for monitoring single ballast particle movement was developed and a series of small box tests were carried out to check the instrumentation repeatability.

4.2 Instrument for Ballast Particle Monitoring

4.2.1 Introduction

Before the new instrument for ballast particle monitoring, which is shown in Figure 4.1, was used in the RTF and the CET, a series of tests were carried out to check the repeatability of the measurement. The idea is to use a stiff steel wire to transfer the ballast particle movement to the LVDT displacement transducer or potentiometer. All instrumented ballast particles were chosen to have particle sizes from 31.5mm to 50mm. Each particle was chosen to have a relatively flat face as the bottom, and a hole was drilled into the top of the particle using a hammer drill. Super AB epoxy adhesive was used to connect the ballast particle to the steel wire which had a diameter 0.9mm. An outer steel flexible sleeve protected the wire, which was strong enough to resist the ballast contact force but was flexible enough to bend with the steel wire. The internal and external diameters of the protection sleeve were 2mm and 5mm respectively.

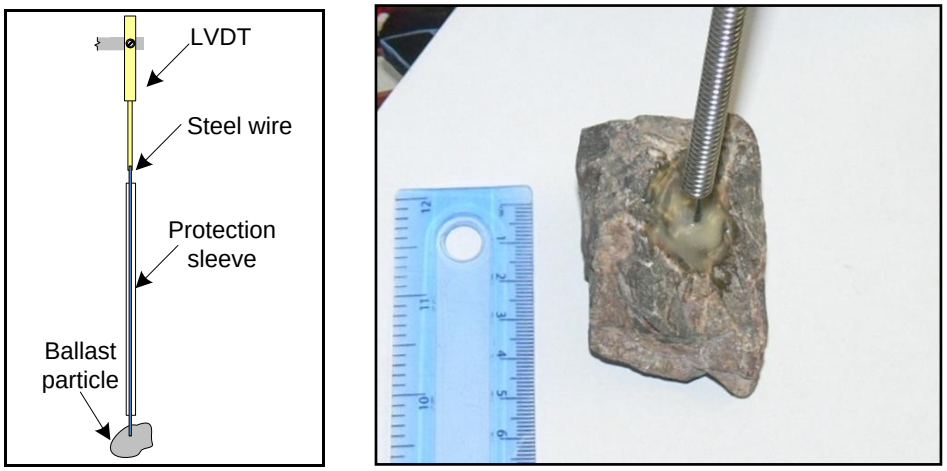

Figure 4.1 Instrument design for single particle movement monitoring

Repeatability tests were carried out in a wooden box with plan dimensions of 400mm by 400mm and a depth of 250mm as shown in Figure 4.2 (a) and (b). A total of twelve tests were carried out with two different ballast depths. Tests1 to 6 and tests 7 to 12 were carried out with the monitored ballast particle at depths of 150mm and 100mm to the bottom of the loading plate respectively. Under the ballast layer, a 20mm thick rubber layer was used to simulate the subgrade.

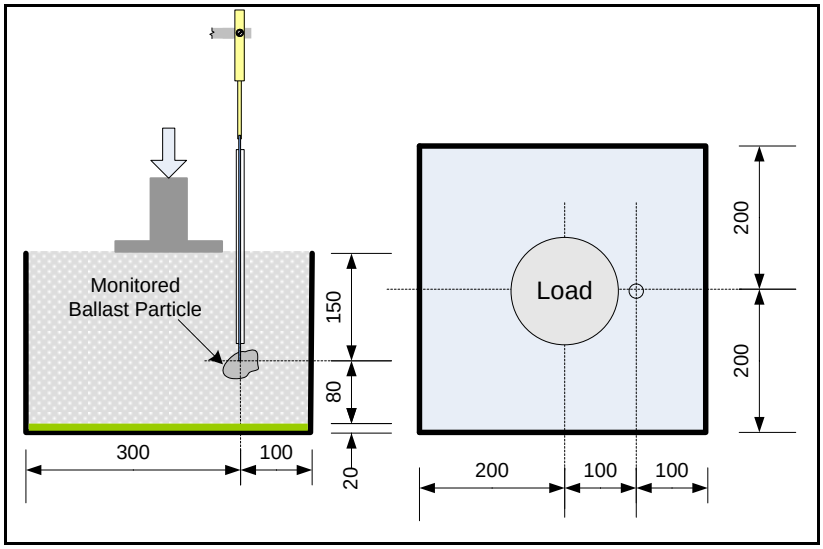

Figure 4.2 (a) Schematic diagram of repeatability tests 1 to 6

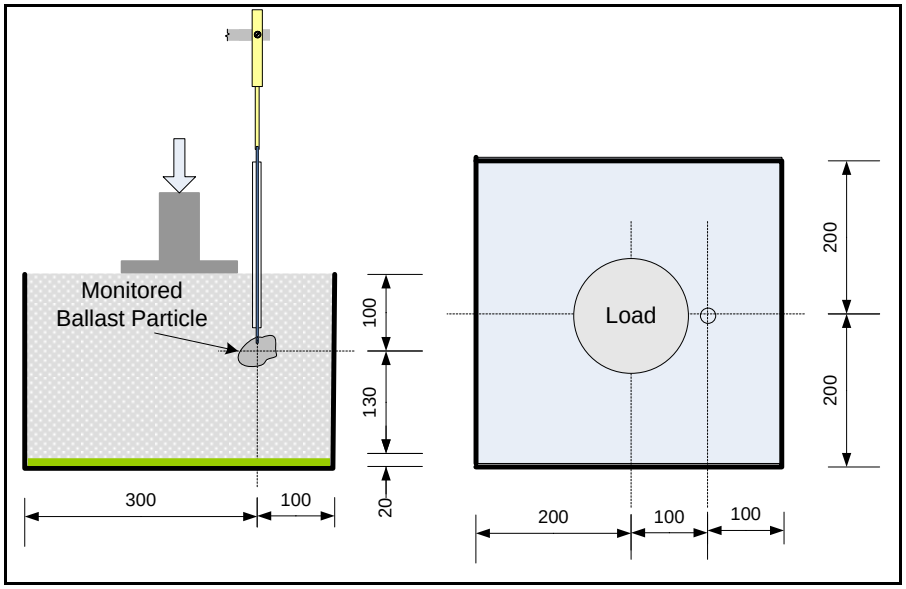

Figure 4.2 (b) Schematic diagram of repeatability test 7 to 12

4.2.2 Repeatability Test Procedures

The loading was applied by a hydraulic jack, which is capable of exerting a 20kN load. The diameter of the loading plate is 16cm. According to Shenton (1975), the maximum vertical stress in the ballast at the sleeper contact varied between 200kPa and 250kPa under 100kN load on the sleeper. However the priority of this repeatability test is not to simulate railway track condition. A relatively large maximum pressure was utilised to ensure a relatively large ballast particle deformation. Hence, a load of 16kN was selected for all repeatability tests. Loading was applied through a cylindrical steel block, as shown in Figure 4.2. A test duration of 10 loading cycles was adopted to allow a relatively quick

turn-round. In order to ensure repeatability and proper validation, the same experimental procedure was maintained for all tests and the same amount of ballast was also used.

In order to make sure that the instrumented ballast particle was in full contact with the surrounding ballast, an electrical vibro-tamper was utilised to compact the ballast surface. During the tests, LVDTs were used to measure the permanent deformation of instrumented particles and the loading plate movement.

4.2.3 Repeatability Test Results

A total of twelve repeatability tests were carried out, and the test results were listed in Table 4.1. The depth of each instrumented ballast particle was measured from the centre of the particle to the bottom of the loading plate. The first six tests (from RT1 to RT6) were carried out with the monitored ballast depth of 150mm, as shown in Figure 4.2 (a). The schematic diagram of the other six tests (from RT7 to RT12) with the instrumented ballast depth of 100mm was shown in Figure 4.2 (b).

Table 4.1 Repeatability test results

Test number	Monitored ballast depth (mm)	Loading plate settlement (mm)	Monitored ballast settlement (mm)	Settlement percentage (%)
RT1	150	5.747	0.55	9.57
RT2	150	4.97	0.28	5.63
RT3	150	5.432	0.47	8.65
RT4	150	5.859	-0.08	-1.36
RT5	150	5.88	0.56	9.52
RT6	150	5.901	0.33	5.59
RT7	100	6.153	0.86	14
RT8	100	6.209	0.58	9.34
RT9	100	5.586	0.61	10.9
RT10	100	5.726	1.08	18.9
RT11	100	5.964	0.72	12.1
RT12	100	5.873	0.78	13.3

The repeatability of this measurement is estimated by the standard deviation. It estimates the root-mean-square deviation of its values from the mean. A smaller standard deviation indicates a higher repeatability. The calculation is described by the following formula:

$$SD = \sqrt{\frac{1}{N}\sum_{i=1}^{N}(x_i - \bar{x})^2} \qquad \text{(Equation 4.1)}$$

where SD is the sample standard deviation, $\bar{x}$ is the arithmetic mean of the values x_i, defined as:

$$\bar{x} = \frac{x_1 + x_2 + \cdots + x_N}{N} = \frac{1}{N}\sum_{i=1}^{N} x_i \qquad \text{(Equation 4.2)}$$

where N is the number of the samples.

The standard deviation of the monitored ballast settlement percentage in Test RT1 to RT6 is 3.8%, and in Test RT7 to RT12 the standard deviation is 3.0%. From Table 4.1, it should be noted that the settlement of the monitored ballast particle in Test RT4 was negative. This means this particle was going up during the loading. From these repeatability tests, it can be seen that one single measurement of ballast particle settlement cannot represent the average ballast movement at that location. Therefore, in order to have correct settlement results, the number of monitored particles in a test should be as many as possible. Furthermore, data which deviates a lot from the average results should not be included in the analysis.

4.3 CET Equipment and Instrumentation

The CET facility was designed as part of the project on 'Geogrid reinforcement of railway ballast' (Kwan, 2006). It allowed a relatively large number of simplified full-scale tests to be carried out within a reasonable time frame. The CET was carried out in a large wooden box with plan dimensions of 1.675m length by

0.75m width. The inner side of the wooden walls were covered with steel sheets to reduce friction. The subgrade underneath the ballast was a 50mm thick layer of graded 10mm maximum sized crushed aggregate sitting on a 14mm thick sheet of shot-blast rubber. A 300mm thick ballast layer was placed above the subgrade for all the CET tests. Before the installation of the sleeper, the ballast layer was compacted by an electrical vibro-tamper applying vibration through a plate to the ballast surface. As in the triaxial tests, ballast from Glensanda Quarry was used to ensure repeatability and validity of the results. Additional overburden ballast was placed on either side of the sleeper, following the procedure developed by Kwan (2006). A schematic diagram of the CET test set-up is shown in Figure 4.3

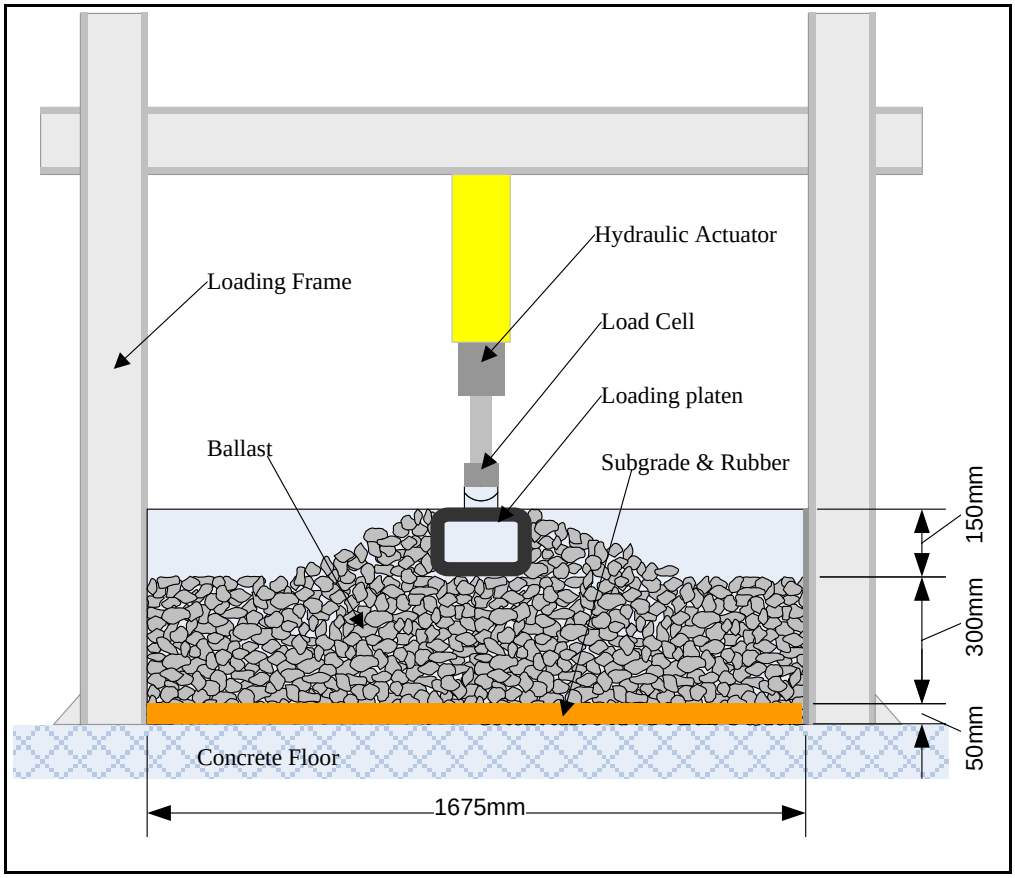

Figure 4.3 Schematic diagram of the CET

To be within the flow capacity of the hydraulic pump for the CET, a load of 20kN at a frequency of 2Hz was selected. Loading was applied by a hydraulic actuator through a rectangular hollow steel beam which was 750mm long by 250mm wide and 150mm high with a 15mm thickness. Between the hydraulic actuator and the loading platen, there was a load cell to measure vertical load. Load and deformation data were recorded with a data logger. Permanent sleeper settlement was measured by two potentiometers placed at each end of the steel beam. This arrangement allowed compensation for the inevitable uneven settlement caused by the random packing of the ballast particles.

4.4 Test Procedures

After the installation of the wooden sides, the subgrade was levelled, and a 310mm deep layer of ballast was placed in the test box. Four holes were then dug to install the instrumented ballast particles at the positions shown in Figure 4.4. Then, the holes were filled with ballast to the original level. The ballast surface was compacted by an electrical vibro-tamper for five seconds at each location. The monitored ballast particles should be installed before ballast compaction, which ensures that the ballast is arranged uniformly under the loading platen. Otherwise if these instrumented ballast particles were installed after compaction, a weaker structured arrangement would be existed and probably less deformation would be measured. After the loading platen was installed, overburden was placed

at the sides. Overburden slopes were compacted with a hand tamper. Then, all instruments, including six potentiometers and two load cells were set up. After checking the work status of the hydraulic actuator and data acquisition system, cyclic loading was started. The sinusoidal loading has a maximum magnitude of 20kN with a frequency of 2Hz. The set-up of the system before testing is shown in Figure 4.5.

According to the previous CET test experience, a standard test duration of 30,000 cycles was adopted. This was sufficient to capture the trend of the ballast settlement behaviour in a relatively short time. All permanent deformation readings were taken at intervals when the cyclic loading was stopped and the load held at 1kN. Measurements were taken after 100, 1000, 2000, 5000, 10000, 20000 and 30000 load cycles.

A total of five CET tests were carried out in this project to check ballast particle settlement at different depths. Because of the time schedule, RTF Test8 was carried out before the CET tests. Based on the experience from the RTF Test 8 (which will be described in Chapter 5), the steel wire connected to the ballast particles was placed vertically to minimise the error, as protection sleeve distortion and ballast movement around the sleeve increase the errors of measurement. Meanwhile, the movement of the surface ballast particles may disturb the measurement as well, which, however, could be minimised by attaching the potentiometers to the end of the steel wires to restrict its horizontal movement. Potentiometers were utilised to measure permanent particle settlement.

Because of space limitation, four ballast particles were monitored in each test. The instrument arrangement is shown in Figure 4.5.

A total of four positions were chosen at which to place the instrumented ballast particles. Figure 4.4 shows a schematic diagram of these four positions in the CET. From these figures, it can be seen that ballast settlement underneath the loading platen was measured at three different levels, 75mm, 150mm, and 225mm from the centre of the ballast particles to the bottom of the sleeper. In addition to these three positions directly underneath the edge of the loading platen, instrumented ballast particles were also placed at a depth of 150mm and 100mm away from the edge to check the ballast settlement behaviour away from the loading platen.

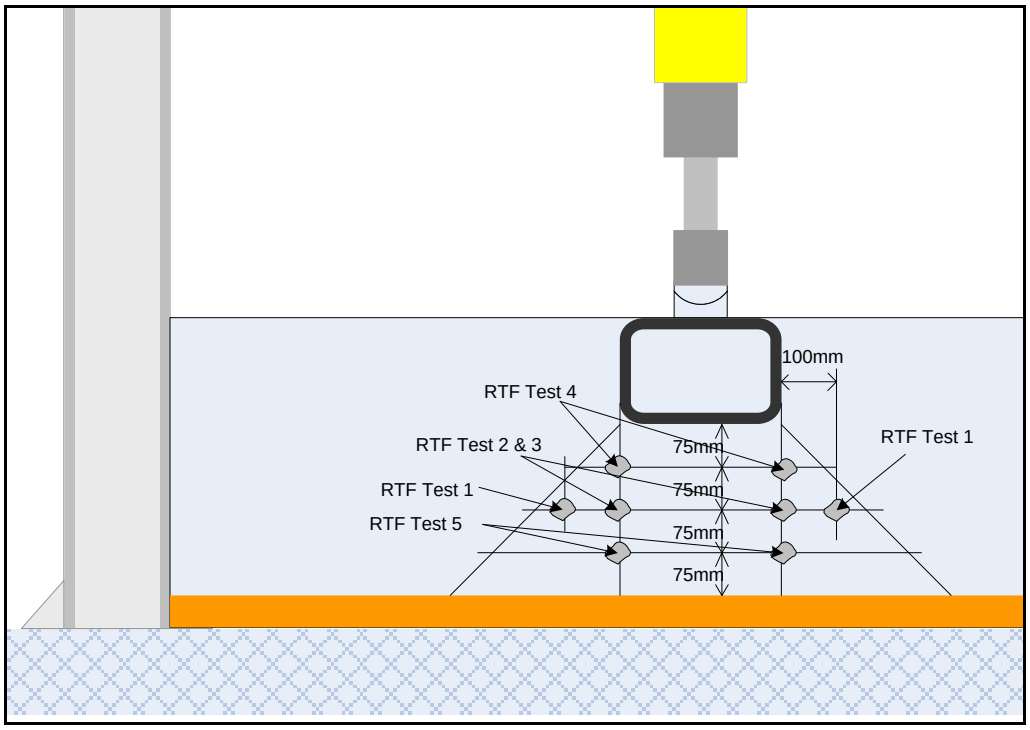

Figure 4.4 Schematic diagram of instrumented ballast particle positions in the CET

Figure 4.5 The CET experimental set-up

4.5 The CET Results

A total of five CET tests were carried out in this project. The permanent loading platen deformation against the number of cycles is shown in Figure 4.6. Settlement was calculated by averaging readings of the two potentiometers placed at both sides of the loading platen. It can be seen that the permanent deformations in CET Tests 2 and 5 were relatively higher than the others. The difference mainly came from the first 100 cycles, which led to the belief that sample preparation played a very important role in permanent deformation at the beginning of the test. Since the total settlement of loading platen in each test was different, in order to

minimise this influence on the comparison of ballast settlement at different depths, the monitored ballast particle settlement was calculated in percentage terms.

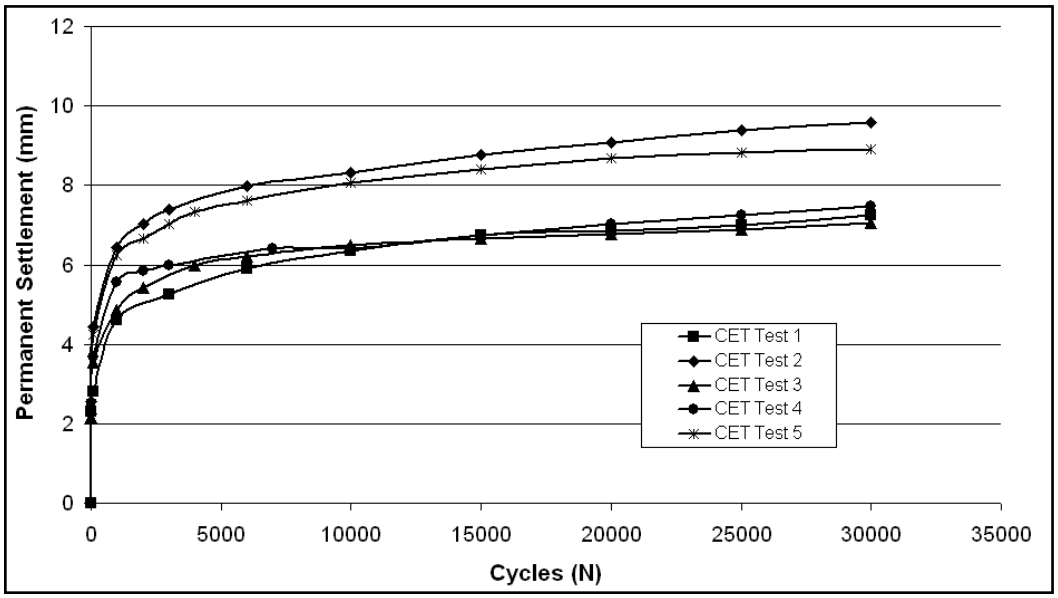

Figure 4.6 Permanent loading platen deformation against the number of cycles

In CET Test 1, the four instrumented ballast particles were placed at a depth of 150mm and 100mm away from the edge of the loading platen, as shown in Figure 4.4. The movement of these ballast particles was transferred by steel wires and measured by four potentiometers. The CET Test 1 results are plotted in Figure 4.7. Little permanent deformation was detected by the monitored ballast particles. It led to a belief that most of the permanent deformation happened directly underneath the loading platen, and that a depth of 150mm and 100mm away from the edge of the loading platen was outside the main deformation zone. Therefore, in the following CET tests all instrumented ballast particles were placed right underneath the edge of the sleeper.

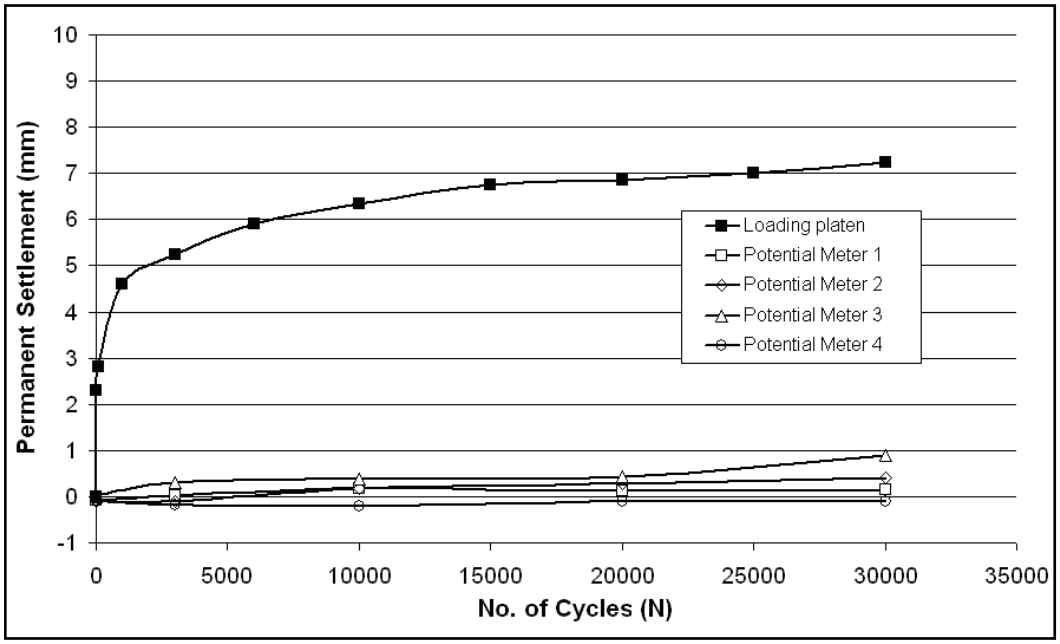

Figure 4.7 Permanent deformation against the number of cycles in CET Test 1

In CET Tests 2 and 3, a total of eight monitored ballast particles were placed at a depth of 150mm and right underneath the edge of the sleeper, as shown in Figure 4.4. The permanent deformation results in CET Tests 2 and 3 are plotted in Figure 4.8 and 4.9 respectively. It should be noted from these figures that most of the monitored particle settlements were between 1mm and 2.5mm. However, Potentiometer 3 in CET Test 2 and potentiometer 1 in CET Test 3 detected particle settlements which were significantly larger than the others. Therefore, these two readings were not included in the calculation of the average permanent deformation.

In CET Test 4, the monitored ballast particles were placed at a depth of 75mm. The measured settlements after 30,000 cycles were between 2mm and 3.5mm as shown in Figure 4.10. In CET Test 5 the monitored ballast particles were placed at

the depth of 225mm. The measured settlements after 30,000 cycles were less than 2mm as shown in Figure 4.11.

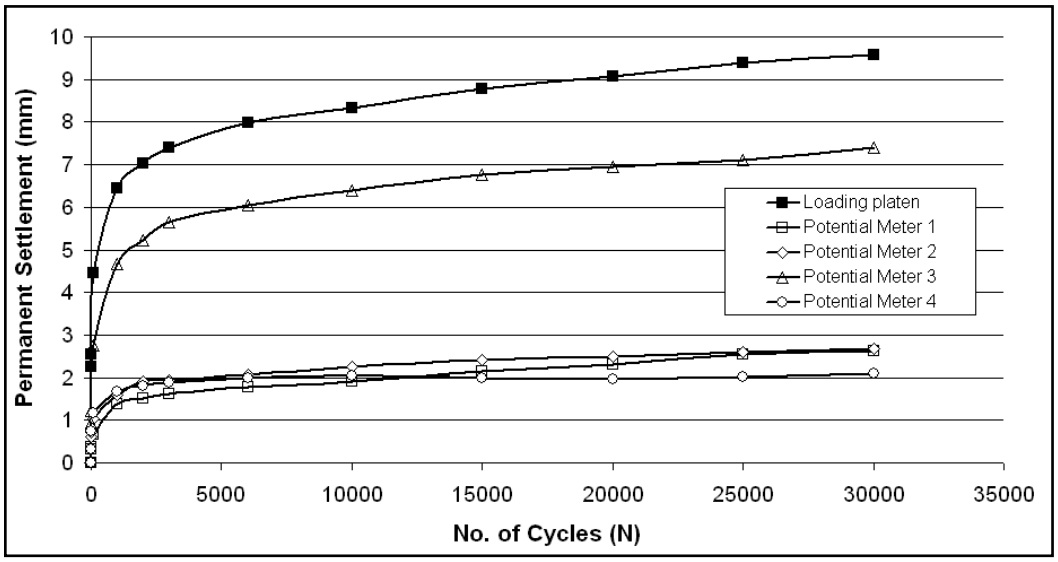

Figure 4.8 Permanent deformation against the number of cycles in CET Test 2

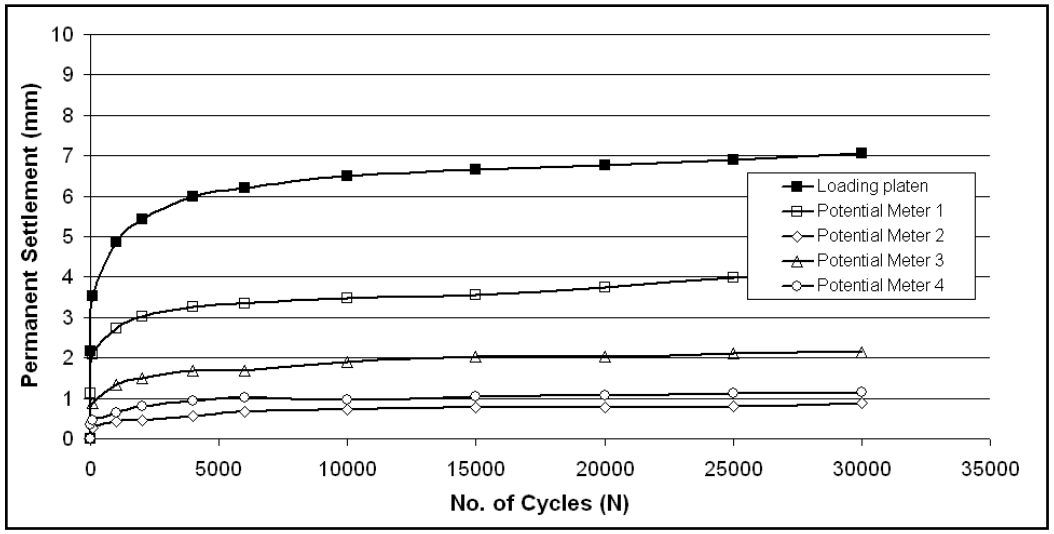

Figure 4.9 Permanent deformation against the number of cycles in CET Test 3

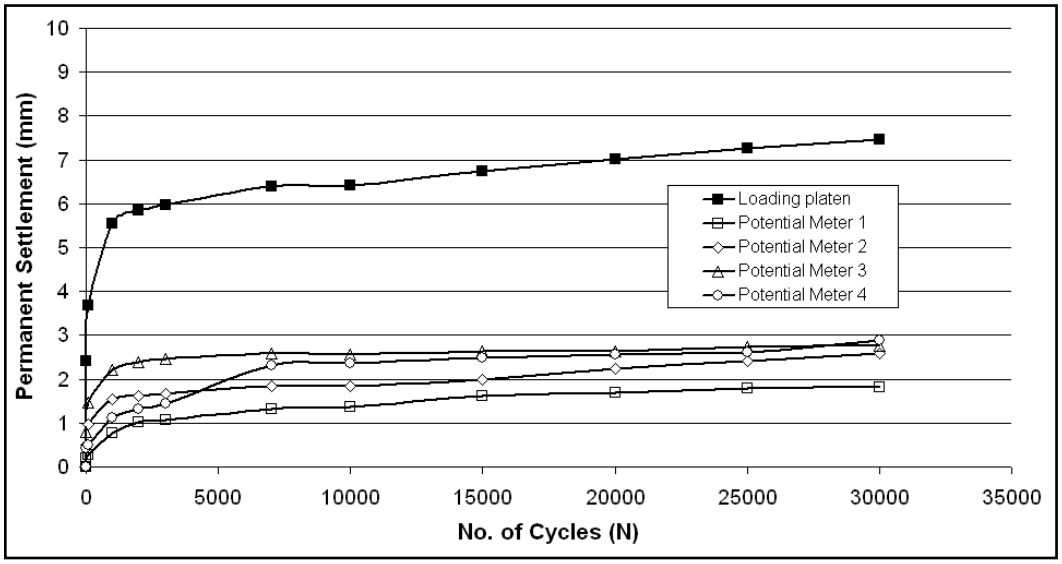

Figure 4.10 Permanent deformation against the number of cycles in CET Test 4

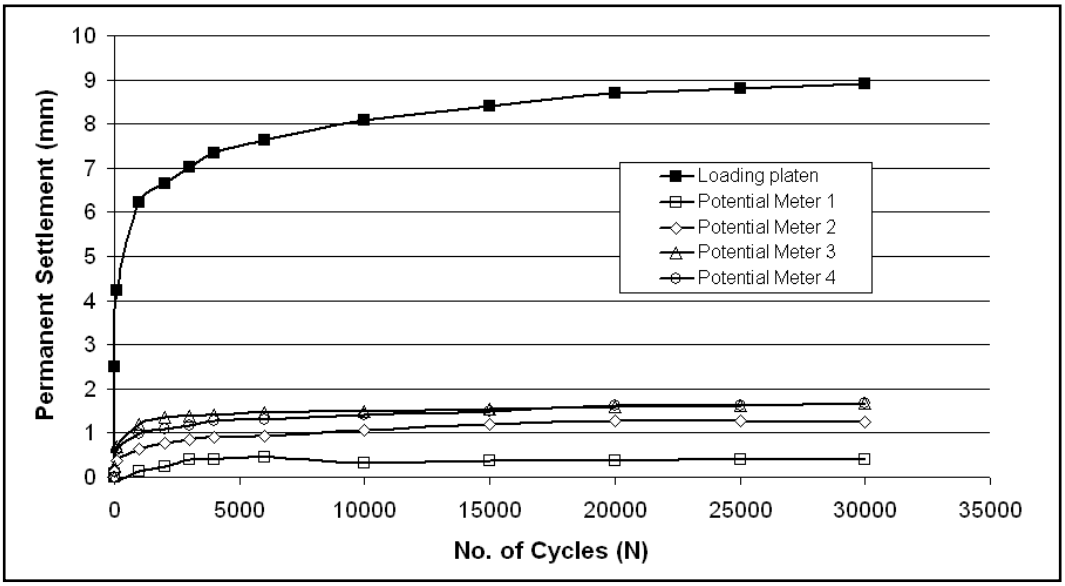

Figure 4.11 Permanent deformation against the number of cycles in CET Test 5

Table 4.2 presents the details of instrumented ballast particle deformation in the CET tests achieved in this project. It can be seen from the table that most of the test settlement happened in the top layer of ballast (0-75mm underneath the sleeper). The average permanent ballast deformation as a percentage of loading

platen settlement against number of cycles is shown in Figure 4.12. From this figure, it can be seen that the ballast permanent deformation percentage at depths of 150mm and 225mm became stable after 2000 cycles. However, at a depth of 75mm, the settlement percentage was increasing until 7000 cycles.

Table 4.2 Details of instrumented ballast particle deformation in the CET tests

<table>
<tr><td>Test number</td><td colspan="4">Monitored ballast particle position and permanent deformation after 30,000 cycles</td><td>Sleeper settlement (mm)</td></tr>
<tr><td rowspan="3">CET Test 1</td><td colspan="4">150mm depth (to the bottom of the sleeper) and 100mm away from the edge of sleeper</td><td rowspan="2">7.25</td></tr>
<tr><td>0.14</td><td>0.41</td><td>0.88</td><td>-0.11</td></tr>
<tr><td colspan="5">4.6% of total settlement on average</td></tr>
<tr><td rowspan="3">CET Test 2</td><td colspan="4">150mm depth and right underneath of the edge of sleeper</td><td rowspan="2">9.58</td></tr>
<tr><td>2.61</td><td>2.69</td><td>7.40</td><td>2.10</td></tr>
<tr><td colspan="5">25.7% of total settlement on average (exclude 7.40)</td></tr>
<tr><td rowspan="3">CET Test 3</td><td colspan="4">150mm depth and right underneath of the edge of sleeper</td><td rowspan="2">7.06</td></tr>
<tr><td>4.11</td><td>0.88</td><td>2.15</td><td>1.14</td></tr>
<tr><td colspan="5">19.7% of total settlement on average (exclude 4.11)</td></tr>
<tr><td rowspan="3">CET Test 4</td><td colspan="4">75mm depth and right underneath of the edge of sleeper</td><td rowspan="2">7.46</td></tr>
<tr><td>1.82</td><td>2.58</td><td>2.76</td><td>2.89</td></tr>
<tr><td colspan="5">33.7% of total settlement on average</td></tr>
<tr><td rowspan="3">CET Test 5</td><td colspan="4">225mm depth and right underneath of the edge of sleeper</td><td rowspan="2">8.91</td></tr>
<tr><td>0.39</td><td>1.24</td><td>1.67</td><td>1.67</td></tr>
<tr><td colspan="5">13.9% of total settlement on average</td></tr>
</table>

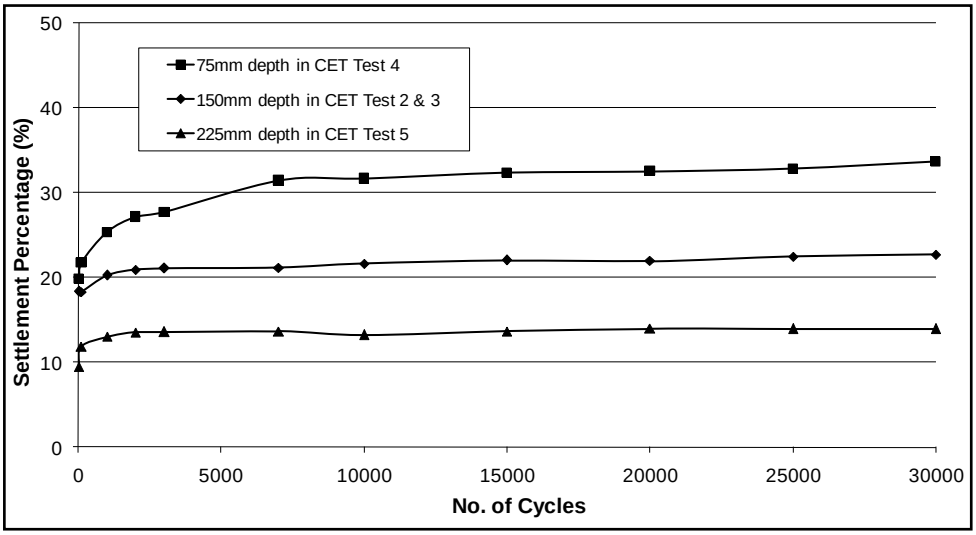

Figure 4.12 The instrumented ballast particle permanent deformation as a percentage of loading platen settlement against number of cycles

4.6 Chapter Summary and Discussion

The repeatability of instrumented ballast particle measurement was demonstrated in the small box tests. To ensure good repeatability, the same preparation, testing and measurement procedures were adopted. From the test results, it was found that due to the random nature of single ballast particle movement, one measurement result cannot represent the settlement of the whole ballast layer. Hence, it is recommended that the number of monitored ballast particles in the test should be as many as possible.

A total of five CET tests were carried out in this project. The ballast deformation in each layer was measured by placing the instrumented ballast particles

underneath the edge of the loading platen at a certain depth. From the test results, it can be seen that there was a significant permanent deformation in the top layer of the ballast to a depth of 75mm. And the permanent deformations in the layers of 75mm-150mm, 150mm-225mm and 225mm-300mm were all similar. Each layer contributed about 10-15% of the total permanent deformation.

Moreover, little permanent deformation was detected when the instrumented ballast particle was placed at a depth of 150mm and 100mm away from the edge of the loading platen. It is believed that this position was probably located outside the main ballast deformation zone.

The instrumentation for ballast particle monitoring in the CET was proved to be adequate in detecting the ballast particle movement, only if the number of monitored particles was sufficient. The analysed CET test results will be used to validate and refine the model equation, which will be presented in Chapter 7.

CHAPTER 5

5. RAILWAY TEST FACILITY (RTF)

5.1 Introduction

The Railway Test Facility (RTF) represents an intermediate approach between conventional laboratory ballast testing and railway track field trials. The RTF tests were carried out to examine and validate the railway settlement model, which will be discussed in Chapter 7. The RTF test is a time-consuming full-scale experiment construction, hence, only two RTF tests were carried out in this project.

As a series of RTF tests have been carried out by Kwan (2006) and Aursudkij (2007), test results in this project could be compared with previous results, such as sleeper settlement during cyclic loading and stress at the top of the subgrade layer. In this project, a more detailed settlement measurement scheme was carried out to further characterise the behaviour of ballasted trackbed under controlled load conditions. The RTF tests carried out in previous projects and this one are listed in

Table 5.1. From this table it can be seen that the same ballast was adopted and no geogrid was involved in both the RTF Tests 1 and 8. Therefore, the results from these two tests could be compared.

Table 5.1 The RTF tests in previous projects and this project

RTF tests in previous projects (Kwan 2006, Aursudkij 2007)		
Test number	Ballast	Description
RTF Test 1	Glensanda	No Geogrid
RTF Test 2	Glensanda	With Geogrid at 50mm above bottom of ballast
RTF Test 3	Glensanda	With Geogrid at bottom of ballast Intermediate tamping after 500,000 cycles
RTF Test 4	Glensanda	No Geogrid Intermediate tamping after 500,000 cycles
RTF Test 5	Croft	No Geogrid
RTF Test 6	Limestone	No Geogrid
RTF Test 7	Limestone	No Geogrid, Concrete slab base, Test stopped due to excessive settlement at 320,000 cycles
RTF tests in this project		
RTF Test 8	Glensanda	No Geogrid
RTF Test 9	Glensanda	With TriAx Geogrid at 50mm above bottom of ballast

5.2 Test Facilities

The RTF test facility is located in a 1.8m deep concrete pit which is 4.1m long and 2.1m wide. Dynamic loads are applied to three full-scale sleepers with the reaction provided by a self-contained frame fitted in the pit. The RTF superstructure can be varied and a full-size tamping machine can be used to pack the ballast. There is a layer of consistent relatively soft silt subgrade under the ballast. Vertical settlement readings were provided by the integral stroke transducers attached to the actuators as well as Linear Variable Differential Transformer (LVDT) attachments on both ends of the middle sleeper. Stress transmitted from the ballast was recorded via three pressure cells installed at 50mm subgrade depth. A schematic diagram and an image of the RTF frame are shown in Figure 5.1. From these diagrams it can be seen that the load actuators provide the dynamic loading to three sleepers to simulate the realistic situation. Meanwhile, the loading on sleepers was spread from the sleeper to the ballast and subgrade. The detailed construction process is described by Kwan (2006) and Aursudkij (2007).

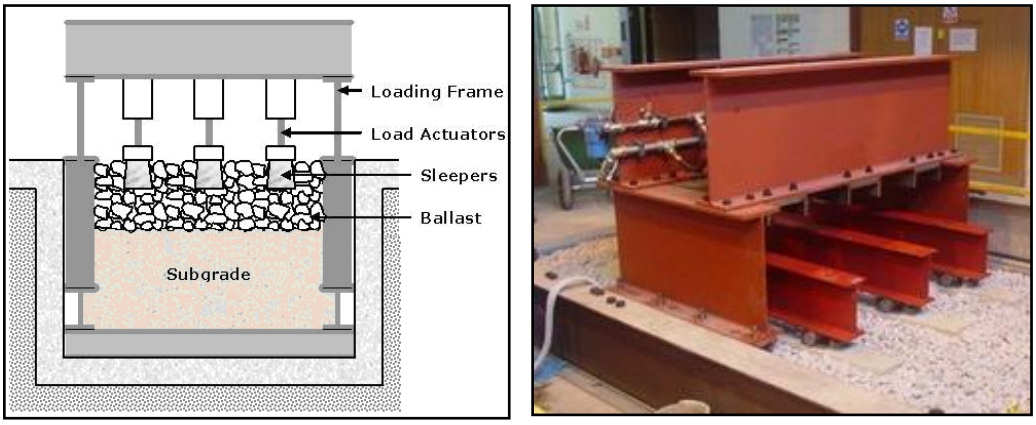

Figure 5.1 The RTF test frame in pit

The loading frame was designed to provide three maximum 100kN vertical loads which mimic the cyclic loading of a passing train. The actuators provide dynamic loads through load cells onto the centres of the spreader beams which are located on the sleepers at the position where the rails would be attached. A stand-alone controller is connected to a computer which stores control functions and the acquired data.

The simulated cyclic loading of a passing train is achieved by applying sinusoidal loading between 4kN and 94kN with a 90° phase lag between each actuator, as shown in Figure 5.2. The loading frequency used for each actuator was 3Hz, which simulates a train with a speed of 28km/hr. This speed is relatively low. However, this frequency was constrained by the pressure and flow capacity of the hydraulic pump.

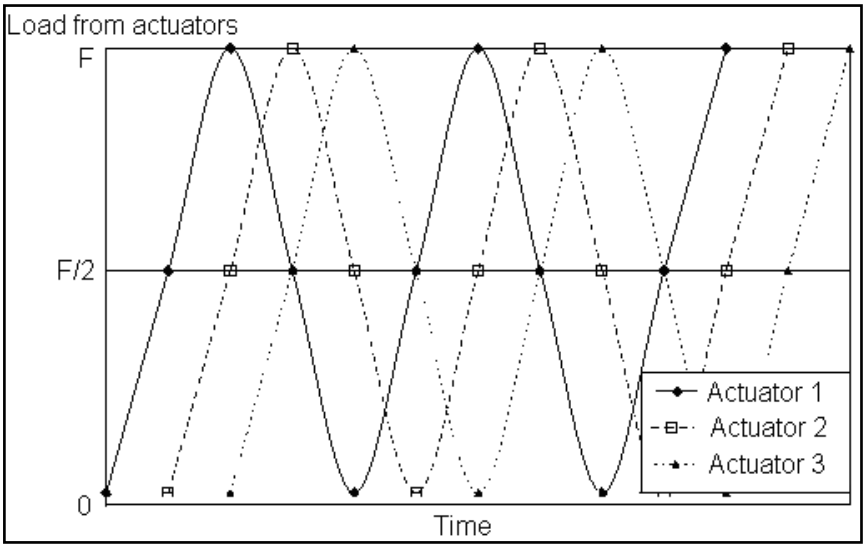

Figure 5.2 Loading pattern used in this project

5.3 Instrumentation

The instrument arrangement for the RTF tests in this project was similar to those in previous tests (Kwan 2006, Aursudkij 2007), except that movement of individual ballast particles was monitored in this project. The instrumentation included three actuator load cells to measure the load applied to the sleepers, integral stroke transducers to measure the average sleeper deflection, and pressure cells to measure stresses near the top of the subgrade. The middle sleeper settlement was measured by both the integral stroke transducer and a LVDT at each end. This arrangement allowed compensation for the inevitable uneven settlement caused by the random packing nature of the ballast particles.

The load cells and stroke transducers were fitted to the shafts of the actuators and connected to the control system, of which a detailed description could be found in Kwan (2006). Three load cells were installed 50mm below the subgrade surface to ensure that no ballast was in contact with load cells. In order to measure the vertical stress under the middle sleeper, the load cells were buried under the loading position, under the centre of the sleeper and mid way between sleepers, as shown in Figure 5.3.

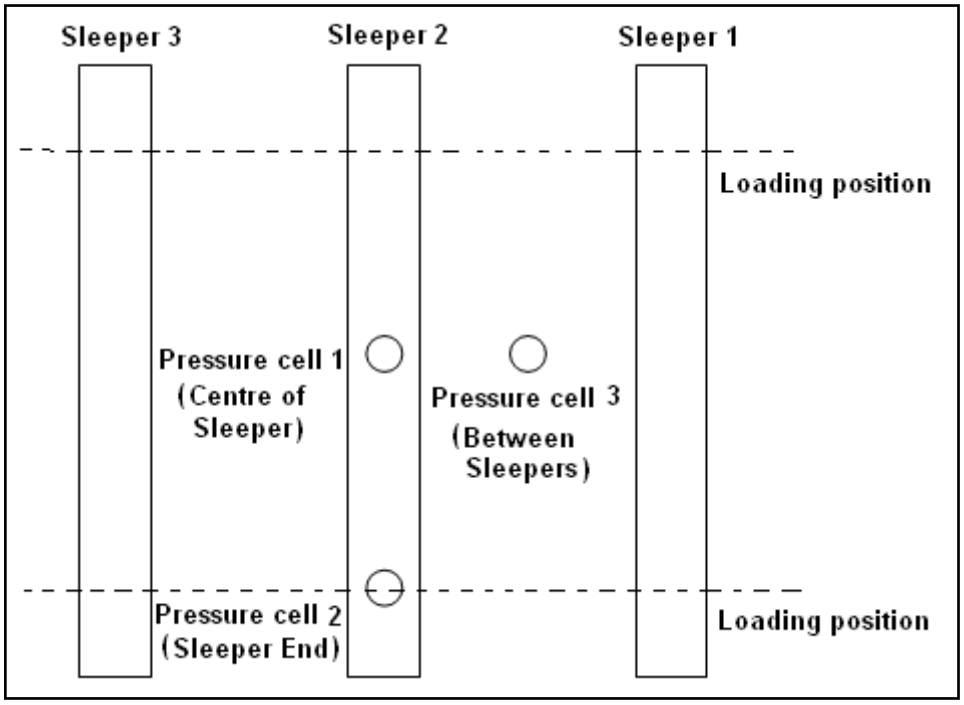

Figure 5.3 Positions of the pressure cells

The instrumentation design for single particle movement monitoring is the same as for the CET tests, shown in Figure 4.1. The monitored ballast particle position arrangements in RTF Tests 8 and 9 are shown in Figure 5.4 and Figure 5.5 respectively. There were a total of twelve monitored ballast particles involved in

RTF Test 8. Figure 5.4 shows six particles under the rail loading position at one end of the sleepers. A similar arrangement was used at the other end. The permanent deformation of the monitored ballast particles was measured by digital photogrammetry analysis. A digital camera with image resolution of 7.1 mega pixels was used to take images of both ballast particle reference points and control points during the tests, as shown in Figure 5.6. The ballast particle reference points were placed at ends of the steel wires which were connected to the monitored ballast particles. The control points were attached to two reference beams which were right over the ballast particle reference points. In order to have accurate readings from photogrammetry analysis, the control points and ballast reference points have to be in the same plane. An image taken by the camera at 900,000 cycles is shown in Figure 5.6. This method is usually used in geotechnical experiments to track the movement of a soil over a series of images, and also used in many other civil engineering projects. Images were taken at the beginning of the test and after 100, 1000, 2000, 5000, 10000, 20000, 50000, 100000, 150000, 200000, 250000, 300000, 400000, 500000, 600000, 700000, 800000, 900000 and 1000000 load cycles. All images were taken with a seating load of 1kN applied on the three sleepers. Then, all images were analysed by MATLAB program to calculate the distance between reference points and control points in pixels. Therefore, the reference point movement could be obtained by the calculation of the size of each pixel from the control points in each reference beam. Besides the permanent deformation, the resilient movement of these ballast reference points was measured by a LVDT.

Because of time schedule, RTF Test 8 was carried out before the CET tests. The instrumented ballast particle arrangement had not fully developed. In order to measure the ballast deformation directly underneath the middle sleeper, four instrumented ballast particles were placed at positions C and D in RTF Test 8, as shown in Figure 5.4. However, the steel wires and protection sleeves for these two positions had to be bent to vertical at the end, because there was a lack of space for the LVDT installation between the loading beams. The protection sleeve distortion and ballast movement around the sleeve increased the error of measurement. Therefore, in order to minimise the error, bent protection sleeves were not used in subsequent tests.

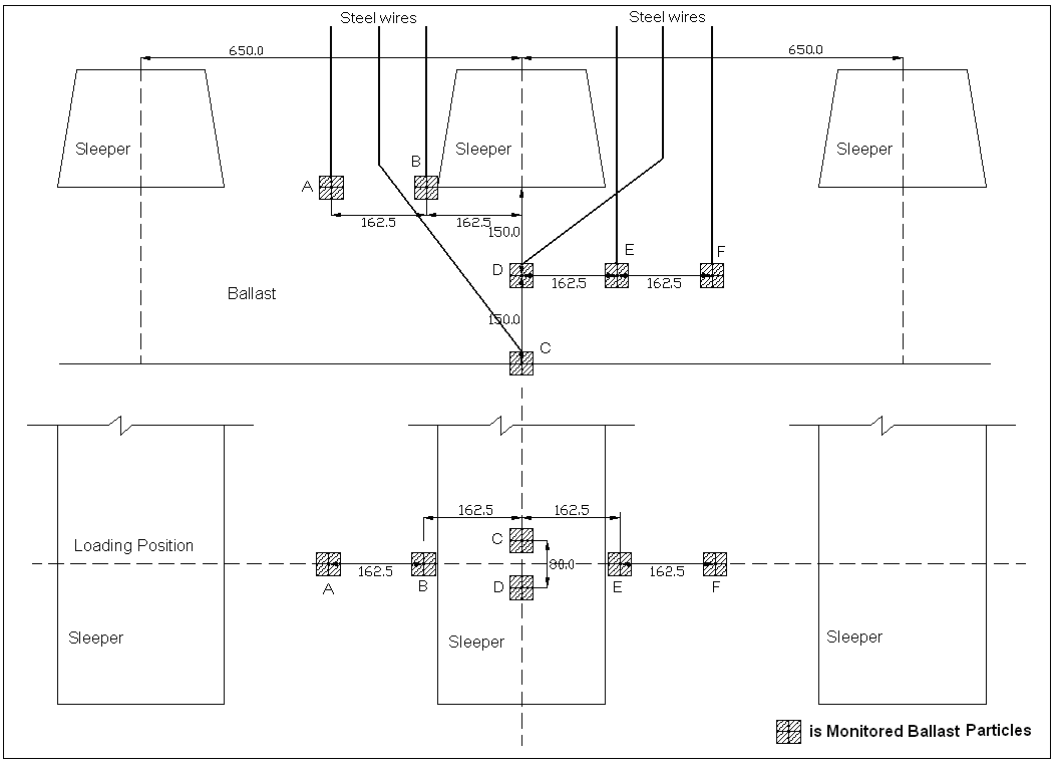

Figure 5.4 Monitored ballast particles in RTF Test 8

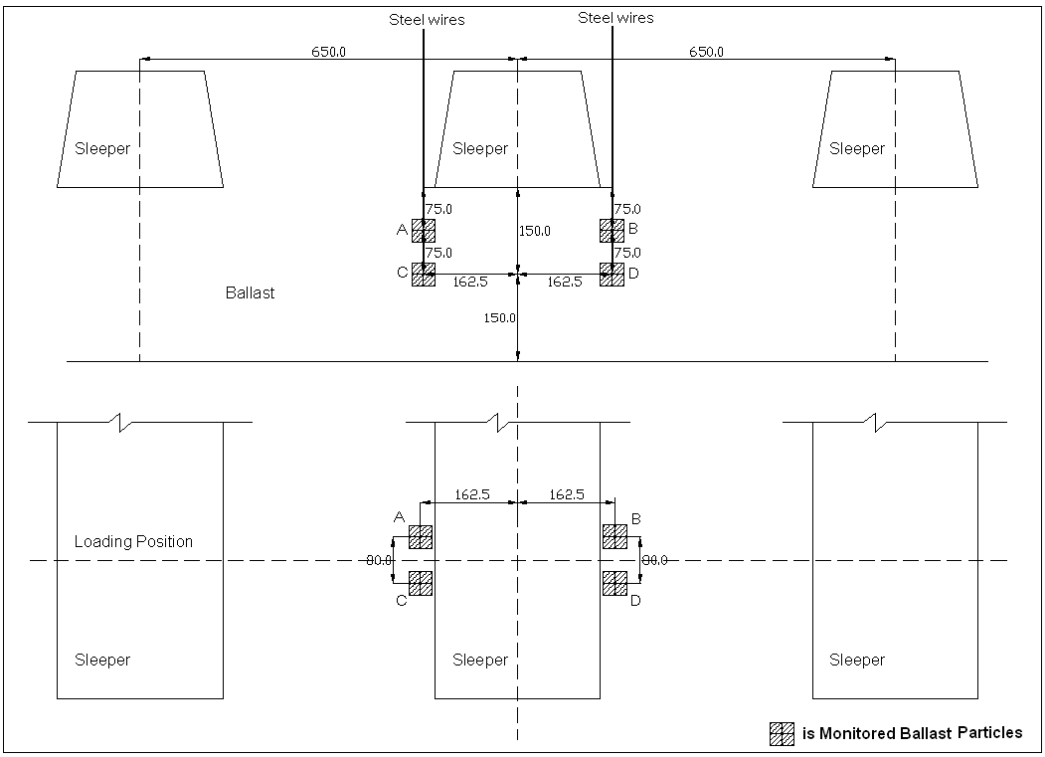

Figure 5.5 Monitored ballast particles in RTF Test 9

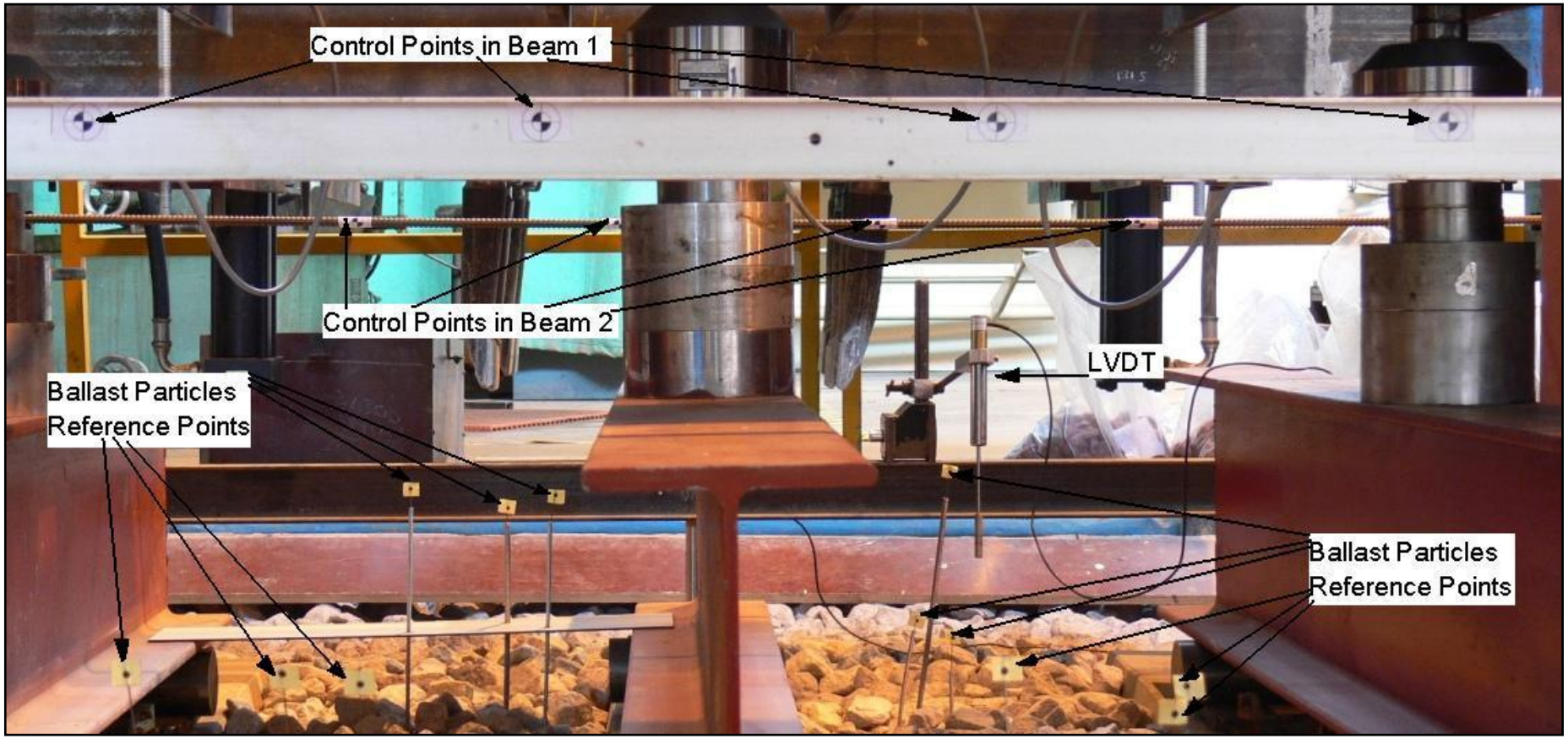

Figure 5.6 Image for photogrammetry analysis at 900,000 cycle in RTF Test

Although photogrammetry analysis is widely used and has proved to be an effective method, there were some disadvantages in using photogrammetry analysis in this particular RTF test. It was found that apart from vertical movement the ballast reference points moved horizontally as well during the test. Furthermore, the horizontal movement was larger than expected. This was probably because the movement of surface ballast particles led to the movement of ballast particle reference points by the impaction between protection sleeves and ballast particles. Therefore, it was recommended that restricting horizontal movement of the steel wires may improve the accuracy of the readings. Hence, potentiometers were used in subsequent tests to take permanent vertical readings and in the meantime to restrict horizontal movement of ballast particle reference points.

With the experience of using instrumented ballast in the CET tests and RTF Test 8, instrumented ballast particles in RTF Test 9 were placed underneath the sleeper edges as Figure 5.5 shows. Although, due to the random nature of ballast particle settlement, as many monitored particles as possible were recommended to be used, only four ballast particles were monitored in RTF Test 9. Because this test was also used for the testing of TriAx Geogrid efficiency, after consideration of Geogrid influence zone, it was decided that all monitored ballast particles should be located at a depth of 0 to 150mm from the centre of the particle to the bottom of the sleeper. Moreover, according to the experience of the previous RTF tests, either the front or rear part of the RTF test frame had to be left empty to allow entry and adjustment of loading frames during the test. Therefore, the ballast

particles were only placed at one end of the sleepers. Furthermore, from the results of small box tests, the CET tests and RTF Test 8, the potentiometers were considered more accurate and reliable than photogrammetry analysis. Because of limited spaces for potentiometer installation, only four potentiometers were attached to the reference beam to monitor ballast particle movement, as shown in Figure 5.7. The data record intervals were the same as in RTF Test 8.

Figure 5.7 Potentiometers arrangement in RTF Test 9

5.4 Test Procedures

The subgrade material for the RTF test was silt. After compaction, it had a density of 1770kg/m^3 and a moisture content of 15.5%. Moisture content of the subgrade material could be adjusted by saturating the subgrade with required amount of water. Before placing ballast, the subgrade stiffness was measured using a light falling weight deflectometer (PRIMA 100) at fifteen chosen positions. The device consists of a 10kg drop weight that falls freely onto a rubber buffer seated on a 300mm diameter circular loading plate. The centre deflection of the loading plate was measured and used to estimate the surface modulus of the foundation (Carl Bro, 2008).

The average of three surface deflection responses of the subgrade to the impact load was used to calculate the stiffness of the subgrade. The stiffness results in the RTF Tests 8 and 9 are shown in Figure 5.8. A comparison with the previous RTF subgrade stiffness values is shown in Figure 5.9. From this figure, it can be seen that the subgrade stiffness is generally increasing after each test, which may have an effect on the permanent deformation.

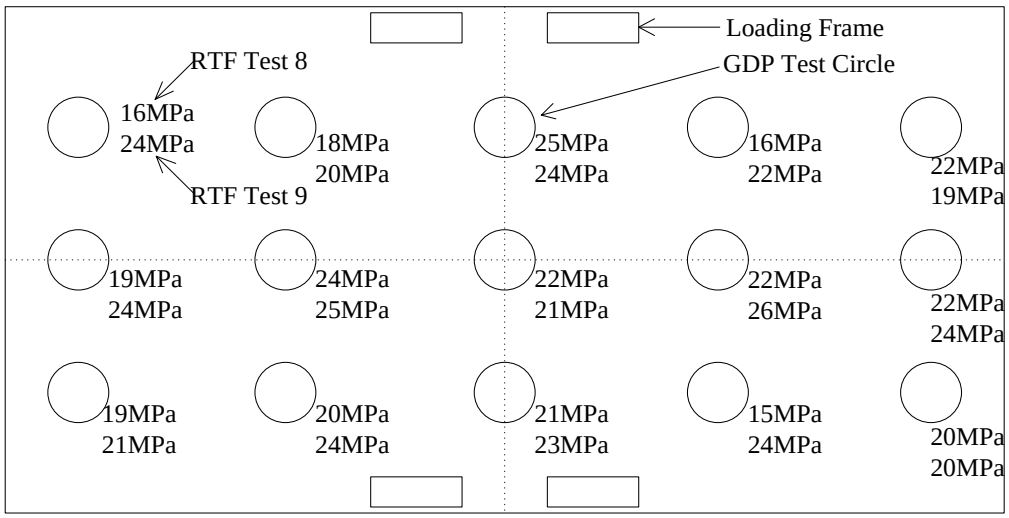

Figure 5.8 Subgrade stiffness measured by GDP

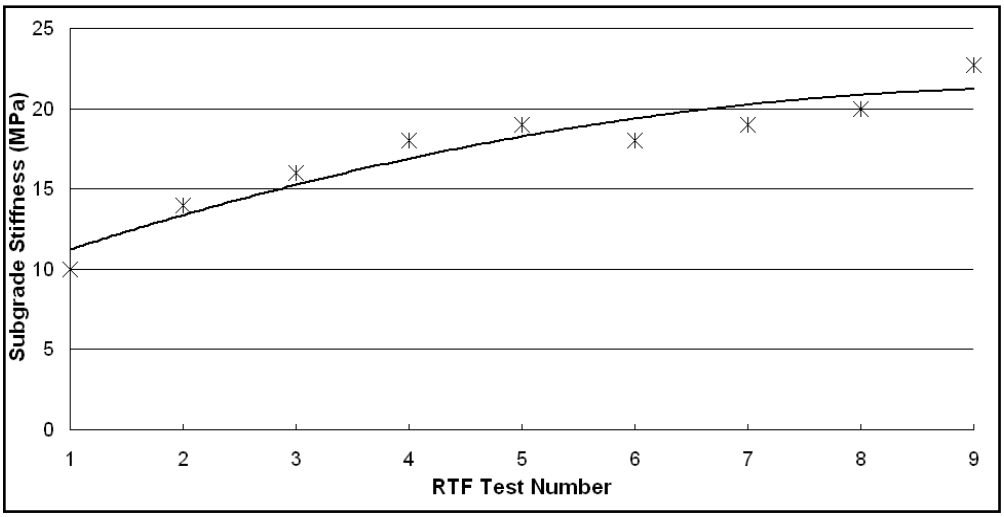

Figure 5.9 Comparison of subgrade stiffness in all the RTF tests

A geosynthetic was placed between the subgrade and the ballast layer to prevent upward migration of the subgrade into the ballast, as shown in Figure 5.10. Ballast was placed over the geosynthetic and compacted at a thickness of 100mm, 200mm and 300mm by a plate vibrator for 5 seconds at each location. The instrumented ballast particle in the bottom layer was installed when the ballast had been filled to 100mm depth but before compaction as shown in Figure 5.10. After

the ballast particle was placed in the right position, the excavated hole was filled to the original level and compacted. The same method was used in the installation of other instrumented ballast particles. Three G44 sleepers were placed on the 300mm thick ballast layer with 650mm centre-to-centre spacing. The G44 sleeper used in the RTF tests is also the standard concrete sleeper used on United Kingdom mainline track. Finally, more ballast was added to fill up the crib between the sleepers and the shoulder areas beyond the sleeper ends. As in the triaxial and CET tests, Glensanda ballast was used throughout to ensure repeatability and validity of results.

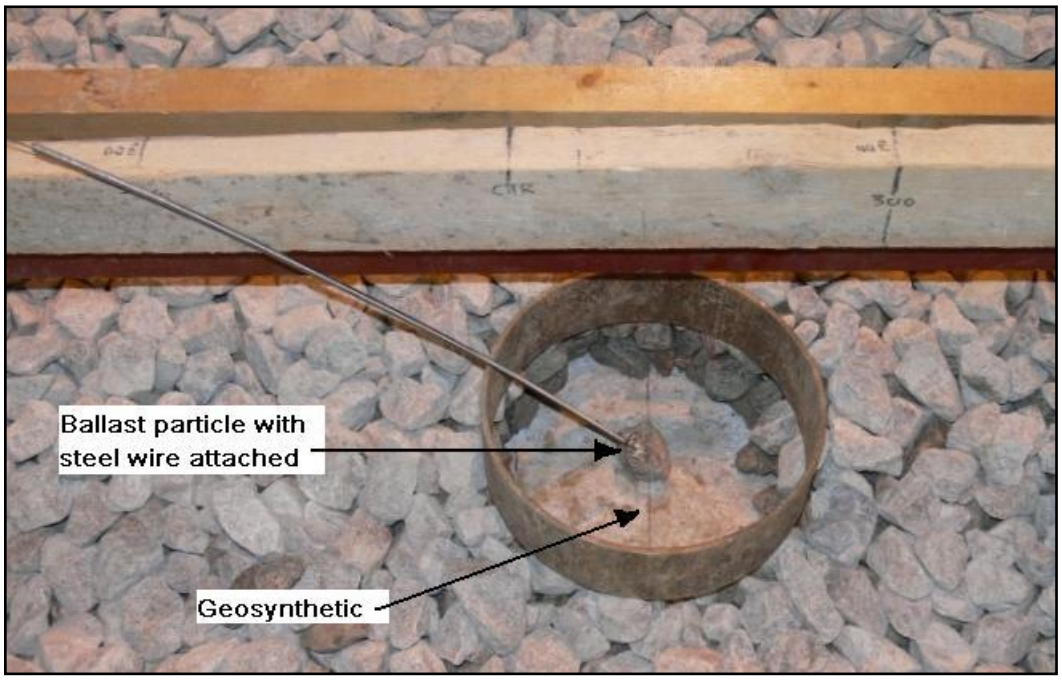

Figure 5.10 Installation of ballast particle with steel wire attached

After the installation, a million cycles of loading were applied. The load pattern was shown in Figure 5.2. Permanent deformation readings were taken at intervals when the cyclic loading was stopped and the load was held at 1kN. The readings

included two LVDTs at the front and rear of the middle sleeper, the integral stroke transducers and ballast particle reference points. Readings from the pressure cells and the resilient movement of ballast particle reference points were measured after 100, 1000, 2000, 5000, 10000, 20000, 50000, 100000, 150000, 200000, 250000, 300000, 400000, 500000, 600000, 700000, 800000, 900000, and 1000000 load cycles. As potentiometers were used in RTF Test 9, no resilient ballast particle movement was measured in this test.

5.5 Results

Although the RTF simulates the passage of a train over a sequence of three sleepers, the results for the middle sleeper are the main focus of these tests. The outer sleepers were included to provide the restraint and loading distribution representative of in-service conditions. The main test results included sleeper settlement, vertical stress on subgrade and the movement of instrumented ballast particles.

5.5.1 Sleeper Settlement

The sleeper settlement was measured by two LVDTs at both ends of the sleeper as well as the integral stroke transducer at the centre. Although the measured

settlement included contributions from both ballast and subgrade layers, it was concluded from earlier investigations that there was minimal settlement within the subgrade layer, and that it was negligible when compared to the ballast settlement (Kwan, 2006 and Aursudkij, 2007).

Figure 5.11 shows the permanent deformation of the middle sleeper in RTF Tests 1, 8 and 9. According to Table 5.1, the same ballast type and test conditions were used in the RTF Tests 1 and 8. Therefore, the permanent deformation of the middle sleeper in RTF Test 1 could be compared with those in Test 8. The final settlement reading in RTF Test 1 was 10.1mm, while in RTF Test 8 the final settlement after 1 million cycles was 12.7mm. From Figure 5.11, it can be seen that the greatest amount of difference between RTF Tests 1 and 8 occurred in the first 100 cycles, from which it is believed that sample preparation played a very important role in permanent deformation in the early stage of the tests.

Because of the effectiveness of the geogrid reinforcement, the magnitude of the settlement in RTF Test 9 was significantly reduced. The TriAx Geogrid was installed over a single layer of ballast stones, approximately 50mm above the bottom of the ballast layer. The final settlement reading after 1 million cycles for the middle sleeper was 7.2mm, which was about 57% of the total settlement in RTF Test 8.

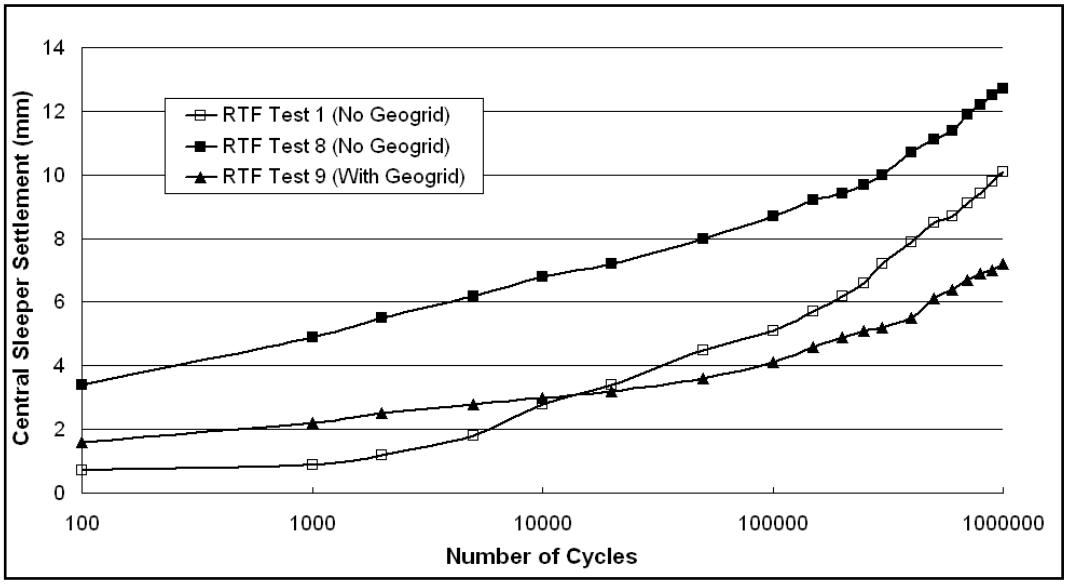

Figure 5.11 Middle sleeper settlements in RTF Tests 1, 8 and 9

5.5.2 Vertical Stress on Subgrade

Three Nottingham pressure cells were installed at a depth of 50mm underneath the surface of the subgrade. The installation arrangement was shown in Figure 5.3. The basic shape adopted for these instruments is a disc which supports a diaphragm in direct or indirect contact with the soil. The pressure cells consist of a recessed disc with 65mm diameter and 11mm thickness. The bottom of the disc forms a 2mm thick diaphragm which has a strain gauge in a wheatstone bridge configuration. A voltage is applied across the bridge and pressure on the diaphragm causes a change in resistance of the gauge which can be used to give a voltage output proportional to the pressure. The cell is buried with the diaphragm upwards in the subgrade taking care that there are no stones in contact with the

diaphragm and its cable run out of the surrounding material for accessibility. The pressure cells were connected to an external data acquisition system with 100-Hz logging rate.

Brown (1977) reviewed various instruments available for taking in-situ measurements of stress, strain, deflection and axle load in pavement experiments. He concluded that in general, pressure cells are suitable for both short-term static and dynamic applications. They are not, however, so suitable for long-term static measurement because of possible zero drift. Temperature changes in-situ will generally not be large but should not be ignored, particular if small changes of stress are envisaged. For dynamic measurement, temperature effects and other causes of slight zero drift are not of importance. Furthermore, Brown (1977) pointed out that most of the pressure cells are developed for particular projects, which emphasizes the need to design instruments to suit particular situations. In this research, dynamic readings from the pressure cells were measured at the intervals which are the same as the measurement of resilient movement and permanent deformation.

The Nottingham pressure cells used in the RTF were bench-calibrated against an oil pressure applied via a piston and cylinder and transmitted by means of rubber membranes clamped across the diaphragm and lid. An understanding of the interaction between pressure cells and the surrounding soil has developed by Brown (1977) and Brodrick (1977). They define the “cell registration” as follows: Stress indicated by cell / free field stress. According to Brodrick (1977) the

average cell registration for the Nottingham pressure cell, as used in the RTF in a static load condition is 0.97 and 0.93 in dynamic condition. Therefore, the bench-calibration results are applied in the experiments described here and the values obtained are expected to be quite close to the in-situ stress values without further correction.

Because the vertical stress readings followed the sinusoidal loading wave form, the peak reading was assumed to be the actual maximum stress for this position. Table 5.2 shows the average pressure cell readings in RTF Tests 8 and 9. As the performance of pressure cells are strongly rely on the accurate installation procedure. There were no results from the positions at the centre of the sleeper and between sleepers, because too much electrical noise was detected by the pressure cells.

Kwan (2006) and Aursudkij (2007) concluded that the highest stress was at the position near the sleeper end, where the load was applied (i.e. below the rail seating), as shown in Figure 5.3. The relatively lower stress positions were at the centre of the sleeper and between sleepers. Aursudkij (2007) further indicated that to be representative of site conditions, the highest stress should be below the rail seating as the ballast would be raised at that position during sleeper installation and tamping.

The vertical stress under the rail seat for RTF Tests 8 and 9 was found to be higher than in RTF Test 1 (45kPa from Kwan, 2006). This is probably because the

subgrade stiffness has been increased from 10MPa to over 20MPa, as shown in Figure 5.9. Additionally, the accuracy of the pressure cells was affected by the consistency of the ballast and the quality of the installation. The obtained pressure cell readings will be used to help validate the finite element method (FEM) stress condition simulation for the RTF, see Chapter 6.

Table 5.2 Average pressure cell reading for RTF Tests 8 and 9

Test Number	Sleeper End (kPa)	Centre of Sleeper (kPa)	Between Sleepers (kPa)
RTF Test 8	79	n/a	n/a
RTF Test 9	76	n/a	n/a

5.5.3 Instrumented Ballast Particle Settlement

The instrumented ballast particle arrangement in RTF Test 8 was shown in Figure 5.4. Because this was the first trial for these instruments, the chosen positions were not ideal and were insufficient to represent fully the ballast deformation underneath the sleeper. The monitored ballast particle settlements are shown in Figure 5.12 (a), (b), (c), (d), (e) and (f). The apparent oscillations in the accumulated settlement measurement are probably due to the error inherent in digital photogrammetry measurement technique. There were two monitored ballast particles at each position, one at the near end and the other at the far end of the sleeper. Best fit curves are given to represent average ballast settlement

behaviour. However, from Figures 5.12 (b) and (d) it can be seen that the two monitored ballast particles at the same position performed quite differently. No best fit curve could be drawn in the two positions.

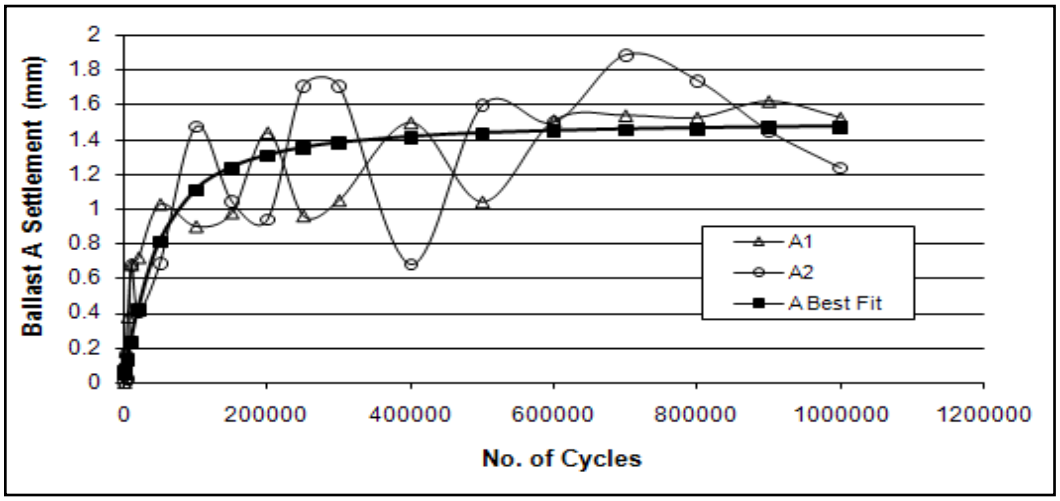

Figure 5.12 (a) Monitored ballast particle settlement at position A in RTF Test 8

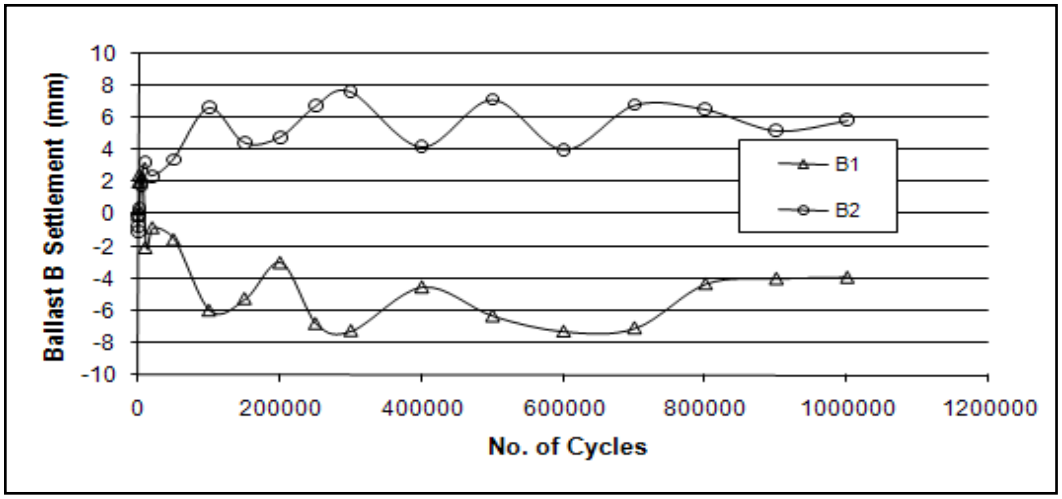

Figure 5.12 (b) Monitored ballast particle settlement at position B in RTF Test 8

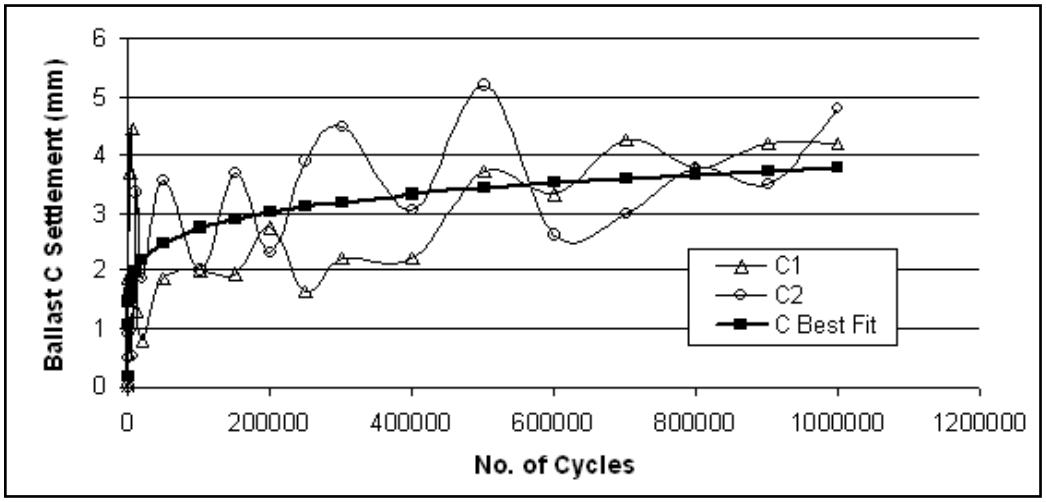

Figure 5.12 (c) Monitored ballast particle settlement at position C in RTF Test 8

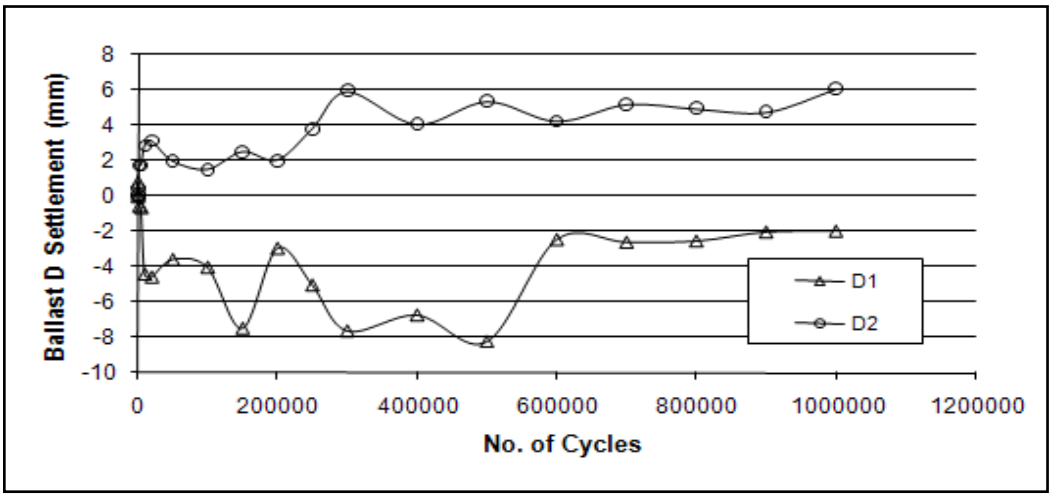

Figure 5.12 (d) Monitored ballast particle settlement at position D in RTF Test 8

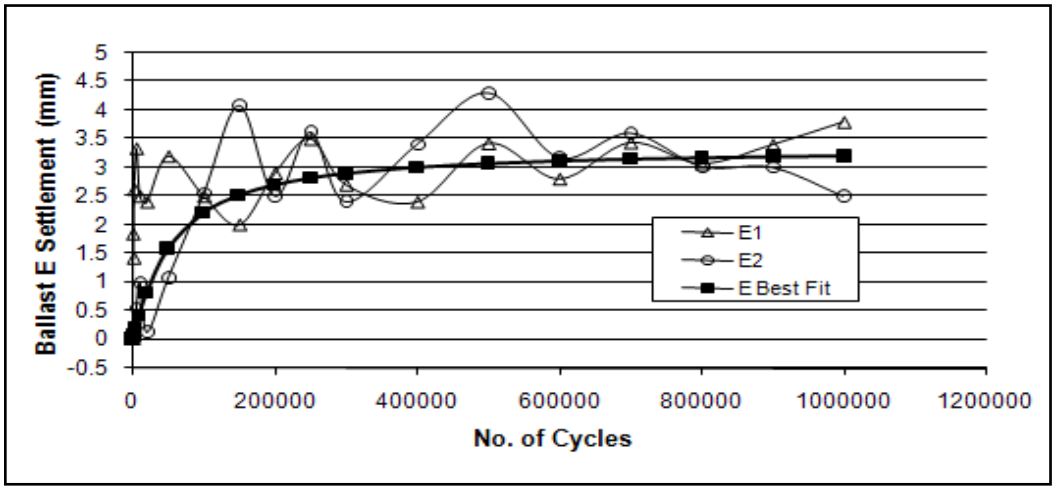

Figure 5.12 (e) Monitored ballast particle settlement at position E in RTF Test 8

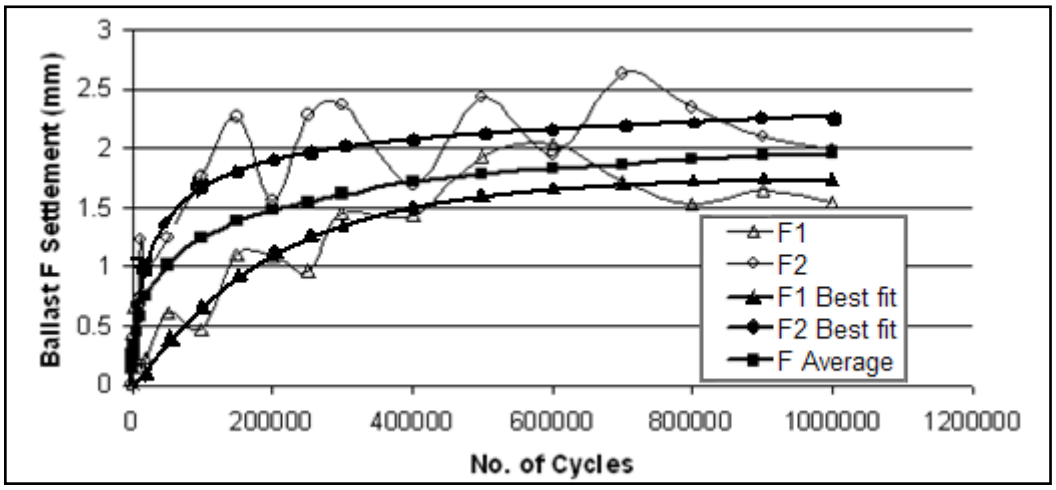

Figure 5.12 (f) Monitored ballast particle settlement at position F in RTF Test 8

At positions C and D in RTF Test 8, the steel wires and protection sleeves were bent to vertical, which was believed to have increased the error of measurement due to sleeve distortion and ballast movement. Theoretically, the ballast at position C (just above the subgrade) would have minor settlement compared to others. However, Figure 5.12 (c) shows that there was a settlement of 3.7mm after one million cycles which was probably mainly due to the effect of the movement

of steel wires and protection sleeves. Therefore, the measured results from positions C and D in RTF Test 8 are not thought to represent the true ballast movement at those positions thus omitted.

Figure 5.12 (b) shows the ballast particle movement right at the bottom corner of the sleeper, where a high stress zone existed. At position B, due to the random nature of the ballast movement, one particle came up and the other settled down. Therefore, no clear conclusion could be draw from this position. However, at a depth of 150mm below the bottom of the sleeper and right underneath the sleeper edge, Figure 5.12 (e) shows a permanent deformation of 3.2mm at position E, which is 25.2% of total ballast layer settlement.

Figures 5.12 (a) and (f) show ballast particle settlement at positions A and F. Two particles were measured at each position and the results were found to be close to each other. Probably, because both positions A and F were outside the main deformation zone, the settlements after 1 million cycles at positions A and F were around 1.5mm and 2mm respectively, which were 11.8% and 15.7% of the total settlement in the ballast layer. Compared with the CET test results, positions A and F had more permanent deformation than similar positions in the CET (4.6%). This was probably because instead of a single cyclic load, a passing wheal loading was simulated in the RTF. The ballast between sleepers in the RTF suffered rotation of principal stress. Therefore, more settlement could be detected in the ballast between sleepers.

The instrumented ballast particle arrangement in RTF Test 9 was shown in Figure 5.5. Four particles were monitored and the results are shown in Figure 5.13. All monitored particles were placed right underneath the edge of the sleeper to quantify the amount of settlement contributed by different layers above the grid reinforcement. Due to the random nature of ballast movement at positions C and D, much less settlement was detected from position C compared with position D. No conclusion could be drawn based on the behaviour of these two monitored particles, which indicated that at least three monitored ballast particles were necessary for each position. However, the instrumented ballast particles at positions A and B show similar settlement profiles over one million cycles. An average total settlement of 2.2mm was measured, which is 30.6% of the total ballast layer settlement.

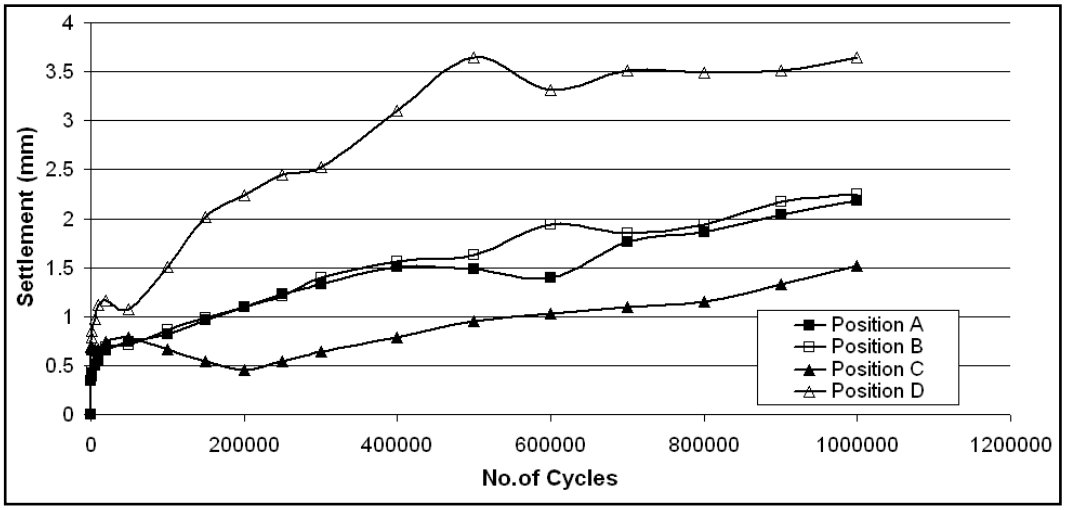

Figure 5.13 Monitored ballast particle settlement in RTF Test 9

Instrumented Ballast Particle Resilient Movement

The resilient movement of instrumented ballast particles was measured during the loading cycles immediately before each measurement interval. Figure 5.14 shows the resilient movement of monitored ballast particles in RTF Test 8. The resilient movement of the middle sleeper was calculated by averaging the readings of the two LVDTs at the front and rear ends of the sleeper. The resilient movement of the instrumented ballast particles was measured by an LVDT attached to each ballast particle reference point in turn, as shown in Figure 5.6. A certain time is required to move the LVDT and record readings, which meant that readings were only acquired from 50,000 cycles.

According to Figure 5.14, the resilient movement of the middle sleeper had a rapid decrease from 1.2mm to 1mm during the first 50,000 cycles. However, both the middle sleeper and instrumented ballast particles show a stable resilient movement from 50,000 cycles to a million. As mentioned before, the bent protection sleeves at positions C and D increased the error of measurement due to sleeve distortion and ballast movement. Movement of the steel wires might contribute a large part of the measured movement. Thus, no conclusion could be presented at positions C and D. The average resilient movements at positions B and E were 0.42mm and 0.35mm respectively. Positions A and F were outside the main deformation zone with resilient movement of 0.22mm and 0.25mm separately. Combined with the permanent deformation results it can be seen that largest resilient movements occurred together with high permanent deformation.

Meanwhile, small resilient movement existed together with low permanent deformation.

Because potentiometers were used in RTF Test 9, no resilient movement was measured for the instrumented ballast particles in this test.

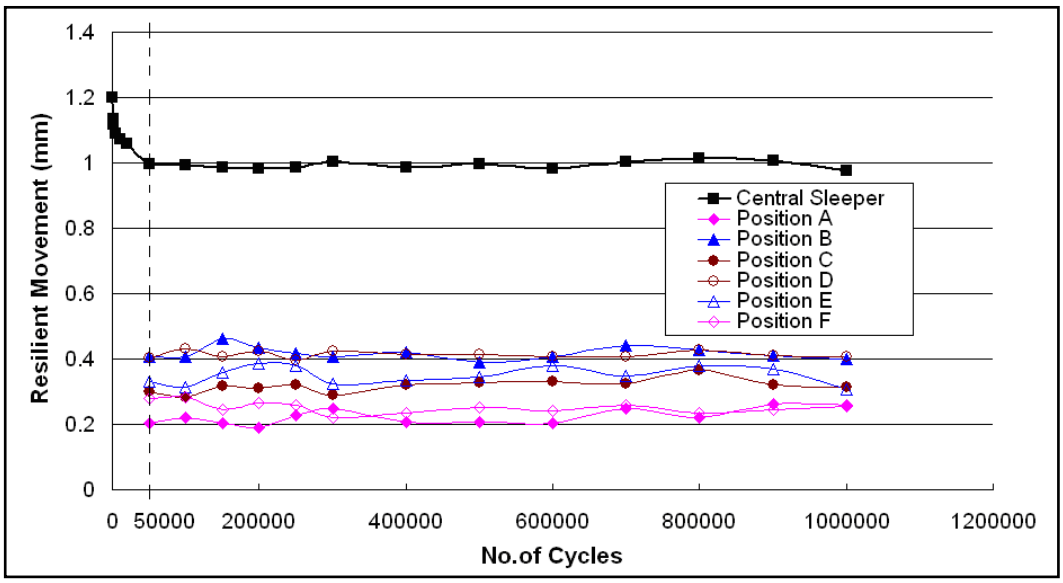

Figure 5.14 Resilient movements in RTF Test 8

5.6 Chapter Summary and Discussion

In order to examine and validate the railway settlement model, the RTF tests were carried out to investigate the ballast permanent and resilient movement in different layers as well as the pressures near the surface of the subgrade. The RTF represented a passing train load by means of three hydraulic actuators which

provided vertical loads of 94kN. Although three sleepers were involved in the RTF, the middle sleeper is the main focus of the tests. Three pressure cells were installed at a depth of 50mm in the subgrade to measure the vertical stress transmitted to the subgrade by the ballast. Due to too much electrical noise, readings were only obtained at the position below the rail seating.

The settlement readings of the middle sleeper were obtained from two LVDTs placed at each end of the sleeper as well as the integral stroke transducer mounted on the actuator. Compared with RTF Test1, the middle sleeper settlement in RTF Test 8 was 12% higher. This was probably due to the effect of sample preparation. In addition, RTF Test 9 showed the benefits of using geogrid in the ballast layer. This type of geogrid reinforcement reduced total permanent deformation by around 43% after one million cycles.

Photogrammetry analysis was used to measure the permanent deformation of instrumented ballast particles in RTF Test 8. However, it was found that this method was not reliable enough in the RTF test. Thus, instead of photogrammetry, potentiometers were used in RTF Test 9 to measure permanent deformation of the instrumented ballast particles. As in the CET tests, the largest permanent deformation was detected in the upper ballast layer under the sleeper in the RTF. A LVDT was used in RTF Test 8 to measure particle resilient movement. The resilient movement showed a broad correlation with the permanent deformation results. Because of the usage of potentiometers in RTF Test 9, no resilient movement was recorded. It is recommended for future RTF tests to have at least

three monitored particles in any one position and only vertical steel wire protection sleeves. Despite the shortcoming of the measurement of the monitored ballast particles, the sleeper deformation and pressure cells reading were accurately recorded and will be useful in validating and refining settlement models.

CHAPTER 6

6. FINITE ELEMENT MODELLING AND ANALYSIS

6.1 Introduction

As railway ballast typically behaves nonlinearly under wheel loading, making an fundamental simulation of railway ballast simulation would be a very difficult and complex task. Finite element method (FEM) is one of the most versatile numerical techniques for engineering analysis, as it enables a good approximation to be made even when a system exhibits non-linear material behaviour. It was decided to make use of the FEM in this research, as an alternative to multilayer linear elastic layered analysis, which was attempted by Kwan (2006) and Aursudkij (2007) using the Shell BISAR program. The finite element program utilised in this project is ANSYS. It is a powerful tool and capable of analysing a wide range of engineering problems including geomechanics. However, the FEM solution is

always an approximation to the real solution, restricted by the assumptions being made in idealising the geometry, boundary conditions and material model.

Finite element analysis has been performed to calculate the stress conditions within the ballast. Initially, an elastic material model was used to simulate a box test. The box test description and modelling will be presented in a subsequent section. The monotonic triaxial test was then analyzed by using a Drucker-Prager material model. Furthermore, after the release of ANSYS Version 11.0, the extended Drucker-Prager material model with hardening was utilised to fit monotonic triaxial test results and calculate stress conditions in the Composite Element Test (CET) and the Railway Test Facility (RTF). Finally, permanent deformations were calculated by the combination of the predicted stress conditions and settlement equations.

6.2 Initial Modelling

Initial modelling was carried out to investigate the ballast response with an elastic material model in a box test simulation and the ballast stress-strain behaviour with a Drucker-Prager material model in a triaxial test simulation.

6.2.1 Initial Box Test Simulation

Test Description

Box tests were carried out by Lim (2004) at the University of Nottingham. The box test facility was built to represent a volume of ballast below a section of sleeper underneath the rail seat. The box has a length of 700mm, width of 300mm and height of 450mm. The base of the box is consists of a 10mm thick rubber sheet to replicate a typical foundation stiffness. To set up a test, a 300mm thick layer of ballast is first placed in the box, tamped and levelled. A 300mm long, 250mm wide and 150mm high rectangular hollow steel section is placed on top of the ballast and surrounded by further overburden ballast. A schematic diagram and a photograph of the box test rig are shown in Figures 6.1 (a) and (b).

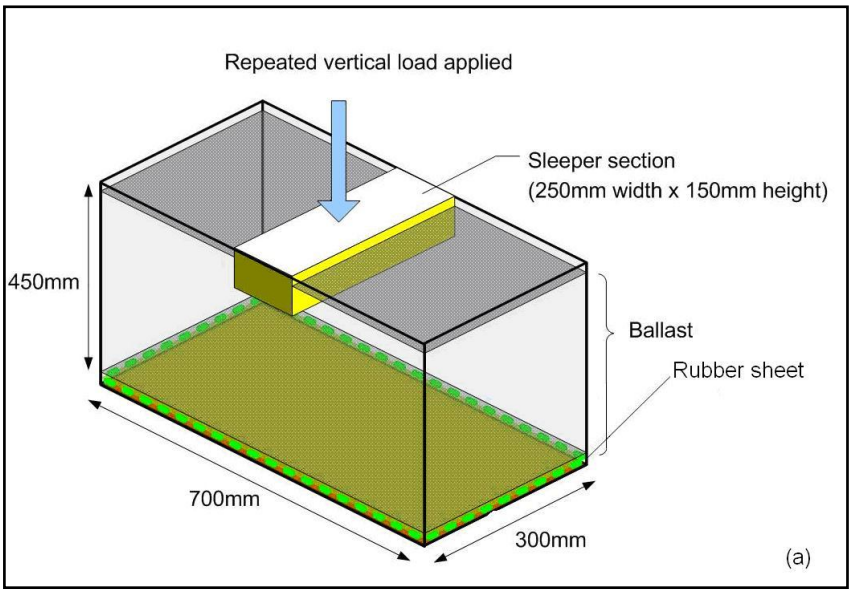

Figure 6.1 (a) Schematic diagram of the box test

Figure 6.1 (b) The box test set-up

Ballast settlement is measured by a LVDT mounted on the sleeper. The load cell attached to the actuator records the load values. Instrument arrangement details can be found in Figure 6.1 (b). Lim (2004) carried out the test with a minimum load of 3kN and a maximum load of 40kN for 1,000,000 cycles with a frequency of 3Hz. In addition, Li *et al.* (2007) carried out box tests on various interlayer systems with a 25kN peak load for up to 1,000,000 cycles with a frequency of 5.5Hz.

Elastic Modelling

The 3-dimensional structural model of the box test simulation with an elastic material model is shown in Figure 6.2 (a). The simulated loading was a monotonic load with a magnitude of 40kN, which was the maximum load value in the cyclic loading test. As this is an elastic model, there is no plastic strain produced by the loading.

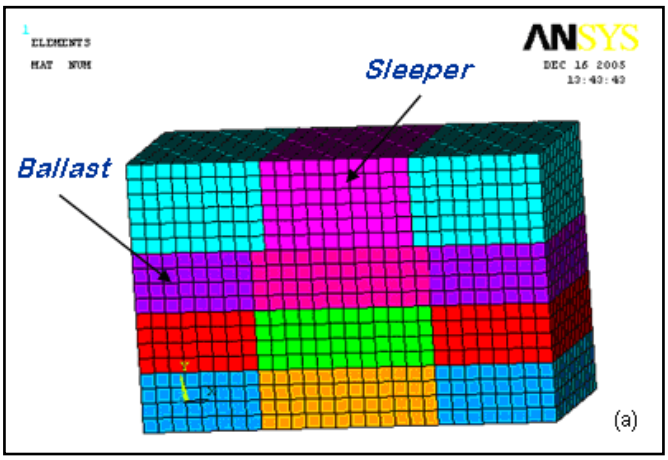

Figure 6.2 (a) Structural details of box test elastic modelling

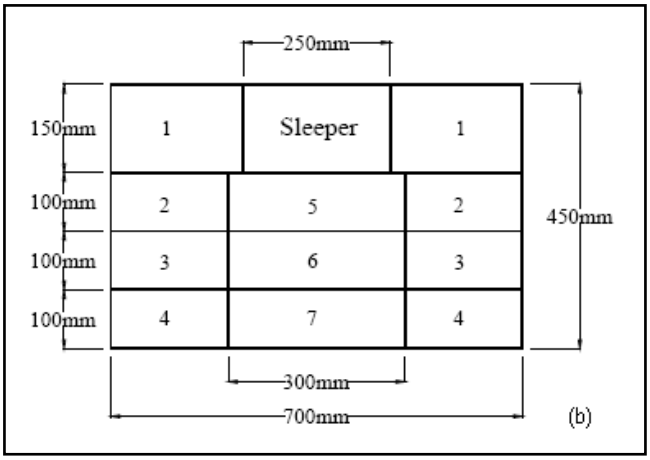

Figure 6.2 (b) Front elevation with different sections of the box test simulation

Figure 6.2 (b) shows the front elevation divided into different sections with different parameters in the simulation. The ballast in different areas under or around the sleeper is assumed to have different parameters, such as density, Poisson's ratio and Young's Modules, due to consolidation and compaction during the ballast installation. Parameter details are listed in the Table 6.1. All parameters were chosen based on the box test results by Lim (2004). The

thickness of the ballast in the box test is 300mm with 150mm thick overburden crib ballast. Different compaction methods were used for the ballast underneath the loading sleeper section and overburden crib ballast. Therefore, the ballast in Section 1 is relatively looser than other sections. Sleeper section is simulated with typical steel properties.

Table 6.1 Parameters used in box test elastic modelling based on Lim (2004)

Ballast Position	Density (kg/m^3)	Poisson's ratio	Young's Modulus (Pa)
Section 1	1700	0.35	100E6
Section 2	1800	0.33	120E6
Section 3	1800	0.33	120E6
Section 4	1800	0.33	120E6
Section 5	1800	0.33	120E6
Section 6	1800	0.33	120E6
Section 7	1800	0.33	120E6
Sleeper section	7850	0.3	200E9

In this model, 3-dimensional 8-node isoparametric structural solid elements were used to simulate both the sleeper and the ballast material. In ANSYS, this element is named Solid 45, which is defined by eight nodes having three degrees of freedom at each node: translation in the nodal *x*, *y* and *z* directions. In order to simplify the model, the boundary conditions of the interfaces between the ballast and the test box were fixed. The top surface of the ballast and the sleeper had free

boundary conditions. The interfaces between the ballast elements and the sleeper elements were glued. Figure 6.3 shows the predicted vertical displacement in the box test simulation. Figures 6.4 and 6.5 show the vertical stress and strain distribution respectively.

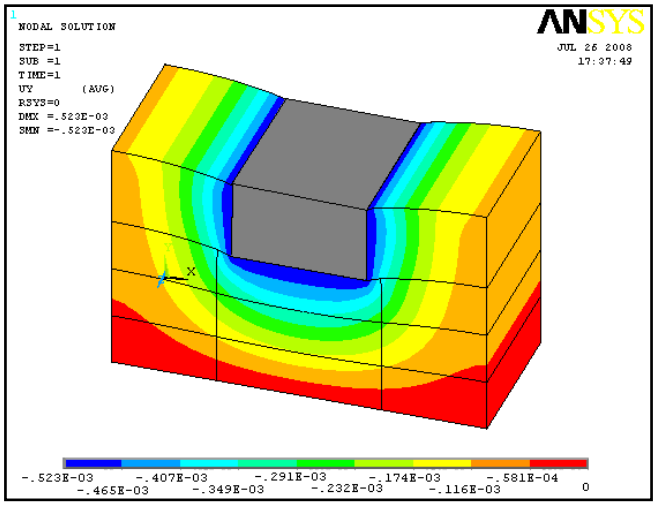

Figure 6.3 Vertical displacement in the box test simulation (Unit: m)

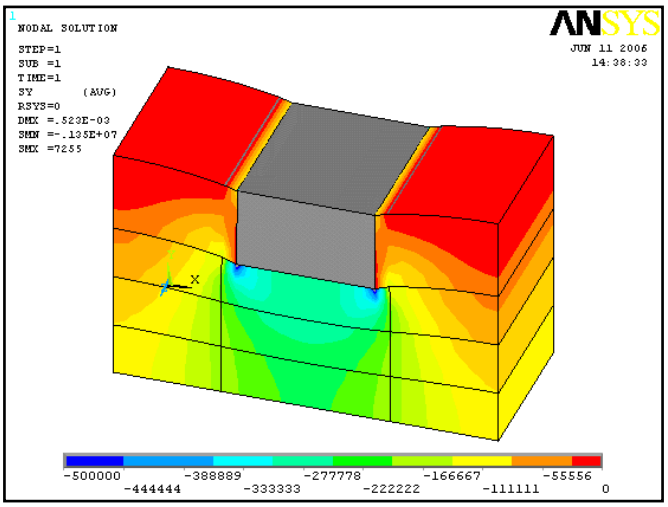

Figure 6.4 Vertical stress distribution in the box test simulation (Unit: Pa)

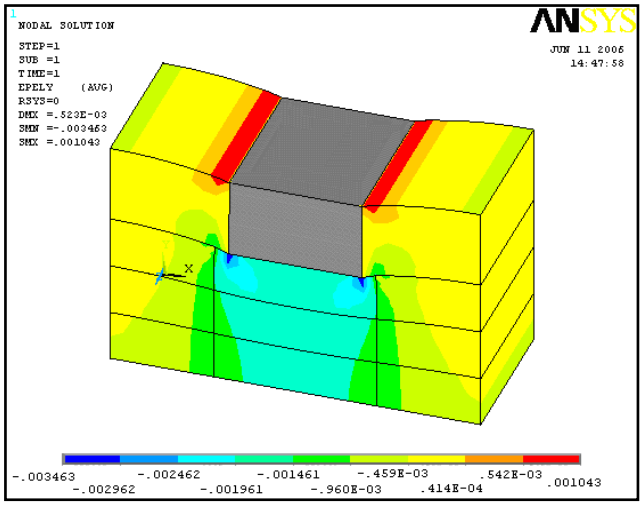

Figure 6.5 Vertical strain distribution in the box test simulation

As seen in Figure 6.3, most of the ballast deformation occurs underneath the sleeper, and this decreases from the top to the bottom. The ballast directly under the sleeper has the largest vertical settlement. Figures 6.4 and 6.5 show stress and strain concentration zones near the sleeper bottom corners. It appears that the ballast at the concentration zones suffers very high stress. This also highlights that the vertical stress and strain under the sleeper (Sections 5, 6 and 7 in Figure 6.2 (b)) are much higher than in the areas on the two sides (Sections 2, 3 and 4 in Figure 6.2 (b)). As the ballast model elements were glued to the sleeper, ballast elements near the top corners of the sleeper show tensile stress and strain, which does not exist in reality. This issue could be solved by applying only sleeper pressure instead of modelling the sleeper fully.

The ballast box test was simulated to investigate the ballast response under the monotonic loading. It was found that the use of elastic material in the model is not appropriate to simulate ballast behaviour, because the permanent deformation has

not been built up. Although the box test simulation provided an understanding of stress and strain distributions in ballast, it was considered necessary to adopt a non-elastic system to better replicate ballast behaviour in subsequent FEM analysis.

6.2.2 Initial Triaxial Test Simulation

As discussed in the literature review, although the Drucker-Prager model is an elastic perfect-plastic model, it has been widely used to simulate inelastic behaviour of granular materials. In this section, ballast behaviour in the triaxial tests has been simulated by a Drucker-Prager material model.

In the triaxial test, a cylindrical sample of ballast is subjected to two independently controlled stress components: pressure acting in every direction through surrounding compressed water and a vertically acting additional load supplied by a central shaft. By means of these two components, confining stress and deviator stress, many loading situations can be effectively simulated.

Due to the sample geometry and loading conditions, triaxial tests can be analysed using a 2-dimensional axisymmetric approach. A 2D 4-node structural solid element, Plane 182 in ANSYS, was used in this simulation. The element can be used as either a plane element (plane stress, plane strain or generalized plane strain) or an axisymmetric element. It is defined by four nodes having two degrees

of freedom at each node: translations in the nodal *x* and *y* directions. The shaded area of the specimen in Figure 6.6 (a) shows the simulated part of the ballast column. Figure 6.6 (b) shows the detailed boundary condition and mesh of the simulation area. The left boundary represents the central specimen axis, which does not move laterally (i.e. vertical degree of freedom only). The boundary condition at the base of the specimen is fixed vertically, while movement in the radial direction is not restricted.

In this study, the parameters for the Drucker-Prager model were taken from the experimental results. Three particular parameters were used for the Drucker-Prager model in ANSYS to simulate the material plastic behaviour: cohesion, frictional angle and dilation angle. As no cohesion exists in granular ballast materials, cohesion was set to zero. Based on the monotonic triaxial tests, a frictional angle of 55° and a dilation angle of 33° were used. The detailed calculation can be found in Chapter 3. Some other parameters used in this model are listed below: the density of the ballast sample was 1540kg/m^3, the Young's modulus was 30MPa, and the Poisson's ratio was 0.3.

A comparison of the monotonic triaxial test results and the simulation results is shown in Figure 6.7. It can be seen that the initial elastic stiffness and the ultimate stress from simulation broadly match with that from the experiments, but overall fit is still far from satisfactory. Due to the limitation of the Drucker-Prager model, the extended Drucker-Prager model with hardening was adopted to simulate

ballast behaviour after initial modelling. Proper scientific deformation responses with proper material modelling will be studied in the following sections.

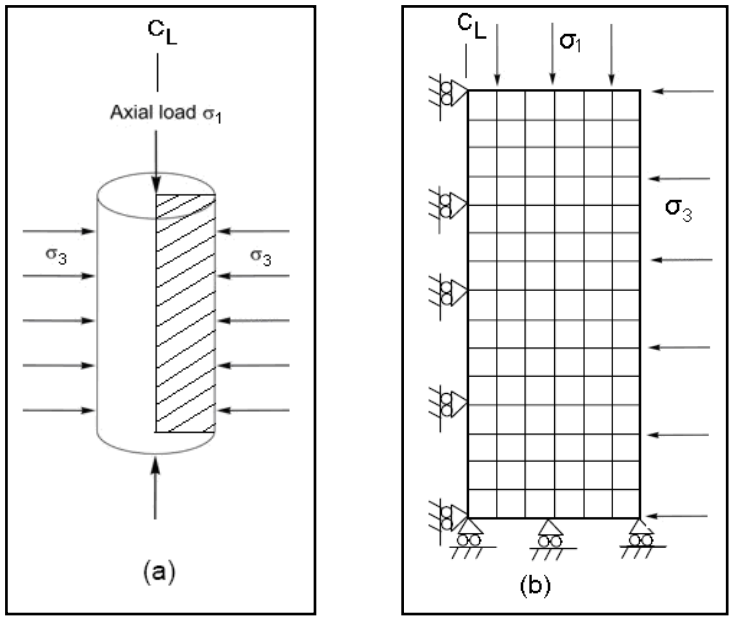

Figure 6.6 (a) The ballast specimen in the triaxial test, (b) Boundary conditions and mesh in triaxial test simulation

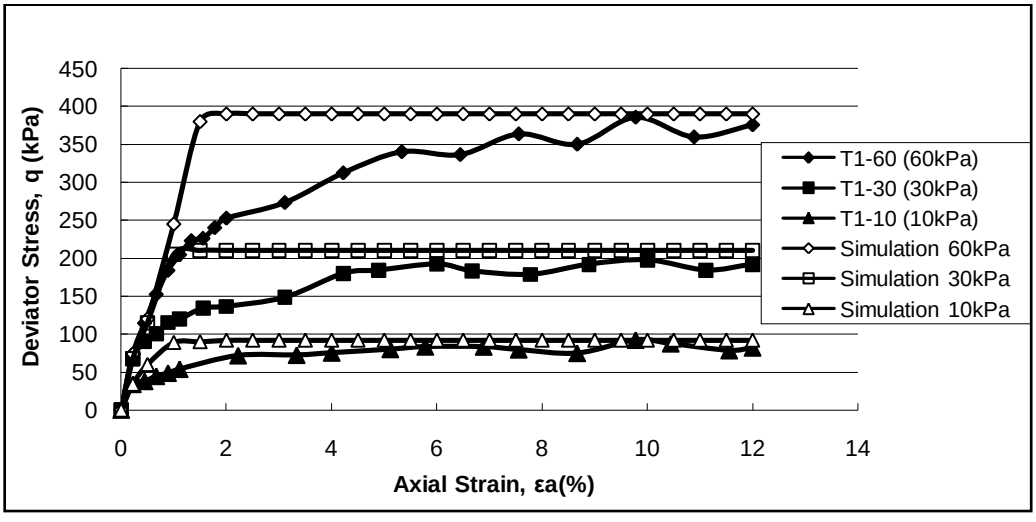

Figure 6.7 Stress-strain behaviour of ballast from the monotonic triaxial tests compared with simulation results

6.3 Material Modelling

6.3.1 Elastoplastic Material Model in the Triaxial Test Simulation

The monotonic triaxial test results were used to validate the parameters in elastoplastic material modelling. As mentioned in the literature review, three extended Drucker-Prager yield criteria are provided in ANSYS: a linear form, a hyperbolic form and a general exponent form. The linear model is intended primarily for applications where the stresses are for the most part compressive. Therefore, the linear yield function extended Drucker-Prager model was chosen for this simulation. As described in Section 2.5, the yield function with linear form is given by:

$$F_s = q + \alpha p' - \sigma_Y(\varepsilon_{pl}) = 0 \qquad \text{(Equation 2.21)}$$

where two input parameters C_1 and C_2 in this equation:

$C_1 = \alpha$ = material parameter referred to pressure sensitive parameter,

$C_2 = \sigma_Y(\varepsilon_{pl})$ = yield stress of material,

$q = [\frac{3}{2}\{s\}^T[M]\{s\}]^{\frac{1}{2}}$, $\{s\}$ = deviatoric stress vector,

p' = mean stress = $\frac{1}{3} \times (\sigma_x + \sigma_y + \sigma_z)$.

The parameter C_1 can be obtained by matching experimental triaxial test data. To calibrate the parameter C_1 for this simulation, it is very important to decide which point on each stress-strain curve is to be used for calibration. Instead of the ultimate yield surface in the Drucker-Prager model, the initial yield surface was used for the extended Drucker-Prager model calibration. The Drucker-Prager model is often used as an ultimate yield surface, in the sense that the material can exhibit unlimited flow when the stress reaches yield. This behaviour is called perfect plastic, as shown in Figure 6.7. In the extended Drucker-Prager model with hardening, initial yield points are used, as shown in Figure 6.8. In this case plastic flow causes the yield surface to change size uniformly with respect to all stress directions. The chosen initial yield points from the monotonic triaxial tests in Figure 6.8 could be plotted in the meridional plane shown in the Figure 6.9. As such, the input parameter $C_1 =$ 1.0731.

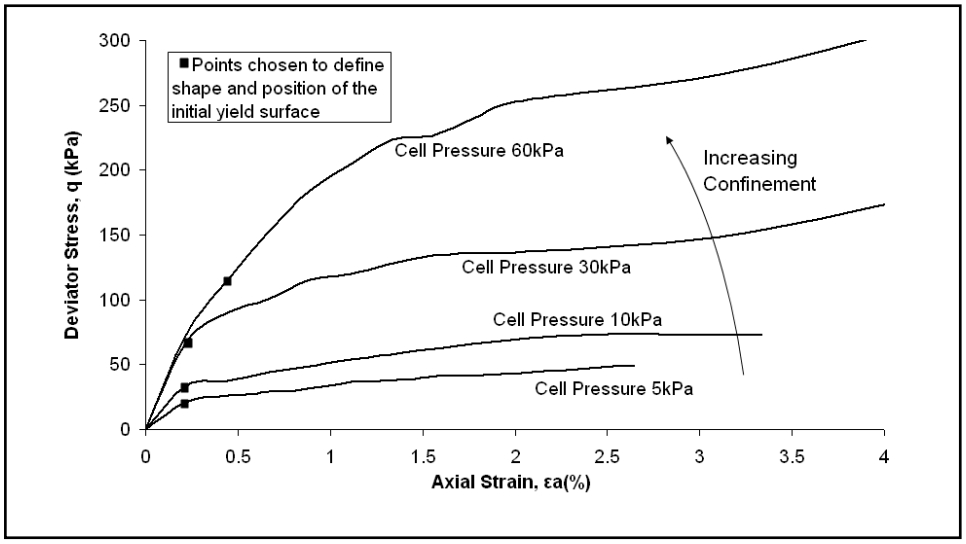

Figure 6.8 Points chosen to define the shape and position of the initial yield surface

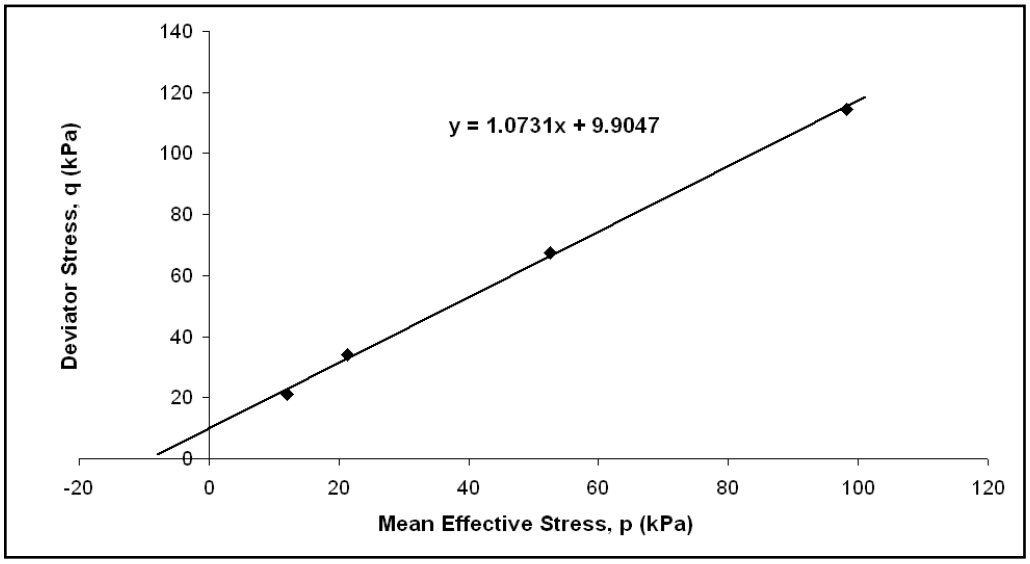

Figure 6.9 Initial yield surface plotted in the meridional plane

Instead of using a single value as the yield stress of the Drucker-Prager material model, in this computer simulation the hardening of material is defined by combining the Multi-linear Isotropic Hardening (*MISO*) option with extended Drucker-Prager plasticity, as the input parameter C_2. The *MISO* option uses the von Mises yield criteria coupled with an isotropic work hardening assumption. This option is often preferred for large strain analyses, and it is defined by the uniaxial stress-strain test results in ANSYS, as shown in Figure 6.10. As it is impossible to carry out a uniaxial test for railway ballast, a series of virtual uniaxial test data were calculated to fit the triaxial experimental results, as shown in Table 6.2. In order to have better representation, the virtual uniaxial stress-strain curves of the ballast were independently defined at different cell pressures.

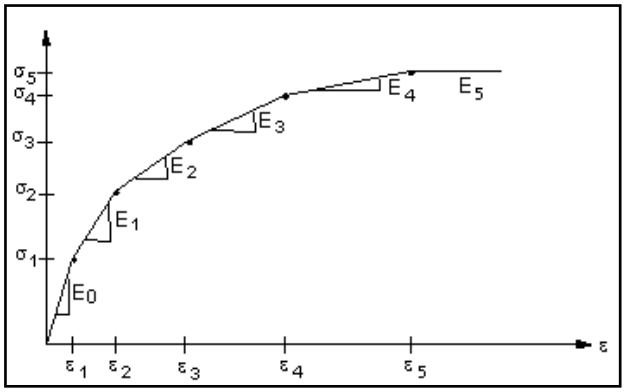

Figure 6.10 Uniaxial stress-strain curve for Multi-linear Isotropic Hardening

(ANSYS, 2007)

Table 6.2 Virtual uniaxial stress-strain curve for hardening simulation

For Cell Pressure =5kPa	
Strain	Stress (Pa)
0.0005	4850
0.008	15000
0.020	20000
0.040	26000
0.060	29500
0.090	30500
0.150	31500

For Cell Pressure =10kPa	
Strain	Stress (Pa)
0.0005	7700
0.008	20000
0.020	25000
0.040	36000
0.060	39000
0.090	42000
0.150	44000

For Cell Pressure = 30kPa	
Strain	Stress (Pa)
0.001	30000
0.008	46000
0.02	55000
0.04	77000
0.06	85000
0.09	91000
0.15	92000

For Cell Pressure = 60kPa	
Strain	Stress (Pa)
0.001	33000
0.008	61000
0.02	92000
0.04	108000
0.06	130000
0.09	161000
0.15	174000

The linear plastic flow potential function in ANSYS is defined as:

$$Q = q + \alpha p' - \sigma_Y(\varepsilon_{pl}) \qquad \text{(Equation 2.25)}$$

where two input parameters C_3 and C_4 are defined as follows:

C_3 $= \alpha$, refers to dilation angle. For granular materials the linear model is normally used with non-associated flow, where the dilation angle is smaller than the friction angle.

C_4 $= \sigma_Y(\varepsilon_{pl})$ = yield stress of material,

q $= [\frac{3}{2}\{s\}^T[M]\{s\}]^{\frac{1}{2}}$, $\{s\}$ = deviatoric stress vector,

p' = mean stress = $\frac{1}{3} \times (\sigma_x + \sigma_y + \sigma_z)$.

The amount of dilatancy (the increase in material volume due to yielding) can be controlled with the dilatancy angle. If the dilatancy angle is equal to the friction angle, the flow rule is associative. If the dilatancy angle is zero (or less than the friction angle), there is no (or less of an) increase in material volume when yielding and the flow rule is non-associated. In ANSYS, when the flow potential is the same as the yield function ($F = Q$), the plastic flow rule is associated, which in turn results in a symmetric stiffness matrix. When the flow potential is different from the yield function ($F \neq Q$), the plastic flow rule is nonassociated, and this results in an unsymmetric material stiffness. The dilation angle is calculated from the volumetric and axial strain measurement in the monotonic triaxial tests. According to the triaxial test results analysis in Chapter 3, the dilation angle (ψ) is 33°; C_3 = 0.58 in radians. Apart from the parameters

mentioned, the other ballast parameters used in this simulation were based on the triaxial test results. The initial density of ballast was 1540 kg/m^3, the Poisson' ratio was 0.3.

In simulating the monotonic triaxial test procedure, two loading steps were applied in the test simulation. In the first load step, the top and the bottom of the specimen were restricted in the vertical direction and the cell pressure was applied, as shown in Figure 6.11 (a). The second load step was to hold the cell pressure and the bottom position of the specimen constant, and then the specimen was forced to contract until the axial strain limit of 12% was reached, as shown in Figure 6.11 (b). In the second load step, the 12% axial strain was achieved by means of 10 small steps (i.e. the specimen contracted 5.4mm in each small step). Each small load step was accumulated by automatic time substeps. Automatic time stepping allows ANSYS to determine appropriate sizes to break the load steps into. Decreasing the step size usually ensures a better accuracy, but this is time consuming. The automatic time stepping feature determines an appropriate balance. In this simulation, the substeps for each small load step were 50, which would set the first substep to 1/50th of the total load. The remaining substeps would be determined based on the response of the material due to the previous load increment in this simulation. The minimum number of substeps in each small step was 10. The maximum was 300, the program stopped if the solution did not converge after 300 substeps. Automatic time stepping also activates the ANSYS bisection feature which will allow recovery if convergence fails.

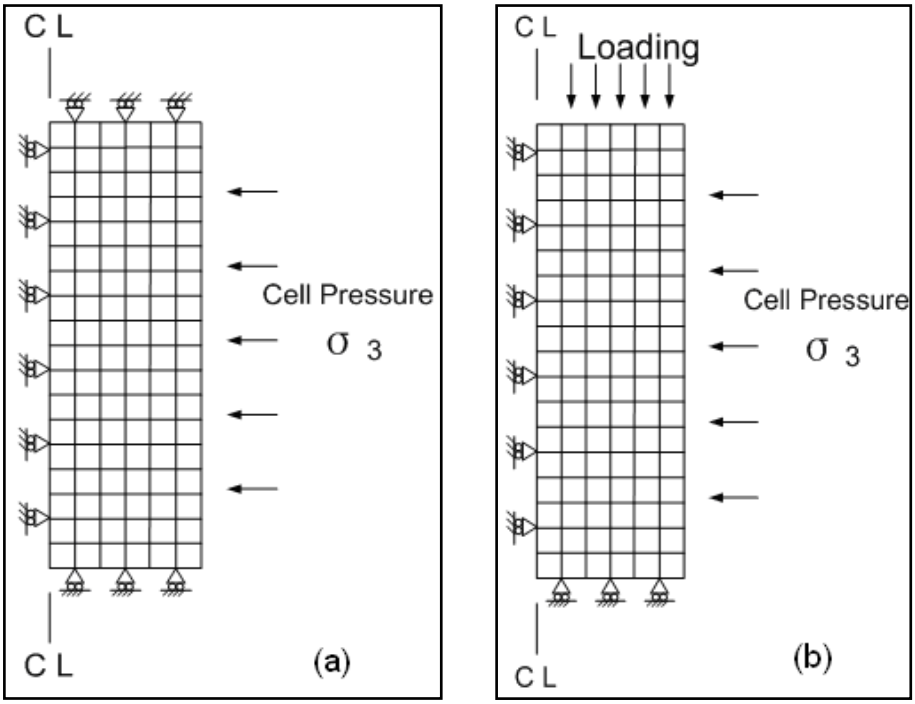

Figure 6.11 (a) Schematic diagram of the first load step in monotonic triaxial test simulation, (b) Schematic diagram of the second load step in monotonic triaxial test simulation.

The comparison of simulated and experimental results is shown in Figure 6.12. In this figure, series number T1-60 means the first series of triaxial tests (i.e. monotonic tests) with a cell pressure of 60kPa. Series number S1-60 means the first triaxial test simulation with a cell pressure of 60kPa. From Figure 6.12, it is clearly seen that the initial elastic stiffness, initial yield stress and the peak stress from simulation and experiments broadly match each other. Compared with the initial triaxial test simulation, the extended Drucker-Prager model with hardening provides a far better representation of the ballast behaviour.

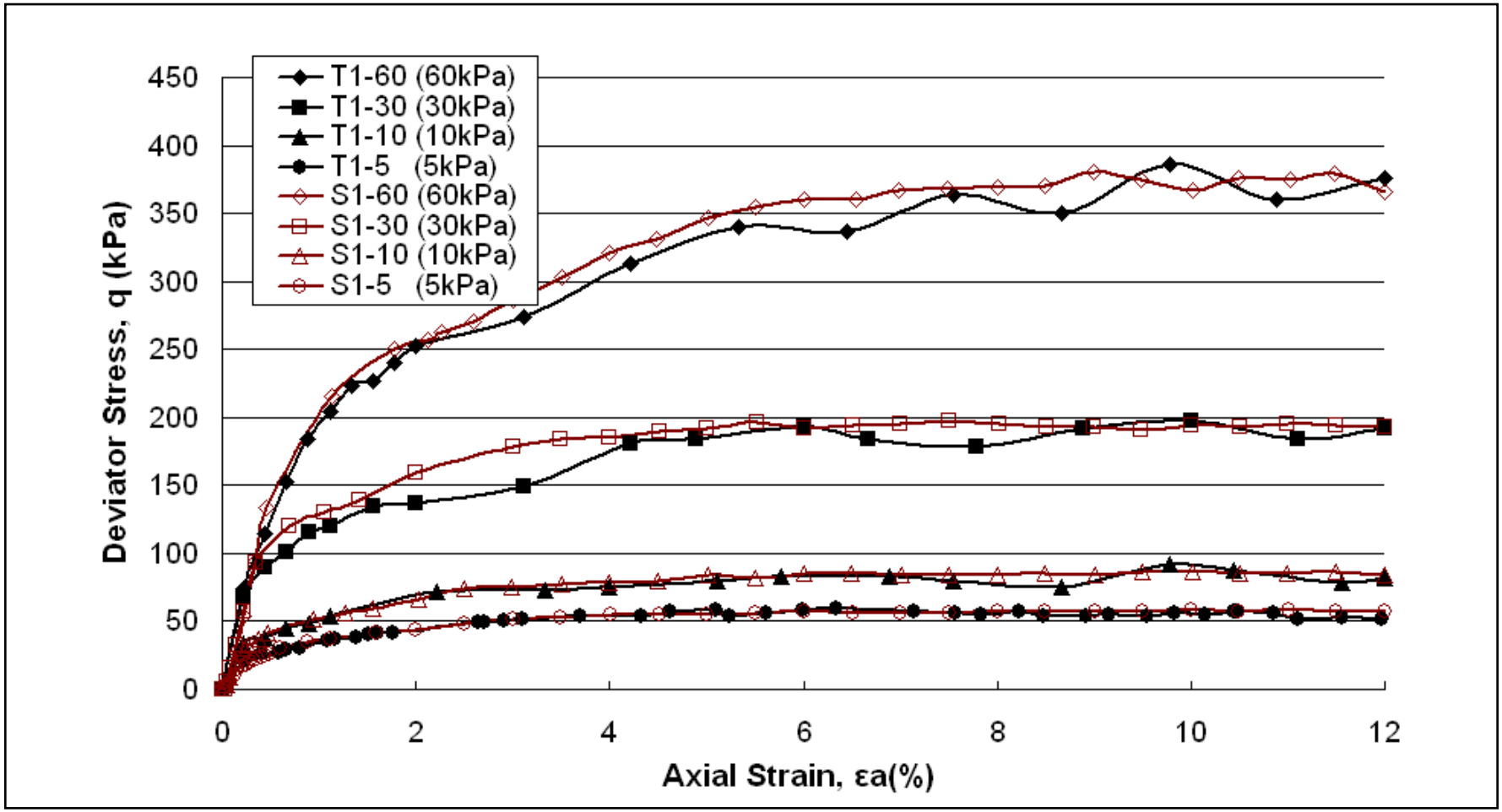

Figure 6.12 Comparison of the triaxial monotonic tests and the simulation result

6.3.2 Elastoplastic Material Model in the CET and RTF Test Simulations

In the CET and RTF simulations, the input parameters for the ballast material model are the same as the parameters for the triaxial test except for the virtual uniaxial stress-strain data, which depends on the applied confining pressures. In order to simulate the CET and the RTF, more elastoplastic material model input parameters at different confining pressures are necessary. Since the uniaxial stress-strain data with cell pressures of 5kPa, 10kPa, 30kPa and 60kPa were obtained from the triaxial tests, interpolation by proportional parts has been used to calculate the data at other confining pressures.

Prior to discussing the confining pressure in the ballast, it is necessary to investigate lateral earth pressure coefficients in general. The in-situ horizontal effective stress, for at rest conditions, is given by $K_0 \times \sigma'$, where (conventionally) $K_0 = 1 - \sin\phi$ is the lateral earth pressure coefficient at rest (ϕ is friction angle) and σ' is the vertical effective stress. Moreover, the Rankine active and passive states were also evaluated. When horizontal stress is decreased to a certain magnitude, the full shear strength of the soil will be mobilized. No further decrease in the horizontal stress is then possible. The horizontal stress for this condition is called the active stress, and the ratio of horizontal to vertical stress is called the coefficient of active stress and is denoted as K_a, $K_a = \tan^2(45 - \phi/2)$. In the passive condition, the soil is compressed in the horizontal direction. The horizontal stress cannot be increased beyond a certain

magnitude called the passive stress. The ratio of horizontal to vertical stress is then called the coefficient of passive stress K_p, $K_p = \tan^2(45 + \phi/2)$.

Taking the RTF test for an example, after calculation, the maximum confining pressure of the ballast underneath the sleeper is 1.5kPa by using the coefficient of lateral earth pressure at rest K_0. The maximum Rankine active stress within the ballast ($K_a \times \sigma'$) is 0.8kPa, and the passive stress $K_p \times \sigma'$ is 83.8kPa. However, as mentioned before, according to Selig and Alva-Hurtado (1982), in-situ confining pressure of self standing ballast perpendicular to the rail was approximately 5-40kPa. Therefore, K_0 and K_a are too small for the ballast condition. Furthermore, since K_p is the maximum horizontal that cannot be achieved, the coefficient in ballast condition (K_b) should be between K_0 and K_p.

$$K_a < K_0 < K_b \text{ (ballast conditon)} < K_p$$

In addition, the initial confining pressure should be related to the ballast friction angle in line with the definitions of earth pressure given above. Hence, $K_b = \tan\phi$ can be used as an approximation. The calculation equation for the initial confining pressure is then:

$$p_c = K_b \times \sigma' = \tan\phi \times \rho g h \qquad \text{(Equation 6.1)}$$

where ρ is the density of the ballast, g is the acceleration due to gravity, h is the depth in the ballast and ϕ is the ballast friction angle. However, it should be noted that there is no exact formula to calculate the initial ballast confining pressure; Equation 6.1 is suggested as a reasonable approach.

The thickness of the ballast in the CET and the RTF is 300mm with a 150mm thick overburden adjacent to the loading platen in the CET and a 200mm thick overburden crib ballast in the RTF. The depth of the ballast was calculated from the top of the overburden. The approximate amounts of ballast were 4500 kg for all RTF tests and 700kg for CET, resulting in ballast density of approximate 1700kg/m^3 in both the CET and the RTF. The 300mm CET ballast layer was divided into three 100mm thick sublayers. According to Equation 6.1, the average confining pressure in the top 100mm sublayer was about 5kPa, in the second layer it was about 7.5kPa, and in the bottom layer it was 10kPa. As the ballast elastoplastic material model input parameters for confining pressures of 5kPa and 10kPa had been validated by monotonic triaxial tests, the virtual data for a confining pressure of 7.5kPa could be calculated by interpolation, as listed in Table 6.3.

In a similar way, the 300mm thick ballast layer was divided into four 75mm sublayers in the RTF simulation. Therefore, the average initial confining pressure in each sublayer was 6.3kPa, 8.3kPa, 10kPa and 12.2kPa. Using the same interpolation method, the virtual uniaxial stress-strain input data are as listed in Table 6.3. By using the virtual uniaxial stress-strain data, the simulated ballast behaviour at different confining pressures for the CET and the RTF is plotted in Figure 6.13.

Table 6.3 Virtual uniaxial stress-strain curve for the CET and RTF tests

For Cell Pressure =6.3kPa	
Strain	Stress (Pa)
0.0005	5562.5
0.008	16250
0.020	21250
0.040	28500
0.060	31875
0.090	33375
0.150	34625

For Cell Pressure =7.5kPa	
Strain	Stress (Pa)
0.0005	6275
0.008	17500
0.020	22500
0.040	31000
0.060	34250
0.090	36250
0.150	37750

For Cell Pressure =8.3kPa	
Strain	Stress (Pa)
0.0005	6987.5
0.008	18750
0.020	23750
0.040	33500
0.060	36625
0.090	39125
0.150	40875

For Cell Pressure =12.2kPa	
Strain	Stress (Pa)
0.0005	9125
0.008	22500
0.020	27500
0.040	41000
0.060	43750
0.090	47750
0.150	50250

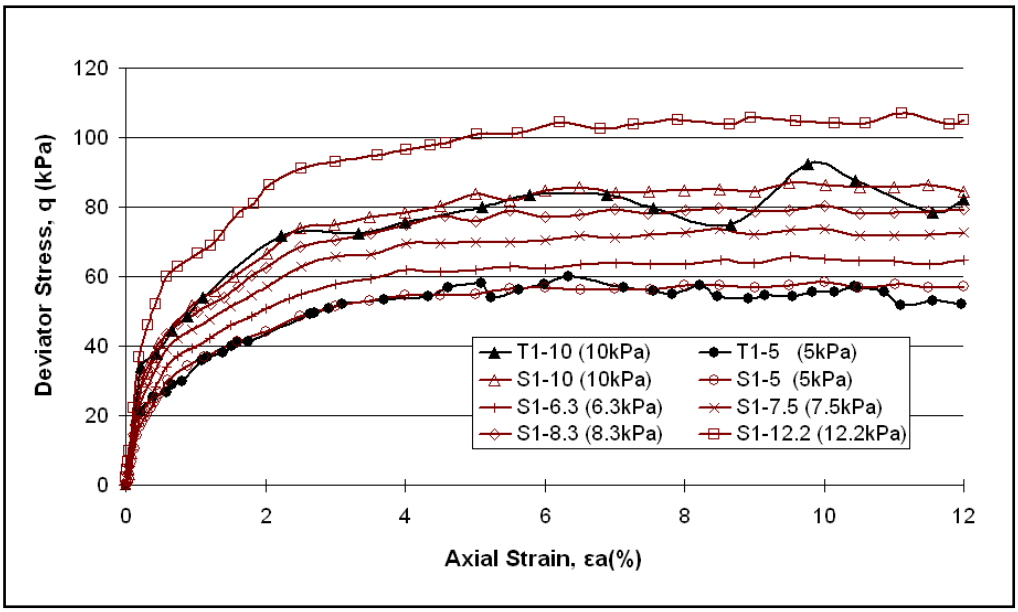

Figure 6.13 Simulated ballast behaviour at different confining pressures for the CET and the RTF

6.4 Finite Element Modelling and Analysis of the CET

The purpose of numerical modelling is to compute the stress and stain distributions in the CET and the RTF. The CET test simulation was focused on the modelling of ballast behaviour under one sleeper, while ballast behaviour in multi-sleeper railway track was simulated in the RTF. Further analysis included principal stress rotation in the RTF simulation.

6.4.1 The CET Modelling

A two-dimensional plane strain model was used in the CET modelling. As mentioned in Chapter 4, the CET model had bilateral symmetry. So, only half of the model was simulated to save calculation time. The element type for the ballast material model was a 2-dimensional 4-node solid structure element. The CET simulation model was built as shown in Figure 6.14. The 300mm thick ballast layer was divided into three equal thickness layers, and the overburden ballast was included in the top layer. The elastoplastic model input parameters for the ballast layers were as presented in Section 6.3.2. In order to simplify this model, the subgrade layer was simulated as an elastic material with a density of 2000kg/m^3, a Poisson's ratio of 0.3 and an elastic stiffness of 20MPa.

The density of mesh influences the accuracy, convergence and speed of the solution. The CET model was automatically meshed with an element edge length of 12.5mm. Boundary conditions chosen were the same as used by researchers (Brunton and Almeida, 1992; Neves and Correia, 2003; Arnold, 2004 and Radampola, 2006) where symmetric geometry is assumed. Moreover, the vertical boundary provided free movement in the vertical direction while in the outward direction was fixed. The boundary at the base is fixed vertically while movement in the radial direction is not restricted. The boundary conditions for the CET model are specified in Figure 6.14. In addition, compared with the fixed boundary, the roller boundary conditions were also utilised to avoid large tensile stress within the ballast.

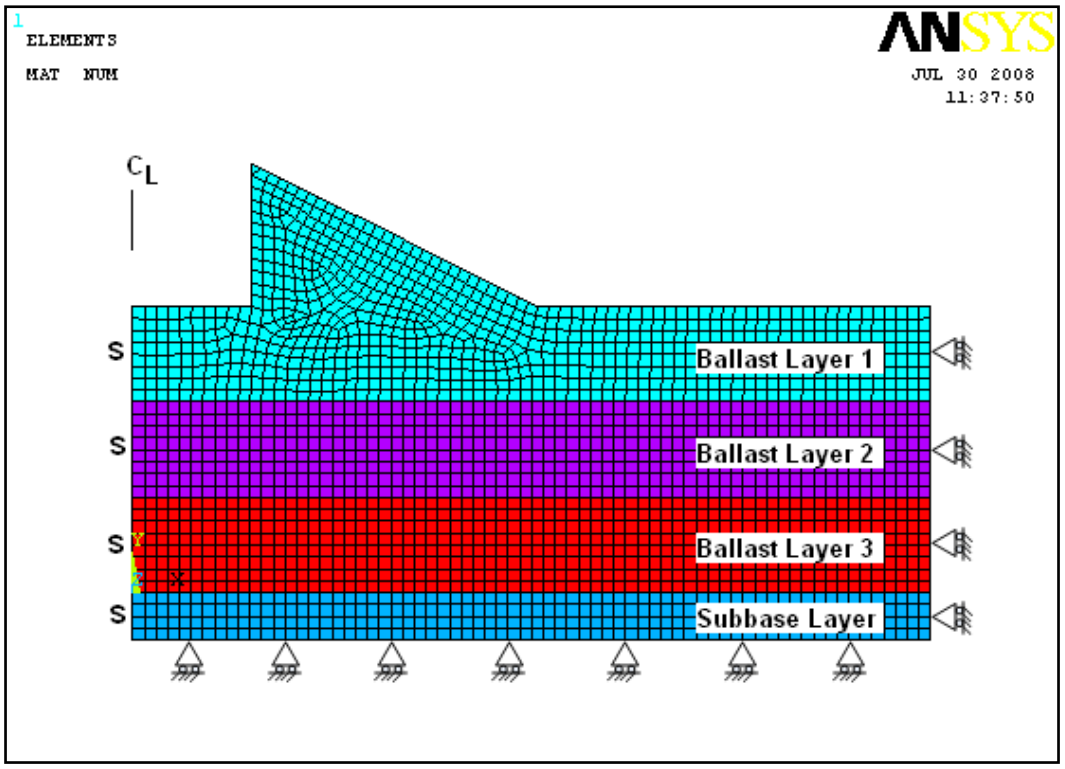

Figure 6.14 The CET simulation model with boundary conditions

The loading area directly influences the stress distribution within the ballast, especially the ballast directly underneath the loading sleeper section. Threrefore, the definition of loading area is quite important in the CET modelling. Figure 6.15 (a) shows the contact area between the steel loading platen and the ballast. It can be seen that the effective loading area was reduced by the rounded corners of the loading platen. Therefore, the loading area was defined from Node 1 to Node 9 in the simulation as shown in Figure 6.15 (b). As the ballast particles directly underneath the sleeper deform uniformly in the CET tests, Nodes 1 to 9 were defined as a set with coupled degree of freedom (i.e. Nodes 1 to 9 would have the same deformation during the simulation). The maximum load applied on the sleeper was 20kN and the equivalent pressure was 127kPa on the nodes in the simulation.

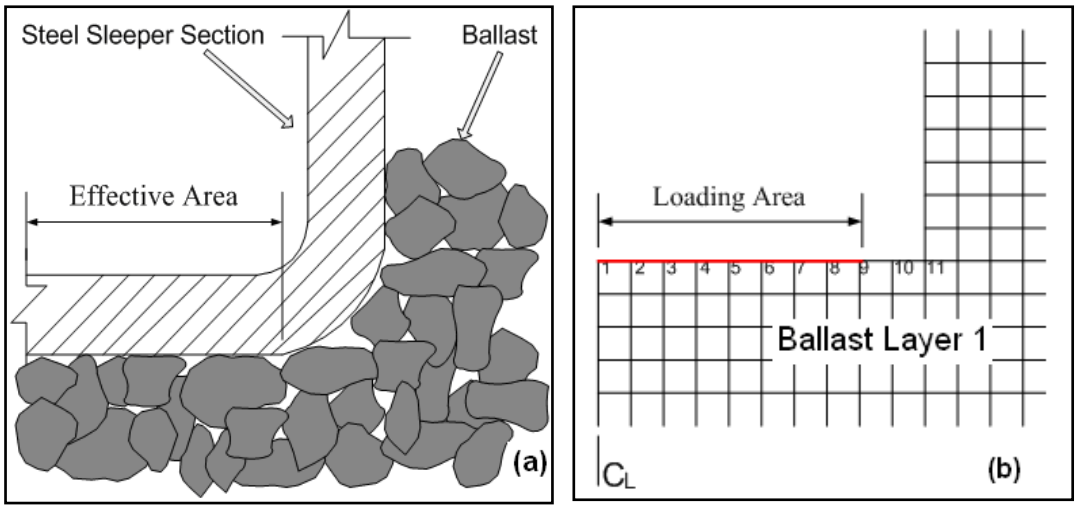

Figure 6.15 (a) Schematic diagram of loading area in the CET, (b) Modelling of loading area in the CET

6.4.2 Results of the CET Modelling

The CET was simulated with a monotonic loading of 20kN. The Y-component (vertical direction) displacement, Y-component stress distribution and X-component (horizontal direction) stress distribution are shown in Figures 6.16, 6.17 and 6.18 respectively.

As in the previous simulation of the box test, Figure 6.16 shows that the ballast directly underneath the sleeper has the largest settlement and that it decreases from the top to the bottom. The maximum settlement under monotonic loading in the CET simulation is approximately 3mm, which includes both the permanent and resilient settlement in the first load cycle.

Figure 6.17 shows the Y-component stress distribution in the CET. It highlights a stress concentration zone near the sleeper bottom corner. The maximum stress in this zone is over 150kPa. It can also be seen that the vertical stress is concentrated under the sleeper and spreads downwards at a narrow angle.

Figure 6.18 shows the X-component stress distribution in the CET. Similar to the vertical stress, there is a high horizontal stress zone within the top layer of ballast near the sleeper bottom corner. However, in contrast to the vertical stress, lower horizontal stress zones are detected in the bottom layer of the ballast directly underneath sleeper and the top layer of ballast adjacent to the sleeper. Although a slightly tensile horizontal stress was detected in the middle of the subgrade layer and in overburden ballast, this will not affect the ballast settlement calculation.

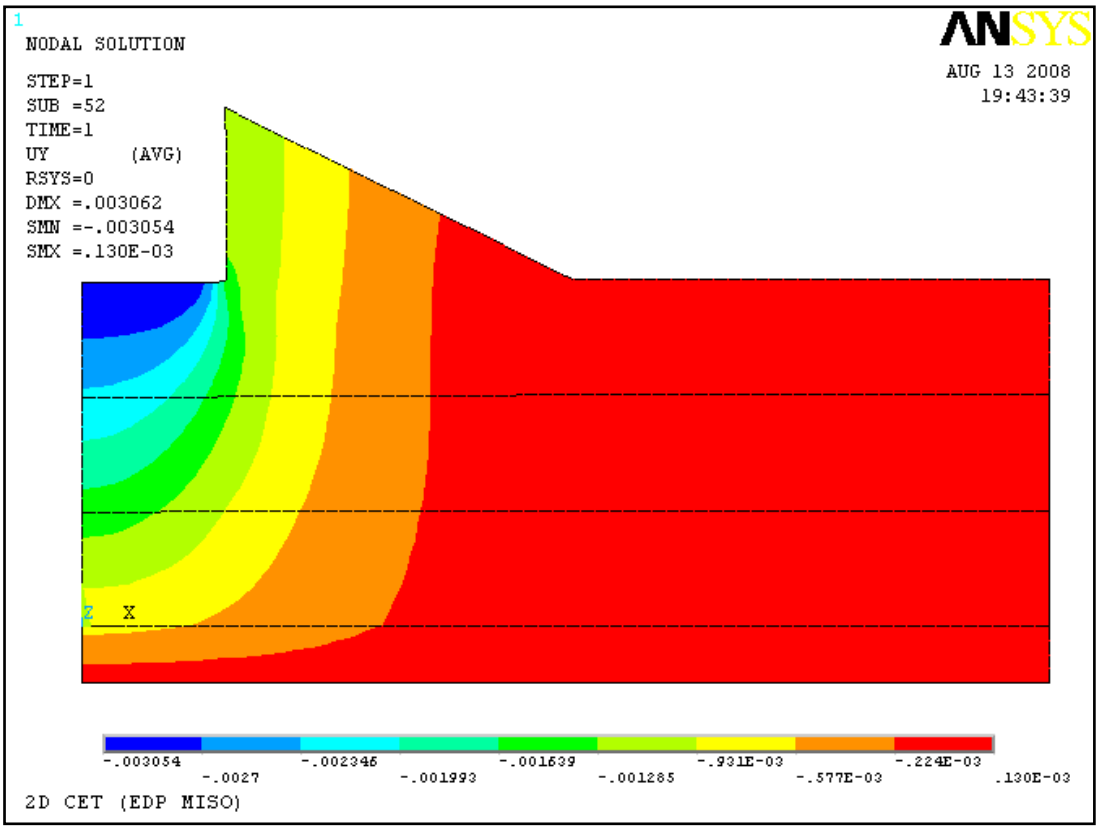

Figure 6.16 Y-component displacement in the CET simulation (Unit: m)

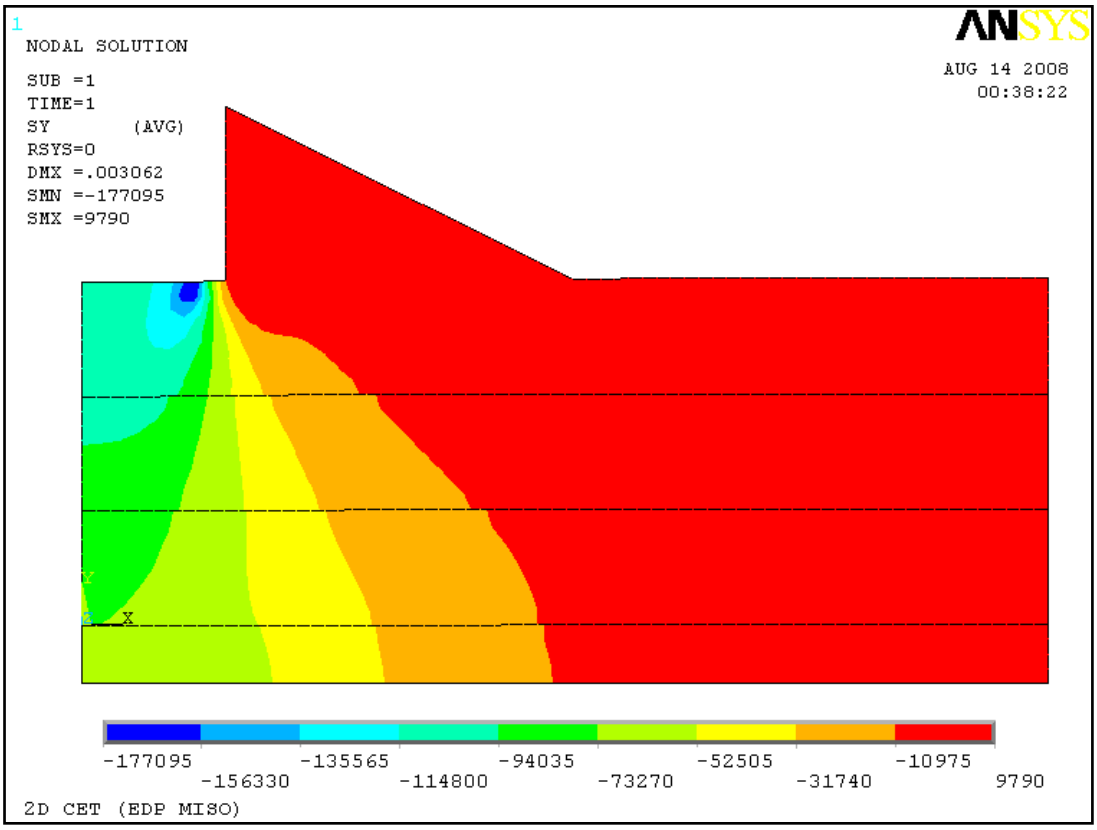

Figure 6.17 Y-component stress distribution in the CET simulation (Unit: Pa)

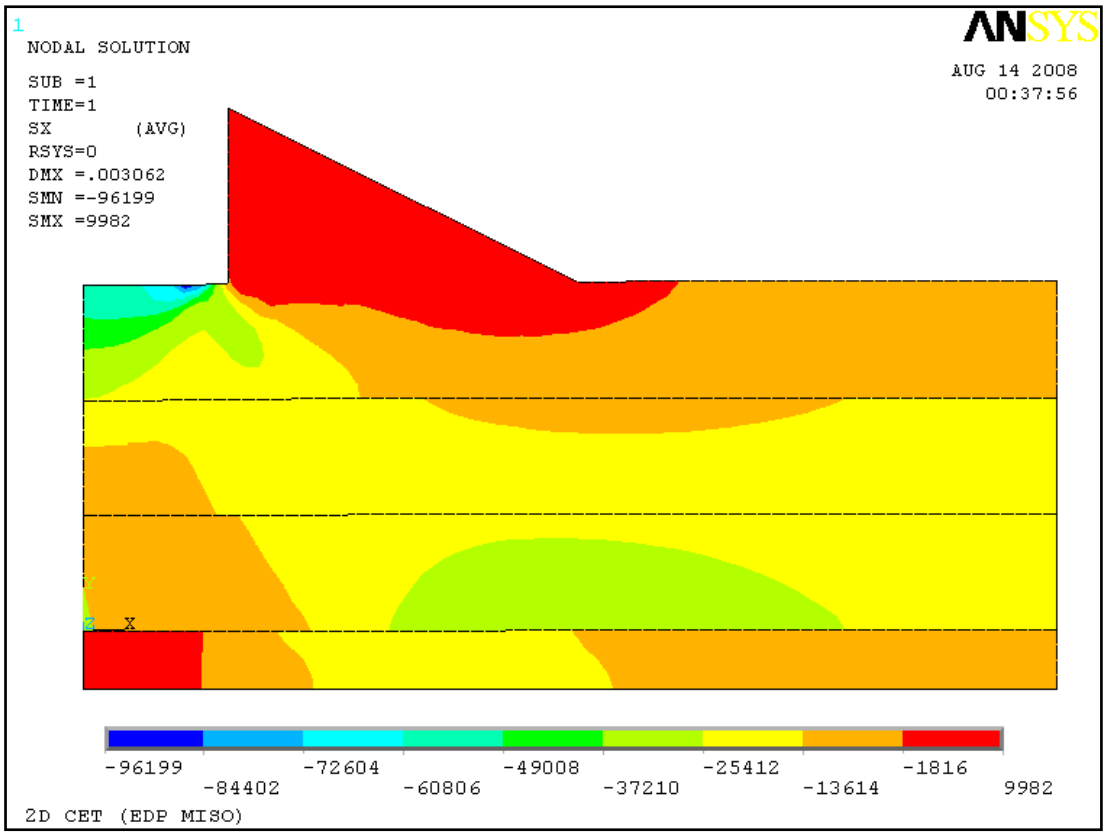

Figure 6.18 X-component stress distribution in the CET simulation (Unit: Pa)

6.5 Finite Element Modelling and Analysis of the RTF

As described in Chapter 5, the RTF mimics the cyclic loading of a passing train over three sleepers. It is an intermediate approach between conventional laboratory ballast testing and on-site observation.

6.5.1 The RTF Modelling

As for the CET, a bilateral symmetric 2-dimensional plane strain model was utilised to simulate the RTF. In addition, the element type for the ballast material model in the RTF was a 2-dimentional 4-node solid structure element. Element type is Plane 182 in ANSYS. As the cross sections in the RTF were different, this model represented the cross section under the loading position (i.e. below the rail seating), as shown in Figure 6.19. The ballast layer was divided into four layers with a thickness of 75mm each, and the overburden ballast was included in ballast Layer 1. In order to obtain a better accuracy, the model had a fine mesh with an element length of 7.5mm in the ballast layer. The element size in the subgrade layer was increased from the top to the bottom to save calculation time. The RTF model chosen was a 2-dimensional symmetric model with boundary conditions the same as for the CET, as shown in Figure 6.19.

Three sinusoidal sleeper loads with a 90° phase difference between them were applied in the RTF. As the main focus of this simulation was the ballast under the middle sleeper, the critical stress condition for permanent deformation of the ballast under the middle sleeper would occur when a full load of 94kN was applied on the middle sleeper and a load of 47kN on the two outer sleepers. Therefore, in this model the applied pressure on the ballast at the bottom of the middle and outer sleepers were 132kPa and 66kPa respectively. The nodes underneath the sleeper were defined as a set with their degrees of freedom coupled together. The input parameters for the ballast layer in the RTF were as presented in Section 6.3.2. The subgrade layer was simulated as an elastic material with a density of 1770kg/m^3, a Poisson's ratio of 0.3

and an elastic stiffness of 20MPa. These subgrade material parameters are based on laboratory test results.

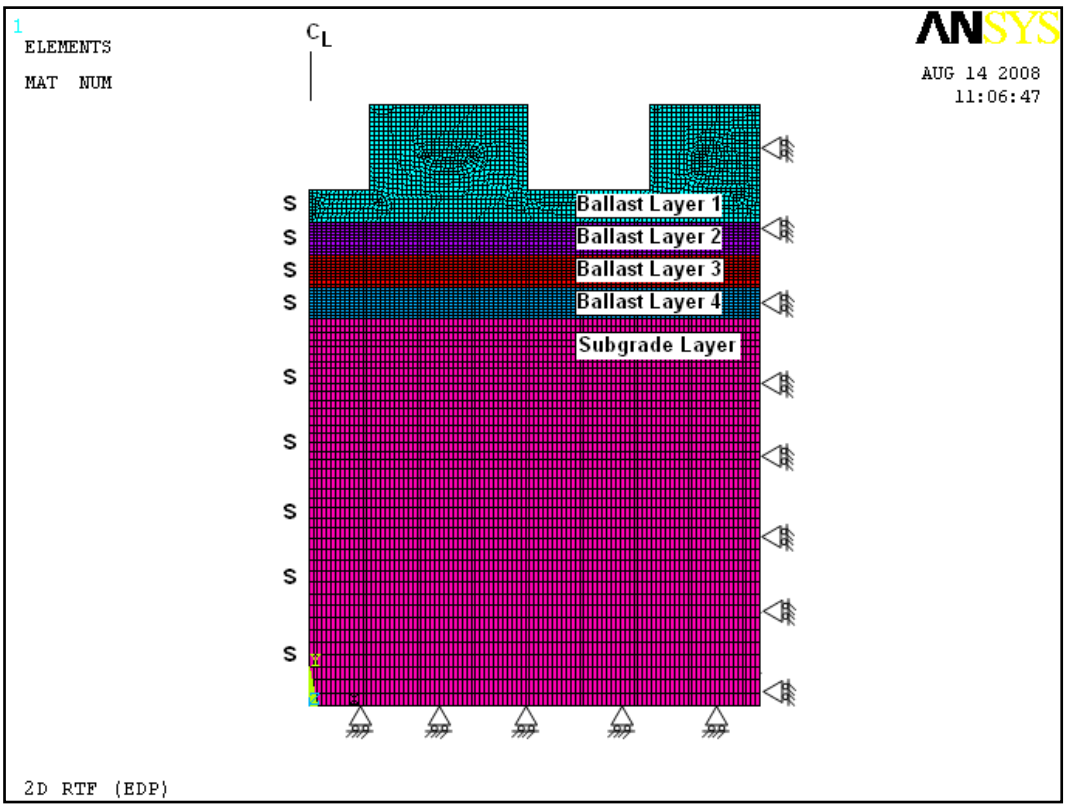

Figure 6.19 The RTF simulation model

6.5.2 Results of the RTF Modelling

Figure 6.20 shows the Y-component displacement under monotonic loading in the RTF. The ballast under the middle sleeper has the largest settlement and it decreases from the top to the bottom. In this simulation the maximum settlement in the subgrade layer is 2.31mm. The total settlement in the ballast layer is 1.678mm, which includes both the permanent and resilient settlement in the first load cycle.

Figure 6.21 shows the Y-component stress distribution in the RTF. It can be seen that the stress condition under the middle sleeper is quite similar to that in the CET. It highlights a stress concentration zone near the middle sleeper bottom corner. The maximum stress in this zone is over 200kPa. Additionally, the main vertical stress is concentrated under the sleeper and spreads downwards at a narrow angle. The stress at a depth of 50mm in the subgrade directly underneath the central sleeper is from 60kPa to 75kPa, which matches with the test results measured by the pressure cells in the RTF, as shown in Table 5.2.

Figure 6.22 shows the X-component stress distribution in the RTF. A high horizontal stress zone is seen in the top layer of ballast directly underneath the middle sleeper. Lower horizontal stress zones exist in the bottom layer of the ballast directly underneath the middle sleeper and in the top layer of ballast adjacent to the outer sleeper.

As a load of 47kN was applied at the outer sleeper position, the ballast deformation and stress under the outer sleeper were smaller than under the middle sleeper. However, compared with the CET simulation, it can be seen that the outer load pressure influences both the X and Y-component stress within the ballast underneath the middle sleeper.

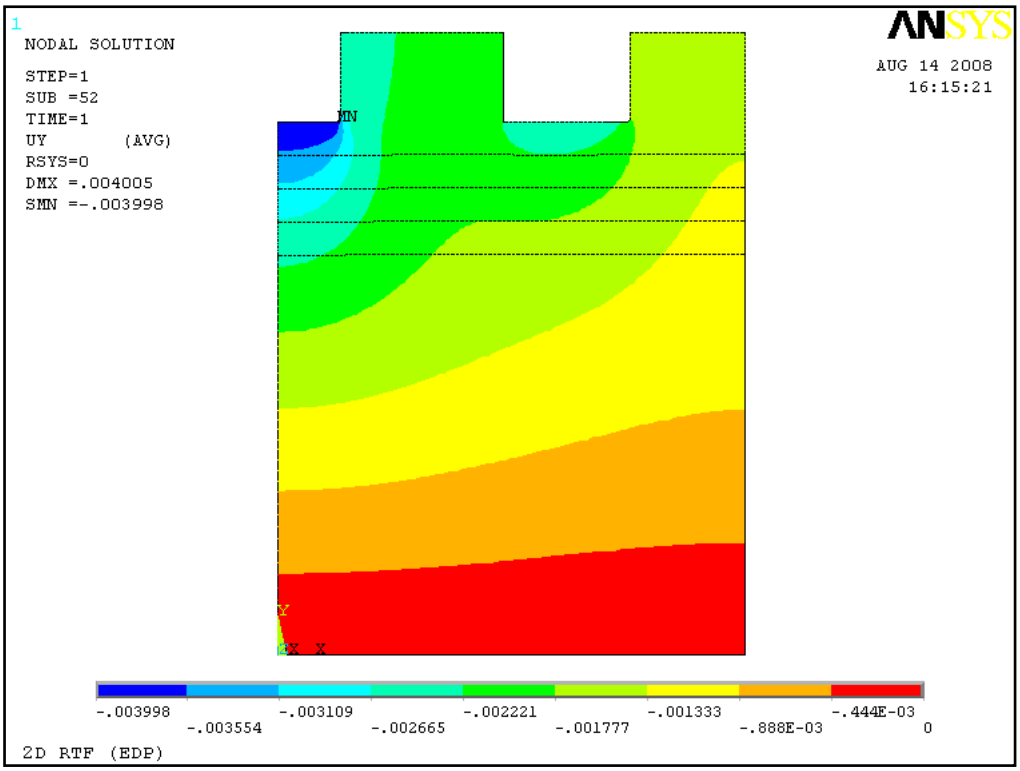

Figure 6.20 Y-component displacement in the RTF simulation (Unit: m)

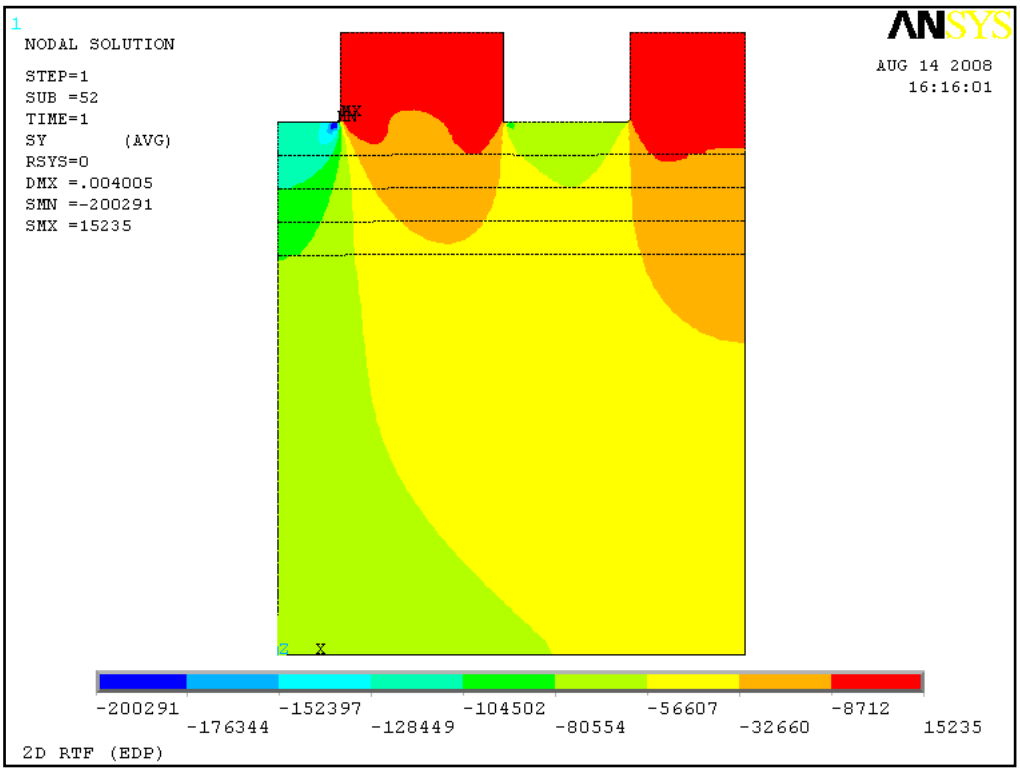

Figure 6.21 Y-component stress distribution in the RTF simulation (Unit: Pa)

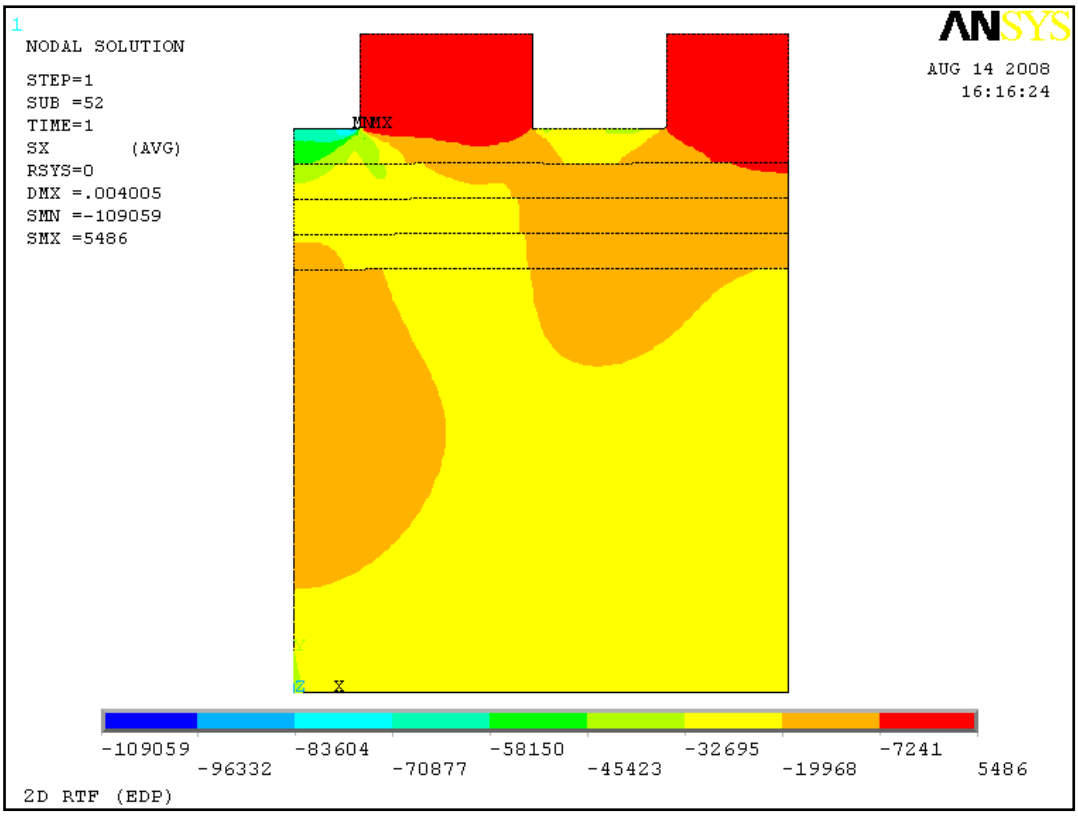

Figure 6.22 X-component stress distribution in the RTF simulation (Unit: Pa)

6.5.3 Principal Stress Rotation Analysis

In contrast to the triaxial test and the CET, the RTF represents a passing train loading over three sleepers. The cyclic loading of a passing train is achieved by applying sinusoidal loading between 4kN and 94kN with a 90° phase difference between sleeper loads, as shown in Figure 6.23. The ballast and subgrade in the RTF suffers continuous change in the direction of principal stress, which increases the accumulation of permanent strain. This effect has been investigated in a detailed finite-element study, which explores the stress field under a passing wheel load.

According to the loading in Figure 6.23, the RTF simulates the passing of wheels with a distance of 2.6m (4-sleeper spaces), as shown in Figure 6.24. Although the vertical loads are exerted by a moving wheel load, it is a common practice to carry out a static analysis in different stages. A stress analysis was performed for each incremental advance of the wheel load (17 positions in total). The loading on each sleeper at each stage was calculated and is shown in Figure 6.23. The stress analysis points were directly underneath the middle sleeper.

A series of finite element models were constructed and solved to investigate the effect of principal stress rotation. The models were constructed using 2-dimensional 4-node solid structure elements. Element type is Plane 182 in ANSYS. As the loading on the two outer sleepers were different, due to the simulation of a passing load, a full size RTF model was built, as shown in Figure 6.25. The material properties used in this model were the same as in the previous RTF simulation. Based on a series of finite element models, the major principal stress rotation, axial stress and shear stress were analysed. These results are presented in the following two sub-sections.

Major Principal Stress Rotation

In ANSYS, the three principal stresses are labeled σ_1, σ_2, and σ_3 (output quantities PRIN1, PRIN2, and PRIN3). The principal stresses are ordered, so that σ_1 (PRIN1) is the most positive (tensile) and σ_3 (PRIN3) is the most negative (compressive). The ANSYS vector plot of the three principal stresses in the RTF, when the wheel load was on the centre of the middle sleeper (Position 9), is shown in Figure 6.26. From this figure it can be seen that the maximum major principal stress occurs directly underneath the middle sleeper and spreads downwards.

Figure 6.27 shows the vector plot of major principal stress magnitudes and axis directions at five stress analysis points in the RTF at different stages. The simulated results demonstrate that as the wheel load approaches and passes over a sleeper, principal stresses increase and then decrease, as well as rotations of the principal stress axes occurring at all analysis points. The maximum principal stress at each point occurs at Position 9, where the wheel load is in the centre of the middle sleeper, and the maximum stress magnitude slightly increases from ballast Layer 1 to Layer 2 and then gradually decreases to the subgrade; this can be detected in Figure 6.26 as well.

According to the principal stress vector plot, two major principal stress rotation stages can be discerned within the ballast layer. Initial rotation occurs from wheel Position 1 to 3, as well as Positions 15 to 17 (end of rotation), where the principal stress magnitudes are relatively small and the rotation angles are large. Secondary rotation occurs from wheel Positions 4 to 14. In contrast, the principal stress magnitudes are large and the rotation angles are small. However, the evidence for separating these two stages is a weaker in the subgrade top layer than in the ballast layer. It should be noted that the major principal stress axes are horizontal at the analysis points in ballast Layer 3, Layer 4 and the subgrade top layer at wheel load Position 1. The stress axes eventually rotate 180 degrees from their original positions. However, the rotation of the principal stress axes in ballast Layer 1 and Layer 2 does not reach the horizontal.

Axial Stress and Shear Stress

Figures 6.28 (a), (b), (c), (d) and (e) show the axial stress and shear stress at the analysis points in the RTF under a passing wheel load. From this figure it can be seen that axial stress remains compressive throughout loading, while shear stress changes its sign according to the position of the loading wheel, as well as its magnitude. Accordingly, principal stress axes rotate in railway ballast during the passage of train loading.

FEM analysis was also utilised to study stress changes in the ground below ballasted railway track during train passage by Momoya and Sekine (2004) and Powrie *et al.* (2007). As both projects were only focused on the stress changes in subgrade below ballast layer, simulation results were compared with the axial and shear stress changes in the subgrade top layer of the RTF simulation shown in Figure 6.28 (e).

Momoya and Sekine (2004) introduced FEM analysis into their studies. The computational results were compared with those of scale model tests to confirm its accuracy. A linear elastic 3D FEM model was build to analyse the deformation and stress change characteristics. Figure 6.29 (a) shows the shear stress at the bottom layer of the subgrade. From this figure, it can be seen that with a fixed constraint at the bottom of the subgrade, the shear stress was greater than that resulting from the scale mode test. To simulate the shear stress properly, horizontal spring elements were introduced to decrease the shear stress at the bottom of the subgrade. When a reasonable value of spring constant was assigned to the spring elements, the FEM result agreed well with the result of the scale model test. Figure 6.29 (b) shows the vertical stresses at the bottom of subgrade. The effect of the constraint at the bottom

of the subgrade was not significant for the vertical subgrade stress. Both figures show good match with the experimental result. Compared with stress paths at the top layer of the subgrade in the simulation of the RTF (Figure 6.28 (e)), although the analysis points were at different depth in the subgrade, the vertical and shear stresses showed similar characteristics. In addition, Powrie *et al.* (2007) investigated the stress paths for a soil element at the surface of subgrade subject to train load by using an elastic material model. Similar outputs can also be found. Furthermore, they stated that these stress paths were not too sensitive to the elastic parameters.

Studies by Ishikawa and Sekine (2007) have shown that principal stress rotation effects could contribute to the development of permanent strain accumulation. Furthermore, their results revealed that cumulative axial strain obtained from a moving load shear test (which included principal stress rotation) could be estimated from accumulative axial strain from a fixed load shear test (without principal stress rotation) by using a ratio of axial strain. The ratio was related to the maximum shear and normal stresses, which will be discussed in Chapter 7.

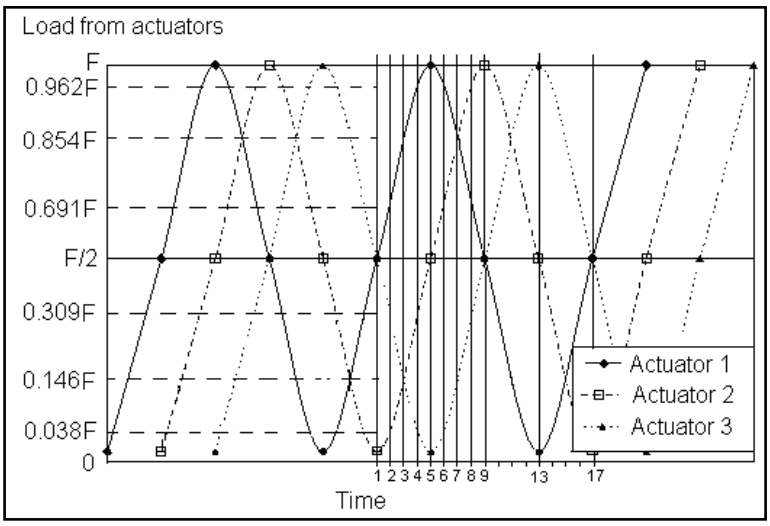

Figure 6.23 Wheel loading on each sleeper at different stages in the RTF

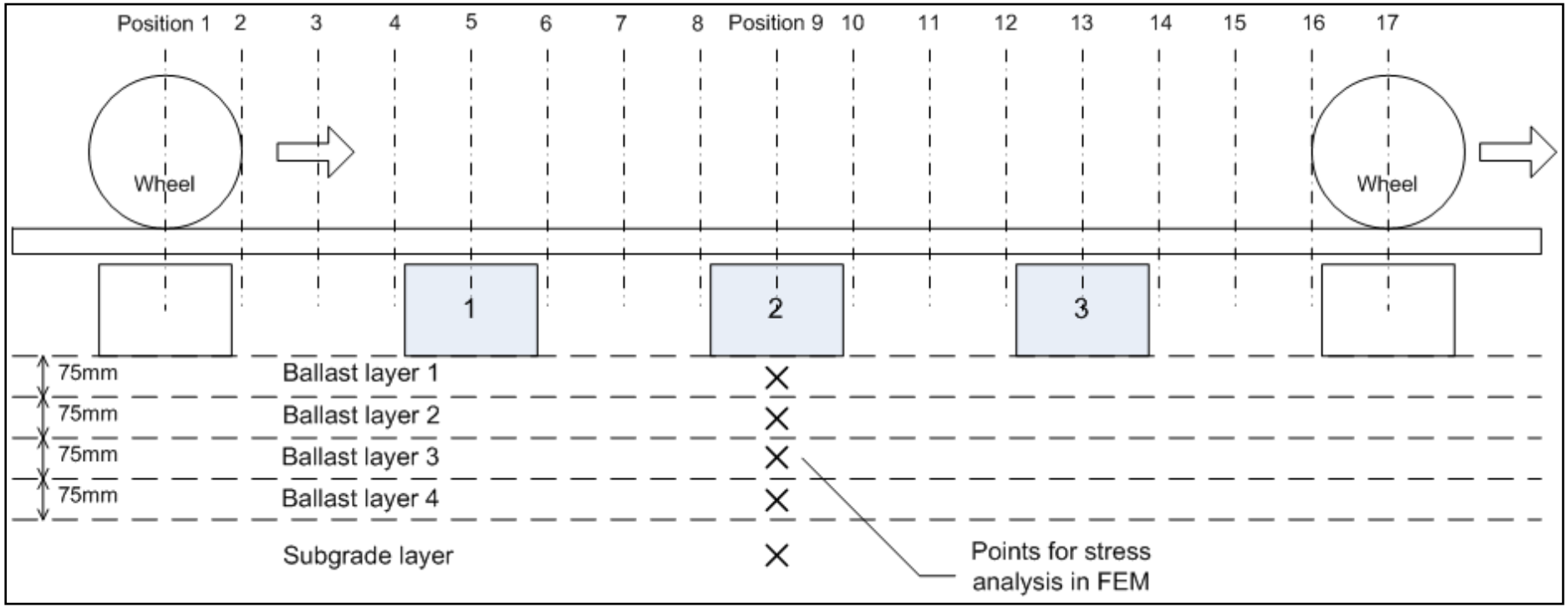

Figure 6.24 Calculation points under moving wheel loading

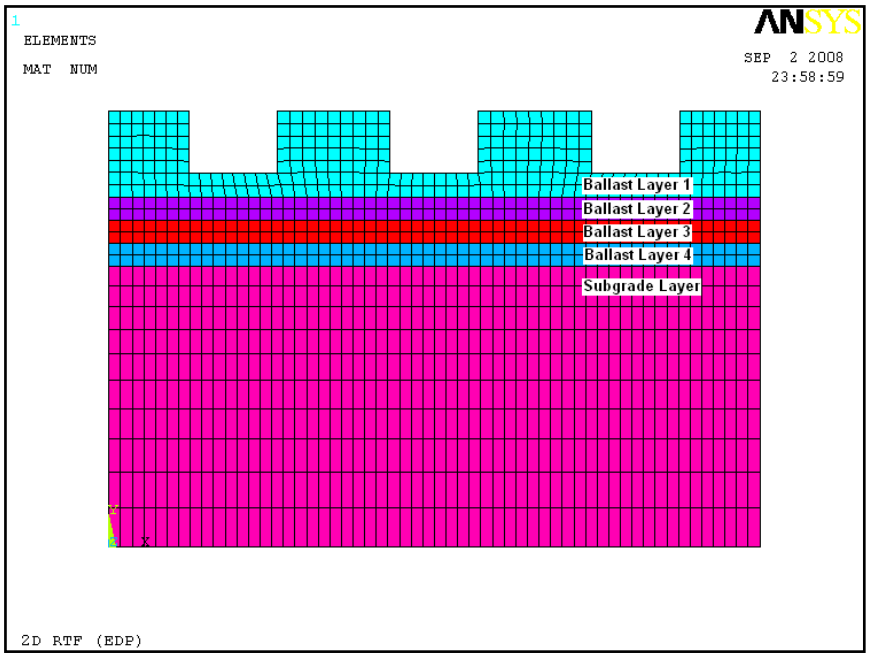

Figure 6.25 RTF simulation model for principal stress rotation analysis

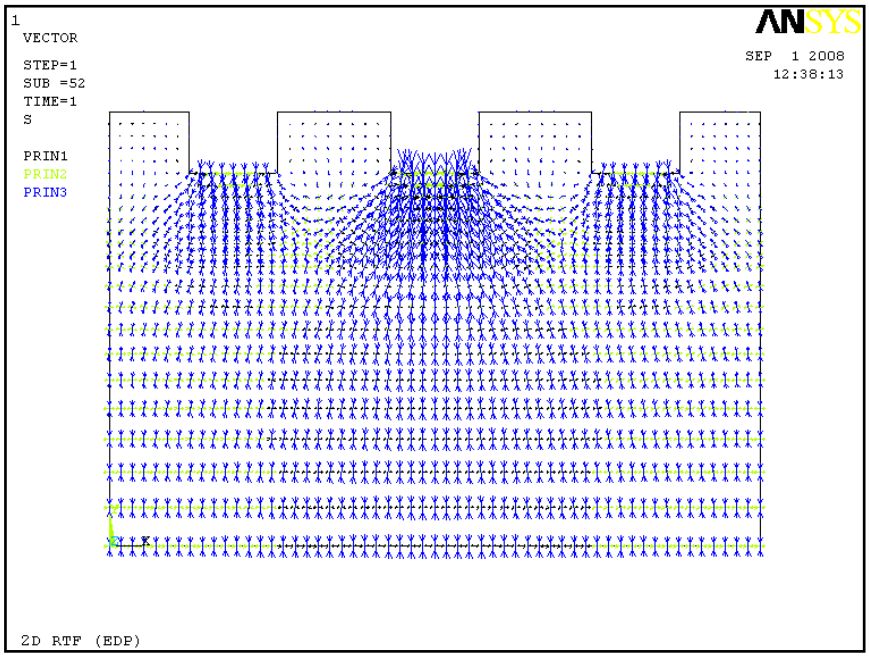

Figure 6.26 Vector plot of principal stress in RTF when wheel load was right on the centre sleeper

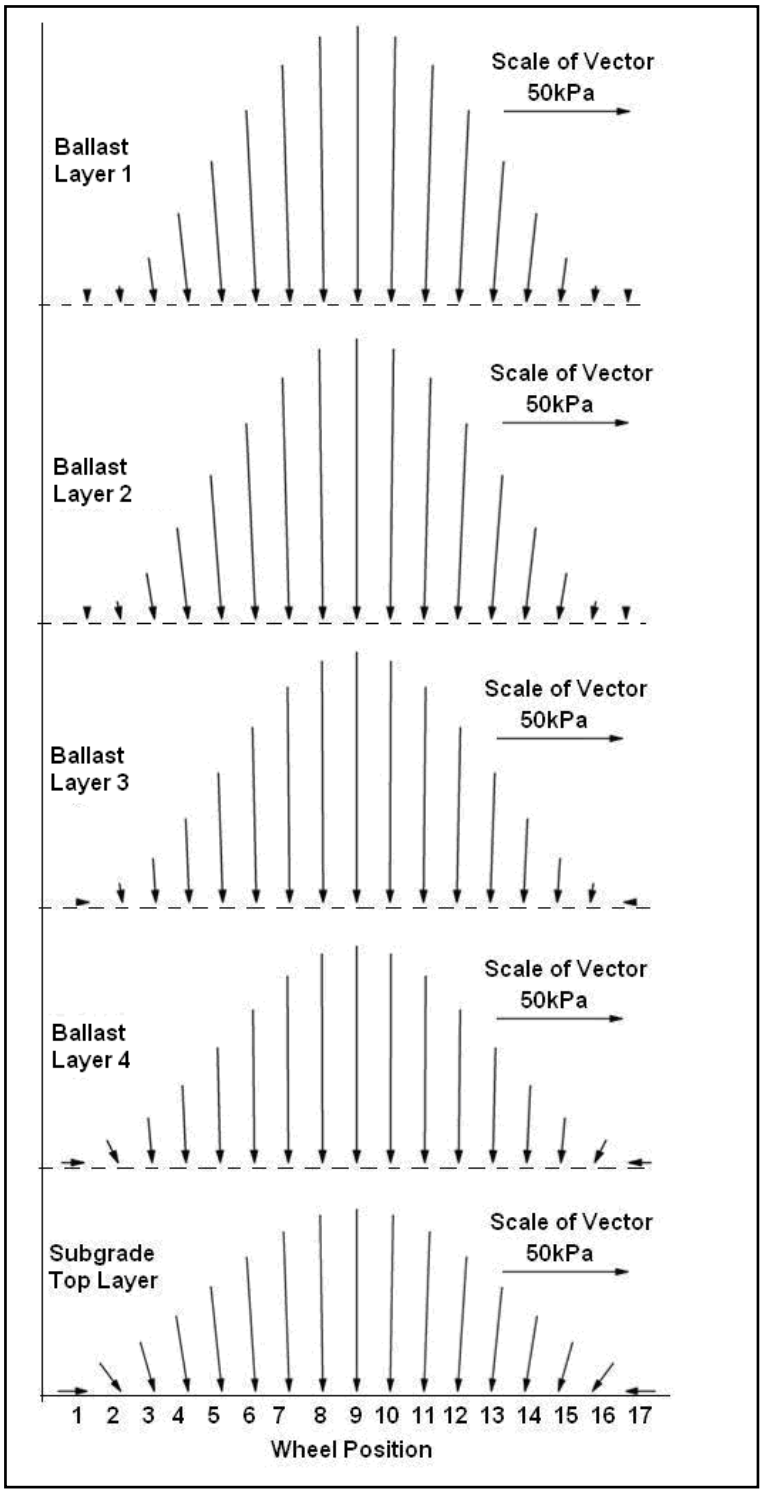

Figure 6.27 Major principal stress development in different analysis points under a moving wheel load

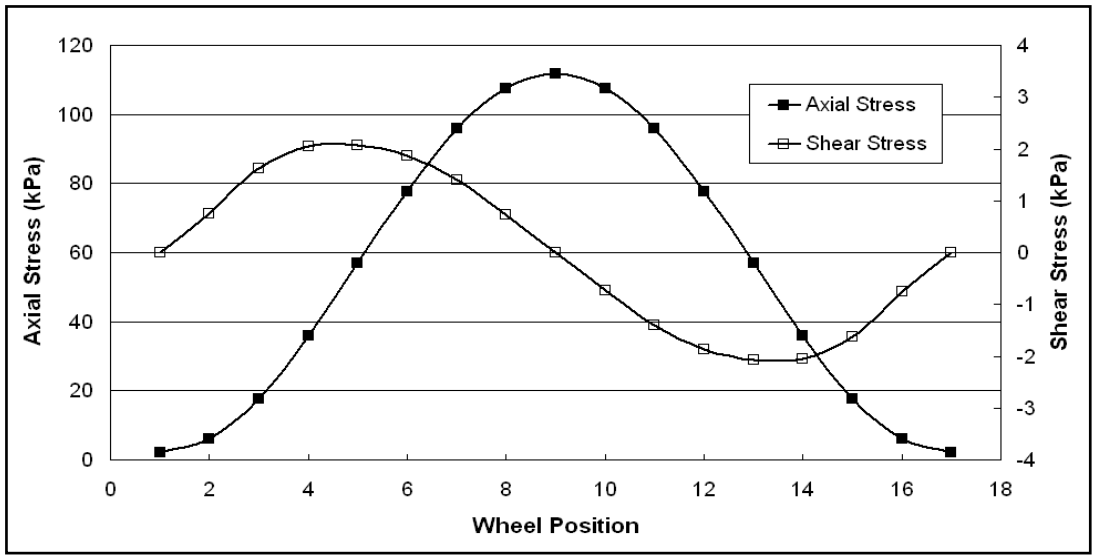

Figure 6.28 (a) Axial and shear stresses at the analysis point in ballast Layer 1 under a moving load

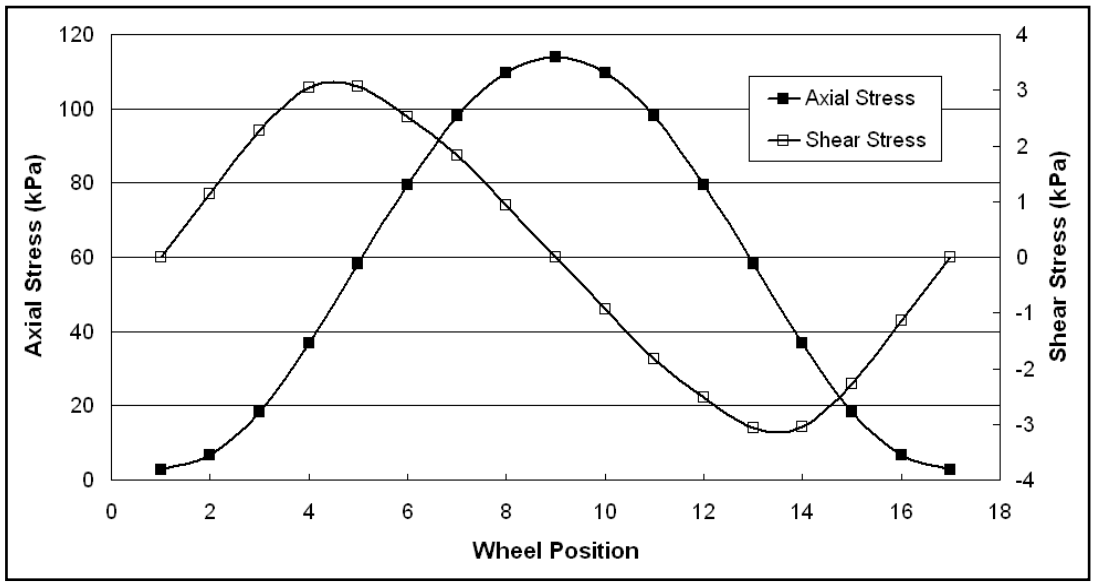

Figure 6.28 (b) Axial and shear stresses at the analysis point in ballast Layer 2 under a moving load

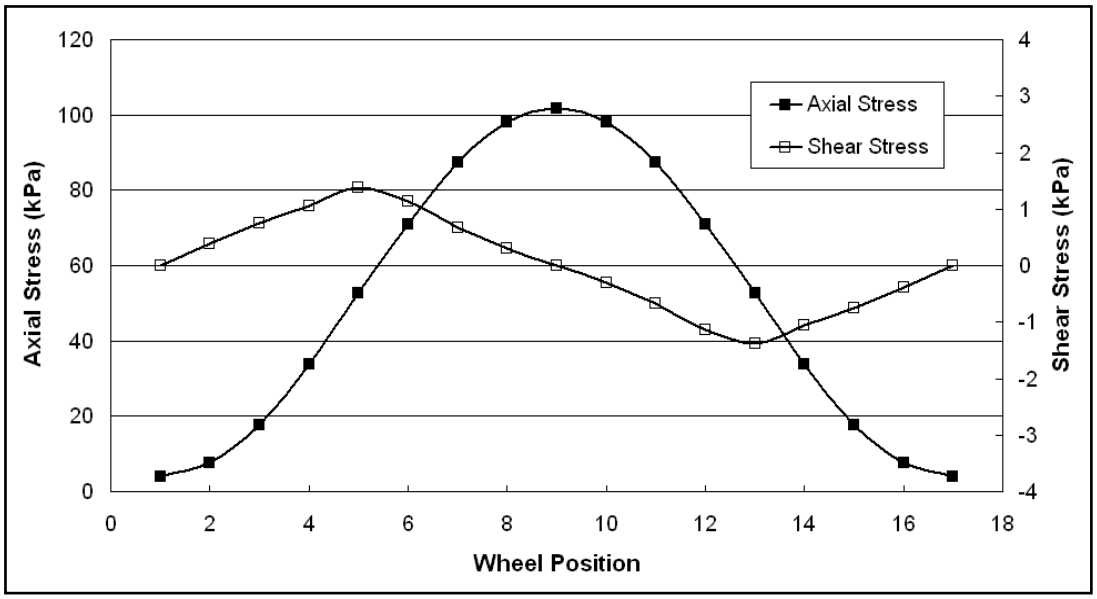

Figure 6.28 (c) Axial and shear stresses at the analysis point in ballast Layer 3 under a moving load

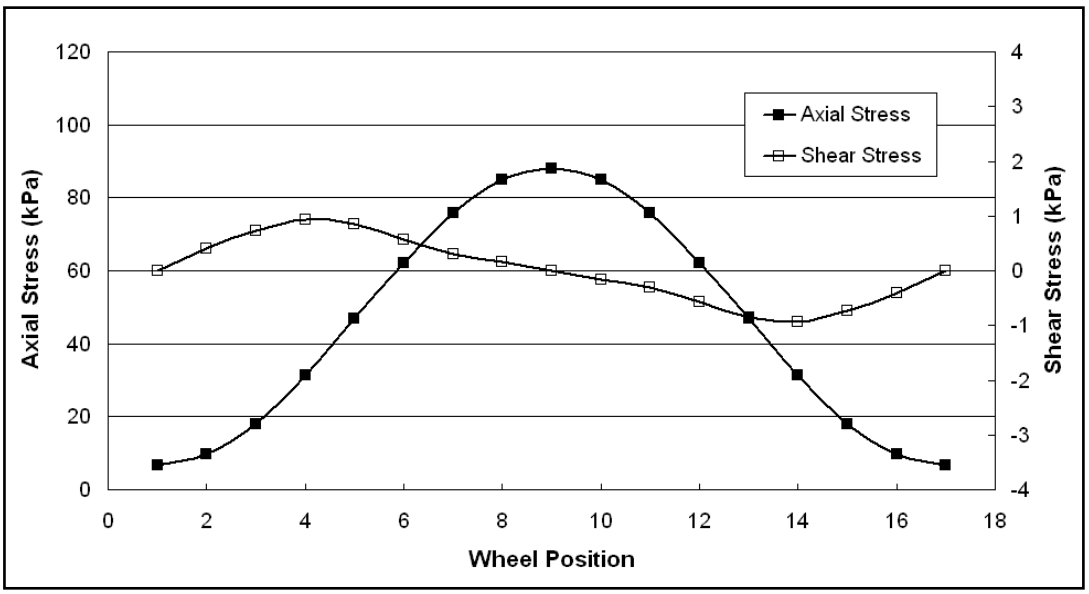

Figure 6.28 (d) Axial and shear stresses at the analysis point in ballast Layer 4 under a moving load

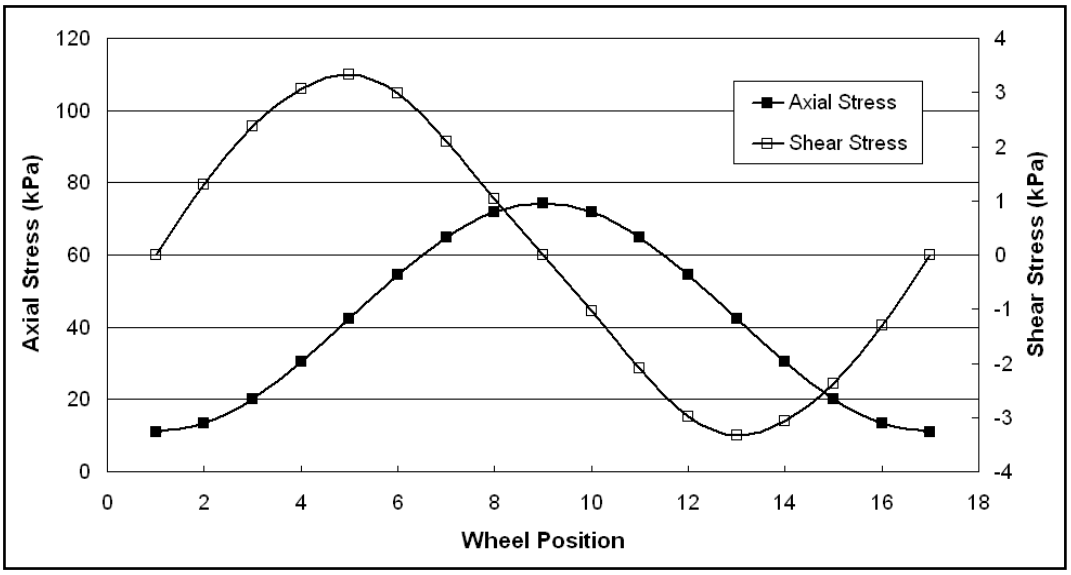

Figure 6.28 (e) Axial and shear stresses at the analysis point in subgrade layer under a moving load

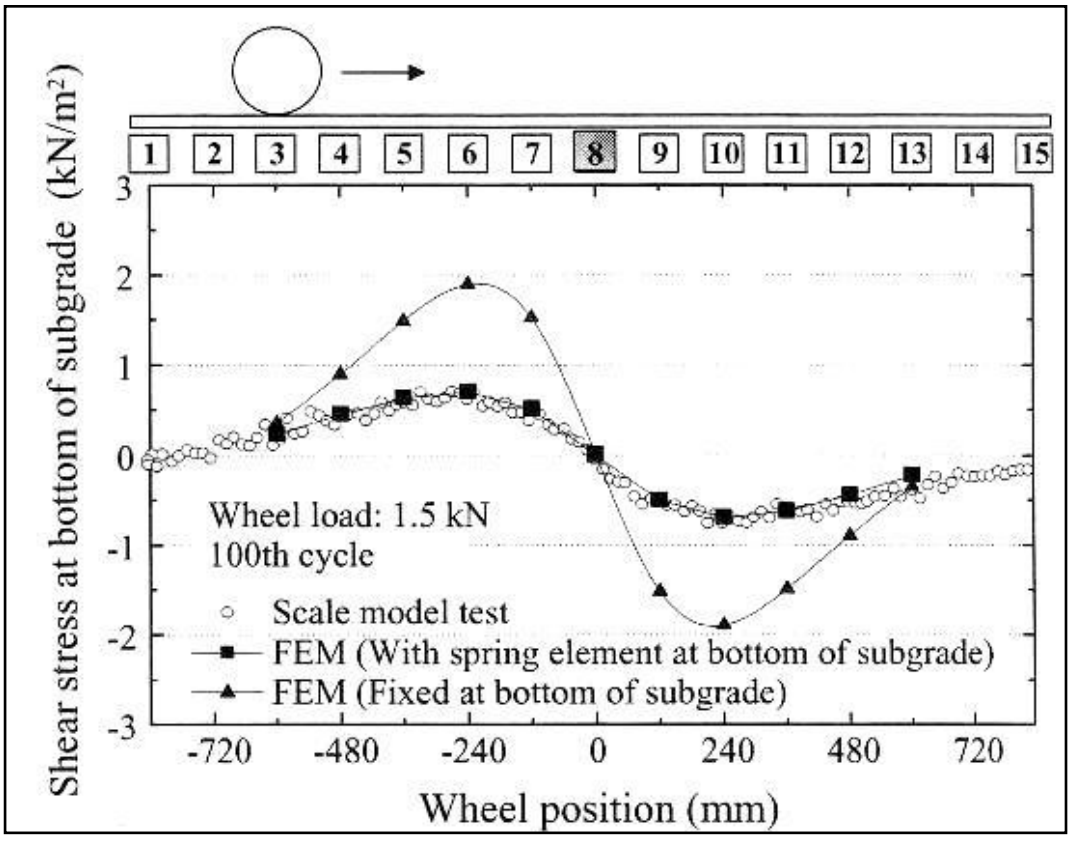

Figure 6.29 (a) Shear stress at bottom of subgrade (Momoya and Sekine (2004))

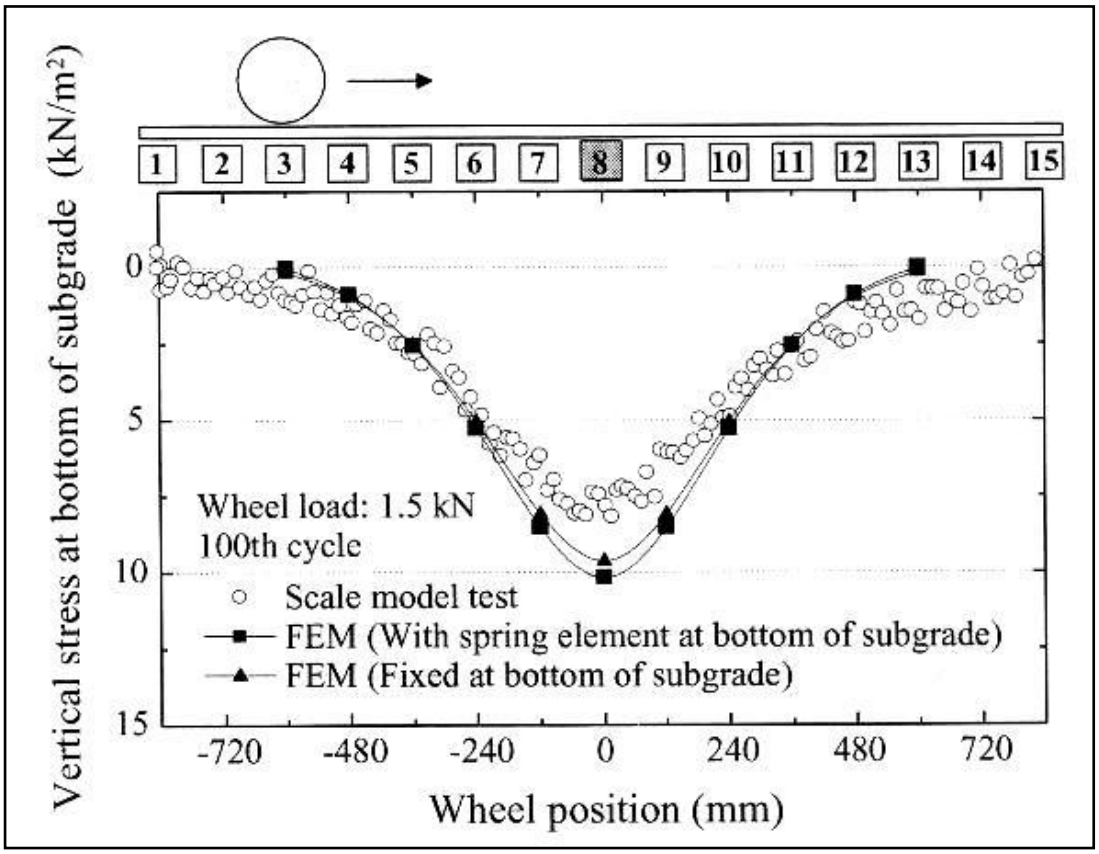

Figure 6.29 (b) Vertical stress at bottom of subgrade (Momoya and Sekine (2004))

6.6 Chapter Summary and Discussion

The permanent deformation of railway ballast is complicated under cyclic wheel load, as large plastic deformation and degradation usually happen in the process. The numerical analysis method used herein is not capable of simulating the plastic deformation accumulation and degradation under cyclic load. However, the FEM analysis provides the information to predict railway ballast deformation in terms of

stress distribution under wheel loading. The predicted stress distribution could be used in combination with settlement equations to predict railway track permanent deformation. The development of settlement equations will be discussed in Chapter 7.

The prediction of ballast stress conditions has been accomplished utilising material models readily available in the commercial finite element program ANSYS. In the initial modelling, the box test was simulated to investigate the ballast response under monotonic loading with an elastic material model. However, it was found that the use of a linear elastic material model was not sufficient to simulate ballast behaviour. Then, the Drucker-Prager model was used to simulate the non-elastic ballast behaviour in triaxial tests. As the Drucker-Prager model was an elastic perfect-plastic model, the simulated results were still far from satisfactory. Therefore, a more detailed analysis using the extended Drucker-Prager model with hardening was carried out. Before the simulation of the CET and the RTF, the triaxial monotonic tests were simulated first to find out the appropriate input material parameters for the CET and RTF simulations. Compared with the Drucker-Prager material model, the extended Drucker-Prager model showed a much better match with the monotonic triaxial test results. Eventually, FEM simulation of the CET and the RTF were carried out to investigate stress distributions. It was found that both vertical and horizontal stresses were concentrated underneath the sleeper in the CET and the RTF. The stress distribution under the central sleeper in the RTF was affected by the loads from the outer sleepers as well.

Besides the simulation of the horizontal and vertical stress distributions in the CET and the RTF, the principal stress at depth increments underneath the middle sleeper of the RTF was obtained from the FEM simulation to analyse the effect of principal stress rotation on permanent deformation. Continuous change in both principal stress magnitudes and rotation was shown by the simulation of a passing wheel load. This continuous rotation of principal stress may have a certain effect on ballast permanent deformation.

CHAPTER 7

7. RAILWAY SETTLEMENT MODEL

7.1 Introduction

After the experiments, another important part of this research concerns fitting settlement equations to the experimental results. A series of settlement equations were derived from the triaxial test results. These equations were then validated and improved by the test results from both the Composite Element Test (CET) and the Railway Test Facility (RTF).

Before the settlement equations' derivation, the multi-stage triaxial test results (with an increasing maximum stress ratio in each test) were transformed to equivalent normal cyclic loading triaxial test results (with a constant maximum stress ratio in each test) to extend the range of stress ratios. Then, settlement equations were derived to match the triaxial test results.

The permanent deformation of ballast has been calculated by the combination of finite element method (FEM) analysis and the settlement equations. The FEM analysis computes the stress distribution within the ballast. The settlement equations allow calculation of the permanent deformation of the ballast under different stress conditions after a certain number of load cycles. Apart from the static stress distribution analysis, principal stress rotation is considered as another important effect on permanent deformation accumulation. In the following sections, the settlement equation development and the settlement model verification are described in detail.

7.2 Settlement Equation Development

The settlement equations have been developed based on the ballast cyclic triaxial tests. The settlement results show a high dependence on stress levels, which is characterised by confining pressure (σ_3) and maximum stress ratio ($(q/p)_{max}$). However, the normal cyclic triaxial tests (with a constant maximum stress ratio in each test) were only carried out at stress ratios of 1.7 and 2.0. In order to cover a wider range of stress conditions, the multi-stage triaxial test results (with an increasing maximum stress ratio in each test) were used to supplement the normal cyclic loading triaxial test results.

7.2.1 Multi-stage Triaxial Test Results

First of all, an assumption was made before the analysis of multi-stage triaxial test results. The effect of a certain number of load applications in lower stress conditions on permanent deformation accumulation can be equivalent to a smaller number of load cycles in higher stress conditions. As detailed in Table 3.1, a total of 3 multi-stage triaxial tests were carried out. The cell pressure in test T3-10m was 10kPa; the maximum stress ratio increased in four different stages with values of 1.7, 2.0, 2.1 and 2.2 respectively. The test results with maximum stress ratios of 2.1 and 2.2 were not used in the normal cyclic triaxial tests (i.e. triaxial test series T2). It is therefore desirable to transform the multi-stage test results at stress ratios of 2.1 and 2.2 to equivalent results under normal cyclic loading conditions. The principle of this transformation is that the effect of 10,000 load cycles in Stage 1 (with $(q/p)_{max}$=1.7) and 10,000 load cycles in Stage 2 (with $(q/p)_{max}$=2.0) on permanent deformation accumulation in the multi-stage triaxial test is considered to be equivalent to a certain number of pre-load cycles in Stage 3 (with $(q/p)_{max}$=2.1). Furthermore, the effect of 10,000 load cycles in Stage 1, 10,000 load cycles in Stage 2 and 10,000 load cycles in Stage 3 is considered to be equivalent to a certain number of pre-load cycles in Stage 4 (with $(q/p)_{max}$=2.2).

In a similar way, the effect on ballast permanent deformation of the first stage (with $(q/p)_{max}$=1.7) and second stage (with $(q/p)_{max}$=2.0) in the multi-stage triaxial test T3-30m is considered to be equivalent to a certain number of pre-load cycles in Stage 3 (with $(q/p)_{max}$=2.1). As the specimen reached failure at the very beginning of the fourth stage (with $(q/p)_{max}$=2.2) in test T3-30m, no transformation is possible for this stage. During test T30-60m, the specimen failed during the third stage (with $(q/p)_{max}$=2.1). Therefore, cyclic triaxial test results with a cell pressure of 60kPa were only available with maximum stress ratios of 1.7 and 2.0.

In order to calculate the equivalent number of cycles, the available multi-stage triaxial test results were plotted in a figure with a coordinate system of $d(number\ of\ cycles,\ N)/d(permanent\ axial\ strain,\ \varepsilon_a)$ against the permanent axial strain (ε_a), as shown in Figure 7.1. The area under every curve is then equal to the number of cycles that have occurred during the test, and in order to determine the equivalent number of cycles from zero strain, each curve is extended to pass through the origin. Therefore, the areas under the extended parts of the curves give estimated equivalent numbers of pre-load cycles.

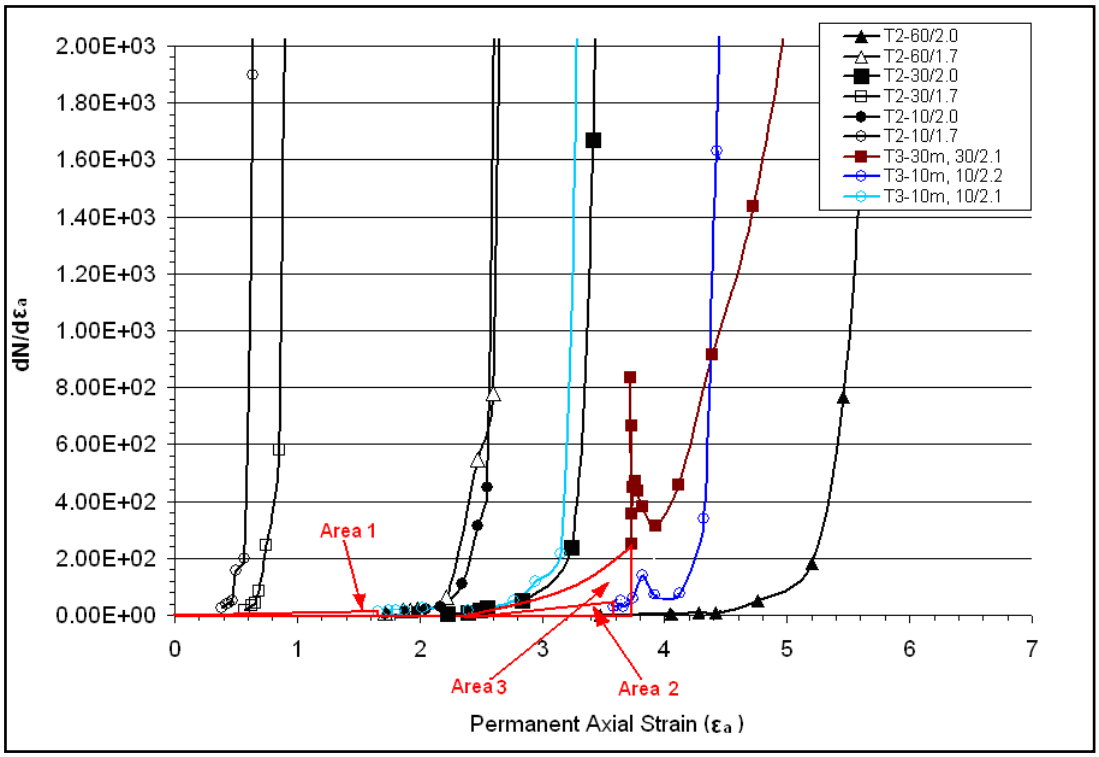

Figure 7.1 Calculation of pre-load cycles for the multi-stage triaxial tests

In Figure 7.1, Areas 1 and 2 give pre-load cycle numbers for Stage 3 (with $(q/p)_{max}$=2.1) and Stage 4 (with $(q/p)_{max}$=2.1) respectively in triaxial test T3-10m. Area 3 gives pre-load cycle numbers for Stage 3 (with $(q/p)_{max}$=2.1) in test T3-30m. From these areas, the resulting pre-load effect of Stages 1 and 2 in test T3-10m is estimated as 7 pre-cycles in Stage 3. And the effect of the first three stages in test T3-10m is estimated as 20 pre-cycles in Stage 4. The pre-load effect of Stages 1 and 2 in test T3-30m is estimated as 135 pre-cycles in Stage 3.

Figure 7.2 shows the permanent axial strain against number of load cycles for all the cyclic triaxial tests including the transformed results from the multi-stage triaxial

tests. It can be seen that when the maximum stress ratios approach failure conditions, the accumulation rates of permanent axial strain are significantly increased. However, it should be noted that because of errors in the method of calculating the pre-load cycles, lines are crossing in Figure 7.2.

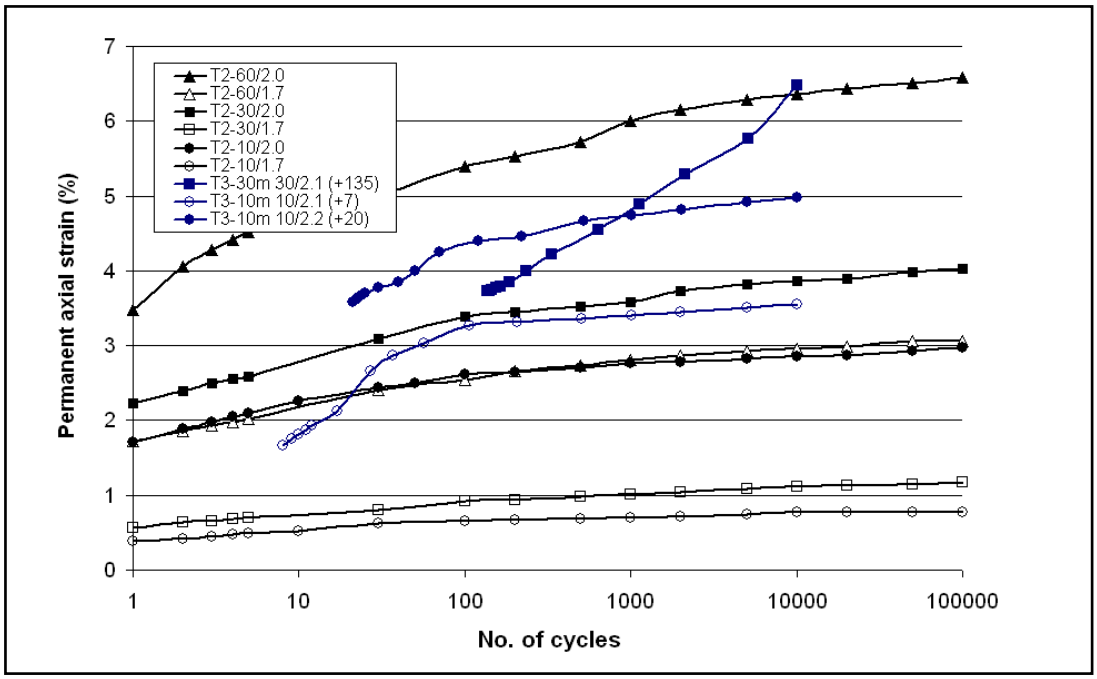

Figure 7.2 Permanent axial strain of all the cyclic triaxial tests vs. number of cycles on logarithmic scale

7.2.2 Settlement Equation Derivation

Various equations were considered to represent the ballast permanent deformation behaviour, in particular those that use stress conditions as parameters. The ideal settlement equation should be able to predict the permanent deformation as a function of stress level, trackbed quality and number of load cycles, and be easy to use for railway track design. From analysis of the triaxial test results, it was found that when the ballast permanent deformation is plotted in a coordinate system of permanent axial strain accumulation rate ($d\varepsilon_a/dN$) against number of load cycles (N) on logarithmic scales, the plotted curves are approximately straight lines, as shown in Figures 7.3 and 7.4. Figure 7.3 shows the axial strain accumulation rate against number of load cycles with different maximum stress ratios at cell pressures of 10kPa, 30kPa and 60kPa. Figure 7.4 shows the axial strain accumulation rate against number of load cycles at different confining pressures with maximum stress ratios of 1.7, 2.0 and 2.1. Therefore, a linear relationship between $\log(d\varepsilon_a/dN)$ and $\log N$ can be written in the form below:

$$\log\frac{d\varepsilon_a}{dN} = A - B\log N \qquad \text{(Equation 7.1)}$$

where A and B are the coefficients. A controls the intercepts of these lines, B is the gradient.

From Figure 7.3, it can be seen that the axial strain accumulation rate decreases with the number of load cycles, and increases with increasing maximum stress ratio at a

given confining pressure. Figure 7.4 shows that the axial strain accumulation rate increases with increasing confining pressure when the maximum stress ratio remains the same. Therefore, coefficient *A* in Equation 7.1 depends on both the confining pressure (σ_3') and the maximum stress ratio ($(q/p')_{max}$).

By integrating Equation 7.1, the following equation of permanent axial strain (ε_a) can be obtained:

$$\varepsilon_a = \frac{10^A}{1-B} N^{1-B} + C \qquad \text{(Equation 7.2)}$$

where *C* is a constant from integration.

In Equation 7.2, when the number of load cycles (*N*) equals zero, the permanent axial strain (ε_a) should be zero as well. Therefore, the constant *C* can be deleted, and Equation 7.2 becomes:

$$\varepsilon_a = \frac{10^A}{1-B} N^{1-B} \qquad \text{(Equation 7.3)}$$

In order to make Equation 7.3 easy to analyse, it is simplified to:

$$\varepsilon_a = k \cdot N^c \qquad \text{(Equation 7.4)}$$

In Equation 7.4, the permanent axial strain (ε_a) after the first cycle equals *k*. Hettler (1984) suggested the initial settlement might be a non-linear function of the

amplitude of the load and a scaling factor, given in the form of Equation 2.11. From the triaxial test results, *k* can be estimated by:

$$k = s \cdot F^{(q/p')_{\max}} + b \qquad \text{(Equation 7.5)}$$

where,

s is a scaling factor, and recommended as: $s = 5 \times 10^{-6}$,

F is a coefficient related to confining pressure, $F = 5 \times \sigma_3' + 400$ (Unit of σ_3': kPa),

$(q/p')_{\max}$ is the maximum stress ratio,

b is a coefficient related to confining pressure and defined as: $b = 0.008 \times 1.08^{\sigma_3'} + 0.48$ (Unit of σ_3': kPa).

In Equation 7.4, $c = 1 - B$, and parameter *B* is the gradient of the curves in Figures 7.3 and 7.4. However, only a slight gradient difference can be detected between these curves. It is suggested that the gradient only becomes sensitive when the maximum stress ratio ($(q/p')_{\max}$) is approaching the peak stress ratio ($(q/p')_p$). For this reason, the peak stress ratio is introduced into the expression for c. According to the computer simulation of the CET and the RTF, there are stress concentration zones underneath the sleeper bottom corners. The maximum stress ratios at these positions theoretically exceed peak stress conditions. In order to apply the settlement equations in practical situations, these equations should therefore be able to cover the conditions in which that stress ratio equals or exceeds failure.

Therefore, it is suggested that parameter c is given by an expression of the form:

$$c = 10^{-9} \times (2 \times 10^{7})\text{^}((q/p')_{\max}/(q/p')_{p}) + 0.05 \qquad \text{(Equation 7.6)}$$

where,

$(q/p')_{\max}$ is the maximum calculated stress ratio,

$(q/p')_{p}$ is the peak stress ratio.

In summary, the permanent axial strain after a certain number of load cycles can be estimated as:

$$\varepsilon_a = (5 \times 10^{-6} \times (5 \times \sigma_3' + 400)^{(q/p')_{\max}} + 0.008 \times 1.08^{\sigma_3'} + 0.48) \times N^{10^{-9} \times (2 \times 10^{7})\text{^}((q/p')_{\max}/(q/p')_{p}) + 0.05} \qquad \text{(Equation 7.7)}$$

where the peak stress ratio ($(q/p')_p$) could be derived from the monotonic triaxial tests results, and is of the from:

$$(q/p')_p = (2.6 - 0.14 \times \ln \sigma_3') \times C_r \qquad \text{(Equation 7.8)}$$

where,

σ_3' is the cell pressure (Unit: kPa),

C_r is a compaction ratio.

Thom (1988) indicated that the effect of compaction on the principal stress ratio (σ_v/σ_h) at failure was dominant, but that the effect with more uniform gradings tended to be weaker than with continuous gradings. Figure 7.5 shows the principal

stress ratios at failure for different compaction levels as well as gradings. The grading parameter (n) in Figure 7.5 was used in the experiment to define the particle size distribution of each sample as show in Figure 2.14(b). Three compaction methods were used in Thom's (1988) experimental tests including heavy compaction, light compaction and uncompacted. The compactive effect was controlled manually. After calculation, the average failure stress ratio in Figure 7.5 for heavy compaction was 2.24; 2.04 in light compaction; and 1.85 in uncompacted condition. Hence, these failure stress ratios were introduced as a guide line to modify the peak stress ratio as a function of the different compaction methods. It should be noted that failure stress ratios were utilised in Thom's (1988) experimental tests, which, however, are not equal to the perk stress ratios. Hence, the correct values of compaction ratio with different compaction method can only be acquired in the comparison experimental tests, which will be recommended for the future study. As different compaction methods have been used for the different experiments in this project, a compaction ratio (C_r) has been used to modify the peak stress ratio ($(q/p')_p$). The compaction ratio for the triaxial test samples has been set to 1. The peak stress ratios from the triaxial test results and the prediction of Equation 7.8 are shown in Figure 7.6. The compaction ratios for the CET and the RTF depend on the different sample preparation methods. In the triaxial tests, the ballast samples were compacted in three layers with equal thickness of 150mm. Each layer was vibrated for 10 seconds on a vibration table. However, light compaction was used in the CET. An electrical vibro-tamper was used to apply 5 seconds vibration in each location on the ballast

surface. With reference to Figure 7.5, C_r = 0.9 is used here as the compaction ratio for the prediction of permanent deformation in the CET. In the RTF, ballast was placed over the geosynthetic and compacted at a thickness of 100mm, 200mm and 300mm by a plate vibrator for 5 seconds at each location. The compaction is greater than CET but less than the triaxial tests. Thus, a compaction ratio of $C_r = 0.94$ is used as the peak stress ratio for modification of the prediction of permanent deformation in the RTF.

Finally, the correlation of permanent deformation strain (ε_a) under cyclic loading between the triaxial test results and the prediction is demonstrated in Figures 7.7 and 7.8. The predicted results show a broad match with the test results. While some difference can still be detected in high stress ratio conditions, this is because the settlement equations are intended to cover stress conditions both before and after theoretically failure. Therefore, it is expected that there are some errors, as the predicted permanent strain increases quicker than the test results when the stress ratio is approaching the peak stress conditions. The permanent deformation will be calculated from the settlement equations applied to the stress conditions simulated in the FEM analysis, which is discussed in following sections.

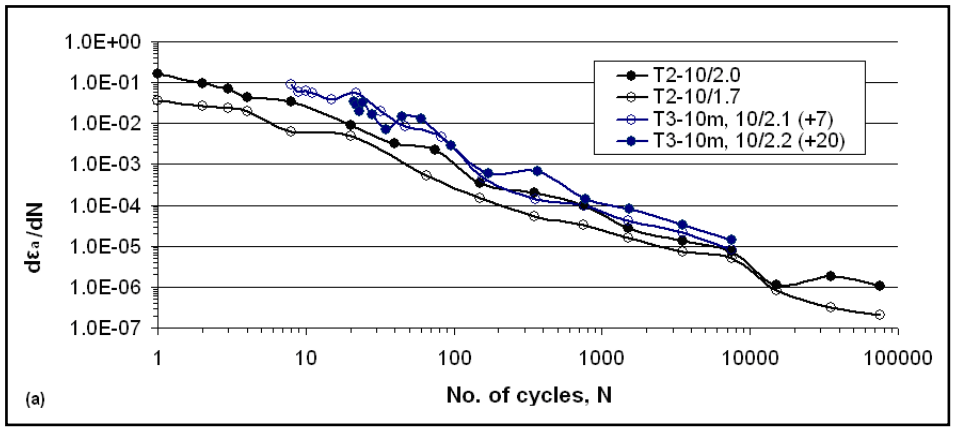

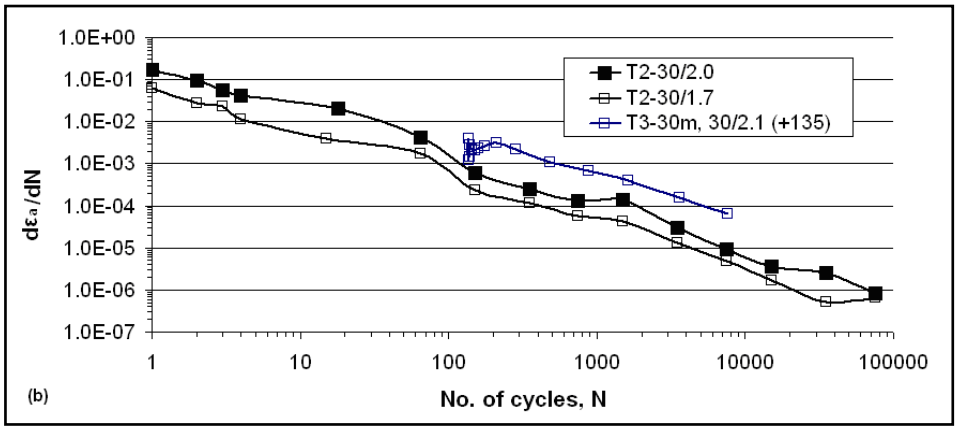

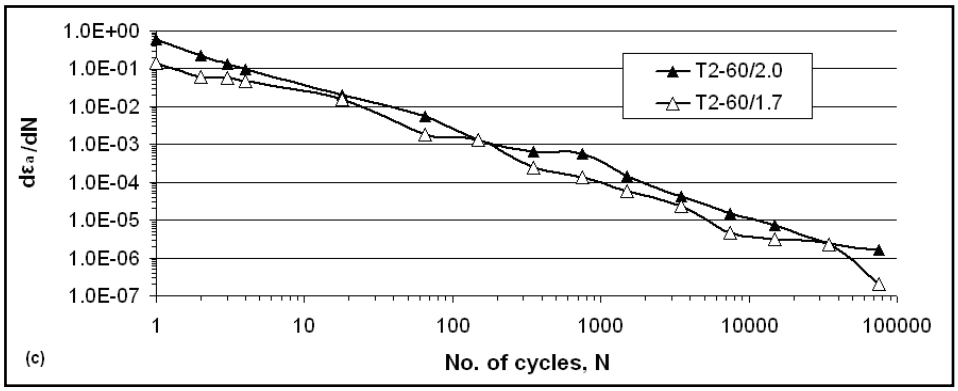

Figure 7.3 Axial strain accumulation rates against number of cycles in different maximum stress ratios, (a) with a cell pressure of 10kPa, (b) with a cell pressure of 30kPa, (c) with a cell pressure of 60kPa.

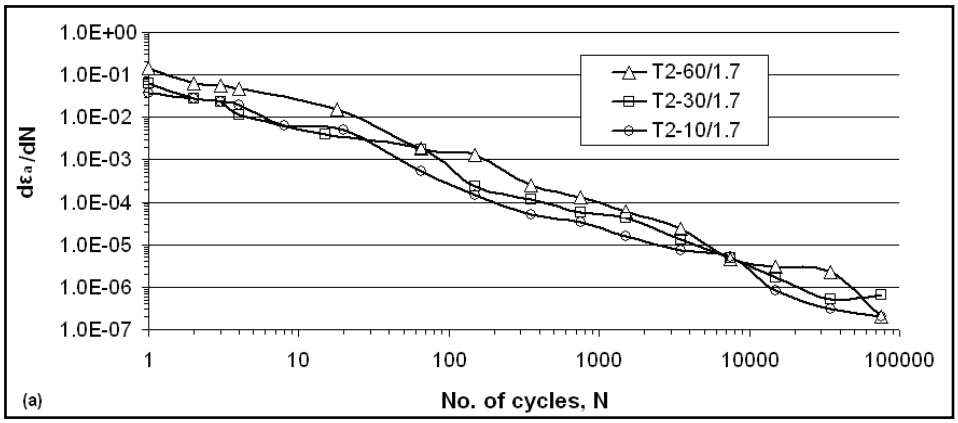

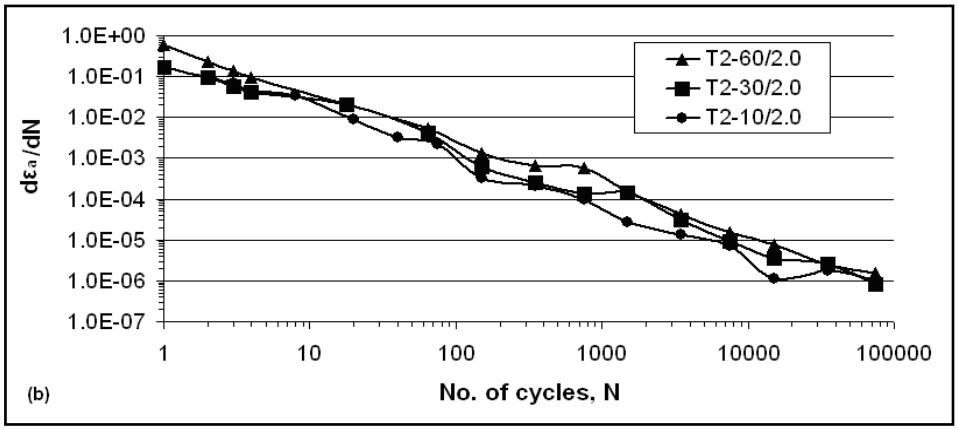

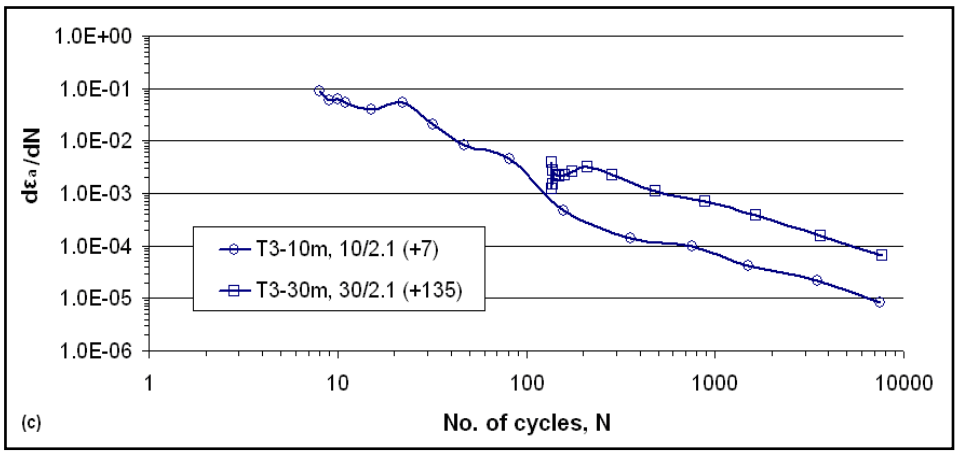

Figure 7.4 Axial strain accumulation rates against number of cycles in different confining pressures, (a) with a maximum stress ratio of 1.7, (b) with a maximum stress ratio of 2.0 (c) with a maximum stress ratio of 2.1

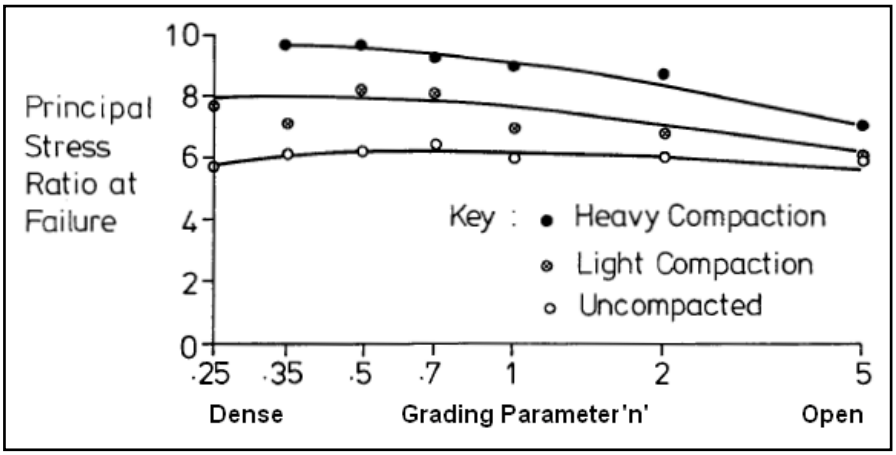

Figure 7.5 Principal stress ratios at failure for different compactions as well as grading (Thom, 1988)

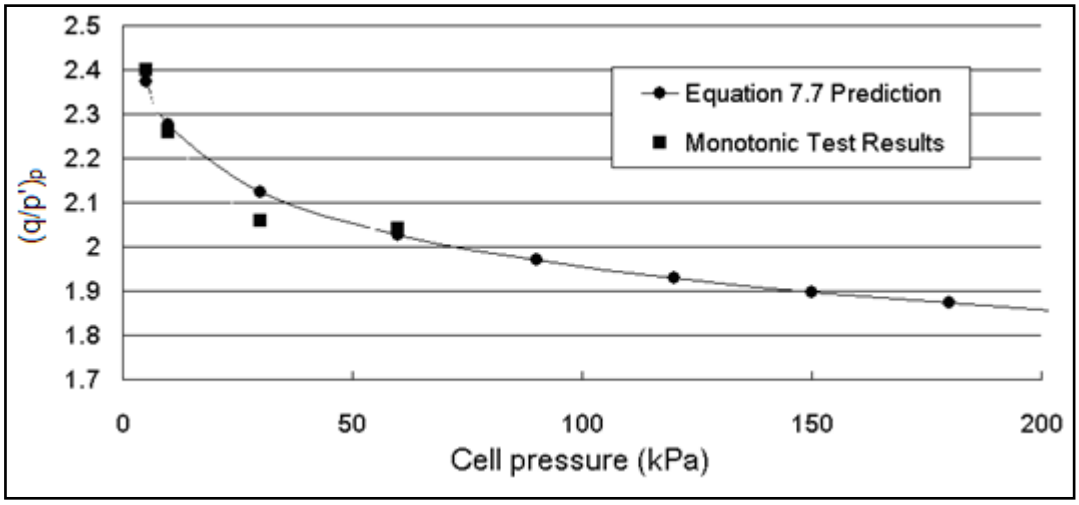

Figure 7.6 Correlation between measured (from the triaxial tests) and predicted (from Equation 7.8) peak stress ratios ($(q/p')_p$)

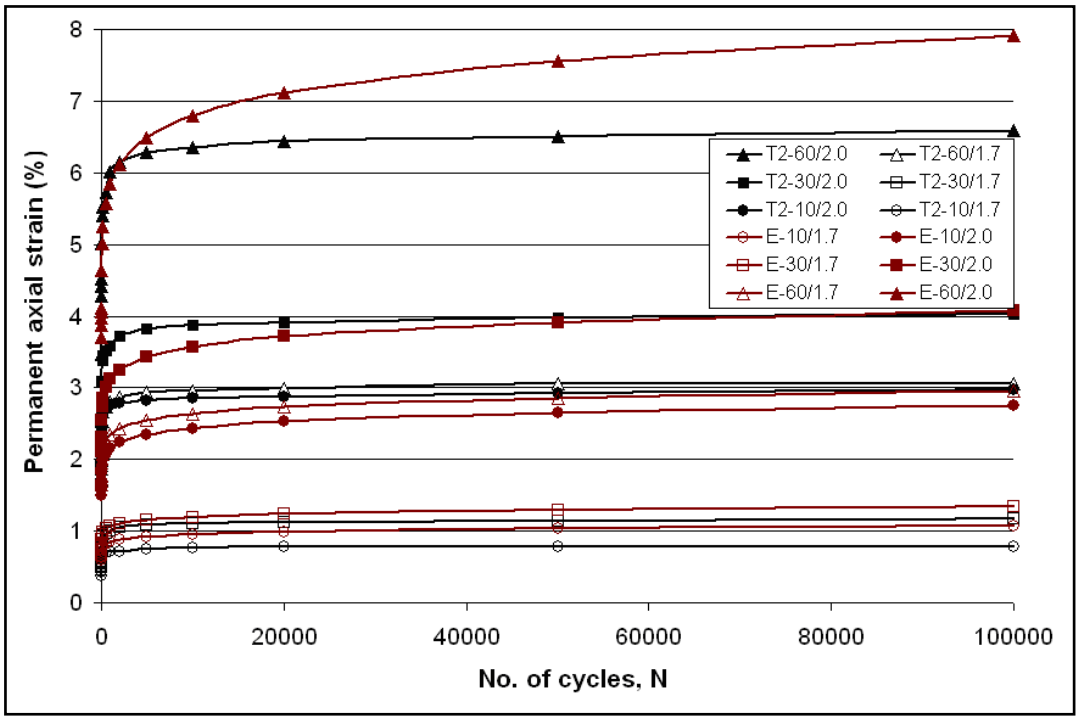

Figure 7.7 Correlation between measured (from the triaxial tests) and predicted (from Equation 7.7) axial strain for the triaxial tests Series 2

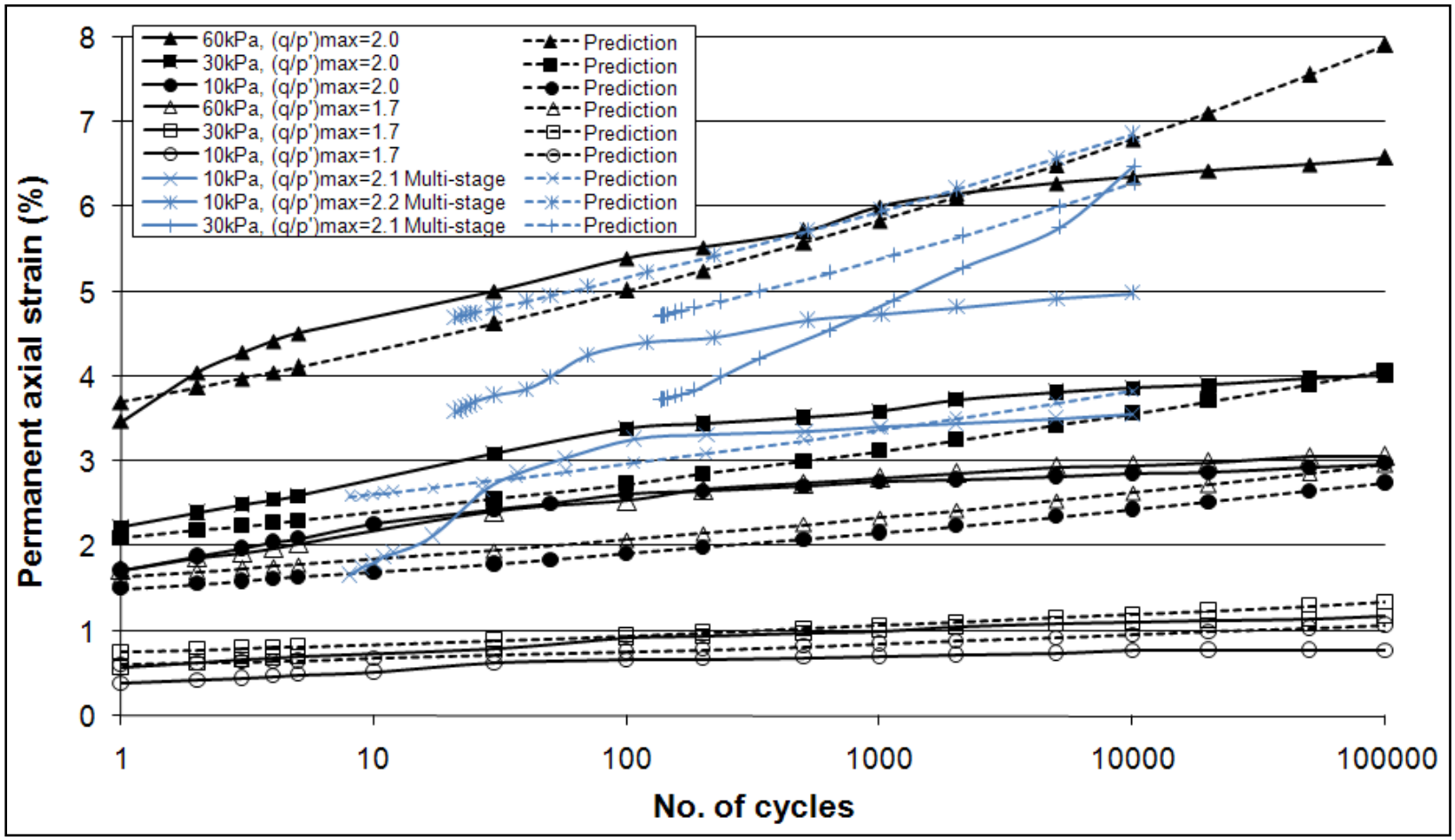

Figure 7.8 Correlation between measured (from the triaxial tests) and predicted (from Equation 7.7) permanent axial stain for the triaxial tests Series 2 and transformed cyclic triaxial tests from Series 3

7.3 Settlement Model Verification

As the settlement equations were developed based on the triaxial test results, a constant confining pressure is necessary for the permanent strain calculation. To use this equation in practice, therefore, the ballast underneath a sleeper could be divided into several layers, and each layer assumed to act as a small sample in a triaxial test. Overall permanent deformation of the ballast could be obtained by summing the deformation calculated at each depth increment from the ballast settlement equations under the stress conditions determined by the FEM analysis. Analytical predictions derived in this way will be compared with the CET and the RTF experimental results to verify and refine the settlement model.

7.3.1 Model Verification by the CET

According to the permanent deformation results of the monitored ballast particles in the CET, most of the settlement occurred immediately underneath the sleeper. Little settlement was detected from the monitored ballast particles at a depth of 150mm and 100mm away from the edge of the sleeper, as shown in Figure 4.7. Additionally, the FEM simulated vertical stress in the CET showed that the stress was concentrated under the sleeper and spread downwards at a steep angle. Therefore, it is proposed the permanent deformation calculation zone is recommended as an area under the sleeper with a 15° spread angle, as shown in

Figures 7.9 and 7.10. Figures 7.9 and 7.10 show the Y-component (vertical) stress and X-component (horizontal) stress from the CET simulation respectively. These two figures were the same stress distributions as in Figures 6.17 and 6.18 but in element stress output, which were easier for calculation and analysis in layers.

Ballast within the calculation zone in the CET is divided into 24 layers with a thickness of 12.5mm in each layer, which is the element size in the FEM simulation of the CET. Each layer is assumed to act as a sample in a triaxial test. The vertical stress on this sample is calculated by averaging the vertical stress of each element within this layer. On the other hand, the confining pressure on the sample is calculated as the horizontal stress of the element at the edge of this layer. The calculated vertical stress and the horizontal confining pressure for each layer are shown in Figure 7.11. From this figure, it can be seen that the vertical stress decreases from the top layer to the bottom layer. However, the horizontal stress significantly increases from depth 0 - 50mm (Layer 1 to Layer 4 in Figures 7.9 and 7.10), and then gradually decreases to the bottom layer. Therefore, relatively lower horizontal stress and higher vertical stress result a significant permanent deformation in the upper ballast layers.

The overall permanent deformation of the ballast is obtained by summing the settlement in each layer, which is calculated by applying the settlement equations to the simulated stress conditions. The correlation between measured and predicted permanent deformation in the CET is shown in Figure 7.12. Broad agreement is found between the model prediction and the experimental results

including both the magnitude and the rate of accumulation. Additionally, Figure 7.12 shows that most permanent deformation occurs at the depth range of 0 - 75mm in the CET, which matches the finding from the CET experimental tests. The reason for this phenomenon is that the ballast peak stress ratio is reached at depths of 0 - 25mm are, and the stress ratio at depths of 25mm - 37.5mm is also close to the peak condition. Therefore, significant permanent deformation is predicted to occur in the upper ballast layers. Figure 7.13 shows the correlation between measured and predicted ballast permanent deformation at different depths in the CET. It can be seen that the measured and the predicted results are close to each other. However, different trends are shown in the first 1000 cycles. This is probably because the settlement equations predict a relatively smaller permanent deformation in the ballast upper layer during the first 1000 cycles.

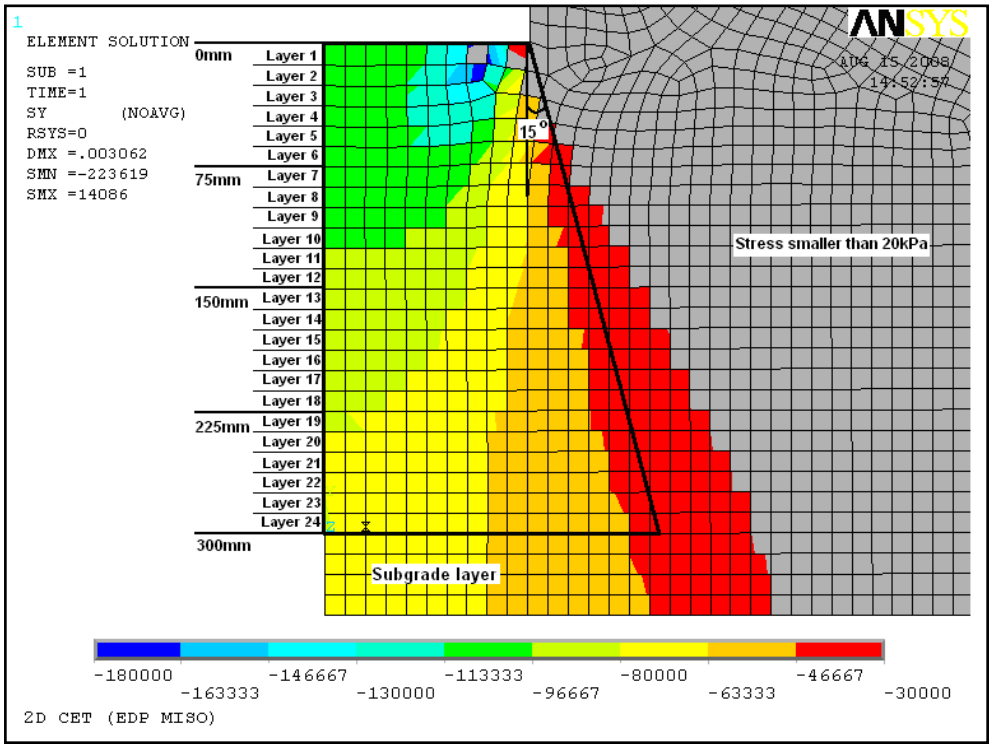

Figure 7.9 Calculation diagram of the Y-component (vertical) stress in the CET (Unit: Pa)

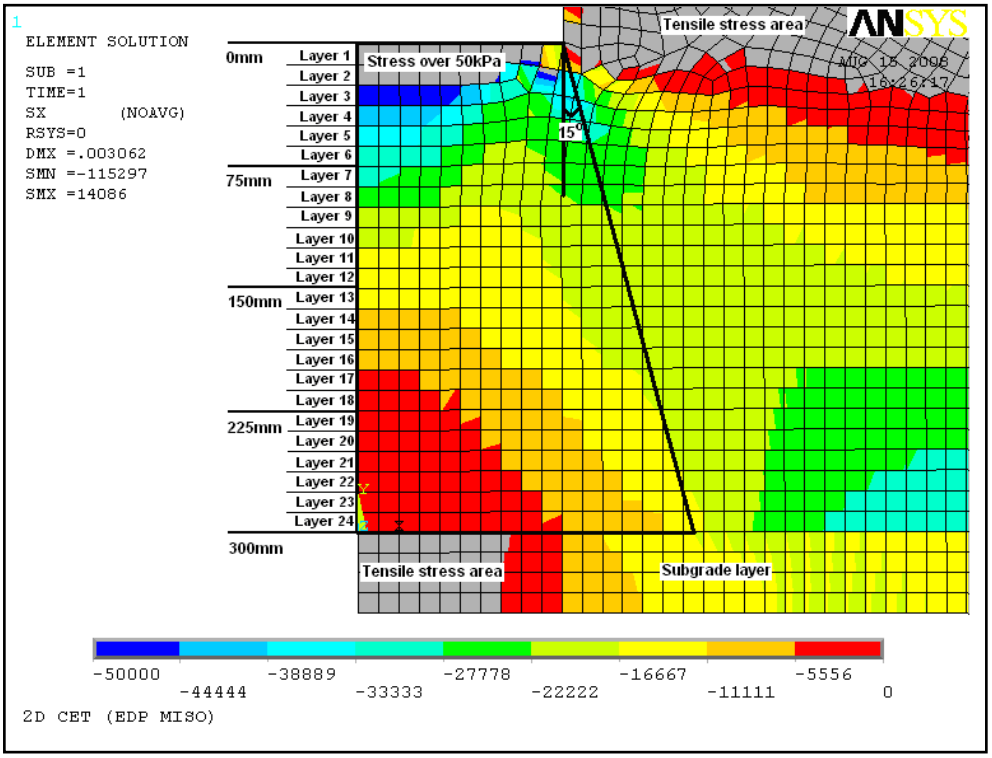

Figure 7.10 Calculation diagram of the X-component (horizontal) stress in the CET

(Unit: Pa)

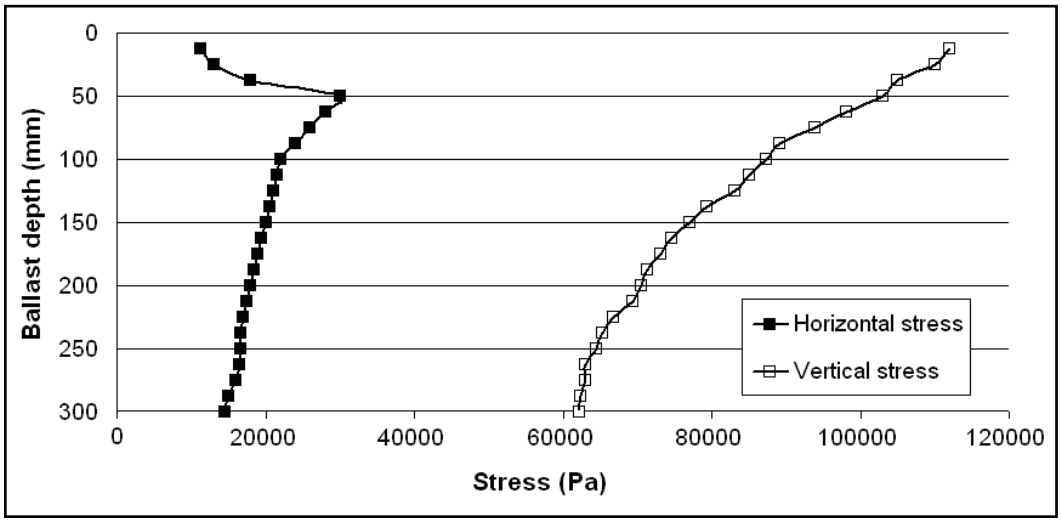

Figure 7.11 Calculated vertical stress and horizontal stress in the CET

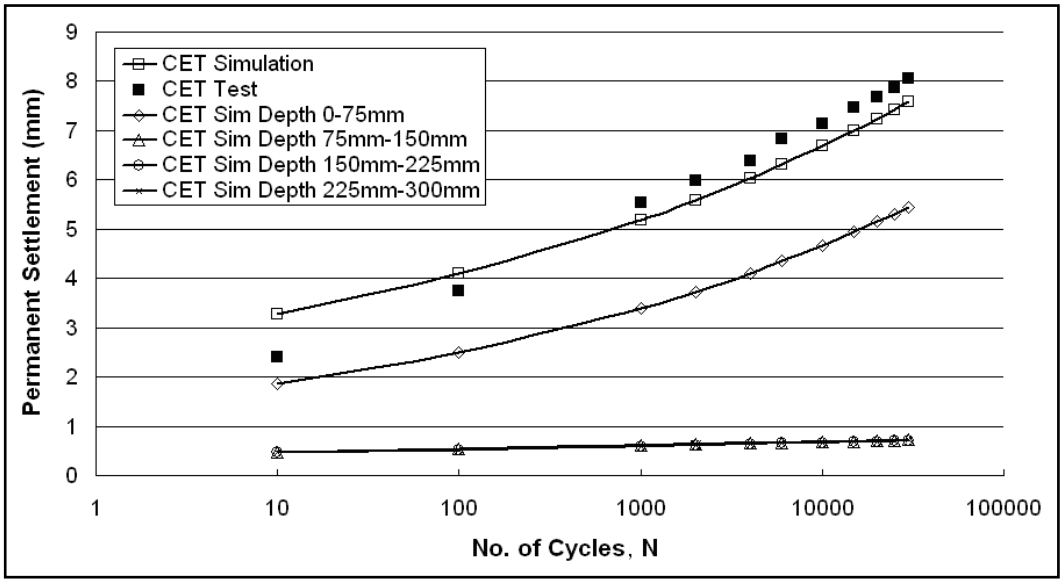

Figure 7.12 Correlation between measured and predicted permanent deformation in the CET

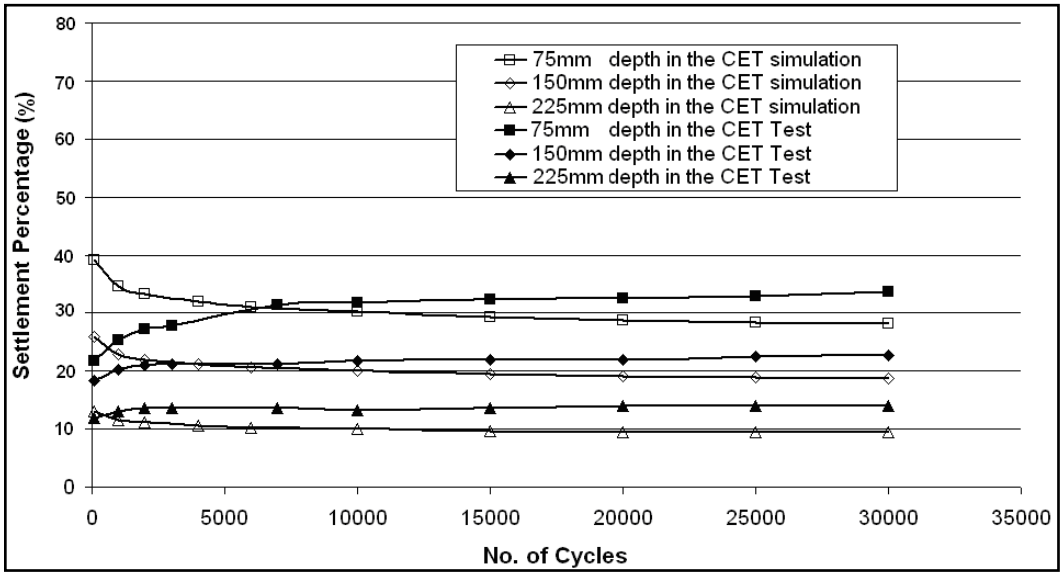

Figure 7.13 Correlation between measured and predicted ballast permanent deformation in the CET

7.3.2 Model Verification by the RTF

A similar calculation method as for the CET has been utilised in RTF permanent deformation calculation. The calculation zone is defined as an area under the sleeper with a 15° spread angle, as shown in Figures 7.14 and 7.15. Figures 7.14 and 7.15 show the Y-component (vertical) stress and X-component (horizontal) stress from the RTF simulation respectively. These two figures give the same stress distributions as in Figures 6.21 and 6.22 but in element stress output, which were easier for the calculation and analysis in layers. Ballast within the calculation zone is divided into 40 layers with a layer thickness of 7.5mm. The vertical calculation stress for each layer is the average Y-component stress of each element within this layer. The horizontal confining pressure is calculated by the X-component stress of the element at the edge of this layer, as shown in Figure 7.16. From this figure, it can be seen that, as for the CET, the vertical stress in the RTF decreases from the top layer to the bottom. The horizontal stress rapidly increases, and then slightly decreases to the bottom layer. Because of the lower horizontal stress and higher vertical stress in the upper ballast layers, there is significantly larger permanent deformation strain within these layers.

The overall permanent deformation in the RTF is obtained by summing the deformation is each sub-layer (40 sub-layers of ballast in the RTF), calculated from the settlement equations applied to the simulated stress conditions. The correlation between measured and predicted permanent deformation in the RTF is shown in Figure 7.17. From this figure, it can be seen that the predicted

permanent deformation is smaller than the experimental results. This is probably due to the moving load in the RTF; the continuous rotation of principal stress may have a certain effect on the ballast permanent deformation, which will be discussed in the following section.

As described in Chapter 5, because of the position arrangement of monitored ballast particles and the photogrammetry analysis in RTF Test 8, only the ballast particle settlement result at the depth of 150mm is available to compare with the settlement prediction at different depths. In RTF Test 8, a permanent deformation of 3.2mm was detected at the depth of 150mm, which is 25.2% of total settlement. Without the consideration of the principal stress rotation in the prediction, the permanent deformation percentage at the depth of 150mm is 18%, which is slightly smaller than the experimental result.

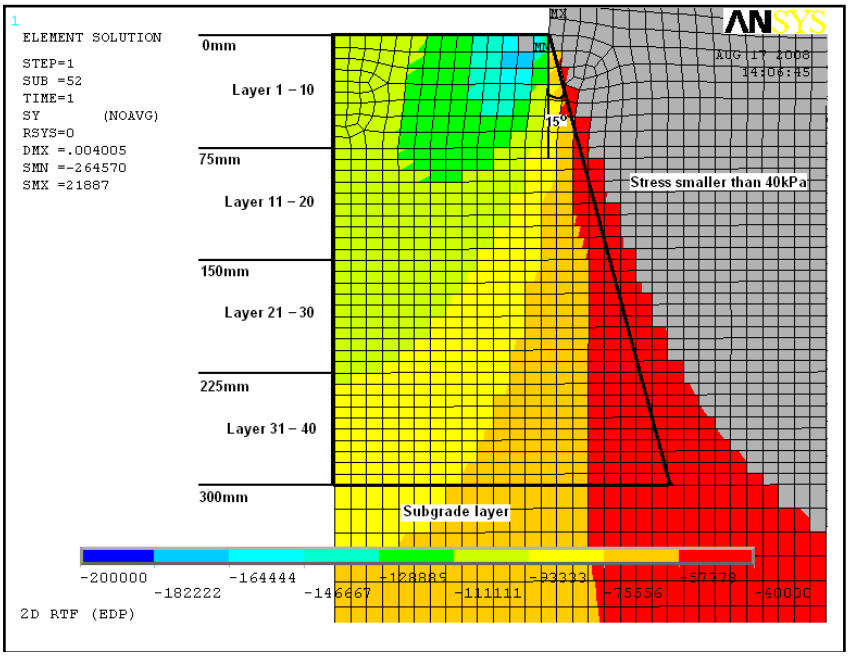

Figure 7.14 Calculation diagram of the Y-component (vertical) stress in the RTF (Unit: Pa)

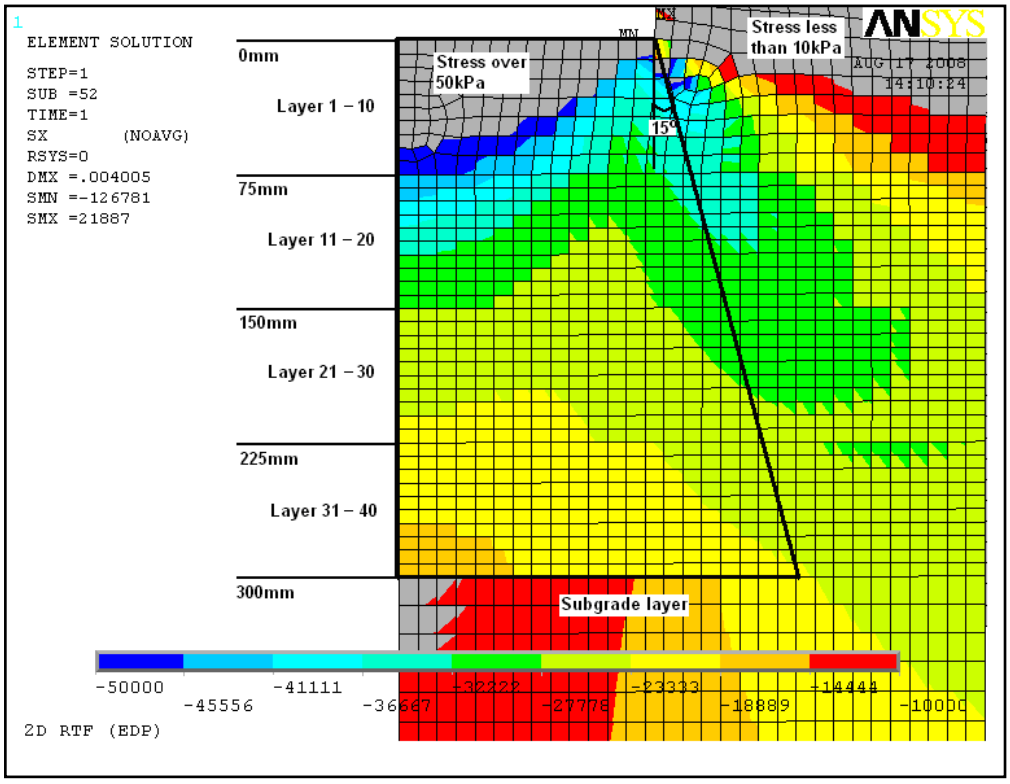

Figure 7.15 Calculation diagram of the X-component (horizontal) stress in the RTF

(Unit: Pa)

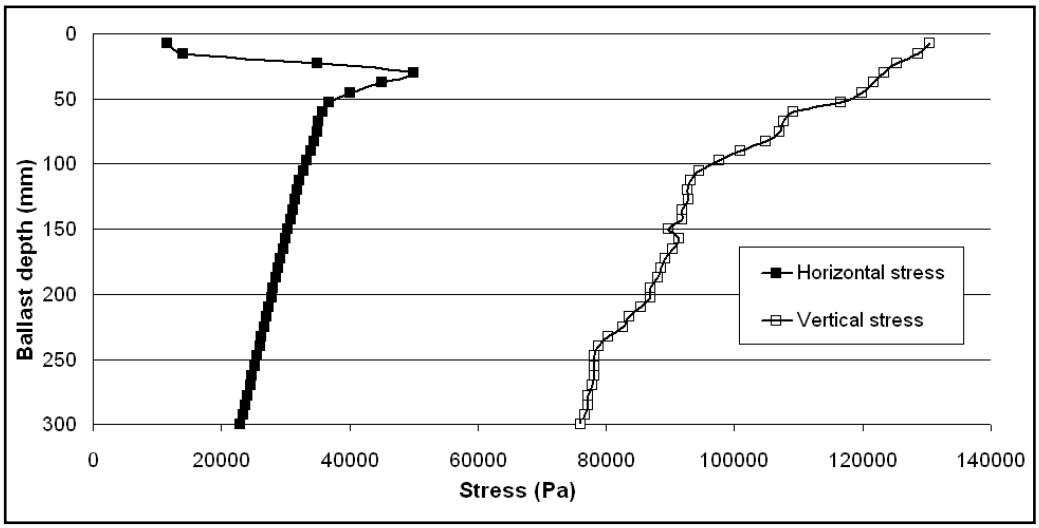

Figure 7.16 Calculated vertical stress and horizontal stress in the RTF

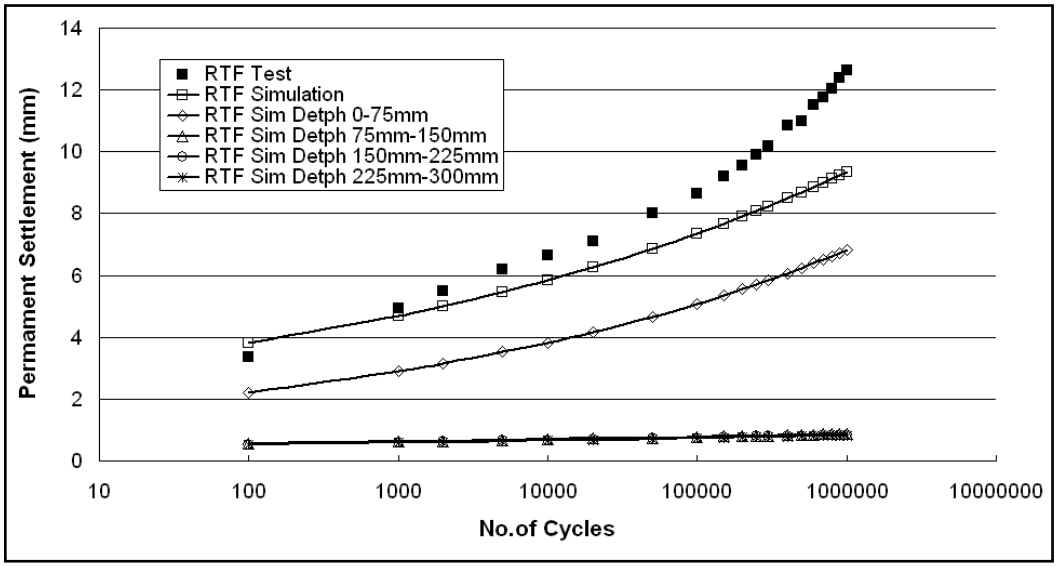

Figure 7.17 Correlation between measured and predicted permanent deformation in the RTF

7.3.3 Effect of Principal Stress Rotation

As concluded in Chapter 6, the effect of principal stress rotation contributes to the accumulation of permanent deformation. Ishikawa and Sekine (2007) revealed that cumulative permanent axial strain obtained from a moving load shear test (including principal stress rotation) could be estimated from permanent axial strain of a fixed load shear test (without principal stress rotation) by using a ratio of axial strain, as given blow:

$$\varepsilon_a^p = R \cdot \varepsilon_a \qquad \text{(Equation 7.9)}$$

where,

ε_a^p is permanent axial strain in principal stress rotation condition,

ε_a is permanent axial strain without principal stress rotation,

R is the ratio of axial strain due to the effect of principal stress rotation.

The ratio of axial strain (R) could express the change in cumulative permanent axial strain due to the change in principal stress axis rotation. It can be estimated by an equation which relates the maximum shear stress and the maximum axial stress:

$$R = \exp(a\frac{\tau_{\max}}{\sigma_{a,\max}}) \qquad \text{(Equation 7.10)}$$

where,

a is a constant parameter,

$\sigma_{a,\max}$ is the maximum axial stress,

$\tau_{\max}$ is the maximum shear stress.

Equations 7.9 and 7.10 were developed based on small scale model tests for railway ballast and laboratory element tests by multi-ring shear test apparatus. Test samples have one-fifth particle size distribution of ballast as used in Japanese railway. According to Ishikawa and Sekine (2007), the test facilities could carry out experimental tests on both fixed-place cyclic loading test without principal stress axis rotation and moving wheel loading test with principal stress axis rotation. Based on the experimental results, Ishikawa and Sekine (2007) concluded that the approximation results agree well with the experimental results, and the average ratio of axial strain to express the change in cumulative axial

strain due to the change in principal stress axis rotation can be estimated by the equation, which regards shear stress and axial stress as an independent variable.

According to Figure 6.30 (a), (b), (c) and (d), the maximum axial stress and the maximum shear stress at the analysis points in the RTF under a moving wheel load can be obtained, as shown in Table 7.1. The constant parameter *a* in Equation 7.10 can be determined by the comparison of a fixed-point RTF test and a normal RTF test, which will be discussed in the Chapter 8. In this simulation, if the parameter *a* was set to 10, the simulation results would give the best match with the experiment. Hence, the ratio of axial strain due to the effect of principal stress rotation (*R*) can be calculated and is given in Table 7.1. According to these calculation results, the effect of principal stress ratio contributes from 12% to 32% increase in permanent deformation accumulation in the RTF at different depths. The maximum influence occurs at the depth range of 75mm - 150mm. Figure 7.18 shows the correlation between measured and predicted permanent deformation with the effect of principal stress rotation. The modified prediction results show a better match with the test results. However, there are some minor differences after 800,000 cycles, which might be governed by other factors such as moving load speed and sleeper distortion.

Table 7.1 Calculation of the axial strain ratio due to the effect of principal stress rotation (R)

Ballast Depth (mm)	Maximum Shear Stress, $\tau_{\max}$ (kPa)	Maximum Axial Stress, $\sigma_{a,\max}$ (kPa)	$\frac{\tau_{\max}}{\sigma_{a,\max}}$	a	R
0 - 75 (Layer 1-10)	2.15	112	0.0192	10	1.21
75 - 150 (Layer 11-20)	3.15	114	0.0276		1.32
150 - 225 (Layer 21-30)	1.40	102	0.0137		1.15
225 - 300 (Layer 31-40)	1.00	88	0.0114		1.12

Other Influence Factors

Depending on train speed, track geometry and quality, vertical loads exerted by a moving load maybe greater than the static values. However, it is common practice to carry out a static analysis, in which dynamic effects are taken into account by multiplying the static load by a dynamic amplification factor (DAF). Esveld (2001) recommended the DAF may normally range from 1.1 to 2.8. Due to a relatively low simulated train speed (28km/hr) in the RTF, the DAF has not been considered in this analysis. Moreover, concrete sleeper distortion may cause an uneven stress distribution underneath the sleeper, which is another factor that should be considered in future study.

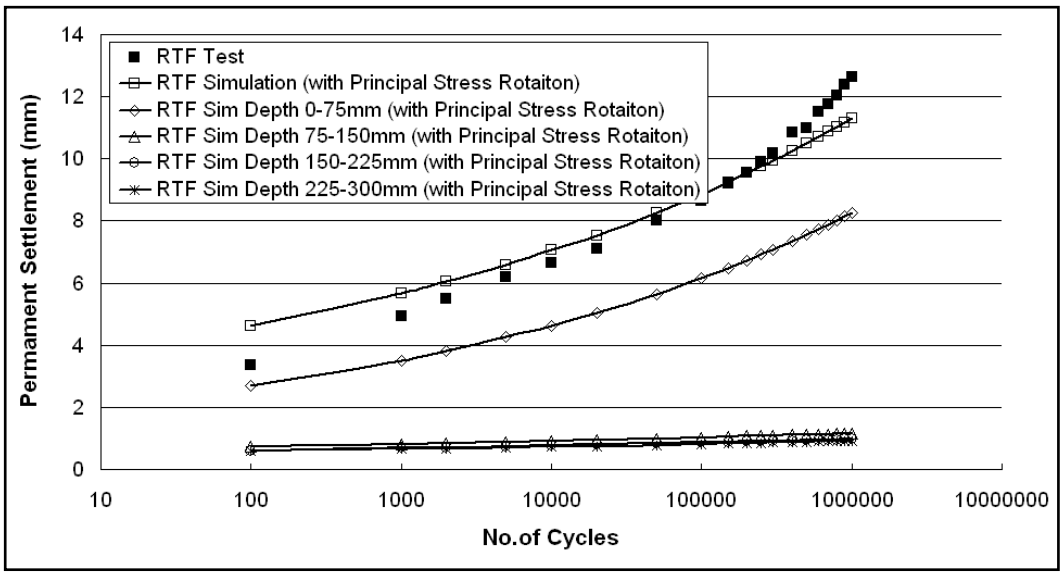

Figure 7.18 Correlation between measured and predicted permanent deformation in the RTF with the effect of principal stress rotation

Comparison of the permanent deformation prediction in the RTF test with different models

One of the most widely used mathematic models for calculating the permanent strain in railway ballast is suggested by Alva-Hurtado and Selig (1981), as given below:

$$\varepsilon_N = \varepsilon_1(1 + C\log N) \qquad \text{(Equation 2.9)}$$

where, ε_N is the accumulated axial plastic strain at any cycles, ε_1 is the axial plastic strain after the first cycle, C is a dimensionless constant controlling the rate of growth of deformation. Selig and Waters (1994) recommended that the typical values of C are between 0.2 and 0.4.

Figure 7.19 shows the permanent deformation prediction of the RTF with Equation 2.9 and Equation 7.7 (with principal stress rotation). As the constant C was recommended as a value between 0.2 and 0.4, three predicted lines (C=0.2, 0.3 and 0.4) were plotted in Figure 7.19. Comparing the two equations, it is noted that after the initial settlement has attenuated, the long-term settlement is modelled quite differently in the two models. Equation 2.9 predicted settlement grow only logarithmically; thus, approximate straight lines were obtained in Figure 7.19. The discrepancy between the two models might be large, especially after a large number of loading cycles. Possibly, the Equation 2.9 can only be used to describe settlement when the ballast is loaded within a small number of load applications. However, Equation 7.7 with principal stress rotation could predict the permanent deformation within the ballast whole life.

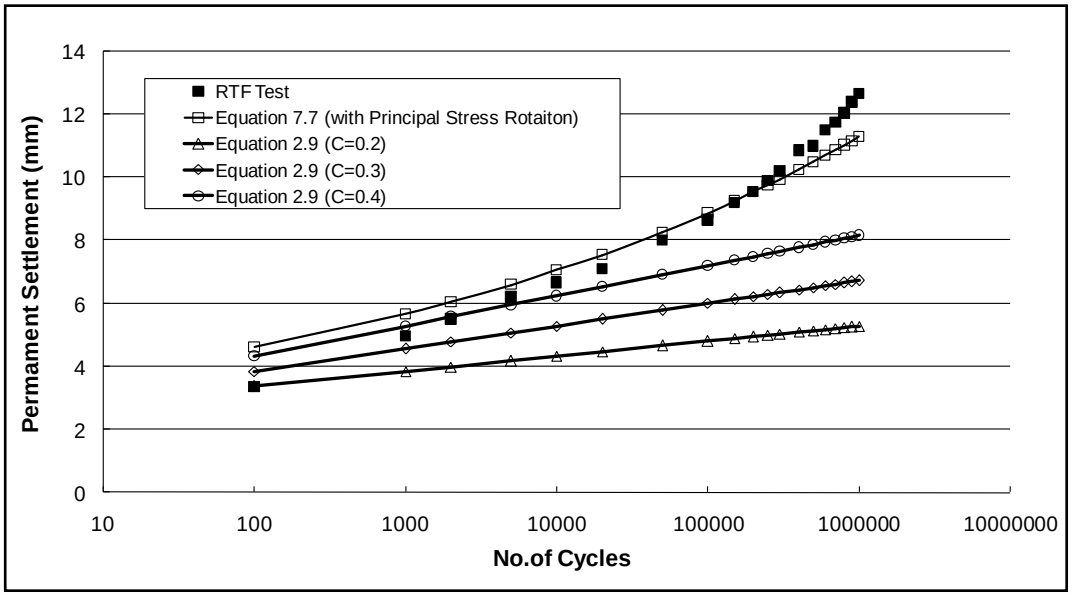

Figure 7.19 Comparison of the permanent deformation in the RTF with Equation 2.9 and Equation 7.7 (with principal stress rotation)

Kwan (2006) used the Shell BISAR computer program to approximate the settlement in the RTF. In addition, Aursudkij (2007) used this program to analyse the stress conditions under the loading area of the RTF. This program is normally used to compute elastic stresses, strains and deflection in the pavement structure from circular uniformly distributed loads at surface. According to Aursudkij (2007), computer analysis results of the RTF showed a decreasing confining pressure from the ballast top layer to bottom, as shown in Figure 7.20. Moreover, it can be seen that below the ballast depth of 150mm, the confining stress starts to become negative. Moreover, computer simulation predicted *q/p'* is over 3, when the confining pressure is low. This is practically impossible, as *q/p'* over 3 results in negative confining pressure. However Aursudkij (2007) indicated that even though BISAR has some deficiencies, it can approximately estimate the stress condition in the RTF.

To compute permanent strain, Kwan (2006) used data from Olowokere (1975) (as show in Figure 2.12) to relate permanent strain to applied stress. Figure 2.12 shows the relationship between applied stress and permanent strain for granite ballast. According to the calculated stress conditions by BISAR and Figure 2.12, the permanent deformation of the RTF can be predicted. In order to fit the RTF results, Kwan (2006) suggested an equation to modify the predicted settlement. The permanent strain for each of the three layers (three equal thickness layers were divided in the RTF settlement prediction), after e.g. 0.25 million cycles, $\varepsilon_{0.25m}$, can be shown by the expression:

$$\varepsilon_{0.25m} = Permanent \;\; strain \;\; of \;\; layer \times RTF \;\; AF \times SPF_{0.25m} \qquad \text{(Equation 7.11)}$$

where, $\varepsilon_{0.25m}$ is finial permanent strain after 0.25 million cycles, Permanent strain of layer is the calculated results from by BISAR and Figure 2.12. *RTF AF* is the RTF Adjustment Factor equals to 0.43, $SPF_{0.25m}$ is a Settlement Plot Factor at 0.25 million cycles, which was applied to each ballast layer at settlement intervals of 0.25, 0.5, 0.75 and 1 million cycles.

After modification, the comparisons of RTF experimental results and the prediction were considered satisfactory as shown in Figure 7.21. Although the experimental results were well matched with the predicted results, Equation 7.11 and its parameters were only proposed to fit the RTF results. Compared with the Equation 7.7 (with principal stress rotation), this settlement model cannot be widely used. Great effort is clearly needed in developing more general equations that have improved theoretical basis.

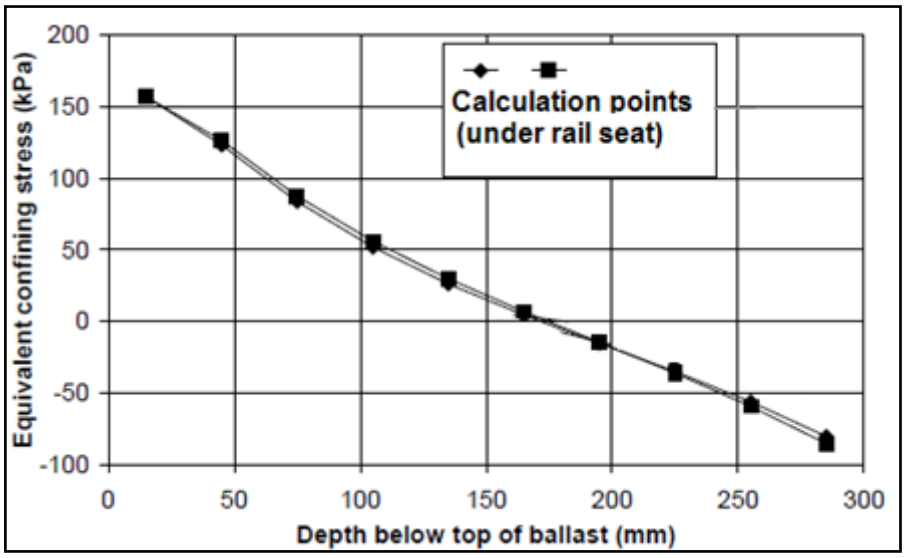

Figure 7.20 Equivalent confining stress vs depth below top of ballast from BISAR analysis (Aursudkij, 2007)

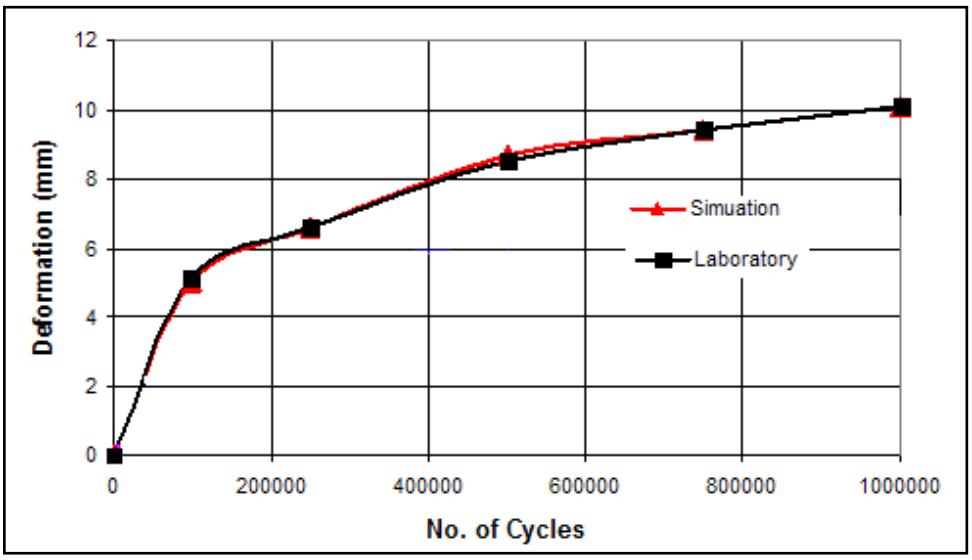

Figure 7.21 Comparison of computed and measured settlement for RTF

7.4 Chapter Summary and Discussion

Based on the FEM simulated stress distribution and the monitored ballast particle settlement in the CET and the RTF, the calculation zone for ballast permanent deformation calculation has been defined as the area underneath the sleeper with a 15° spread angle. The overall permanent deformation of the ballast is obtained by summing the settlement calculated at each depth increment from the ballast settlement equations applied to the stress conditions determined from the FEM analysis. Several layers with the same thickness are defined within the calculation zone, which are assumed to act as samples in triaxial tests with constant confining pressures.

The predicted settlement matches the CET test results well showing the same trend and magnitude. In the RTF, the prediction of permanent deformation appears smaller than the experimental results. However, an adjustment of the settlement equations by multiplying by a ratio due to the effect of principal stress rotation results in an accurate prediction of permanent deformation in the RTF. Furthermore, more factors should be considered in the prediction of permanent deformation in railway track such as DAF and concrete sleeper distortion.

A limitation of the settlement equations proposed for the prediction of permanent deformation is that in high maximum stress ratio conditions predictions are larger than experimental results. This is because the equations are intended to cover stress conditions both before and after failure. However, this wide stress ratio spectrum covered by the settlement equations may be considered to be an advantage to use. Additionally, it should be noted that several assumptions were made during the development of the settlement model, which may have had effects on the prediction results. First, the calculation zone for ballast permanent calculation was defined as the area underneath the sleeper with a 15° spread angle. Second, within the calculation zone, several layers with the same thickness were assumed as samples in triaxial tests with constant confining pressure. Meanwhile, in the settlement equations, the accurate compaction ratios and the principal stress ratios need further experimental tests to define. It is recognised that the railway settlement model only approximates the real conditions in a railway track, as the ballast could be easily contaminated and properties may vary considerably, factors which are not considered in this model. Despite these

limitations, the settlement model results in adequate prediction for permanent deformation in railway track.

In summary, several steps have been used and are proposed for research into ballast settlement. The steps are:

1. Undertake monotonic triaxial tests to determine parameters for FEM modelling.
2. Analyse the stress distribution beneath a railway track under a moving wheel load by FEM simulation.
3. Predict the permanent deformation using the settlement equations applied to the stress conditions determined from the FEM analysis.
4. Modify the predicted permanent deformation by a ratio to account for the effect of principal stress rotation, DAF and sleeper distortion.
5. Before final acceptance of the prediction, consideration is required of the expected long-term durability of the ballast material and railway track contamination.

CHAPTER 8

8. CONCLUSIONS AND RECOMMENDATIONS

8.1 Conclusions

General Observations

Railway ballast shows a complex behaviour when subjected to repeated loading in laboratory experiments, especially under moving traffic loading. Growth of permanent deformation in railway ballast is a gradual process, during which each load application contributes a small increment to the accumulation. Furthermore, ballast settlement increases non-linearly with increasing number of load cycles. The permanent deformation accumulation in railway ballast is affected by several factors including stress level, principal stress rotation and number of load applications.

Triaxial Tests

Results from the monotonic triaxial tests clearly show that higher confining pressure leads to higher peak deviator stress and tends to shift the overall volumetric strain towards compression. On the other hand, lower confining pressure tends to allow dilation. Larger dilation is accompanied by smaller breakage which is probably due to the ballast particles in the sample being able to rearrange themselves more freely with larger volume expansion. The ballast peak friction angle decreases with increasing confining pressure. Moreover, the initial elastic modulus of ballast increases with increasing confining pressure.

From the railway ballast cyclic triaxial tests, it can be seen that both permanent deformation and resilient movement behaviour depend on the levels of applied stress. With the same confining pressure, the breakage increases with increasing deviator stress. The ballast permanent deformation has a strong positive relationship with ballast particle breakage in the cyclic triaxial tests. The multi-stage triaxial tests covered a relatively wide spectrum of stresses expected to occur in railway track. Experimental results show that low stress levels result in the ballast sample reaching a final equilibrium state whereas high stress levels lead to rapid growth of permanent strain and eventual failure. In addition, permanent deformation equations were successfully developed based on the cyclic and multi-stage triaxial test results. These equations are able to describe the settlement of ballast under a single stress condition.

Composite Element Test (CET) and Railway Test Facility (RTF) Tests

The results from the CET include successful detection of ballast settlement at different depths. The monitored ballast particle settlements from the CET were in good agreement with those from the RTF, where most of the deformation occurred in the upper ballast layer.

Finite Element Method (FEM) Analysis and Modelling

FEM analysis provides a useful way to simulate the behaviour of ballast. The initial simulations using a nonlinear elastic material model and a Drucker-Prager material model show the potential of FEM to build a rigorous scientific analysis, which gives a reliable simulation of stress condition. The extended Drucker-Prager model with hardening was adopted in the later FEM simulations to capture the yield stress hardening features of ballast. The simulation provided the stress levels within the ballast, which were used in settlement equations to compute ballast settlement.

Railway Settlement Model

The permanent deformation in railway ballast is generally based on the effect of applied stress and number of load application. Initial density, described by degree of compaction, is believed to have a pronounced impact on the long-term behaviour of railway ballast as is the peak stress ratio ($(q/p)_p$). The settlement equations obtained from cyclic and multi-stage triaxial test results, unlike conventional stress-strain constitutive models, are able to provide strain prediction even when the stress ratios exceed peak condition.

The railway settlement model derived from the combination of FEM analysis and settlement equations can calculate the overall permanent deformation in ballast for any given number of load cycles. Analytical predictions of ballast settlement behaviour were compared with the CET and the RTF experimental results, which demonstrated that the railway settlement model provides good indication of the overall permanent deformation in ballast. Furthermore, predictions approximately match measured movement of individual strains.

8.2 Recommendations for Future Study

This thesis has presented and validated a method to predict the permanent deformation of railway ballast, which has highlighted several aspects of ballast behaviour that need to be investigated in more detail. The following issues are recommended for future research.

Triaxial Tests

It is recommended that further tests are carried out at each stress condition to check repeatability, and that more stress conditions are covered in these further tests. A multi-stage triaxial test procedure should be developed, in which a minimum number of tests is conducted, but which still has the ability to determine the material model parameters for computer analysis. This will reduce the cost of conducting the triaxial tests. Investigating the effect of the degree of compaction

or initial density on ballast settlement performance would be particularly useful in refining the railway settlement model.

CET and RTF Tests

A larger number of monitored ballast particles should be utilised to measure ballast movement in both the CET and the RTF. Alternative technology, such as accelerometers, could be introduced to investigate ballast particle movement in different layers at various points. Besides the vertical movement of ballast particles, the lateral flow of ballast could be monitored by these instrumented ballast particles, horizontally installed. Ballast lateral flow is an important characteristic that accompanies ballast settlement and stiffness change, and which needs further research.

A fixed-point RTF test is recommended to check the effectiveness of principal stress rotation on the permanent deformation. In this test, the two outer sleepers would be maintained at a certain level of load to provide confining pressure. Meanwhile, the middle sleeper would be subjected to repeated cyclic loading. The fixed-point test results could be compared with normal RTF test results to calculate the parameter *a* in Equation 7.10.

Comparison experimental tests were recommended to identify the effect of compaction methods on the permanent deformation accumulation. Based on the experiments, the compaction ratio (C_r in Equation 7.8) could be calculated.

FEM Analysis and Modelling

An increased ability to simulate actual railway track is necessary, and additional influences should be introduced into the model. Moving multi-wheel loads on the rails could be applied on top of the sleepers to mimic moving train wheels.

The ANSYS finite element model used in this thesis was an approximation to reality. Therefore, further research is required to develop more appropriate material models and computational techniques that can simulate the build up of stress under multi-cyclic load. In particular, Discrete Element Modelling simulation is an alternative method that should be evaluated.

Railway Settlement Model

Modelling is an important requirement in dealing with material performance. Although settlement equations combined with FEM analysis has been presented and it fitted the CET and the RTF results well, great effort is clearly needed in developing more general procedures and models that have improved theoretical basis and also have wider applicability.

REFERENCES

ANSYS, (2007). *Release 11.0 Documentation for ANSYS*. ANSYS, Inc. USA

Allen, J.J. and Thompson, M.R., (1974). "Resilient Response of Granular Materials Subjected to Time-Dependent Lateral Stresses." *Transportation Research Record*, 510, pp. 1-13.

Alva-Hurtado, J.E. and Selig, E.T., (1981). "Permanent Strain Behaviour of Railroad Ballast". *Proc. of 10th International Conference on Soil Mechanics and Foundation Engineering*, Stockholm, Sweden, Vol. 1, 543-546, 1981. A. A. Balkema, Rotterdam, the Netherlands.

Arnold, G.K., (2004). *Rutting of Granular Pavements*, PhD Dissertation, School of Civil Engineering, the University of Nottingham, UK.

Aursudkij, B., (2007). *A Laboratory Study of Railway Ballast Behaviour under Traffic Loading and Tamping Maintenance*. PhD Dissertation, School of Civil Engineering, the University of Nottingham, UK.

Banimahd, M. and Woodward, P.K., (2007) "3-Dimensional Finite Element Modelling of Railway Transitions." *Proceedings of 9th International Conference on Railway Engineering,* London, UK.

Barbero, E.J., (2008). *Finite Element Analysis of Composite Materials.* Taylor & Francis Group, Boca Raton, New York and Oxon.

Barksdale, R.D. and Itani, S.Y., (1989). "Influence of Aggregate Shape on Base Behavior." *Transportation Research Record,* 1227, pp. 173-182.

Bishop, A.W. and Green, G.E., (1965). "The Influence of End Restraint on the Compression Strength of a Cohesionless Soil." *Geotechnique* **15**, pp. 243-266.

Brodrick, B.V., (1977) *The development and performances of a wheel loading facility and in situ instruments for pavement experiments.* Thesis submitted to the University of Nottingham for the degree of Master of Philosophy.

Brown, S.F., (1974). "Repeated Load Testing of a Granular Material." *Journal of the Geotechnical Engineering Division, ASCE,* 100 (GT7), pp. 825-841.

Brown, S.F., (1977). "State-of-the-art report on field instrumentation for pavement experiments." *Transportation Research Record, no.*640, p13-28, Transportation Research Board, Washington D.C.

Brown, S.F., (1996). "Soil mechanics in pavement engineering." *Geotechnique,* 1996, 46(3), 384-426.

Brown, S.F. and Hyde, A.F.L, (1975). "Significance of cyclic confining stress in repeated load triaxial testing of granular material." *Transportation Research Record,* 537, Transportation Research Board, Washington D.C. 49-58.

Brown, S.F. and Selig, E.T., (1991). "The Design of Pavement and Rail Track Foundations." *Cyclic Loading of Soils: from Theory to Design*, Blackie and Son Ltd, New York, pp. 249-305.

Brunton, J. M. & Almeida, J. R. (1992). "Modelling material non-linearity in a pavement backcalculation procedure, Transp." *Tran. Res. Record* No.1377, Transportation Research Board, Washington, DC, 99-106.

Boyce, J.R., Brown, S.F., and Pell, P.S., (1976). "The Resilient Behavior of a Granular Material under Repeated Loading." *Proceedings Australian Road Research Board*, 8, pp. 8-19.

Boyce, J.R. (1980). "A Non-linear Model for the Elastic Behaviour of Granular Materials under Repeated Loading." *International Symposium on Soils under Cyclic and Transient Loading*, Pande, G.N. and Zienkiewicz, O.C. eds., Brookfield Pub Co, Swansea.

Carl Bro, (2008). Falling Weight Deflectometer PRIMA100. http://www.pavement-consultants.com/en/Menu/Falling+Weight+Deflectometer/PRIMA+100+LWD/PRIMA100.htm (December, 2008)

Chen, W.F. (1994). *Constitutive Equations for Engineering Materials*, Elsevier, New York.

Chen, Y.L., Azzam R. and Zhang F.B., (2005) "The Displacement Computation and Construction Pre-control of a Foundation Pit in Shanghai Utilizing FEM and Intelligent Methods."

Cope, D.L. and Ellis, J.B., (2001). *British Railway Track Volume 4 Plain Line Maintenance*. Irongate Digital Solutions, Derby England.

Cundall, P.A. and Strack, O.D.L., (1979). "A discrete numerical model for granular assemblies." *Geotechnique*. 29. No.1, 47-65.

Dawson, A.R. (1990). "Introduction to Soils and Granular Materials." *Lecture Notes from Residential Course, Bituminous Pavement Materials, Design and Evaluation*, the University of Nottingham, UK

Dawson, A.R., Thom, N.H. and Paute, J.L., (1996). "Mechanical Characteristics of Unbound Granular Materials as a Function of Condition." *Flexible Pavements*. A. G. Correia ed. Rotterdam, A. A. Balkema. pp. 35-44.

Dahlberg, T., (2001). "Some Railroad Settlement Models - A Critical Review." *Proceedings of the Institution of Mechanical Engineers*, 215 (4) Part F, pp. 289-300.

Dahlberg, T., (2002). "Linear and Non-linear Track Models for Simulation of Track Responses." *Report LiTH-IKP-R-1228, Solid Mechanics,* IKP, Linköping University, Linköping, Sweden, 2002.

Dehlen, G.L., (1969). *The Effect of Non-Linear Material Response on the Behavior of Pavements Subjected to Traffic Loads.* PhD Dissertation, the University of California

Dunlap, W.A., (1963). "A Report on Mathematical Model Describing the Deformation Characteristics of Granular Materials." *Tech. Rep. No. 1, Proj. 2-8-62-27,* Texas Transp. Inst., Texas A&M University, College Station, Tex.

Esveld, C., (1989). *Modern Railway Track.* MRT-Productions, the Netherlands.

Esveld, C., (2001). *Modern Railway Track (Second Edition).* MRT-Productions, the Netherlands.

Eisenmann, J., Leykauf, G. and Mattner, L., (1994). "Recent Developments in German Railway Track Design." *Proceedings of the Institution of Civil Engineers, Transportation*, 105, pp. 91-96.

Fair, P. (2003) "The geotechnical behavior of ballast materials for railway track maintenance." PhD Dissertation, University of Sheffield.

Festag, G. and Katzenbach, R., (2001) "Material Behaviour of Dry Sand under Cyclic Loading." *Proc. 15th Int. Conf. on Soil Mech. & Geotech. Engg.*, Istanbul, Vol. 1, pp. 87-90

Gaskin, P.N. and Raymond, G., (1976). "Contribution to Selection of Railroad Ballast." *Transportation Engineering Journal, ASCE*, 102 (TE2), pp. 377-394.

Gustavson, R. and Gylltoft, K., (2002) "Influence of Cracked Sleepers on the Global Track Response: Coupling of a Linear Track Model and Non-linear

Finite Element Analyses," *Proc Instn Mech Engrs* Vol 216 Part F: J Rail and Rapid Transit

Hettler, A. (1984) "Bleibende Setzungen des Schotteroberbaus." *Eisenbahn-technische Rundschau (ETR)*, 33(11), 847–853.

Hicks, R.G., (1970) "Factors in flensing the resilient properties of granular materials." PhD Dissertation, University of California, Berkley, California.

Hicks, R.G. and Monismith, C.L., (1971) "Factors Influencing the Resilient Properties of Granular Materials," *Highway Research Records* 345, pp: 15-31.

Hjortnaes-Pedersen, A. and Molenkamp, F., (1982) "Accuracy and reproducibility of triaxial tests." In P.A. Vermeer, and H.J. Lager, eds., *Deformation and failure of granular material*, A.A.Balkema, Rptterdam, The Netherlands, 391-401.

Hoff, I. Nordal, S. Nordal, R. (1999). "Constitutive Model for Unbound Granular Materials Based on Hyperelasticity. Unbound Granular Materials – Laboratory Testing, In-situ Testing and Modeling." Edited by A. Gomes Correia, Technical University of Lisbon. *Proceedings of an International Workshop on Modelling and Advanced Testing for Unbound Granular Materials*, Lisbon

Indraratna, B., Ionescu, D. and Christie, H.D., (1998). "Shear Behaviour of Railway Ballast Based on Large-scale Triaxial Tests." *Journal of Geotechnical and Geoenvironmental Engineering* 124, No. 5, pp. 439-449.

Ionescu, D., Indraratna, B. and Christie, H.D. (1998). "Behaviour of Railway Ballast under Dynamic Loads." *Proc. 13th Southeast Asian Geotechnical Conference,* Taipei, pp. 69-74.

Ishikawa, T. and Sekine, E., (2007). "Effect Evaluation of Moving Load on Cyclic Deformation of Crushed Stone." *13th Asian Regional Conference of Soil Mechanics & Geotechnical Engineering*, Kolkata, India

Jacobs, M.M.J., Bondt, A.H., Molenaar, A.A.A. and Hopman. P.C., (1992). "Cracking in Asphalt Concrete Pavements." *Proc. on 7th International Conference on the Structural Design of Asphalt Pavements.* 1:89-105.

Jeffs, T. and Marich, S., (1987). "Ballast Characteristic in the Laboratory," *Conference on Railway Engineering,* Perth, pp.141-147

Jeffs, T. and Tew, G.P., (1991). *A Review of Track Design Procedures, Vol. 2, Sleepers and Ballast,* Railways of Australia.

Kaya, M (2004). *A study on the stress-strain behavior of railroad ballast materials by use of parallel gradation technique.* The Middle East Technical University.

Kempfert, H.G. and Hu, Y., (1999). "Measured dynamic loading of railway underground." *Proc. 1the Pan-American Conf. on Soil Mech. And Geotech. Engg.*, Brazil, pp. 843-847

Key, A., (1998). *Behaviour of two layer railway track ballast under cyclic and monotonic loading*. PhD Dissertation, University of Sheffield.

Khedr, S., (1985). "Deformation Characteristics of Granular Base Course in Flexible Pavements." *Transportation Research Record*, 1043, pp. 131-138.

Knutson, R.N., (1976). *Factors Influencing the Repeated Load Behaviour of Railway Ballast*. PhD Dissertation, University of Illinois at Urbana-Champaign.

Knutson, R.M. and Thompson, M.R., (1977). "Resilient Response of Railway Ballast." *Transportation Research Record*, 651, pp. 31-39.

Kolisaja, P., (1997). *Resilient deformation characteristics of granular materials*. PhD Dissertation, Tampere University of Technology. Publ. No.223, Tampere, Finland.

Kramer, S.L., Swvaneswaran, N. and Davis, R.D., (1990). "Analysis of membrane penetration in triaxial test." *Journal of Engineering Mechanics*, Vol.116, No.4, pp. 773-789.

Kwan, C.C.J., (2006). *Geogrid Reinforcement of Railway Ballast*, PhD Dissertation, School of Civil Engineering, the University of Nottingham, UK.

Lackenby, J., (2006). *Triaxial Behaviour of Ballast and the Role of Confining Pressure under Cyclic Loading*. The University of Wollongong, Australia

Lekarp, F., (1997). *Permanent Deformation Behaviour of Unbound Granular Materials.* Licentiate Thesis, Royal Institute of Technology, Stockholm

Lekarp, F. and Dawson, A., (1998). "Modelling Permanent Deformation Behavior of Unbound Granular Materials." *Construction and Building Materials* 12, No. 1, 9-18.

Lekarp, F., Isacsson, U. and Dawson, A., (2000a). "State of the Art I: Resilient Response of Unbound Aggregates." *Journal of Transportation Engineering*, ASCE. Vol. 126, No. 1, pp. 66-75.

Lekarp, F., Isacsson, U. and Dawson, A., (2000b). "State of the Art II: Permanent Strain Response of Unbound Aggregates." *Journal of Transportation Engineering*, ASCE. Vol. 126, No. 1, pp. 76-83.

Li, K.H., Brough, M., Sharley, P., Thomas, B., Sharpe, P. and Thom, N.H., (2007). "Alternative To Sand Blanket: Anti-Pumping Geocomposites In Maintenance & Track Renewal," *Railway Engineering 2007, 9th International Conference and Exhibition*, London

Liao, C., Chang, T. and Young, D., (1995). "Elasto-Plastic Constitutive Modelling of Granular Assembly," *International Journal of Solids and Structures*, 32 (8-9), pp. 1121-1133.

Lim, W.L., (2004). *Mechanics of Railway Ballast Behaviour*, PhD Dissertation, School of Civil Engineering, the University of Nottingham, UK.

Long, F., Govindjee, S. and Monismith, C., (2002). "Permanent Deformation of Asphalt Concrete Pavements: Development of a Nonlinear Viscoelastic Model for Mix Design and Analyses." *Ninth International Conference on Asphalt Pavements*, August 17-22, 2002, Copenhagen Denmark. International Society for Asphalt Pavements.

Lu, M., (2008). *Discrete Element Modelling of Railway Ballast*, PhD Dissertation, School of Civil Engineering, the University of Nottingham, UK.

Maree, J.H., Freeme, C.R., Van Zyl, N.J. and Savage, P.F., (1982). "The Permanent Deformation of Pavements with Untreated Crushed Stone Bases as Measured in Heavy Vehicle Simulator Tests." *Proc., 11th ARRB Conf.*, Part 2. 16-28.

May, R.W. and Witczak, M.W., (1981). "Effective Granular Modulus to Model Pavement Responses." Transp. *Res. Rec. 810*, Transportation Research Board, Washington, D.C., 1-9.

McDowell, G.R., Bolton, M.D. and Robertson, D., (1996). "The Fractal Crushing of Granular Materials." *J. Mech. Phys. Solids* 44, No. 12, 2079-2102.

Miura, S. and Kawamura, S. (1996). "A procedure minimizing membrane penetration effect in undrained triaxial test." *Soil and foundations,* Vol. 36, No.4. pp.119-126 Tokyo, Japan.

Mohammad, F., Collop, A. and Brown, S., (2003). "The Effects of Surface Cracking on Primary Responses in a Flexible Pavement Structure." ASCE

Momoya, Y. and Sekine, E. (2004)) "Reinforced roadbed deformation characteristics under moving wheel loads." *QR of RTRI*, Vol. 45, No. 3

Network Rail (2007), *Business Plan 2007*, Network Rail, London

Neves, J. and Correia, A. (2003). "Influence of non-linear behaviour of unbound granular materials on pavement reinforcement design." MAIRPAV '03. 3rd Symposium on Maintenance and Rehabilitation of Pavements and Technological Control, July 7-10, 2003.

Office for Research and Experiments (ORE), (1970). "Stresses in Rails, the Ballast and the Formation Resulting from Traffic Loads." *Question D71, Report No. 10, Vols. 1 and 2, International Union of railways,* Utrecht, Netherlands.

Olowokere, D.O., (1975). *Strength and Deformation of Railway Ballast Subject to Triaxial Loading*. PhD Dissertation, the Queen's University.

Pappin, J.W., (1979). *Characteristics of Granular Material for Pavement Analysis.* PhD Dissertation, School of Civil Engineering, the University of Nottingham, UK.

Pezo, R.F., (1993). "A General Method of Reporting Resilient Modulus Tests of Soils - A Pavement Engineer's Point of View." *72nd Annu. Meeting of the TRB.*

Powrie, W., Yang, L.A. and Clayton, C.R.I. (2007). "Stress changes in the ground below ballasted railway track during train passage." *JRRT.* Proc. IMechE Vol.221.

Raad, L., and Figueroa, J.L., (1980). "Load Response of Transportation Support Systems." *Transportation Engineering Journal, ASCE*, 106 (TE1), pp. 111-128.

Radampola, S.S., (2004) *Evaluation and Modelling Performance of Capping Layer in Rail Track Substructure.* Central Queensland University, Australia

Railtrack Line Specification (2000). RT/CE/S/006 Issue 3. *Track Ballast.*

Raymond, G. P. and Bathurst, R.J., (1994). "Repeated-load Response of Aggregates in Relation to Track Quality Index." *Canadian Geotech. Journal*, Vol. 31, pp.547-554

Raymond, G. P. and Diyaljee, V. A., (1979). "Railroad Ballast Load Ranking Classification." *Journal of the Geotechnical Engineering*, ASCE 105, No. 10, 1133-1153

Raymond, G.P. and Williams, D.R., (1978). "Repeated Load Triaxial Tests on Dolomite Ballast." *Journal of the Geotechnical Engineering Division*, 104 (GT7), pp. 1013-1029.

Rowshanzamir, M.A., (1995). *Resilient Cross-Anisotropic Behaviour of Granular Base Materials under Repetitive Loading.* PhD Dissertation, the University

of New South Wales

Salim, M.W., (2004). *Deformation and Degradation Aspect of Ballast and Constitutive Modelling Under Cyclic Loading*. PhD Dissertation, the University of Wollongong

Sato, Y., (1995). "Japanese Studies on Deterioration of Ballasted Track." *Vehicle System Dynamics*, Vol. 24(Supplement), 197-208, 1995.

Seed, H.B., Chan, C.K. and Lee, C.E., (1962). "Resilience Characteristics Subgrade Soils and Their Relation to Fatigue Failures." *Proc. Int. Conf. Structural Design of Asphalt Pavements,* Ann Abor, Michigan, pp. 611-636.

Selig, E.T., (1984). "Ballast for Heavy Duty Track." *Track Geotechnology*, Proc. of a Conf. organized by the Inst. of Civil Engineers and held at University of Nottingham, pp. 245-252.

Selig, E. T. and Alva-Hurtado, J. E. (1982). Predicting effects of repeated wheel loading on track settlement *Proceeding of the 2nd International Heavy Haul Conference*, Colorado Springs, pp. 476-487.

Selig, E.T. and Waters, J.M., (1994). *Track Geotechnology and Substructure Management*. Thomas Telford, London.

Shahnazari, H. and Towhata, I., (2002). "Torsion Shear Tests on Cyclic Stress-Dilatancy Relationship of Sand." *Soils and Foundations*, 42 (1), pp. 105-119.

Shenton, M.J., (1975). "Deformation of Railway Ballast under Repeat Loading Conditions." *Railroad Track Mechanics and Technology* (Kerr ed.), Proc. of a Symposium held at Princeton Univ., pp. 387-404

Shenton, M. J., (1985). "Ballast Deformation and Track Deterioration." *In Proceedings of a Conference on Track Technology*, University of Nottingham, 11–13 July 1984, 1985, pp. 253–265 Thomas Telford Limited, London.

Skoglund, K.A., (2002). *A study of some factors in mechanics railway track design*, PhD Dissertation, Norwegian University of Science and Technology.

Stewart, H.E., (1986). "Permanent Strains from Cyclic Variable Amplitude Loadings." *J. of Geotechnical Engineering, ASCE,* Vol. 112, No. 6, pp. 646-660

Shenton, M.J., (1974) "Deformation of Railway Ballast under Repeated Loading Conditions", British Railway Research and Development Division.

Suiker, A. S. J., Selig, E. T., and Frenkel, R. (2005). Static and cyclic triaxial testing of ballast and subballast *Journal of geotechnical and geoenvironmental engineering*, ASCE. Vol. 131, No. 6, pp. 771-782.

Sweere, G.T.H., (1990) *Unbound Granular Basis for Roads*, PhD Dissertation, University of Delft, the Netherlands.

Tam, W.A. and Brown, S.F., (1988). "Use of the Failing Weight Deflectometer for In Situ Evaluation of Granular Material in Pavements." *Proc., 14th ARRB Conf.*, Vol. 14, Part 5, 155-163

Thom, N.H., (2005). "Railway Engineering." *Lecture Notes from Railway Engineering Course*, School of Civil Engineering, the University of Nottingham, UK

Thom, N.H., (1988). *Design of Road Foundations*. PhD Dissertation, School of Civil Engineering, the University of Nottingham, UK.

Thom, N.H. and Brown, S.F., (1987) "Effect of Moisture on the Structural Performance of a Crushed-limestone Road Base", *Transp. Res. Rec.* 1121, pp: 50-56.

Thom, N.H. and Brown, S.F., (1988). "The Effect of Grading and Density on the Mechanical Properties of a Crushed Dolomitic Limestone." *Proceedings of the 14th Australian Road Research Board Conference*, Part 7, pp. 94-100.

Thom, N.H. and Brown, S.F., (1989). "The Mechanical Properties of Unbound Aggregates from Various Sources." *Unbound Aggregates in Roads*, (eds. R.H. Jones, and A.R. Dawson), 130-142. London: Butterworth.

Thom N.H. and Dawson A.R., (1996) "The Permanent Deformation of a Granular Material under Repeated Wheel Loading", *ibid*, pp 65-80.

Thom, N.H. and Oakley, J., (2006) "Prediction Differential Settlement in a Railway Trackbed." *Railway Foundations,* Birmingham, UK

Thompson, M.R., Tutumluer, E. and Bejarano, M., (1998). "Granular Material and Soil Moduli – Review of the Literature." *COE Report No. 1, Center of Excellence for Airport Pavement Research,* Dept. of Civil Engineering, University of Illinois, Illinois, USA

Uzan, J., (1985) "Characterization of Granular Material," *Transportation Research Record,* 1022, pp: 52-59.

Wright, S.E., (1983). "Damage Caused to Ballast by Mechanical Maintenance Techniques." *British Rail Research Technical Memorandum* TM TD.

Yoder, E.J. and Witczak, M.W., (1975). *Principles of Pavement Design 2nd Edition*. John Wiley and Sons, New York.

Zaman, M., Chen, D.H., and Laguros, J., (1994). "Resilient Moduli of Granular Materials." *Journal of Transportation Engineering*, 120 (6), pp. 967-988.